Cesium dihydrogen phosphate as electrolyte for Intermediate Temperature Proton Exchange Membrane Water Electrolysis (IT-PEMWE)

A Thesis Submitted By

ASIER GOÑI URTIAGA

For the Degree of Doctor of Philosophy

School Of Chemical Engineering and Advanced Materials (CEAM)
Newcastle University

Newcastle upon Tyne, United Kingdom.

May 2014

ABSTRACT

In this work the potential application of CsH_2PO_4 as intermediate temperature electrolyte for Proton Exchange Membrane Water Electrolysis (PEMWE) was studied. This material, from the phosphate-based solid acid family, was previously reported as a promising electrolyte for intermediate temperature PEM fuel cells although no study as electrolyte in a PEMWE system had been carried out before.

The physico-chemical properties of phosphate-based solid acids in terms of structure and morphology were investigated and their thermal stability evaluated. Proton conductivity at the intermediate temperature range (150 – 300 °C) was measured and the influence of humidity on the stability of CsH_2PO_4 in terms of dehydration and water solubility determined.

Different approaches for the fabrication of CsH_2PO_4-based membranes are proposed in order to improve the mechanical properties and reduce the thickness and ohmic resistance of the electrolyte. Membrane fabrication techniques including casting of polymer/CsH_2PO_4 composites, glass-fibre reinforcement, polymer doping or electrospinning were developed and the resulting membranes characterised in terms of structure, proton conductivity and mechanical stability.

The compatibility of CsH_2PO_4 with IrO_2 was evaluated and compared to standard acid electrolyte solutions in a three-electrode half-cell in the low temperature range (40 – 80 °C). The performance of IrO_2 towards oxygen evolution reaction (OER) in a CsH_2PO_4 concentrated solution exhibited poor activity, which was attributed to a high kinetic activation caused by the high pH and high phosphate concentration in solution.

Finally the performance of CsH_2PO_4 as solid-state electrolyte in the electrolysis cell was evaluated at intermediate temperatures (235 – 265 °C). Electrodes were optimised in terms of catalyst and ionomer loading for an intimate catalyst/electrolyte contact and characterised by cyclic voltammetry. The electrolysis system was characterised by quasi-steady polarisation curves and electrochemical impedance spectroscopy. The maximum performance obtained by a Pt/CsH_2PO_4/IrO_2 MEA system at 265 °C was 20 mA cm^{-2} at 1.90 V. This low activity, in good agreement with the results obtained in the half-cell, was mainly attributed to kinetic losses generated in the CsH_2PO_4/IrO_2 interface. The low acidity of the electrolyte is considered to affect the active oxidation state of iridium,

creating a non-hydrated oxide layer, which influenced negatively to the performance of the electrolyser.

It is therefore concluded that despite the promising results reported for CsH_2PO_4 as electrolyte in intermediate temperature fuel cells, this material, and presumably the rest phosphate-based solid acids, are not to be considered as potential electrolytes for PEM water electrolysers.

Keywords: Water electrolysis; proton exchange membrane (PEM); inorganic proton conductors; solid acids; intermediate temperature.

ACKNOWLEDGEMENTS

I would like to take this opportunity to thank all the people who helped and supported me during these years and thanks to whom I was able fulfill this work.

First of all I would like to sincerely thank my supervisor, Prof. Keith Scott, for offering me the opportunity to complete my postgraduate studies and for his guidance and support during my PhD. I would like to express a special thank to my colleague and friend Dr. Mohamed Mamlouk, for being always ready to help and to discuss any matters related, or not, to this work. Thanks also to Dr. Dimitrios Prevytes and Dr. Anca Dumitru for their advice and friendship during these years and to the rest of colleagues in the electrochemistry lab.

I want to thank the technical support team of CEAM for their help overcoming the many problems I found during this work and to the ACMA characterisation group for their help and advice with the characterisation of materials.

To the European Commission for their financial support through SUSHGEN (Sustainable Hydrogen Generation) project under the 7^{th} framework Marie Curie ITN program and to all the partners involved on it; Norges Teknisk-Naturvitenskapelige Universitet (NUTNU), Bulgarian Institute of Electrochemistry and Energy Systems (IEES), Foundation of Research and Technology - Hellas Institute of Chemical Engineering and High Temperature Process (FORTH/ICE-HT), CIDETEC - IK4 Research Alliance, Advent Technologies and Centre National de la Recherche Scientifique (CNRS) - Universite Montpellier 2. I would like to take the chance to thank Dr. Deborah J. Jones and Prof. Jacques Rozieré for offering me the opportunity to work in their facilities and to the entire group in Montpellier for the nice treatment I had from them in the three months I spent in the lovely south of France. I will not forget, of course, the great team of PhD students that gathered this project, which I am glad to be part of. Thank you Agnieszka, Anita, Nivedita, Stepan, Pablo and Radostina, I hope our paths cross again in the future.

Azkenik, ezingo nuke amaitu Algortan dauzkadan familia eta lagun guztiei nire esker beroenak eman gabe. Nahiz eta azkenengo urte hauetan asko ez bagaren ikusi, bueltatzen naizen bakoitzean etxean sentitzea zeozer paregabea bezain garrantzitsua delako niretzat. Beraz, nire gurasoei, anaiei eta, noski, kuadrillari, bihotz-bihotez, eskerrik asko.

And last but not least, thank you Fred, for being always there for me, no matter what.

TABLE OF CONTENTS

LIST OF FIGURES

CHAPTER 1 – INTRODUCTION AND OBJECTIVES

CHAPTER 2 – LITERATURE REVIEW. SOLID ACIDS

CHAPTER 3 – EXPERIMENTAL METHODS

CHAPTER 4 – SYNTHESIS AND CHARACTERISATION OF PHOSPHATE-BASED SOLID ACIDS

CHAPTER 5 – FABRICATION OF CsH_2PO_4-BASED PROTON CONDUCTING MEMBRANES

CHAPTER 6 – THE EFFECT OF THE ELECTROLYTE ON THE EAS AND OER

CHAPTER 7 – CsH_2PO_4 AS ELECTROLYTE IN IT-PEMWE

APPENDIX A – SUPPORTING INFORMATION

LIST OF TABLES

CHAPTER 1 – INTRODUCTION AND OBJECTIVES

CHAPTER 2 – LITERATURE REVIEW - SOLID ACIDS

CHAPTER 4 – SYNTHESIS AND CHARACTERISATION OF PHOSPHATE-BASED SOLID ACIDS

CHAPTER 5 – FABRICATION OF CsH_2PO_4-BASED PROTON CONDUCTING MEMBRANES

CHAPTER 6 – THE EFFECT OF THE ELECTROLYTE ON THE EAS AND OER

CHAPTER 7 – CsH_2PO_4 AS ELECTROLYTE IN IT-PEMWE

LIST OF NOMENCLATURE

Symbols:

b	Tafel slope	V dec^{-1}
C_p	Heat transfer coefficient	J mol^{-1}
D	Diffusion coefficient	m^2 s^{-1}
E	Cell potential	V
E_0	Standard cell potential	V
E_a	Activation energy	J mol^{-1}
E_{onset}	Onset potential	V
E_{rev}	Reversible cell potential	V
F	Faraday constant	C mol^{-1}
G_R	Gibbs free energy of reaction	J mol^{-1}
H_R	Enthalpy of reaction	J mol^{-1}
i	Current	A
i_0	Exchange current	A
i_L	Limiting current	A
R	Resistance	Ω
J	Flux density	mol m^2 s^{-1}
j	Current density	A cm^{-2}
j_0	Exchange current density	A cm^{-2}
j_L	Limiting current density	A cm^{-2}
K	Shape factor	Å
K_a	Acidity constant	
m	Mass	g
M	Molecular weight	g mol^{-1}
n	Number of electrons	
P	Pressure	bar
$P_×$	Partial pressure	bar
Q	Heat	J
q	Coulombic charge	C
q_{in}	Inner charge	C
q_{out}	Outer charge	C
q_T	Total charge	C
R	Gas constant	J K^{-1} mol^{-1}
S_R	Entropy of reaction	J $K^{-1}mol^{-1}$

T	Temperature	K
T_g	Glass-transition temperature	K
V_r	Reversible voltage	V
V_{th}	Thermoneutral voltage	V
Y	Young modulus	Pa
α	Charge transfer coefficient	
β’	Broadening	rad
β	Symmetry factor	
δ	Nerst diffusion layer	cm
η	Overpotential	V
η_{el}	Electrolyser efficiency	
θ	Bragg angle	rad
λ	Wavelength	Å
σ	Proton conductivity	S cm^{-1}
τ	Minimum crystallite size	Å

Abbreviations:

AWE	Alkaline water electrolysis
CDP	Cesium dihydrogen phosphate
CDP_f	Cesium dihudrogen phosphate fibers
$CDP_{f\text{-}RH}$	Rehydrated cesium dihudrogen phosphate fibers
CDP_p	Partially polymerized cesium dihydrogen phosphate
CE	Counter electrode
CEAM	Chemical engineering and advanced materials
CHS	Cesium hydrogen sulfate
CHSe	Cesium hydrogen selenate
CV	Cyclic voltammetry
DI	Deionised water
DMAc	Dimethyl acetamide
DSC	Differential scanning calorimetry
EAS	Electrochemical active surface
EDS	Energy dispersive X-ray spectroscopy
EIS	Electrochemical impedance spectroscopy
E-SEM	Environmental scanning electron microscopy
FEG	Field emission gun
GDE	Gas diffusion electrode

GDL	Gas diffusion layer
HER	Hydrogen evolution reaction
HHV	Higher heating value
HPA	Heteropolyacid
ICDD	International crystallographic diffraction database
IEA	International energy agency
iR	Ohmic resistance
IT	Intermediate temperature
LSV	Linear sweep voltammetry
MAS	Magic angle spinning
NMP	N-methyl-2-pyrrolidone
OER	Oxygen evolution reaction
PBI	Polybenzimidazole
PEM	Proton exchange membrane
PEMFC	Proton exchange membrane fuel cell
PEMWE	Proton exchange membrane water electrolysis
Pt/C	Carbon supported platinum
PVDF	Polyvinylidene difluoride
P-XRD	Powder X-ray diffraction
RDS	Rate determining step
RE	Reference electrode
RH	Relative humidity
RHE	Real hydrogen electrode
RIR	Relative intensity ratio
SHE	Standard hydrogen electrode
SOWE	Solid oxide water electrolysis
S-PEEK	Sulphonated poly-ether ether ketone
S-PSf	Sulphonated polysulphone
NMR	Nuclear magnetic resonance spectroscopy
TGA	Thermo-gravimetric analysis
UTS	Ultimate tensile strength
WE	Water electrolysis
WE	Working electrode
η_{An}	Anode overpotential
η_{Cath}	Cathode overpotential

CHAPTER 1

INTRODUCTION AND OBJECTIVES

In this chapter an overall view of the global energy production and consumption system is explained and the feasibility of hydrogen as an alternative energy carrier to carbon based fuels by different hydrogen sources and production methods studied. The potential role of renewable energies coupled to a water electrolysis system in the future energy scenario is discussed. The advantages (and disadvantages) of proton exchange membrane water electrolysis (PEMWE) over other different electrolysis methods is discussed and the attraction of operating in the intermediate operating temperature (150 – 300 °C) addressed. Finally the objectives of this research are described and an overview of the content of this thesis explained.

1.1. Background

For centuries human being has been exploiting the resources of the planet with no measure or conscience of the consequences that may arise from it. We now realise that the natural resources used for our every-day living are finite and at the rate of consumption of our increasing population, close to 7 billion people now, those resources will be soon finished. We are also aware of the high negative impact the human kind and our way of living have in the fragile equilibrium of the planet by burning fossil fuels and cutting down massive areas of forests. It is crucial for the wellbeing of the planet, and of course for our own and for the generations coming, that we change the energy production and consumption model our societies are based on to a more sustainable alternative [1, 2].

Nowadays more than 80 % of the total energy production of the planet is based on the combustion of fossil fuels such as oil, natural gas or coal (figure 1.1-a) [3]. This burning process produces high amounts of the so-called greenhouse gases (i.e. CO_2, CH_4) which are trapped in the atmosphere generating a global warming effect on the planet. The International Energy Agency (IEA) pictures a scenario in which global energy demand will rise by one-third in the period to 2012 – 2035, with a consequent rising of CO_2 emissions of 20 % [4]. Besides, the natural reservoirs of fossil fuel resources are limited and therefore different alternatives of energy resources must be considered in a short-term view.

Moreover, the distribution of these natural resources is uneven in the world (figure 1.1-b) which generates socio-political issues between countries and often ends in wars to gain their control with the consequent death of many innocent people. For instance, the Gulf War, taking place in 1990 – 1991, where the control of the oil reserves in the Middle East was the highest driving force, civilian casualties between 50.000 – 100.000 were estimated [5].

Energy security, as a concept of uninterrupted availability of energy sources at an affordable price, was introduced by the International Energy Agency (IEA) in 1974. It was created in order to secure and control the fuel supply (oil and natural gas mostly) and power generation in which the modern energy market is based on. The global character of this energy model and the uneven location of fossil fuel reservoirs, localised in few countries or regions in the world, makes the management and control of this energy system very complicated and highly dependent on political agreements.

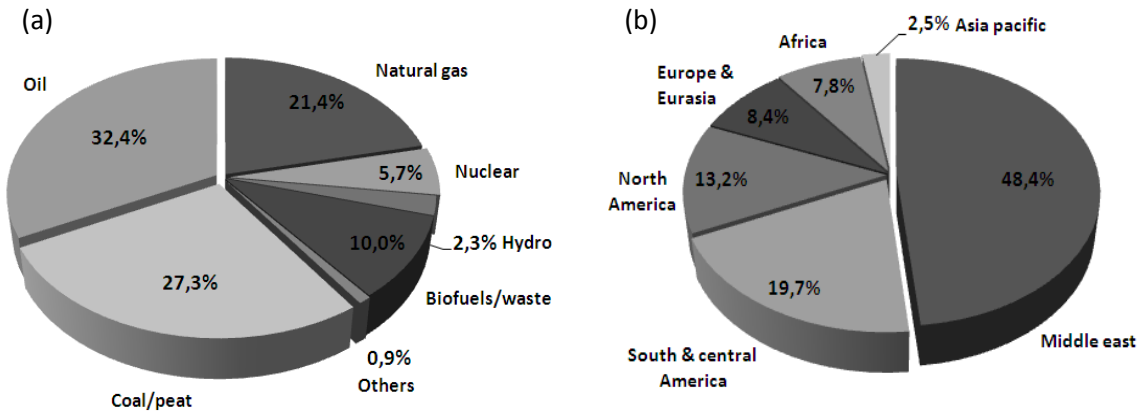

Figure 1.1. Pie charts of (a) the total world energy supply by source at 2010 ('others' includes wind, solar, thermal, etc.) [3] and (b) world distribution of proved oil reserves in 2012 [6].

Energy production in big oil, natural gas and coal thermal plants or nuclear plants is nowadays the mayor electricity production system. The system operates in a centralised manner where high amounts of electricity are produced in a specific location and then distributed to the grid for its consumption by the user. This energy production system exhibits two main drawbacks; (1) a high energy loss by the electric power transmission through the grid and (2) the control of electricity prices is strongly influenced by the fuel producer. The first of these issues is mainly caused by the transmission of electricity by cable networks, where a considerable amount of the energy transmitted in electricity form is lost as heat derived from the *Joule effect*, this is, the production of heat resulting from

current flowing through a conductor. Some of the energy losses are also produced by the transformers in the power plant. Overall, the total energy loss between a power plant and users varies between 8 – 15 % [7]. The second issue mentioned, that is, the variability on the price of electricity, is greatly influenced by the fuel price and supply, which is determined by the fuel producer. Although the global energy market running nowadays is complicated and depends on many variables, the fuel and electric power production in a centralised and global model is the basic issue that allows the producers to control the price [8]. For these reasons the local production of energy in a decentralised manner or in small communities is of great interest.

Alternative ways of energy production by sustainable resources such as wind or solar energy have been proposed in the last decades. Learning how to use these renewable and unlimited energy sources in an efficient way is necessary to develop and implement the technology. The main drawback of the mentioned renewable energy sources, such as wind or solar power, is that the energy is not produced in a continuous and homogeneous rate. This variability in the power production makes the balance between energy production (electricity produced by generators) and energy demand (electricity consumed) decompensated and therefore many energy excesses and shortages are produced. The storage of those energy excess peaks is the key technological issue for a real implantation of these renewable technologies [9].

As electricity cannot be efficiently stored it must be used the same instant it is produced, meaning that supply and demand must always be balanced. One of the ways to storage this excess power is the production of hydrogen, which has to be synthesised by input of energy, as it does not exist in nature in its molecular structure. It acts as an energy carrier (or vector), storaging the energy applied to produce it as chemical energy. This hydrogen can then be utilised for electricity production in hydrogen fuel cells, which being electrochemical devices not dependant on Carnot´s cycle, exhibit efficiencies as high as 60 % and produce as only emissions heat and water. When water is used as the source of hydrogen production by renewable energy, this energy production/consumption model is often called the *Hydrogen cycle*. It is very important, for this cycle to be sustainable and in order to build this model independent from fossil fuels, that the energy used for hydrogen production comes from a renewable source and the hydrogen prime source to be non-fossil, preferably water.

Although there are many different methods for hydrogen production and nowadays most of it is produced from fossil fuels, the electrolysis of water by renewable energy input is one of the few methods to proof sustainable in the *hydrogen cycle*. 'Green hydrogen' can be produced by coupling a water electrolysis system to either wind or solar power plants, for instance. Besides, the scale of these systems is very broad, being able to produce hydrogen in relatively small plants, in a local scale and for local consumption, without high environmental impact. The energy model based on the production of hydrogen is a real alternative for the implementation of renewable energies in our societies and for the necessary change to a more sustainable and environmentally friendly energy system [10].

1.2. H_2 production by Water Electrolysis

Nowadays most of the global production of hydrogen is used in industrial processes such as the production of ammonia, oil processing or as a hydrogenating agent. Only ca. 1 % of the produced hydrogen is used as direct energy source, mostly in space programs [11]. The hydrogen used for these purposes is mainly produced from fossil fuels; natural gas, oil (as side product in refinering) and coal (figure 1.2).

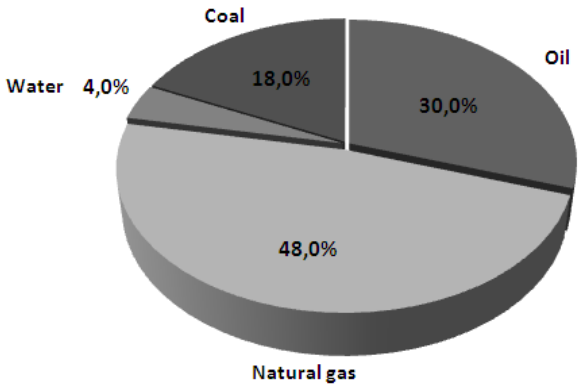

Figure 1.2. Hydrogen production by source at 2008 [12].

The mayor hydrogen production methods comprise thermal processes, such as steam reforming of natural gas, gasification of coal or biomass or thermochemical water splitting (produced in nuclear fission reactors). All these processes generate undesirable side products, either greenhouse gas emissions or nuclear waste. In order to build an energy model, independent from fossil fuels, the production of hydrogen needs to be based on water. However, the global production of hydrogen from water is only of ca. 4 %, mostly produced by alkaline electrolysis, due to its higher cost of production comparing to the

above mentioned thermal methods [12]. The development of a highly efficient electrolysis system with low cost materials is therefore needed for a higher implementation of this technology in hydrogen production.

The electrochemical conversion of water to hydrogen and oxygen is considered a well-known principle to produce oxygen and hydrogen gas, first observed by Henry Cavendish in 1766 [13]. The core of an electrolysis unit is an electrochemical cell, which is filled with pure water and has two electrodes connected to an external power supply. At a certain potential, the electrodes start to produce hydrogen gas at the negative electrode and oxygen gas at the positive electrode following equation 1.1.

$$H_2O \rightarrow \frac{1}{2} O_2 + H_2 \qquad (1.1)$$

The amount of gases produced per unit time is directly related to the current that passes through the electrochemical cell. Nicholson and Carlisle developed this technique in 1800 by inducing a static charge to acidic water. In 1939 the first large water electrolysis plant with a capacity of 10,000 $Nm^3H_2\ h^{-1}$ was built and started operating [13, 14].

From its early days water electrolysis has been greatly studied and different electrolysis methods were developed. The main three electrolysis methods operating nowadays are Alkaline Water Electrolysis (AWE), Proton Exchange Membrane Water Electrolysis (PEMWE) and Solid Oxide Water Electrolysis (SOWE) or Steam Electrolysis [15]. The main differences in the characteristics of these systems are given in table 1.1.

Figure 1.1. Characteristic of different types of electrolysers.

	AWE	**PEMWE**	**SOWE**
Charge carrier	OH^-	H^+	O^{2-}
Reactant	H_2O	H_2O	H_2O, CO_2
Electrolyte	NaOH or KOH	Polymer	Ceramic
Electrode	Raney Ni	Pt, Ir	Ni-cermet
Temperature / °C	40 – 90	20 - 90	800 - 1000

Alkaline Water Electrolysis (AWE) is a mature and reliable process, highly developed since its first operating system in 1978. It is the standard technology for large scale water electrolysis nowadays [16]. It operates using an alkaline solution of KOH or NaOH (ca. 30 % wt.) as electrolyte, nickel electrode in the anode and carbon supported platinum or nickel electrode in the cathode. A porous diaphragm, conventionally asbestos, although recently polymeric porous films or NiO diaphragms are under investigation, is used to avoid the produced gases from mixing together. The principle of this process is based on the reduction of two molecules of water to one molecule of hydrogen and two hydroxyl ions at the cathode. The hydrogen escapes from the surface of the cathode in gaseous form and the hydroxyl ions migrate under the influence of the electrical field between cathode and anode through a porous diaphragm. In the anode the two hydroxyl ions are combined to form ½ molecule of oxygen and one molecule of water. These reactions are shown in equations 1.2 and 1.3. This system usually operates at a potential range of 1.8 – 2.2 V with current densities varying between 0.2 – 0.6 A cm^{-2} [16]. It exhibits efficiencies between 70 - 85 %, based on the High Heating Value (HHV) of hydrogen, depending on the operating potential (equation 1.12).

$$\text{Cathode (-):} \quad 2H_2O + 2e^- \rightarrow H_2 + 2OH^- \tag{1.2}$$

$$\text{Anode (+):} \quad 2OH^- \rightarrow \tfrac{1}{2}\, O_2 + H_2O + 2e^- \tag{1.3}$$

In order to reduce the cathodic overpotential and improve the efficiency of these devices great effort has been focused in the development of alternative catalysts for hydrogen evolution. Mostly transition metal bi or trimetallic compounds, such as $PtMo_3$ or PdTi, are under investigation for this purpose [17]. Investigations on non-precious materials, catalysts based on Ni or Fe, have also been carried out in order to reduce the overall cost of the device [18]. Although conventional alkaline electrolysers operate at a pressure range of 1 – 5 bar, more developed advanced electrolysers can operate at elevated pressure, as high as 30 bar [19]. This high pressure provides a way to reduce the cost of further pressurisation of hydrogen to the overall process.

The first ***Proton Exchange Membrane Water Electrolyser (PEMWE)***, or solid polymer electrolyte (SPE) electrolysis system, was built by General Electric [20] after the development of Nafion® proton exchange membrane by Dupont. The system was then developed by Membrel electrolyser technology over the years 1976 – 1989 [21]. Big effort

for the development of this technology is still carried out nowadays. The heart of this system is the so-called Membrane Electrode Assembly (MEA). The MEA is composed of a proton conducting membrane (i.e. perfluorosulfonic polymer, such as Nafion®) sandwiched between two electrodes, with platinum in the cathode (hydrogen evolution) and a metal oxide (i.e. iridium oxide) in the anode (oxygen evolution). The reactions taking place in the system are shown in equations 1.4 and 1.5. The catalysts are in contact with a gas diffusion layer, which is commonly based on carbon fibres in the cathode and porous titanium in the anode. Each of these electrodes is also in contact with a bipolar plate in order to build a single PEM electrolysis cell. An electrolysis stack is built by assembling in series several of these cells. The system can exhibit efficiencies as high as 90 %, based on the High Heating Value (HHV) of hydrogen [22].

$$\text{Anode (+):} \quad H_2O \rightarrow \tfrac{1}{2}O_2 + 2H^+ + 2e^- \tag{1.4}$$

$$\text{Cathode (-):} \quad 2H^+ + 2e^- \rightarrow H_2 \tag{1.5}$$

Highly pure water is fed to the anode, where oxygen evolution takes place. The protons produced in the electrochemical reaction in presence of metal oxide catalyst (i.e. IrO_2) travel through the proton conducting membrane to the cathode. There, the protons and electrons recombine in presence of platinum to form hydrogen gas.

Although in industrial plants the alkaline medium is preferred to acidic systems, because of a more easily controlled corrosion and cheaper construction materials, PEMWE exhibits several advantages over AWE systems. First, PEMWE can operate at much higher current densities, being able to operate up to 3.0 A cm^{-2} in comparison to 0.2 – 0.6 A cm^{-2} current densities exhibited by AWE at 1.8 – 2.2 V [16, 22, 23]. Secondly, as in PEMWE system a solid thin membrane is used as electrolyte, the volume of the cell is greatly reduced, and thus, stacks can be fabricated in a modular way. This is a very important characteristic to take into account for a decentralised hydrogen production system, where hydrogen is produced in a low scale in small communities, and issues related to its distribution are reduced [10]. PEMWE are also prepared to operate at high differential pressures, being able to directly produce pressurised and highly pure hydrogen. Although a lifetime of 5 years is considered to be achievable in PEMWE [24], durability is still an issue needing to be addressed in these systems. Recent studies proved a stable operating PEMWE system with catalyst loadings as low as 0.1 – 0.2 mg cm^{-2} for 4000 h with no degradation [25].

Solid Oxide Water Electrolysis (SOWE), or steam electrolysis, is a promising technology, still under development, which can reach higher efficiencies than alkaline or PEM electrolysis systems [26]. This system operates at temperatures between 800 – 1000 °C. This high temperature provides a series of advantages over the rest electrolysis technologies. From a thermodynamic point of view, the electric energy demand required to split a molecule of water, that is, the Gibbs free energy of the process, is considerably reduced (figure 1.4-a). Besides, the high temperature accelerates the reaction kinetics, reducing the overpotential of the reactions and providing higher efficiency to the electrolysis cell. It was reported single cells operating at 0.3 mA cm^{-2} current densities achieving 100% of Faraday efficiency at a voltage as low as 1.07 V [27].

This technology employs oxygen ion conducting ceramics as electrolytes, such as ZrO_2 - stabilised Y_2O_3, MgO or CaO, nickel-cermet electrode for hydrogen evolution and lanthanum, strontium and cobalt mixed oxide electrode for oxygen evolution. Water vapour is fed to the cathode where it splits to hydrogen gas and O^{2-} ions. The oxygen ions are then transported through the ceramic electrolyte to the anode, where they combine to form oxygen gas. These reactions are shown in equations 1.6 and 1.7.

$$\text{Cathode (-):} \quad H_2O + 2e^- \rightarrow H_2 + O^{2-} \tag{1.6}$$

$$\text{Anode (+):} \quad O^{2-} \rightarrow \tfrac{1}{2} O_2 + 2e^- \tag{1.7}$$

Lately, proton conducting ceramic materials have also been under investigation for their application as electrolytes in PEM steam electrolysis. These systems use materials such as Y-doped $BaZrO_3$ or $SrCeO_3$-based perovskites for the electrolyte [28], being the reactions taking place in the system the same as shown in equations 1.4 and 1.5. These materials operate at a more modest temperature range of 500 – 800 °C.

Although advantageous in many ways, operating a system at such high temperatures carry other important issues, such as material degradation. The materials used to build the electrolysis cell must be corrosion resistant at high temperature and voltage, and issues such as the durability of the ceramic materials, sealing materials or the thermal expansion factors must be well addressed. The development of this technology is therefore focused in material science and in the engineering of the cell [23, 29].

In order to take advantage of the higher efficiency provided at high temperature and overcome the issue of the aggressive conditions subjected to the materials, high interest has

grown in the development of an intermediate temperature (100 – 300 °C) PEM electrolysis system. At this temperature range, the conditions are much milder and therefore a higher variety of materials can be used for the fabrication of the electrolysis cell. The main issue to make this system operate is that few materials have been proved to be proton conductors in the intermediate temperature range. The development of an intermediate temperature proton conducting membrane is therefore a critical issue for the development of this technology in the future.

1.3. Intermediate Temperature Proton Exchange Membrane Water Electrolysis (IT-PEMWE)

The electrochemical conversion of water to hydrogen and oxygen by utilising a renewable electrical energy source provides a clean and efficient way to produce pure hydrogen while reducing dependence on carbon based fuels [30]. In addition, water electrolysis offers a convenient method of localised hydrogen supply which overcomes problems and issues of its distribution [31, 32]. Although alkaline electrolysis is currently the dominant technology used due to its lower cost, proton exchange membrane water electrolysis (PEMWE) (figure 1.3) offers a series of advantages of great importance. It enables hydrogen production from pure water and electricity and has greater energy efficiency, higher production rates per unit electrode area and a more compact design. Nevertheless, because of its high electric energy requirement, there is no large scale use of PEMWE systems. There is a number of variables which have to be studied in order to enhance the performance of this device and the overall electrolysis system efficiency for more widespread commercial adoption.

The main variables affecting the operating behaviour of the electrolyser are temperature and pressure, while the water management in the system plays a very important role. Increasing the operating temperature can have multiple beneficial effects in the system, such as the reduction of the required electrical energy and faster electrode kinetics. An increased operating pressure would lead to increased overall system efficiency as direct production of pressurised hydrogen could be carried out. Designing the system in such a way that only one reactant phase is present in each chamber (gaseous phase), would greatly simplify the system and eliminate the need of elegant solutions to avoid water management. The above points are discussed in detail below.

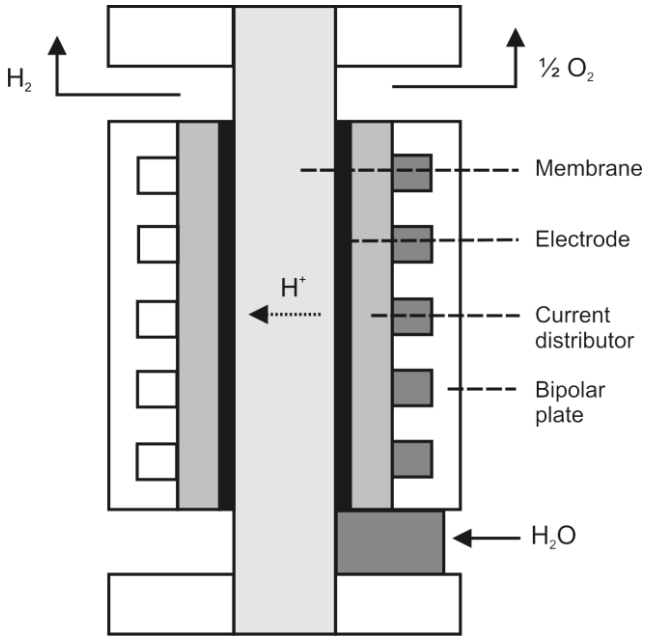

Figure 1.3. Schematic drawing of a PEM electrolysis cell [33].

1.3.1. Temperature

Two reactions take place in a PEM electrolyser; water splitting in the anode (oxygen evolution reaction) and hydrogen evolution (proton reduction) in the cathode (equations 1.4 and 1.5). The enthalpy of formation of one mole of water corresponds to the energy required to split one mole of water into hydrogen and oxygen. A fraction of this amount of energy, according to the second principle of thermodynamics, can be applied as thermal energy thus reducing the amount of electrical energy required (equations 1.8 – 1.9) [33, 34]:

$$\Delta H_R = \Delta G_R + T\Delta S_R \quad (1.8)$$

$$\Delta H_R = \Delta G_R + Q \quad (1.9)$$

Where ΔH_R stands for enthalpy of reaction of water splitting, ΔG_R for the Gibbs free energy of reaction, which corresponds to the minimum amount of energy that needs to be applied as electrical energy and $T\Delta S_R$ represents the product of entropy of reaction and temperature, which corresponds to the maximum amount of energy that needs to be applied as heat, termed Q in the above equation.

The thermoneutral voltage, V_{th}, corresponding to the minimum cell voltage required to split a mole of water, is related to the total energy demand, ΔH_R. The reversible voltage,

V_r, is related to the electric energy demand, ΔG_R, of the cell. These relations are shown in equations 1.10 and 1.11.

$$V_{th} = \frac{\Delta H_R}{nF} \tag{1.10}$$

$$V_r = \frac{\Delta G_R}{nF} \tag{1.11}$$

where n is the amount of electrons exchanged in the electrochemical reaction and F is Faraday constant (96485 C mol^{-1}). As depicted in figure 1.4-a, the enthalpy, ΔH_R, which corresponds to the total energy demand of the reaction, exhibits a sudden drop at 100 °C after which it rises slightly with temperature. That sudden drop corresponds to the enthalpy of evaporation of water. The fraction of the total energy needed as electricity, ΔG_R, decreases with increasing the temperature while the fraction corresponding to heat requirement, Q, increases. The sum of the two, as expressed in equation 1.8, is almost constant (considering the slight increase in ΔH_R). The thermoneutral, V_{th}, and reversible potential, V_r, are directly proportional to ΔH_R and ΔG_R respectively and therefore follow the same trend (figure 1.4-b). Above 100 °C V_{th} increases only slightly with increasing the temperature while V_r drops significantly [30, 35]. The electric energy applied in an electrolyser for water splitting reaction results in a significant amount of heat generated. This heat is used towards heat requirement, Q, which is needed for the reaction. The thermodynamic efficiency of the electrolyser is defined in equation 1.12.

$$\eta_{el} = \frac{HHV_{H_2}}{(\Delta G_R + Q)} \tag{1.12}$$

where HHV_{H2} is the produced hydrogen higher heating value and ΔG_R and Q the electricity and heat used, respectively. With HHV_{H2} corresponding to ΔH_R at 25 °C and 1 atm and taking into account that Q = 0 because the operating potential is higher than the thermoneutral potential, the efficiency becomes:

$$\eta_{el} = \frac{\Delta H_R}{\Delta G} \;\leftrightarrow\; \eta_{el} = \frac{V_{th}}{V} \tag{1.13}$$

The efficiency of the electrolyser is thus inversely proportional to the potential of the cell. However, as the applied potential is above the thermoneutral voltage an excess of heat is

produced making the use of a cooling system necessary, affecting the overall efficiency and complexity of the system. It is worth noting that although the thermodynamic efficiency drops by increasing the temperature, the overall system efficiency can increase because of improved kinetics and reduced ohmic losses at higher temperatures.

In the case of conventional PEM electrolysis, liquid water has to be fed in the anode. Another advantage of working in temperatures above 100 °C is the presence of only gaseous phase of reactants in the electrode compartment. Therefore water management does not need to be taken into account when designing the system. A possible problem in intermediate temperature PEM electrolysis could be the formation of cold spots during start-up and shut-down of the system which could lead to water condensation.

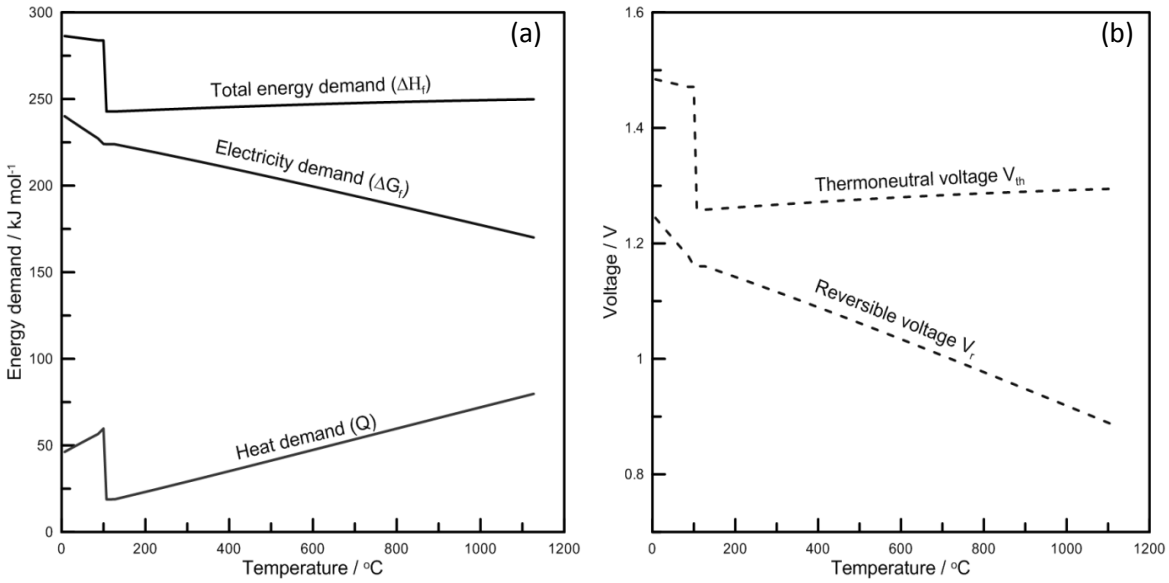

Figure 1.4. Temperature dependence of (a) enthalpy, Gibbs free energy and heat requirement and (b) thermoneutral and reversible potentials, for water splitting reaction in liquid and gaseous phase at 1 atm.

1.3.2. Pressure

A proton exchange membrane (PEM) electrolyser can also work under pressurised conditions [30]. The operating pressure will affect the potential of the electrolyser according to Nerst equation:

$$E = E_0 - RTln\frac{\left(P_{H_2}P_{O_2}^{1/2}/P_{H_2O}\right)}{nF} \tag{1.14}$$

where E is the applied potential, E_0 the standard potential and P_x is the partial pressure of the reactants. As pressure is increased in the device, each species' partial pressure increases, as well as its concentration. If we consider that there is no pressure gradient in the two sides of the membrane the above equation changes to equation 1.15.

$$E = E_0 - RTln\frac{\left(1/P^{1/2}\right)}{nF} \tag{1.15}$$

Operating a pressurised electrolyser could prove advantageous in several ways. Direct production of pressurised hydrogen can simplify the overall system and reduce the cost as the use of an external compressor can be avoided. *Marangio et al*. compared the power needed for the operation of an atmospheric electrolyser system with subsequent compression of the produced H_2 versus the power needed by pressurised electrolysis systems [36]. They concluded that the required power in the case of pressurised electrolysers is smaller, as shown in figure 1.5. This conclusion has been supported by other groups for PEM electrolysis [37, 38]. Nevertheless, operating at high pressure has been reported to increase hydrogen permeation through the membrane which, not only reduces the efficiency and degrades product quality, but may also exhibit safety issues [30].

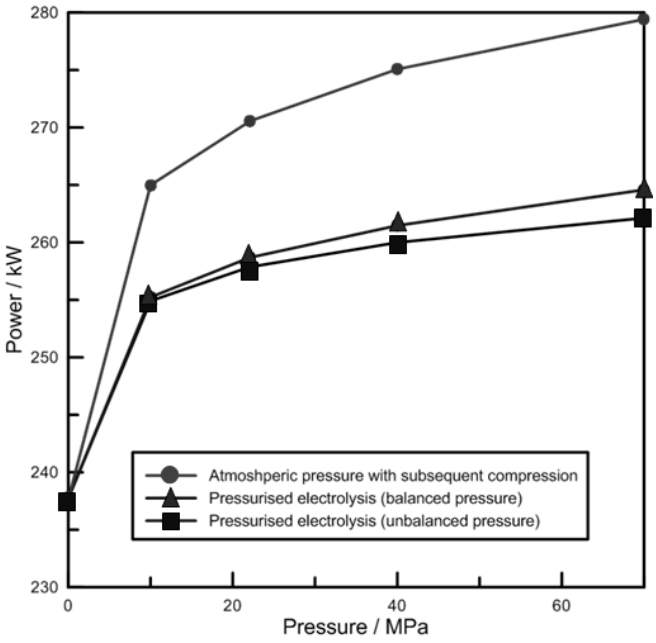

Figure 1.5. Comparison of required power vs pressure to produce 1 mol s^{-1} (80.64 Nm^3 h^{-1}) of hydrogen in system operating at ambient temperature with subsequent pressurisation and pressurised systems [36].

1.3.3. Previous work in IT-PEMWE

In spite of the advantages arising from operating the electrolysis system in the intermediate temperature range (100 - 300 °C) from the thermodynamic, kinetic and engineering point of view, few studies have been reported in the area. The main drawback to develop this technology is accessing suitable proton conducting materials in this temperature range.

The use of conventional proton exchange polymeric membrane, such as Nafion® or sulfonated polyethers, in a pressurised PEM electrolysis system at 125 – 150 °C has been reported [39]. As the higher pressure of the system allows the presence of liquid water at temperatures higher than 100 °C, conventional proton conducting membranes with proton conducting mechanism based on water can be used. When the system is not pressurised and liquid water is not present to act as proton carrier, this type of membranes cannot be used. An alternative is to substitute water by phosphoric acid as the proton carrier. *Aili et al.* reported a PEMWE system operating with H_3PO_4 – doped Nafion® and H_3PO_4 – doped polybenzimidazole (PBI) as electrolyte at ambient pressure and 130 °C. Performances of 300 mA cm^{-2} and 500 mA cm^{-2} at 1.75 V were obtained respectively, although H_3PO_4/PBI system exhibited much lower durability [40]. *Hansen et al.* also reported a PEMWE system operating with H_3PO_4 – doped Aquivion® with values of 775 mA cm^{-2} at 1.80 V, also at 130 °C and ambient pressure [41]. They also reported degradation issues due to the presence of free phosphoric acid at high temperature and high potentials. Durability issues related to the corrosion of titanium-based electrodes and bipolar plates were also reported [42]. Important durability and corrosion issues are therefore related to IT-PEMWE system based on phosphoric acid-doped membranes. This is caused by the presence of free phosphoric acid in the system, which permeates through to membrane to the electrodes and bipolar plates. It has also been widely reported that this free H_3PO_4 limits the kinetics of oxygen reduction reaction (ORR) by the low oxygen permeability and phosphate adsorption onto the catalyst surface [43, 44]. These kinetic limitations are also expected to happen in the oxygen evolution reaction (OER) taking place in the electrolyser.

In order to develop an intermediate temperature proton conducting electrolyte without the presence of free phosphoric acid, research focused on inorganic materials such as solid acids *(see Chapter 2)*, heteropolyacids [45] or pyrophosphates [46] and composite polymeric/inorganic materials [47] are being widely studied. Although considerable effort has been made in the study of these intermediate temperature solid proton conductors for

PEMFCs, the sister technology to PEMWE, the application of these materials in a PEM electrolysis system has not been yet reported.

The development of an intermediate temperature PEMWE system remains therefore as a challenge, where material development and system engineering play an important role.

1.4. Research objectives

This research is focused in the study of solid acid proton conducting materials for application as electrolyte in an intermediate temperature proton exchange membrane water electrolyser (IT-PEMWE).

The research objectives were the following:

- Synthesis and characterisation of medium temperature proton conducting phosphate-based solid acids in order to select the most promising material for application as electrolyte in a water electrolyser.
- Determine the feasibility of CsH_2PO_4 as electrolytic material in an IT-PEMWE in terms of physico-chemical stability.
- Develop different methodologies to fabricate thin membranes based on CsH_2PO_4 to use in the electrolyser cell and provide lower ohmic resistance than a pellet.
- Study the effect of CsH_2PO_4 as electrolytic aqueous medium in the activity of IrO_2 towards oxygen evolution reaction (OER) by half-cell electrochemical characterisation.
- Investigate the viability of CsH_2PO_4 as electrolyte to develop a phosphoric acid-free proton exchange membrane water electrolyser in the intermediate temperature range (230 – 300 ºC).

1.5. Overview of the thesis

This thesis is presented as a series of eight chapters. All experimental work was carried out by the author, Asier Goñi-Urtiaga at the school of Chemical Engineering and Advanced Materials in Newcastle University, unless stated, such as the results obtained in a three-moth secondment in CNRS-Montpellier II Université (France) or material characterisation results obtained by the University of Durham. In the end of all chapters a reference section

is included where the bibliography used is summarised. The content of the thesis is divided as follows:

Chapter 1 gives an overview of the global energy production and consumption systems in use nowadays and the negative effects arising from them. Hydrogen is proposed as an alternative energy carrier and its sustainable production from water and renewable energy sources by electrolysis is explained. The advantages of intermediate temperature PEM water electrolysis over other electrolysis system are defended and the drawbacks for the development of this technology explained.

In *Chapter 2* a literature review of intermediate temperature proton conductors is carried out with special focus on solid acids. The characteristics of this family of materials are discussed and their applicability in PEM water electrolysis systems considered.

Chapter 3 describes the experimental methods used in this research. The physico-chemical and electrochemical characterisation techniques performed for the study and evaluation of materials are detailed and the measurement conditions described.

Chapters 4, 5, 6 and 7 describe and discuss the experimental results obtained during the three years of this research.

In *Chapter 4* the synthesis and characterisation of phosphate-based solid acids is explained. The properties of these materials in terms of crystal structure, morphology, proton conductivity and thermal stability are evaluated. The suitability, in terms of physical and chemical stability, of CsH_2PO_4 as proton conducting electrolyte for application in a PEM water electrolysis system is further studied.

In *Chapter 5* five different methods for the fabrication of composite membranes based on CsH_2PO_4 are proposed. The properties of the resulting membranes in terms of composition, proton conductivity and mechanical strength are evaluated and their applicability as proton conducting electrolytes discussed.

Chapter 6 explores the effect of CsH_2PO_4, as electrolyte in its aqueous form, on the electrochemical active surface (EAS) of platinum black and iridium oxide and on the activity of iridium oxide towards oxygen evolution reaction (OER). All results are compared to aqueous solutions of sulfuric and phosphoric acids. Kinetic parameters for the evaluation of CsH_2PO_4 as electrolytic medium are calculated and discussed.

In *Chapter 7* the evaluation of CsH_2PO_4 as a solid state proton conducting electrolyte in PEM water electrolysis is carried out. The effect of the ohmic and kinetic losses provided by the electrolyte in the overall performance of the electrolysis system is analysed and discussed.

Chapter 8 summarises the conclusions obtained in this research and evaluates the applicability of CsH_2PO_4 as proton conducting material for application in intermediate temperature PEM water electrolysis. Different approaches and suggestions for potential future work are proposed.

Appendices A and B gather the supporting experimental data and the list of publications and dissemination of this work, respectively.

1.6. References

1. Goldemberg, J., *The promise of clean energy*. Energy Policy, 2006. **34**(15): p. 2185-2190.
2. Everett, R., Boyle, G., Peake, S. and Ramage, J., *Energy Systems and Sustainability: Power for a Sustainable Future*. 2012: Oxford Univerity Press.
3. I.E.A., *Key world energy statistics.* www.iea.org, 2012.
4. I.E.A., *World Energy Outlook.* WEO 2013, 2013.
5. Fisk, R., *The great war for civilisation: the conquest of the Middle East*. 2006: Harper Collins UK.
6. B.P., *BP Statistical Review of World Energy* June 2013.
7. I.E.C., *Efficient electrical energy transmission and distribution.* International Electrotechnical Commission, 2007.
8. Michaels, R., *The Concise Encyclopedia of Economics. Electricity and Its Regulation.* Library of Economics and Liberty, 2008.
9. Chen, H., Chen, H., Cong, T.N., Tan, C., Li, Y. and Ding, Y., *Progress in electrical energy storage system: A critical review.* Progress in Natural Science, 2009. **19**(3): p. 291-312.
10. Clarke, R.E., S. Giddey, and S.P.S. Badwal, *Stand-alone PEM water electrolysis system for fail safe operation with a renewable energy source.* International Journal of Hydrogen Energy, 2010. **35**(3): p. 928-935.
11. Mueller-Langer, F., Tzimas, E., Kaltsmitt, M. and Peteves, S., *Techno-economic assessment of hydrogen production processes for the hydrogen economy for the short and medium term.* International Journal of Hydrogen Energy, 2007. **32**(16): p. 3797-3810.
12. Evers, *Hydrogen Association.* 2008.
13. Stock, J.T., *Two centuries of quantitative electrolytic conductivity.* Analytical Chemistry, 1984. **56**(4): p. 561A-570A.
14. Kreuter, W. and H. Hofmann, *Electrolysis: The important energy transformer in a world of sustainable energy*. International Journal of Hydrogen Energy, 1998. **23**(8): p. 661-666.
15. Zoulias, E., Varkaraki, E., Lymberopoulos, N., Christodoulou, C.N. and Karagiorgis, G.N., *A review on water electrolysis.* TCJST, 2004. **4**(2): p. 41-71.
16. Zeng, K. and D. Zhang, *Recent progress in alkaline water electrolysis for hydrogen production and applications.* Progress in Energy and Combustion Science, 2010. **36**(3): p. 307-326.
17. Stojić, D.L., Grodzic, T.D., Umicevic, B. and Maksic, A.D., *A comparison of alkaline and proton exchange membrane electrolyzers.* Russian Journal of Physical Chemistry A, Focus on Chemistry, 2008. **82**(11): p. 1958-1960.
18. Kjartansdóttir, C.K., L.P. Nielsen, and P. Møller, *Development of durable and efficient electrodes for large-scale alkaline water electrolysis.* International Journal of Hydrogen Energy, 2013.
19. Varkaraki, E., N. Lymberopoulos, and A. Zachariou, *Hydrogen based emergency back-up system for telecommunication applications.* Journal of Power Sources, 2003. **118**(1–2): p. 14-22.
20. LaConti, A., A. Fragala, and J. Boyack. *Solid polymer electrolyte electrochemical cells-Electrode and other materials considerations*. in *Symposium on Electrode Materials and Processes for Energy Conversion and Storage*. 1977.

21. Oberlin, R. and M. Fischer, *Status of the Membrel Process for Water Electrolysis.* Hydrogen Energy Progress VI, 1986. **1**: p. 333-40.

22. Millet, P., Mbemba, N., Grigoriev, S.A., Fateev, V.N., Aukaulo, A. and Etiévant, C., *Electrochemical performances of PEM water electrolysis cells and perspectives.* International Journal of Hydrogen Energy, 2011. **36**(6): p. 4134-4142.

23. Carmo, M., Fritz, D.L., Mergel, J. and Stolten, D., *A comprehensive review on PEM water electrolysis.* International Journal of Hydrogen Energy, 2013. **38**(12): p. 4901-4934.

24. Millet, P., Dragoe, D., Grigoriev, S., Fateev, V. and Etievant, *GenHyPEM: A research program on PEM water electrolysissupported by the European Commission*. International Journal of Hydrogen Energy, 2009. **34**: p. 4974–4982

25. Debe, M.K., Hendricks, S.M.,Vernstrom, G.D., Meyers, M., Brostrom, M., Stephens, M., Chan, Q.,Willey, T., Hamden, M., Mittelsteadt, C.K.,Capuano, C.B.,Ayers K.E. and Anderson, E.B., *Initial Performance and Durability of Ultra-Low Loaded NSTF Electrodes for PEM Electrolyzers.* Journal of The Electrochemical Society, 2012. **159**(6): p. K165-K176.

26. Doenitz, W. and E. Erdle, *High-temperature electrolysis of water vapor—status of development and perspectives for application.* International Journal of Hydrogen Energy, 1985. **10**(5): p. 291-295.

27. Laguna-Bercero, M.A., *Recent advances in high temperature electrolysis using solid oxide fuel cells: A review.* Journal of Power Sources, 2012. **203**(0): p. 4-16.

28. Kreuer, K., *Proton-conducting oxides.* Annual Review of Materials Research, 2003. **33**(1): p. 333-359.

29. Lessing, P., *A review of sealing technologies applicable to solid oxide electrolysis cells.* Journal of Materials Science, 2007. **42**(10): p. 3465-3476.

30. Barbir, F., *PEM electrolysis for production of hydrogen from renewable energy sources.* Solar Energy, 2005. **78**(5): p. 661-669.

31. Erdle E, G.J., Meyringer V, *Proceedings of the Third International Workshop.* Vol. 2 High Temperature Technology and its Applications: p. pp. 23–27.

32. Sherif, S.A., F. Barbir, and T.N. Veziroglu, *Wind energy and the hydrogen economy—review of the technology.* Solar Energy, 2005. **78**(5): p. 647-660.

33. Smolinka, T., *Encyclopedia of electrochemical power sources.* Institute for Solar Energy Systems ISE, Freiburg, Germany, 2009: p. 394.

34. Laoun, B., *Revue des Energies Renouvelables.* 2007. **10**: p. 435.

35. LeRoy, R., Bowen, CT., *The thermodynamics of aqueous water electrolysis.* Journal of The Electrochemical Society, 1980. **127**: p. 1954-1962.

36. Marangio, F., Pagani, M., Santarelli, M. and Cali, M., *Concept of a high pressure PEM electrolyser prototype.* International Journal of Hydrogen Energy, 2011. **36**(13): p. 7807-7815.

37. Onda, K., Kyakuno, T., Hattori, K. and Ito, K., *Prediction of production power for high-pressure hydrogen by high-pressure water electrolysis.* Journal of Power Sources, 2004. **132**(1–2): p. 64-70.

38. Degiorgis, L., M. Santarelli, and M. Calì, *Hydrogen from renewable energy: A pilot plant for thermal production and mobility.* Journal of Power Sources, 2007. **171**(1): p. 237-246.

39. Linkous, C.A., Anderson, H.R., Kopitzke, R.W. and Nelson, G.L., *Development of new proton exchange membrane electrolytes for water electrolysis at higher temperatures.* International Journal of Hydrogen Energy, 1998. **23**(7): p. 525-529.

40. Aili, D., Kalmar Hansen, M., Pan, C., Li, Q., Christensen, E., Jensen, J.O., Bjerrum, N.J., *Phosphoric acid doped membranes based on Nafion®, PBI and their blends – Membrane preparation, characterization and steam electrolysis testing.* International Journal of Hydrogen Energy, 2011. **36**(12): p. 6985-6993.

41. Hansen, M.K., Aili, D., Christensen, E., Pana, C., Eriksen, S., Jensen, J.O.,Barner, J.H., Li, Q. and Bjerrum, N.J., *PEM steam electrolysis at 130 °C using a phosphoric acid doped short side chain PFSA membrane.* International Journal of Hydrogen Energy, 2012. **37**(15): p. 10992-11000.

42. Bjerrum N.J., Petrushina I.M., Bandur V.A. and Nikiforov A.V., *Water electrolysis at elevated temperatures.*International Conference on Hydrogen Material Science and Chemistry of Carbon Nanomaterials, August 2009, Yalta, Ukraine: pp. 842-843.

43. Liu, Z., Wainright, J.S., Litt, M.H. and Savinell, R.F., *Study of the oxygen reduction reaction (ORR) at Pt interfaced with phosphoric acid doped polybenzimidazole at elevated temperature and low relative humidity.* Electrochimica Acta, 2006. **51**(19): p. 3914-3923.

44. Mamlouk, M. and K. Scott, *Phosphoric acid-doped electrodes for a PBI polymer membrane fuel cell.* International Journal of Energy Research, 2011. **35**(6): p. 507-519.

45. Peighambardoust, S.J., S. Rowshanzamir, and M. Amjadi, *Review of the proton exchange membranes for fuel cell applications.* International Journal of Hydrogen Energy, 2010. **35**(17): p. 9349-9384.

46. Jin, Y., Y. Shen, and T. Hibino, *Proton conduction in metal pyrophosphates (MP_2O_7) at intermediate temperatures.* Journal of Materials Chemistry, 2010. **20**(30): p. 6214-6217.

47. Bose, S., Kuila, T., Xuan, T., Nguyen, B., Kim, N.H., Lau, K. and Lee, J.H., *Polymer membranes for high temperature proton exchange membrane fuel cell: Recent advances and challenges.* Progress in Polymer Science, 2011. **36**(6): p. 813-843.

CHAPTER 2

LITERATURE REVIEW - SOLID ACIDS

In this chapter a literature review of proton conducting materials with special focus in solid acids is detailed. The characteristics of the most studied solid acids and their composites in terms of structure and proton conductivity in the medium temperature range is summarised. A final section analyses the results obtained by previous researches in the application of medium temperature proton conductors in PEM fuel cells.

2.1. Electrolyte materials

Perfluorosulfonic acid polymers, such as Nafion®, are the state-of-the-art solid electrolytes used in proton exchange membrane (PEM) electrolysers and fuel cells at the present time. These polymers have limitations in the operating temperature as well as high production costs, and also their mechanical properties limit the device operating conditions. Therefore, several materials are under study nowadays in order to address those issues in proton exchange membrane electrochemical devices.

Figure 2.1 depicts the conductivity of a number of proton conductive materials and their respective operating temperatures. Currently there is a need of materials that can fill the gap shown in figure 2.1. Those materials, or their composites, would make ideal candidates for use in water electrolysers and fuel cells combining satisfactory proton conductivity, chemical stability and good mechanical properties.

The use of organic materials (i.e. Nafion®, PEEK, PBI) has been widely studied as they have good proton conduction and relatively good mechanical properties [1-3]. These materials exhibit a proton conduction mechanism called 'vehicle mechanism' [4, 5]. According to this mechanism the conduction path for protons is formed between adjacent acidic groups (i.e. $–SO_3^-$) attached to the polymer backbone using a proton solvent (i.e. H_2O-H_3O^+) as a carrier [6]. Nevertheless, they exhibit limitations regarding the operating temperature. Perfluorosulfonic acid (e.g. Nafion®) [7] or sulfonated aromatic [8, 9] (i.e. S-PEEK, S-PSf) membranes are limited to operating temperatures below the boiling point of water, as proton conduction is dependent on the presence of water that acts as a bridge between the sulfonic groups. Other organic materials such as polybenzimidazole (PBI) can

use H_3PO_4 as proton carrier which allows them to work at higher temperatures, of about 180 ºC [10, 11]. Other materials based on different basic groups (i.e. pyridine) have also been under study with this purpose [1, 12].

The operating temperature of the above mentioned membranes can be increased if materials such as inorganic oxides (i.e. SiO_2, TiO_2), metal phosphates (i.e. ZrP, TiP) or heteropolyacids (HPAs) are introduced in the membrane structure [2, 13-18]. The hygroscopic nature of these materials can help retain water within the membrane thus enabling operation above 100 °C, usually around 120 – 130 °C. These materials may also provide higher mechanical stability to the composite membrane.

The use of inorganic materials such as solid acids may provide an interesting alternative to fill the gap proposed in figure 2.1. These materials exhibit anhydrous proton conductivity and they could be used in a wide range of applications.

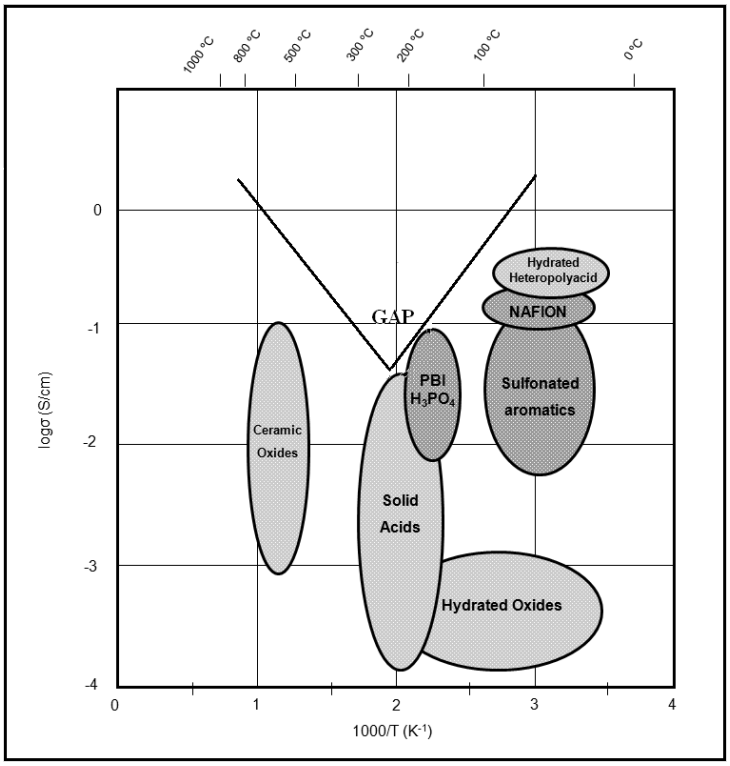

Figure 2.1. Conductivity of various proton conductive materials with potential use as electrolytes in water electrolysers and fuel cells [14].

In summary, there is a wide range of materials which can be used as proton conductors in electrolyte materials [2, 14]. They can be divided in two main groups; inorganic and organic materials. The mixture of inorganic/organic components provides a synergetic way

to combine the advantageous properties of each material in order to form a composite hybrid membrane with improved properties [15, 17, 19-21].

2.2. Solid acids

Solid acid compounds exhibit properties which lie between those of a normal acid and a salt and consist usually of an alkali metal (or NH_4) and tetrahedral oxyanions chains linked together by hydrogen bonds. The generic formula is given by equation 2.1.

$$M_xH_y(AO_4)_z \quad (M = Li, K, Rb, Cs, NH_4;\ A = S, Se, P, As) \tag{2.1}$$

These materials exhibit low proton conductivity at ambient temperature, but above certain temperatures, proton conduction is increased by several orders of magnitude. There is a dispute in literature regarding the reason to which this change in proton conduction should be attributed. *Ortiz* [22] and *Lee* [23] explained this conduction enhancement by water loss in the material caused by a thermal decomposition reaction, where the generated water is responsible for the mobility of protons through the electrolyte material. The proposed dehydration reaction is given in equation 2.2.

$$M_xH_yAO_4\ (s) \rightarrow MH_{y-yx}AO_{4-x}(s) + xH_2O\ (g) \tag{2.2}$$

Other authors such as *Baranov* [24] or *Haile* [25] attribute this conductivity enhancement to a phase change in the bulk of the material. According to this theory, at temperatures above around 130 ºC (depending on the material), the material undergoes a structural change to a high temperature stable superprotonic phase. In that phase, the oxyanions acquire higher rotational freedom in the crystal lattice. This leads to a disorder in the hydrogen bonding between the oxyanion groups, because of the lattice rearrangement, allowing more combinations of possible hydrogen bonds. Between all the possible hydrogen bonds only a fraction of them is actually occupied enabling the protons to move among the proton vacancies of the lattice (hopping). This conduction mechanism is known as ‘grotthus mechanism’ [5] (figure 2.2) and is different from the ‘vehicle mechanism’ in the fact that conduction is achieved by proton hopping between oxyanions rather than conduction by a proton solvent.

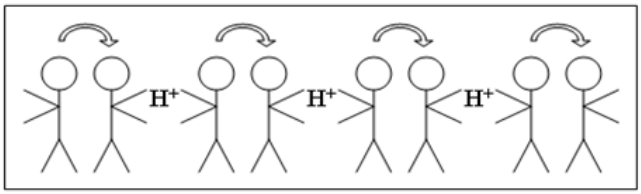

Figure 2.2. Grotthus conduction mechanism.

In figure 2.3 the conductivity of the most commonly studied cesium-based solid acids is presented. Because of the properties discussed above those materials are suitable for use as electrolytes in intermediate temperature (150 – 300 ºC) electrochemical devices. The potential use of these materials is both for proton exchange membrane (PEM) fuel cell and electrolysers.

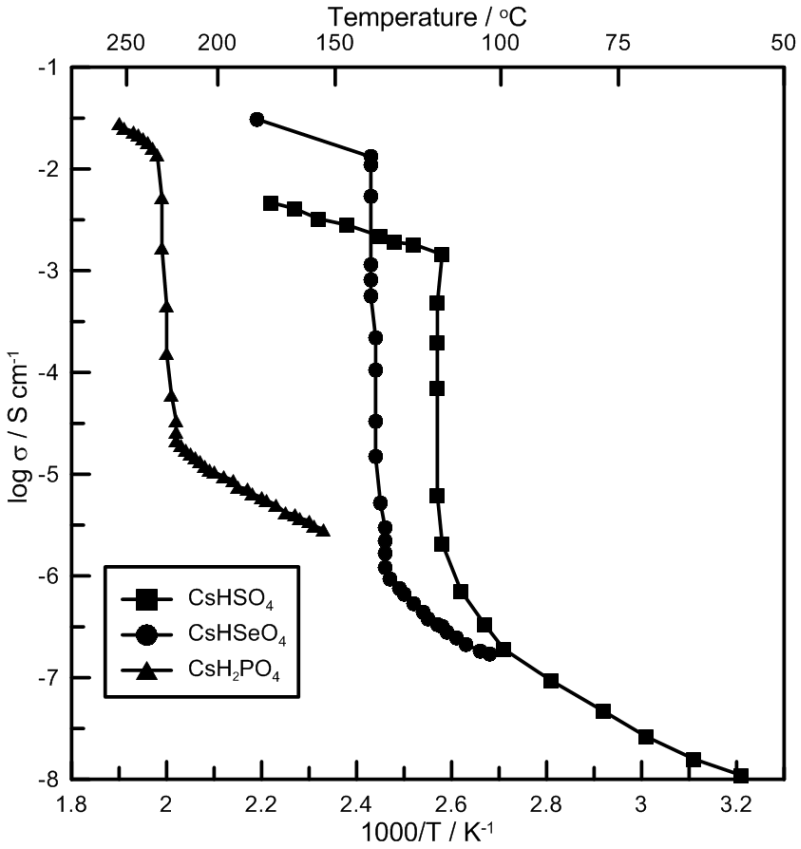

Figure 2.3. Arrhenius plot of the conductivity of various Cs-based solid acids [24, 26].

However, there are some issues that must be addressed before applying these materials as electrolytes. They exhibit chemical and mechanical limitations in the temperature range that would be interesting for electrolyser applications. Solid acids are crystallic materials and have ductile mechanical properties, especially in the superprotonic state at elevated temperatures, therefore it is hard to fabricate a robust and thin electrolyte structure [25].

These materials are also water soluble and the large amount of water fed to the device must be considered when using them as electrolyte. The big amount of water present could lead to problems during the start-up and shut-down of the system in which case the temperature could be lower than 100 ºC leading to water condensation.

Nevertheless, if we compare these materials with traditional polymer membrane materials, they show rather interesting properties. They conduct protons in the absence of water, which allows higher working temperature on the device, and have a very good impermeability to hydrogen and oxygen gases, which should lead to a lower overpotential on the electrolysis cell. Both factors can have a positive effect on the efficiency of the electrolyser.

Some of the most studied solid acid materials are discussed below, highlighting the working temperature range, proton conduction values and other properties.

2.2.1. Sulfate and selenate oxyanion based solid acids ($MHSO_4$, $MHSeO_4$)

Some of the earliest studies on solid acid materials were conducted on alkali hydrogen sulfates and selenates due to their ferroelectric and ferroelastic properties [24]. They were found to undergo various phase transitions in the solid state, exhibiting increased proton conductivity by several orders of magnitude.

There is a large number of sulfate and selenate based solid acids compounds studied, i.e. $CsHSO_4$ / $CsHSeO_4$ [24, 27], $RbHSO_4$ / $RbHSeO_4$ [27, 28], $KHSO_4$ / $KHSeO_4$ [27, 29]. Materials with combinations of oxyanions or alkali metals have also been studied, i.e. $CsH(SO_4)_x(SeO_4)_{1-x}$ [30], $RbH(SO_4)_x(SeO_4)_{1-x}$ [31], $Rb_x(NH_4)_{1-x}HSO_4$ [32]. Disulfate and diselenate solid acids with general formula $M_3H(AO_4)_2$ such as $Rb_3H(SeO_4)_2$ [33], $K_3H(SO_4)_2$ [34], $Cs_3H(SeO_4)_2$ [35] or $Tl_3H(SO_4)_2$ [36, 37] have been studied and exhibit relatively high proton conductivity in the order of 10^{-2} - 10^{-3} S cm^{-1} and low activation energy for proton conduction [38].

The synthesis of sulfate and selenate solid acids is usually made by the reaction in an aqueous medium at room temperature, as shown in equations 2.3 and 2.4.

$$M_2CO_3 + 2H_2SO_4 \rightarrow 2MHSO_4 + H_2O + CO_2 \quad (2.3)$$

$$M_2CO_3 + 2H_2SeO_4 \rightarrow 2MHSeO_4 + H_2O + CO_2 \quad (2.4)$$

where M is an alkali metal provided to the reaction by either the carbonate or by hydroxide ($M(OH)_2$) precursor. Single crystals of the compound can be obtained by evaporation of the aqueous solution or cooling the melted material. Precipitation of polycrystalline powders can be induced by the addition of methanol to the solution.

Not all the sulfate and selenate based solid acids studied exhibit transition to superprotonic phase. The properties of each material are based on the alkali metal used in each case. For instance, the decomposition and melting temperature of those compounds increases as the size of the alkali metal cation is increased, e.g $LiHSO_4$ has lower melting temperature than $CsHSO_4$. Also the superprotonic phase transition tends to appear in the presence of bigger size cations [38]. When the sulfate/selenate solid acids undergo the superprotonic phase transition the crystal lattice is rearranged in such a way that two of the four oxygen atoms per molecule participate in the formation of hydrogen bonds. This makes the number of possible proton sites double the number of protons [24].

It was also reported [39] that HAO_4^- ions (A = S, Se) can form infinite chains such as in room temperature phases of $CsHSO_4$, $RbHSO_4$, $RbHSeO_4$, NH_4HSeO_4 or cyclic dimers, as in high temperature phase β-$CsHSeO_4$ [40]. Depending on the formation of infinite chains $(HAO_4^-)_n$ or cyclic dimers $(HAO_4^-)_2$ the hydrogen bonding length, and thus its strength, varies, being longer and thus weaker in the case of cyclic dimers compared to infinite chains [38]. Generally, hydrogen bonds in cyclic dimers are weaker than the corresponding infinite chains as it was shown for several compounds (i.e. formic [41] and acetic acid [42] or hydrogensulphates [39]). The strength of the H-bonding was deeply studied in the case of $CsHSO_4$ and $CsHSeO_4$ where the transition from infinite chains into cyclic dimers during the phase transition was addressed by several techniques (i.e. Raman and Infrared spectroscopy, X-Ray and Neutron diffraction) [38, 39, 43].

Also materials in the disulfate/diselenate category exhibit much higher conductivity values in their structural a-axis than in the c-axis, with differences of 1 to 2 orders of magnitude, which is explained by the hydrogen bonding arrangement in these materials [35].

Studies of the thermal properties of sulfate and selenate based solid acids reveal that at intermediate temperatures and under reducing conditions in the presence of hydrogen, they react according to the following reactions (equations 2.5 – 2.7) [44]:

$$MHAO_4 \rightarrow MH_{1-2x}AO_{4-x} + xH_2O \quad (2.5)$$

$$2MHAO_4 + 4H_2 \rightarrow M_2AO_4 + 4H_2O + H_2A \quad (2.6)$$

$$2M_3H(AO_4)_2 + 4H_2 \rightarrow 3M_2AO_4 + 4H_2O + H_2A \quad (2.7)$$

Dehydration of the compounds (equation 2.5) could be avoided in the potential use in an electrolyser due to the large amount of water present. Pt catalysed reactions (equations 2.6 and 2.7) generate H_2S and H_2Se products which act as effective catalyst poison on the surface of precious metals. This is an important drawback when we consider these materials as electrolytes in electrochemical devices.

$CsHSO_4$ and $CsHSeO_4$ compounds have been the most studied materials in the sulfate/selenate family.

2.2.1.1. $CsHSO_4$ and $CsHSeO_4$

The structure of sulfate and selenate oxyanions based cesium solid acids (CHS and CHSe) is discussed in this section. These materials undergo various phase transitions with increasing temperature. Figure 2.4 depicts the phase diagram of CHS. In conditions of relatively low pressure and temperature, both compounds grow as crystals in the γ-phase from an aqueous solution. This is usually called phase III and in that phase the material exhibits monoclinic crystal structure. Conductivity in phase III is in the range of 10^{-6} - 10^{-8} S cm^{-1}. In that phase the HSO_4^- form infinite chains and the protons are divided in one of two equilibrium sites in the lattice. At a temperature of 76 ºC for CHS and 69 ºC for CHSe these materials shift to β-phase (phase II) which is also monoclinic. Although this temperature is well defined for single crystals, it can strongly vary depending on external conditions for the powdered samples [45]. In this case unit cell parameters differ from the previous phase (i.e. smaller unit cell volume, larger H-H distances) but conductivity is still low [46] and the formation of the infinite chains shifts to a cyclic dimer structure among sulfates. A shift to tetragonal α-phase (phase I) occurs at 141 ºC in the case of CHS and 128 ºC for CHSe in which the conductivity is in the order of 10^{-2} -10^{-3} S cm^{-1}.

As mentioned earlier, in that tetragonal state, each sulfate group can form between one and four hydrogen groups, with only one donor oxygen atom per bond. It has been suggested though, that in the high conductivity state, what is increased, is the mobility of oxygen defects rather than the concentration of the defects in the material [26]. Others [22, 23] attribute this property to the dehydration on the compound and the generation of water in

the surface of the particles. According to reaction 2.2, the materials undergo a dehydration/polymerisation reaction where poly- and pyro-sulfates and water are generated. This produced water would be the responsible for proton conductivity within the material. Lately *Kamazawa et al*. [47] reported self-diffusion of the proton along the material. The different phase transitions of CHS are plotted in the phase diagram on figure 2.4.

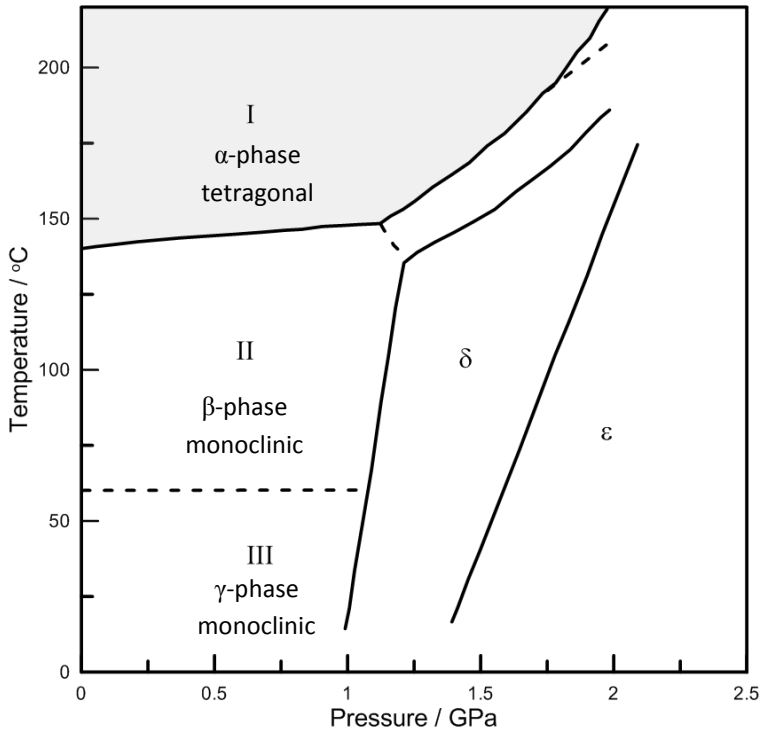

Figure 2.4. P-T phase diagram of $CsHSO_4$ [46].

Haile et al. [25], reported that a conductivity 8×10^{-3} S cm^{-1} was reached for $CsHSO_4$ at 160 ºC under water saturated conditions. Other authors [24, 48] previously reported that the selenate based compound had conductivities in the range of $2.08 – 3.70 \times 10^{-3}$ S cm^{-1} and even 5×10^{-2} S cm^{-1} at around 215 ºC [49].

Nevertheless, the decomposition reaction (equations 2.6 and 2.7) under reducing atmospheres has to be considered. Such decomposition could lead to the formation of products that poison the catalyst significantly, e.g. H_2S. According to *Ponomareva et al.* [50] platinum is very active in cesium hydrogen sulfate reduction.

Various composite materials based on hydrogen sulfate and selenate oxyanions have been studied using a variety of additives as explained in section 2.2.4.

2.2.2. Phosphate oxyanions based solid acids (MH_2PO_4)

Synthesis of the material is carried in the same way as for sulfate/selenate solid acids (equation 2.8):

$$M_2CO_3 + 2H_3PO_4 \rightarrow 2MH_2PO_4 + H_2O + CO_2 \quad (2.8)$$

Not all the phosphate based solid acids exhibit the superprotonic phase transition. The most studied compounds in this area are discussed below.

2.2.2.1. CsH_2PO_4

Cesium dihydrogen phosphate (CDP) seems to be one of the most widely studied solid acids. This compound exhibits a monoclinic structure at room temperature. In that state the phosphate groups are linked together with hydrogen bonds of two different kinds: symmetric double minima and asymmetric single minimum [26]. It has been reported that phase III of the material is characterised by the formation of layers of phosphates in 2D formed by strong H-bonds linked in a 3D structure with weaker H-bonds among the layers [26, 38]. At 149 ºC it undergoes a phase transition to another monoclinic structured phase and at 230 ºC the structure changes into a cubic superprotonic phase prior to melting. This behaviour has been corroborated using several techniques such as X-Ray Powder Diffraction (XRPD), Differential Scanning Calorimmetry (DSC) and Thermogravimetric Analysis (TGA) [51, 52]. The conductivity rises to ca. 2.0×10^{-2} S cm^{-1} at 230 ºC, when the superprotonic phase is achieved [26, 53].

The superprotonic phase transition for CsH_2PO_4 has been identified to take place at 230 ºC [26, 54, 55] as depicted in figure 2.5. In the superprotonic phase, the lattice becomes cubic (Cs-Cl-like structure) with the oxyanion placed in the centre of a cube with Cs atoms on each corner. The oxyanion can take one of six possible orientations within the cube and therefore there are six possible ways hydrogen bonds can be formed. However there is no clear mechanism to explain the high conductivity in the superprotonic state but it is considered that hydrogen bond disorder and phosphate group disordered must play an independent part in the proton conduction [26]. The melting point of this material is about 345 ºC, high enough for this material to be suitable for electrolysis and fuel cell applications.

It is reported [26, 53, 56] that CsH_2PO_4 is stable under oxidising and reducing atmospheres at 240 ºC, even under platinum catalysed environment and no H_xP species are generated. Nonetheless, it decomposes due to the dehydration reaction in two steps (equations 2.9 and 2.10).

$$2CsH_2PO_4 \rightarrow Cs_2H_2P_2O_7 + H_2O \quad (2.9)$$

$$CsH_2PO_4 \rightarrow CsPO_3 + H_2O \quad (2.10)$$

The compound reacts forming intermediate hydrogen pyrophosphates and polyphosphates until its complete decomposition to $CsPO_3$. In a fuel cell, this issue can be addressed by the humidification of the feeding gases by a water partial pressure of 0.4 atm [26, 56].

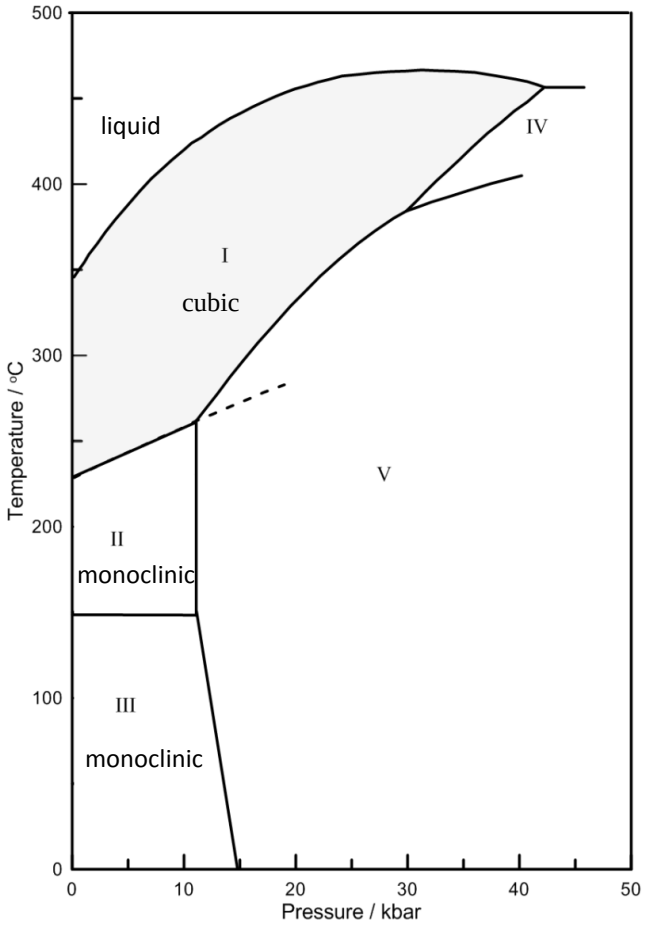

Figure 2.5. P-T phase diagram of CsH_2PO_4 [57].

There is still an open discussion where some authors believe that the superprotonic properties of this material at intermediate temperatures are due to thermal decomposition to $CsPO_3$ instead of a consequence of a phase change in the bulk [22, 58]. According to this

theory, the water produced by reaction 2.9 and 2.10 would be responsible for the proton mobility within the material.

2.2.2.2. RbH_2PO_4

The RbH_2PO_4 material structure is very similar to the structure of CsH_2PO_4 compound, sharing similar material properties although still some differences exist between them. This material, as reported by some authors [57, 59, 60], undergoes various phase transitions, enhancing material proton conduction when increasing temperature. RbH_2PO_4 room temperature phase is tetragonal (phase III) and it undergoes a phase change to a monoclinic structure (phase II) between 90 – 130 ºC. Both phases coexist in this temperature range. At 276 ºC the material undergoes another phase change from monoclinic to a yet unclear superprotonic phase (phase I) with proton conductivity values of around 10^{-2} S cm^{-1} at 285 ºC [61]. All these phase changes are shown in the phase diagram (figure 2.6).

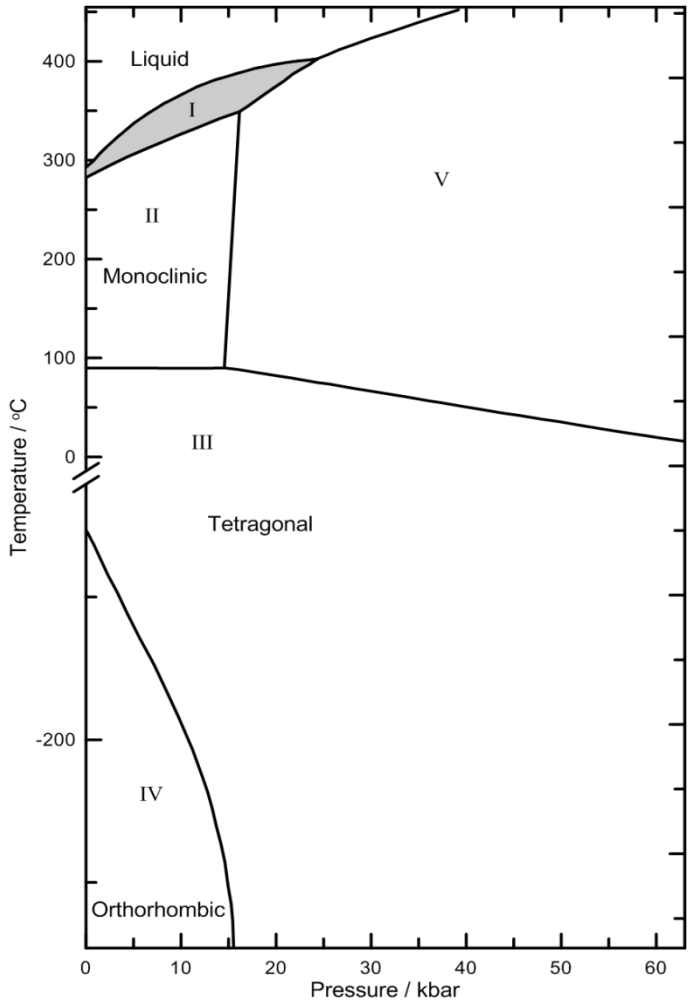

Figure 2.6. P-T phase diagram of RbH_2PO_4 [57]

The crystal structure of the monoclinic RbH_2PO_4 (above 130 ºC) is almost identical to the monoclinic room temperature phase of CsH_2PO_4. This suggests that RbH_2PO_4 also undergoes a polymorphic structural change to a high-symmetry disordered phase which provides superconductive properties. The conductivity of RbH_2PO_4 increases on orders of magnitude when increasing temperature and phase-change is generated. Several studies have been made to investigate the proton conduction mechanism [60, 62].

The monoclinic phase is stable up to temperatures of 210 – 250 ºC [52, 59] where the compound suffers a dehydration reaction following equations 2.11 and 2.12.

$$2RbH_2PO_4 \rightarrow Rb_2H_2P_2O_7 + H_2O \quad (2.11)$$

$$RbH_2PO_4 \rightarrow RbPO_3 + H_2O \quad (2.12)$$

Dehydration takes places at reaction sites on the external surface of RbH_2PO_4 particles, leading to a 4.9 % weight loss at 320 ºC due to generation of $Rb_2H_2P_2O_7$ and a total weight loss of 9.9 % at 450 ºC by the formation of the $RbPO_3$ compound. Water partial pressure of 0.56 atm avoids these reactions happen [61].

It is also claimed [63] that structural phase change does not exist in this material and that the proton conduction properties are caused by the water produced in the polymerisation/ dehydration reaction.

2.2.2.3. KH_2PO_4 and LiH_2PO_4

Early studies reported that KH_2PO_4 exhibits two different phase transitions at 187 and 233 ºC, changing from tetragonal to a monoclinic structure [57, 64]. Nevertheless, several studies in this area [52, 62, 65, 66] stated that the potassium and lithium based solid acids do not suffer structural phase transition to a superionic phase but a thermal decomposition and polymerisation in the surface of the material.

$$MH_2PO_4 \rightarrow MPO_3 + H_2O \ (M = Li, K) \quad (2.13)$$

Conductivity values around 10^{-4} S cm^{-1} have been reported for the potassium based compound [67, 68] at 190 ºC. At higher temperatures the material starts to decompose and loses water from its structure as shown in equation 2.13. As reported by *Boysen et al.* [62], the overall dehydration reaction causes a 13,2 % mass loss in the material.

Nevertheless this material has been used [69] to fabricate a composite using a pyrophosphate as matrix and generating by this way a new high proton conducting phase as explained in section 2.2.4.

In the case of LiH_2PO_4 a study reports a doubtful conductivity value as high as 10 S cm^{-1} at 200 ºC which is attributed to the dehydration/polymerisation reaction of the compound (equation 2.13) [66]. Other studies report more reasonable conductivity values in the range of 10^{-4} – 10^{-3} S cm^{-1} [70, 71]. These results make these materials still interesting for electrolyte applications in electrochemical devices.

2.2.2.4. Zirconium hydrogen phosphate (ZrP)

ZrP is another solid acid with a structure based on two layers with water trapped between them [72]. It is expressed in two ways, depending on the amount of water molecules, as shown in equation 2.14.

$$\alpha, \gamma\text{-ZrP} = Zr(HPO_4)_2 \cdot nH_2O \quad [\alpha: (n=1); \gamma: (n=2)] \qquad (2.14)$$

The conduction mechanism of this material differs from the other solid acids as there is not a superprotonic phase transition involved and it is not based on the grotthus mechanism [5]. Instead, due to the morphology of the ZrP, conduction based on vehicle mechanism takes place using the water trapped between its layers. A α-ZrP single crystal has a conductivity value of 10^{-5} S cm^{-1}, however it has been reported that in the surface of the crystal proton conduction is several orders of magnitude higher [17].

The need for water to make proton conduction possible, places this material in a lower temperature range application, which would not fill the 'gap' referred to in figure 2.1. As reported by some authors [73, 74] it is possible to create proton conducting composites by the incorporation of ZrP in a polymeric matrix, with enhanced mechanical properties and working temperature of 120 – 130 °C. There are also similar compounds such as titanium hydrogen phosphate which are under study [75, 76].

2.2.3. Arsenate oxyanions based solid acids (MH_2AsO_4)

Although alkali metal hydrogen arsenate compounds are mentioned as potential solid acids electrolytes, few reports appear on these materials. Some structural studies of CsH_2AsO_4

[77, 78] and $NH_4H_2AsO_4$ [79] as well as reports about combined oxyanion formed solid acids can be found [80, 81]. It is reported that $NH_4H_2AsO_4$ solid acid undergoes a dehydration reaction starting at 165 ºC and completing at 475 ºC. This suggests that probably other arsenate based solid acids could also suffer from dehydration. KH_2AsO_4 conductivity around 10^{-4} S cm^{-1} has been reported [67]. These compounds exhibit interesting properties but further research is needed before they are considered for use as electrolytes.

Table 2.1 summarises the main studied solid acids, highlighting the superprotonic phase transition temperature and their conductivity.

Table 2.1. Conductivity and phase transition temperature of various solid acids

Compound	**Superprotonic transition T / °C**	**Proton conductivity / S cm^{-1}**	**Reference**
$CsHSO_4$	141	8×10^{-3}	[24, 27]
$RbHSO_4$	160 - 170	$\sim 10^{-4}$	[27]
$KHSO_4$	150 – 180	$\sim 10^{-4}$	[27, 29]
$CsHSeO_4$	128	$\sim 10^{-3}$	[24]
$RbHSeO_4$	170		[28]
NH_4HSeO_4	136	$\sim 10^{-3}$	[38]
$Cs_3H(SeO_4)_2$	180	2×10^{-4}	[35]
$Rb_3H(SeO_4)_2$	185	5×10^{-4}	[33, 35]
$K_3H(SeO_4)_2$	120	$\sim 10^{-3}$	[35]
$K_3H(SO_4)_2$	200	10^{-2} - 10^{-3}	[34, 35]
$Tl_3H(SO_4)_2$	130	10^{-3}	[36, 37]
CsH_2PO_4	230	2.2×10^{-2}	[26, 53]
RbH_2PO_4	276	$\sim 10^{-2}$	[57, 59, 60]
KH_2PO_4	190	10^{-4}	[52, 62, 65]
LiH_2PO_4	178	10^{-3} - 10^{-4}	[66]
CsH_2AsO_4	160		[77, 78]
KH_2AsO_4	150	10^{-4}	[67, 68]
$NH_4H_2AsO_4$	125	2.5×10^{-3}	[79]

2.2.4. Solid acid composites

In a composite membrane, two or more materials with different properties are combined to form a membrane with useful properties from all of them. An example of that would be to achieve a balance between conductivity, stability and ease of fabrication. Several studies have been conducted on the interaction between ionic salts and oxides targeting the fabrication of ion-conducting (nano)composites [82, 83].

In an ionic-salt/oxide (MX/O) composite, when the oxide particle size is large, the conductivity is attributed to the charge mechanism proposed by Wagner and Maier [84]. The M cations are adsorbed on the oxide surface causing an enrichment of the interphase space-charge region by cation vacancies. This is corroborated by the fact that the values of the activation energy of conductivity and migration energy of cation vacancies are close. This mechanism, though, postulates that the bulk and surface properties of the material do not change and does not consider the formation of a new interphase.

In nanocomposite materials, the surface contact area of the different compounds is very high. When the particle size of each material is reduced, the contact area between them will increase and thus, the interaction between components will acquire higher importance. These interactions change the bulk characteristics of the compounds due to the formation of a new interphase. The structural characteristics and stability of the new nanocomposite material is greatly affected by the interface and grain-boundary energies. The main thermodynamic reason for the formation of the nanocomposite and stabilization of interfaces is the adhesion energy (σ_a) [85]. An increase in this variable favours the wetting effect of the MX onto the oxide surface and leads to the formation of the nanocomposite. At high amounts of well dispersed, small size, oxide particles, the new phase material will be abundant and the properties will differ more from bulk MX. The new phase can be crystalline or amorphous [82, 83, 85, 86]. With substitution of a certain amount of the alkali metal or by the addition of an oxide to the solid acid a new disordered or amorphous phase with higher conductivity at low temperatures can be achieved, due to their chemical interaction in the interphase [85].

Composite materials were studied using solid acids (i.e. $CsHSO_4$, $Cs_5H_3(SO_4)_4$, CsH_2PO_4) and metal oxides (i.e. SiO_2, Al_2O_3, TiO_2) [85]. Depending on the oxyanion and the surface energy of the oxide, which can be modified by surface functionalisation, different

interactions would happen between the materials leading to differently behaving composite [87].

2.2.4.1. Sulfate and selenate oxyanion based solid acid composites

In the case of SO_4^{2-} and SeO_4^{2-} based solid acid composites, $CsHSO_4$ compound appears to be the most studied. The use of this material as filler in a polymer matrix has been reported by some groups [88, 89] although a composite material of $CsHSO_4$ with several oxides has been studied more extensively [27, 28, 85, 90-92]. The addition of highly dispersed metal oxides has been found to improve the conductivity properties of the solid acid based composite material at temperatures below the superprotonic transition. The addition of SiO_2 particles led to a higher increase on the conductivity [28, 92] than using TiO_2 [90] or Al_2O_3 particles [27] (figure 2.7). The addition of SiO_2 has positive effect on conductivity up to the amount of 60 % wt. Larger quantities of SiO_2 cause a drop in conductivity. The authors propose that the increase in conductivity could be due to the generation of an amorphous phase of the solid acid caused by the chemical interactions of the material with the solid oxide particles.

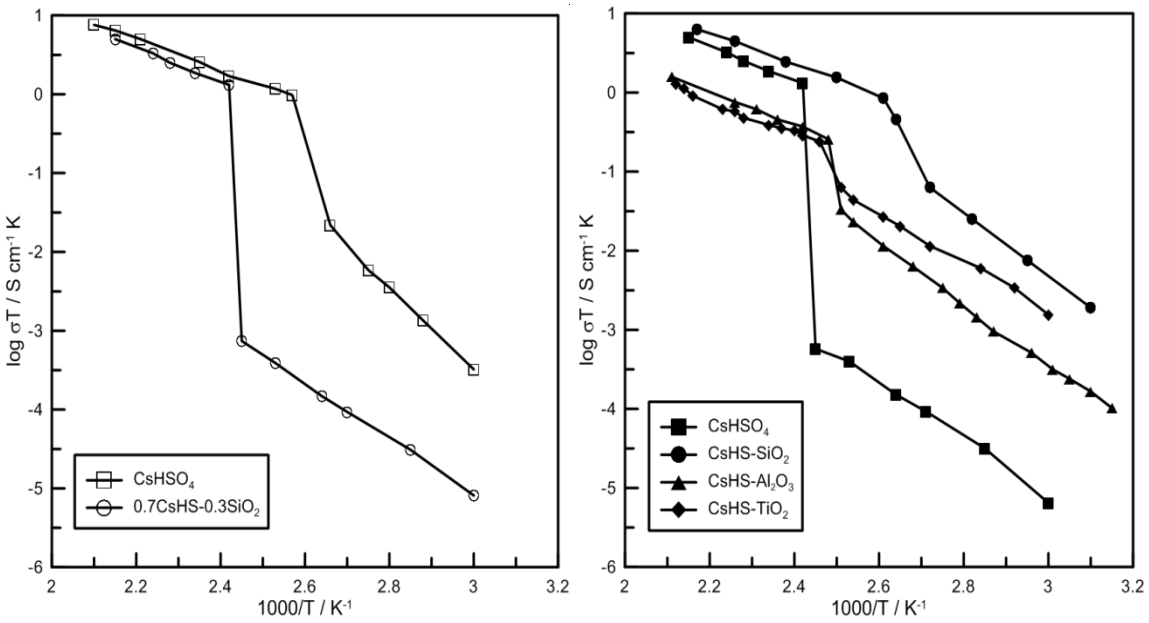

Figure 2.7. Arrhenius plots of different composites of solid acids [27].

All the surface interactions between both materials can be changed by the functionalisation of the surface chemistry of the oxide particles by sulfuric or phosphoric acid. Other variables such as the particle size of the oxides, the dispersion into the solid acid matrix or

the pore size and distribution of the particles have a great influence on the composite material properties [92].

2.2.4.2. Phosphate oxyanion based solid acid composites

Although CsH_2PO_4 solid acid is a promising electrolyte due to its satisfactory conductivity at elevated temperatures, for practical use in electrolysers and fuel cells enhanced mechanical properties and physicochemical stability are required. Therefore, the addition of oxides and pyrophosphates in order to improve both properties has been studied with this purpose.

β-Al_2O_3, TiO_2 and SiO_2 oxide particles are the most widely studied materials up to date and SiP_2O_7 and TiP_2O_7 pyrophosphates also are under study to form a solid acid composite. These materials can retain water at high temperatures due to their layered structure preventing this way the dehydration of the proton conducting material. They can generate an amorphous phase due to the interaction solid acid / oxide particle, as explained earlier [85]. They can also provide mechanical strength to the composite material and enhanced proton conduction below the superprotonic transition temperature.

Reported by *Ponomareva et al.* [91], proton conducting CsH_2PO_4 / SiO_2 composite was synthesised by mechanical ball-milling and pressing of the mixture. The composites were fabricated by varying the molar ratio of both materials and also by modifying silica oxides by acidic additives, such as, H_2SO_4, H_3PO_4 and $CsHSO_4$ in order to induce a hydrophilic surface in the oxide. The oxide particle size, and thus surface area, seems to have a great influence on the resulting composites. These CsH_2PO_4 / SiO_2 composites exhibit proton conductivity of about 10^{-2}- 10^{-3} S cm^{-1} at 130 – 250 ºC and relatively high thermal stability at lower water partial pressure. Other studies have also been carried out on SiO_2 addition to phosphate based solid acids and its effect in phase transitions [93]. Recently, *Chisholm et al.* reported the fabrication and operation in a fuel cell of a mechanically strong CsH_2PO_4 membrane with 10 % wt. SiO_2 [94].

As reported by *Matsui et al.,* silicon pyrophosphates can be used in the synthesis of a composite material [69, 95-97]. When SiP_2O_7 is used as additive, CsH_2PO_4 reacts with the pyrophosphate leading to a new ionic-conducting phase $CsH_5(PO_4)_2$ / SiP_2O_7. This material exhibited high proton conductivity of 4.4 × 10^{-2} S cm^{-1} at 266 ºC under 30 % H_2O/Ar atmosphere. At 230 ºC dehydration of the material and condensation of phosphates takes

place, resulting in a weight loss of the electrolyte material. This can be avoided by introducing water in the feeding stream, in amounts of 10 – 30 %. There is also an interesting study of *Ponomareva et al.* in the fabrication of CsH_2PO_4 / SiO_2 composites [98].

As reported by *Li et al.* RbH_2PO_4 / SiO_2 composites can be fabricated [99, 100]. The proton transport of the electrolyte material was studied varying the molar ratio between solid acid/oxide. It was found that at low temperatures, conductivity was enhanced when the amount of SiO_2 was below 60 % wt. However, in the case of high temperatures conductivities of the composite were always lower than pure RbH_2PO_4.

Muroyama et al. [69] also reported a study of MH_2PO_4 / SiP_2O_7 composite systems with RbH_2PO_4 as solid acid compound. The proton conducting $RbH_5(PO_4)_2$ compound is generated by the interaction of the solid acid with the pyrophosphate. As reported by this group, this compound (as well as $CsH_5(PO_4)_2$ and $KH_5(PO_4)_2$) exhibit high proton conductivity, over 10^{-1} S cm^{-1} at 150 – 300 ºC as shown in figure 2.8**.** This value decreases to 5 × 10^{-2} S cm^{-1} when SiP_2O_7 (molar ratio: 1/4) is added in the composite. The high conductivity exhibited by these materials make them potentially applicable as electrolytes in PEM fuel cells and electrolysers, filling the gap proposed in figure 2.1.

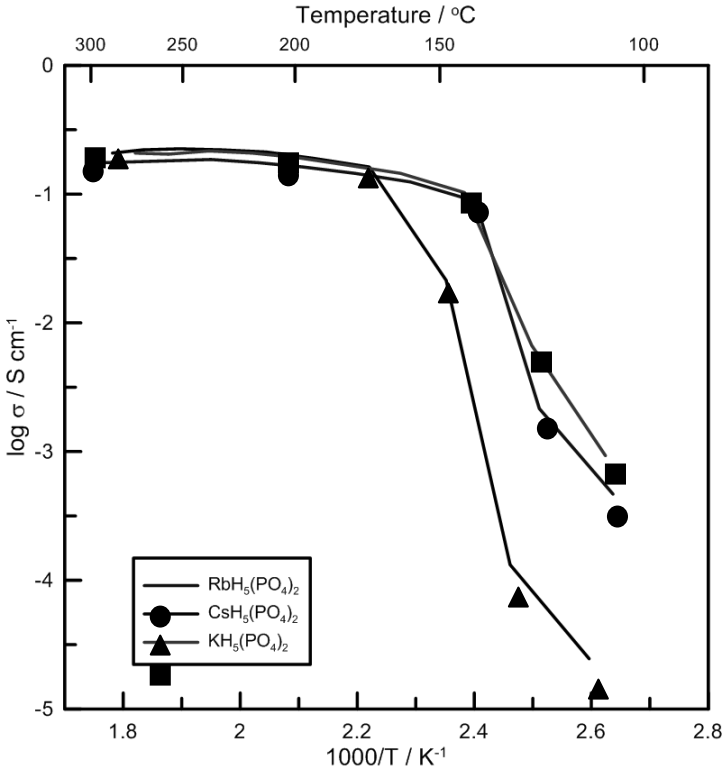

Figure 2.8. Arrhenius plot of various solid acid/silicon pyrophosphate composites [69].

Extensive research has focused on the use of layered metal (IV) acid phosphate particles as filler in polymer composite membranes. The addition of ZrP was found to improve conductivity, chemical stability and mechanical properties. An example of that is the use of α and β – ZrP particles dispersed into a PSFA or aromatic polymer matrixes [17, 73, 101].

There are several ways of preparing a composite membrane which depend either on the filler particles size, polymeric matrix nature and composite membrane preparation method. *Alberti and Casciolla* [17] and *Jones and Rozière* [21] reported composite fabrication techniques such as direct filling by filtration or in-situ formation of phosphates in the membrane. There is also the possibility of functionalizing the metal (IV) phosphates with inorganic and organic groups (e.g. $Zr(O_3P\text{-}OH)(O_3P\text{-}C_6H_4SO_3H)$ which has been widely studied by several groups [75, 76, 102-109]. Other metal phosphates, like titanium phosphate (TiP) have also been studied with the same purpose [75, 76].

2.3. Intermediate temperature Proton Exchange Membrane Fuel Cells (PEMFC)

Research and development of PEMFC in the intermediate temperature range (150 - 300 ^oC) has attracted extensive interest. In this section a series of proton conducting materials applied in PEMFC are reviewed. Such membranes include proton conducting materials such as acid-doped polymers, heteropolyacids, pyrophosphates, solid acids and their composites.

Poly[2,2'-m-(phenylene)-5,5'-bibenzimidazole] (PBI) is a commonly used polymer in intermediate temperature fuel cell technology. The basic nature of the polybenzimidazole allows an acid-base interaction between the polymer and an acid, making it possible to provide the membrane with high proton conductivity by doping it with phosphoric acid [1, 10, 11]. This polymeric membrane can operate at temperatures up to 180°C. Polymers based on pyridine groups have also been studied with the same purpose [1, 12].

As mentioned in the previous section Nafion® / ZrP is a composite membrane with application in intermediate temperature PEMFC. The performance improvement of a fuel cell with the addition of ZrP in the Nafion membrane [101] is shown in figure 2.9. *Stein et al.* improved the performance by using zirconium and titanium sulfophenyl phosphonates [108]. Conductivity values of 10^{-1} S cm^{-1} have been reported for Nafion® / TiP in temperatures of 100 ºC [75]. *Hogarth et al.* [76] reported conductivity values of $4.4 – 1.9 \times 10^{-3}$ in sol-gel titanium phosphates.

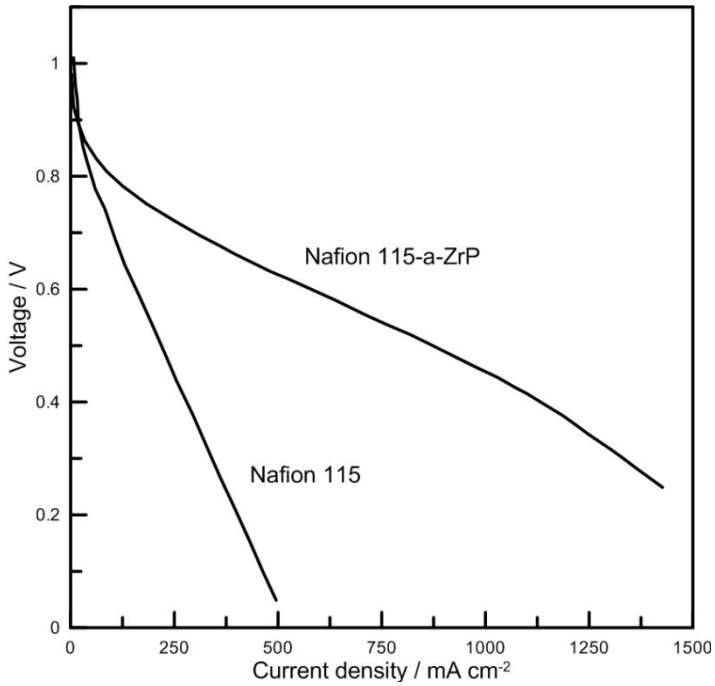

Figure 2.9. IV curves of Nafion115 and Nafion115/α-ZrP composite membrane [101]

Heteropolyacids (HPA) are inorganic compounds with high conductivity even at room temperature. The basic structure unit of these acids is a cluster called Keggin unit $[XM_{12}O_{40}]^{3+}$, where X is a cation such as P, Si or B and M a metal like Mo or W, and they are found in hydrated form. Typical compounds include $H_3PW_{12}O_{40}{\cdot}nH_2O$ (PWA), $H_3PMo_{12}O_{40}{\cdot}nH_2O$ (PMoA), and $H_4SiW_{12}O_{40}{\cdot}nH_2O$ (SiWA). These compounds are water soluble and would wash out of a PEM unless they are immobilised.

To address this issue HPAs are covalently attached to a polymer, such as aromatic polymers or nafion [18, 110, 111]. *Helen et al.* [112] reported good proton conductivity of 10^{-2} S cm^{-1} by fabricating Nafion® composites with functional compounds such as silicotungstic acid. The addition of this compound seemed to decrease methanol crossover through the membrane, nevertheless the conductivity of Nafion is not enhanced. Hybrid HPA-polymers could be optimised for higher temperature and drier fuel cell operation by controlling the morphology and structure of the polymers. Heteropolyacids trapped in nano-silica matrices is also reported [113]. Some groups [18, 111, 114] reported the fabrication of composite membranes with Nafion® and HPA reaching values of 1.5×10^{-1} S cm^{-1} at 120 ºC operating at 30 % relative humidity. However, the operating temperature was still limited by the polymer properties to 150 ºC. A copolymer composite membrane of $H_3PW_{12}O_{40}$ heteropolyacid and directly polymerised sulfonated poly(arylene ether

sulfone), reported by *Kim et al.* [110], exhibited good thermal stability (decomposition temperature in nitrogen > 300 °C) and proton conductivity of 0.15 S cm^{-1} at 164ºC.

Other acids such as phosphoantimonic acid ($HSbP_2O_8$) have been studied due to their high proton conductivity. *Krishnan et al.* [115] reported conductivity values of 4.5×10^{-2} S cm^{-1}, at 70 ºC and 100 % RH. The composite membranes of sulfonated poly-ether-ether ketone (s-PEEK) with $HSbP_2O_8 \cdot H_2O$ content up to 40 % wt. were prepared by introducing the solid proton conductor from an aqueous suspension. Phosphatoantimonic acids ($H_nSb_nP_2O_{3n+5} \cdot xH_2O$ (n = 1, 3, 5)) were reported by *Deniard-Courant et al.* [116], as early as in 1988, to be a good proton conductor.

Metal pyrophosphates (MP_2O_7, M = Sn, Ti, Si, Ge, Ce and Zr) have been studied due to their high proton conductivity, in the range of $10^{-1} – 10^{-3}$ S cm^{-1}, at temperatures up to 250 ºC and low humidity conditions. Pyrophosphates of tetravalent metals are promising and various MP_2O_7 (i.e. M=Si, Zr, Ti) were used to fabricate proton conductive composite membranes with CsH_2PO_4, RbH_2PO_3 [69] or NH_4PO_3 [117]. *Hibino et al.* reported extensive studies on SnP_2O_7 [118]. The proton conductivity of SnP_2O_7 can be increased by doping with trivalent elements such as In and Al [118-125]. It was found that partial substitution of the metal species (M^{4+}) by a lower valence metal (M^{2+} or M^{3+}) can provide enhancement in proton conductivity up to values of 0.195 S cm^{-1} and a PEMFC power density of 264 mW cm^{-2} in the case of 350 μm thickness In^{3+} doped SnP_2O_7 electrolyte at 250 °C (figure 2.10) [119]. *Chen et al.* [122] reported a fuel cell power density of 15 mW cm^{-2} using a thin $Sn_{0.9}In_{0.1}P_2O_7$ membrane with unhumidified H_2 and air at 170ºC and compared it to the performance of a pure CsH_2PO_4 electrolyte. *Jin et al.* [123] recently reported satisfactory fuel cell performance using the same compound to build a phosphoric acid free electrode for intermediate temperature fuel cells. Additionally, *Sun et al.* [126] studied CeP_2O_7 for intermediate temperature fuel cells, which exhibited proton conductivity above 10^{-2} S cm^{-1} and resulted in 25 mW cm^{-2} power output at 250 ºC in a H_2/O_2 fuel cell. *Li et al.* [127] studied Y-doped zirconium pyrophosphate nanofilms which exhibit conductivities up to 5×10^{-4} S cm^{-1}. However, it was found that the conductivity of such metal (IV) pyrophosphates depends greatly on the preparation method [121]. Besides, similar to perovskite type oxides, water vapour may have interactions with electron holes or oxygen vacancies in a pyrophosphate lattice [128].

Solid acids have also been used in PEMFC systems. *Haile et al.* built a fuel cell system using a 1 – 1.5 mm $CsHSO_4$ thick membrane as electrolyte and platinum black electrodes

of loading from 3.8 to 38 mg cm^{-2} [25]. This system operating at 160 ^{o}C under water saturated gas streams, although yielding 1.1 V open circuit potential, performed rather poorly. The poor performance was mainly attributed to high thickness of the electrolyte.

CsH_2PO_4 was reported as a viable electrolyte for intermediate temperature (150 - 300 ^{o}C) fuel cells by *Uda et al.* [129]. The CsH_2PO_4 membrane had thickness of 25 μm and electrode Pt loadings of 7.7 mg cm^{-2} (Pt black on the anode and C-supported Pt on the cathode). The cell operated at 250 ºC and the peak power density was 415 mW cm^{-2} (figure 2.10). The high overpotential observed in the fuel cell system was attributed to the slow electrocatalysis rate on the cathode side. The main obstacles that have to be overcome in the design of the fuel cell were the fabrication of a mechanically strong self-supported membrane and the control of the operating temperature and humidification to avoid dehydration or decomposition. A composite material using CsH_2PO_4 and SiO_2 particles has been used to enhance the mechanical properties of the membrane providing less mechanical deformation [94]. Another study in this area compares the performance using Pt or Pd based electrocatalysts [130].

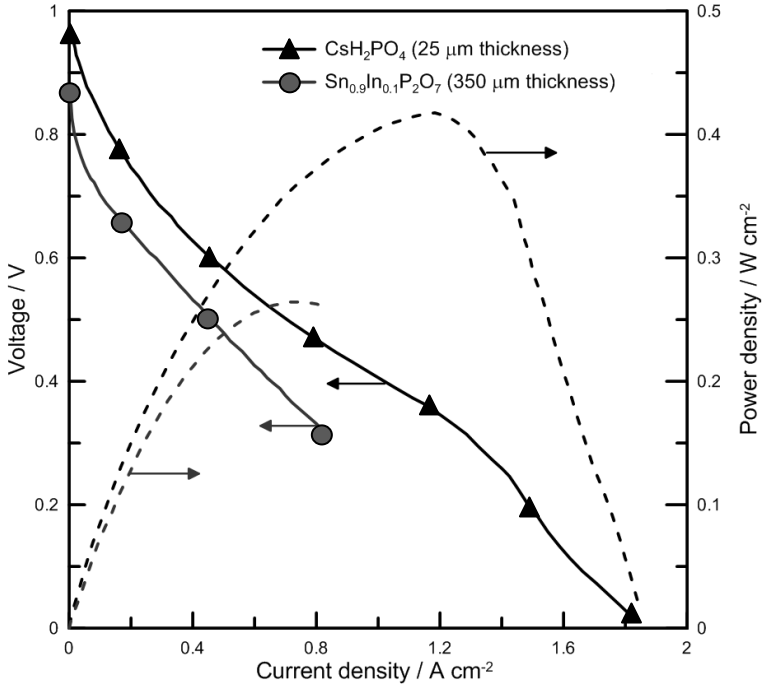

Figure 2.10. Fuel cell performance of CsH_2PO_4 [129] and $Sn_{0.9}In_{0.1}P_2O_7$ [119] membranes at 250 °C.

Solid acid based materials also look promising for direct methanol fuel cells due to low fuel permeation. This could help avoid the high overpotentials generated in DMFC caused by the MeOH permeation in Nafion®-like membranes.

2.4. Conclusions

Proton exchange membrane water electrolysers (PEMWE) have practical limitations in their operation due to the use of Nafion® as electrolyte that restricts operating temperature below 100 ^{o}C. In order to increase the working temperature and therefore reduce the amount of electrical energy required in an electrolyser, an intermediate temperature electrolyte is required. A stable proton conducting material in the range of 150 – 300 ºC would prove critical in the development of intermediate temperature electrolysis.

Solid acids exhibit high proton conductivity in anhydrous conditions at temperatures above 130ºC and therefore are suitable for this use. The mechanism of enhanced proton conductivity in the superionic state is not yet clear and there is a debate in literature as to this should be attributed to dehydration or to a solid state phase change. The most widely studied materials in the family of solid acids are $CsHSO_4$ and CsH_2PO_4 exhibiting proton conductivities higher than 10^{-2} S cm^{-1}. However, solid acids are inorganic crystalline materials and have poor mechanical properties in comparison to polymer-based electrolytes and therefore further development of these materials or membrane fabrication methods is required.

CsH_2PO_4 has been used as electrolyte in H_2/O_2 system fuel cell systems, achieving acceptable performances of 415 mW cm^{-2}. These materials, however, have never been applied as electrolytes in a water electrolysis system.

2.5. References

1. Smitha, B., S. Sridhar, and A.A. Khan, *Solid polymer electrolyte membranes for fuel cell applications, a review.* Journal of Membrane Science, 2005. **259**(1-2): p. 10-26.
2. Peighambardoust, S.J., S. Rowshanzamir, and M. Amjadi, *Review of the proton exchange membranes for fuel cell applications.* International Journal of Hydrogen Energy, 2010. **35**(17): p. 9349-9384.
3. Bose, S., Nguyen, T., Hien-Kim, T-X., Lau, N-H., Kin-tak Lee and Hee, J., *Polymer membranes for high temperature proton exchange membrane fuel cell: Recent advances and challenges.* Progress in Polymer Science, 2011. **36**(6): p. 813-843.
4. Kreuer, K.D., A. Rabenau, and R. Messer, *Proton conductivity in the layer compound $H_3OUO_2AsO_4{\cdot}3H_2O$ (HUAs).* Applied Physics A: Materials Science & Processing, 1983. **32**(2): p. 45-53.
5. Kreuer, K.-D., *Proton Conductivity:Materials and Applications.* Chemistry of Materials, 1996. **8**(3): p. 610-641.
6. K-D. Kreuer, S.J.P., E. Spohr, M Schuster, *Transport in proton conductors for Fuel Cell applications: Simulations, elementary reactions and phenomenology.* Chem. Rev, 2004. **104**: p. 4535.
7. Mauritz, K.A., Moore, R.B., *State of understanding of Nafion.* Chem. Rev., 2004. **104**: p. 4535.
8. Kreuer, K.D., *On the development of proton conducting polymer membranes for hydrogen and methanol fuel cells.* Journal of Membrane Science, 2001. **185**(1): p. 29-39.
9. Kreuer, K.D., *On the development of proton conducting materials for technological applications.* Solid State Ionics, 1997. **97**(1-4): p. 1-15.
10. Li, Q., et al., *High temperature proton exchange membranes based on polybenzimidazoles for fuel cells.* Progress in Polymer Science, 2009. **34**(5): p. 449-477.
11. Qingfeng, L., H.A. Hjuler, and N.J. Bjerrum, *Phosphoric acid doped polybenzimidazole membranes: Physiochemical characterization and fuel cell applications.* Journal of Applied Electrochemistry, 2001. **31**(7): p. 773-779.
12. J. K Kallitsis, *Polymer electrolyte membranes for high-temperature fuel cells based on aromatic polyethers bearing pyridine units.* Polym Int., 2009. **58**: p. 1226-1233.
13. Baglio,V., Ornelas, R., Matteucci, F., Martina, F., Ciccarella, G., Zama, I., Arriaga, L.G, Antonucci, V. and Aricò, A. S., *Solid Polymer Electrolyte Water Electrolyser Based on Nafion-TiO_2 Composite Membrane for High Temperature Operation.* Fuel Cells, 2009. **9**(3): p. 247-252.
14. Norby, T., *Solid-state protonic conductors: principles, properties, progress and prospects.* Solid State Ionics, 1999. **125**(1-4): p. 1-11.
15. Antonucci, P.L., Aricò, A. S., Cretì, P., Ramunni, E., Antonucci, V., *Investigation of a direct methanol fuel cell based on a composite Nafion®-silica electrolyte for high temperature operation.* Solid State Ionics, 1999. **125**(1-4): p. 431-437.
16. Antonucci, V., A. Di Blasi, V. Baglio, R. Ornelas, F. Matteucci, J. Ledesma-Garcia, L.G. Arriaga, A.S. Aricò, *High temperature operation of a composite membrane-based solid polymer electrolyte water electrolyser.* Electrochimica Acta, 2008. **53**(24): p. 7350-7356.
17. Alberti, G. and M. Casciola, *Composite membranes for medium temperature PEM fuel cells.* Annual Review of Materials Research, 2003. **33**(1): p. 129-154.

18. Tazi, B., Savadogo, O., *Effect of vaious heteropolyacids (HPAs) on the characteristics of Nafion® - HPA membranes and their H_2/O_2 polymer electrolyte fuel cell parameters* J. of new materials for electrochemical systems, 2001. **4**(3): p. 187.

19. Baglio, V., Aricò, A. S., Blasi, A., Antonucci, V., Antonucci, P. L., Licoccia, S., Traversa, E. Fiory, F. Serraino, *Nafion-TiO_2 composite DMFC membranes: physico-chemical properties of the filler versus electrochemical performance.* Electrochimica Acta, 2005. **50**(5): p. 1241-1246.

20. Park, K.T., Jung, U. H., Choi, D. W., Chun, K., Lee, H. M., Kim, S. H., *ZrO_2-SiO_2/Nafion® composite membrane for polymer electrolyte membrane fuel cells operation at high temperature and low humidity.* Journal of Power Sources, 2008. **177**(2): p. 247-253.

21. Jones, D. and J. Rozière, *Advances in the Development of Inorganic–Organic Membranes for Fuel Cell Applications*, in *Fuel Cells I*, G. Scherer, Editor. 2008, Springer Berlin / Heidelberg. p. 219-264.

22. Ortiz, E., R.A. Vargas, and B.E. Mellander, *On the high-temperature phase transitions of some KDP-family compounds: a structural phase transition? A transition to a bulk-high proton conducting phase?* Solid State Ionics, 1999. **125**(1-4): p. 177-185.

23. Lee, K.-S., *Hidden nature of the high-temperature phase transitions in crystals of KH_2PO_4-type : Is it a physical change ?* Journal of Physics and Chemistry of Solids, 1996. **57**(3): p. 333-342.

24. Baranov, A.I., Shuvalov, L.A. and Shchagina, N.M., *Superion conductivity and phase transitions in $CsHSO_4$ and $CsHSeO_4$ crystals* Journal of Experimental and Theoretical Physics Letters, 1982. **36**: p. 459.

25. Haile, S.M., Boysen, Dane A., Chisholm, Calum R. I., Merle, Ryan B., *Solid acids as fuel cell electrolytes.* Nature, 2001. **410**(6831): p. 910-913.

26. Haile, S.M., Chisholm C., Sasaki, K., Boysen, D.A., Uda, T. , *Solid acid proton conductors: from laboratory curiosities to fuel cell electrolytes.* Faraday Discussions, 2006.

27. Ponomareva, V.G. and G.V. Lavrova, *The investigation of disordered phases in nanocomposite proton electrolytes based on $MeHSO_4$ (Me=Rb, Cs, K).* Solid State Ionics, 2001. **145**(1-4): p. 197-204.

28. Niznansky, D., Plocek, J., Svobodova, M., Nemec, I., Rehspringer, J. L., Vanek, P., Micka, Z., *Preparation and Characterization of the Nanocomposites SiO_2 / H-Bond Hydrogensulphate (Hydrogenselenate).* Journal of Sol-Gel Science and Technology, 2003. **26**(1): p. 447-451.

29. Yoshida, Y., Y. Matsuo, and S. Ikehata, *NMR study on phase transitions in $KHSO_4$.* Ferroelectrics, 2004. **302**: p. 85-90.

30. Gargouri, M., Mhiri, T., Bouachir, M., Daoud, A., Senegaz, J. and Réau, J.M. *Investigation of the proton mobility in $CsH(SO_4)_{0.76}(SeO_4)_{0.24}$ crystal by ^1H NMR spectroscopy.* Journal of Molecular Structure, 1998. **440**(1-3): p. 187-192.

31. Gargouri, M., Mhiri, T., Daoud, A. & Réau, J. M., *Disorder and protonic conductivity in $RbH(SO_4)_{0.81}(SeO_4)_{0.19}$ mixed crystals.* Solid State Ionics, 1999. **125**(1-4): p. 193-202.

32. Feki, H. and et al., *H^+ -ion conductivity and ferroelectric properties of rubidium ammonium hydrogen sulphate.* Journal of Physics: Condensed Matter, 2001. **13**(37): p. 8509.

33. Plakida, N.M.a.S., W., *The Improper Ferroelastic Phase Transition in Superionic $Rb_3H(SeO_4)_2$ Crystals.* Physica status solidi (b), 1988. **148**: p. 473.

34. Matsuo, Y., Hatori, J., Nakashima, Y. & Ikehata, S., *Superprotonic and ferroelastic phase transition in $K_3H(SO_4)_2$.* Solid State Communications, 2004. **130**(3-4): p. 269-274.

35. Kamimura, H., Matsuo, Y., Ikehata, S., Ito, T., Komukae, M. and Osaka, T., *On the mechanism of superionic conduction in the zero-dimensional hydrogen-bonded crystals $M_3H(XO_4)_2$ with M = K, Rb, Cs and X = S, Se.* Physica status solidi (b), 2004. **241**(1): p. 61-68.

36. Matsuo, Y., Saito, K., Kawashima, H. & Ikehata, S, *Novel solid acid fuel cell based on a superprotonic conductor $Tl_3H(SO_4)_2$.* Solid State Communications, 2004. **130**(6): p. 411-414.

37. Matsuo, Y., Takahashi, K., Hatori, J. & Ikehata, S., *Proton dynamics in superionic phase of $Tl_3H(SO_4)_2$.* Journal of Solid State Chemistry, 2004. **177**(11): p. 4282-4285.

38. Colomban, P., *Proton conductors: Solids, membranes and gels - materials and devices*, 2 ed. Cambridge university press, 1992.

39. Colomban, P., M. Pham-Thi, and A. Novak, *Influence of thermal and mechanical treatment and of water on structural phase transitions in $CsHSO_4$.* Solid State Ionics, 1987. **24**(3): p. 193-203.

40. Badot, J.C. and P. Colomban, *RF-microwave dielectric relaxations and phase transitions in superionic protonic acid sulphates (selenates).* Solid State Ionics, 1989. **35**(1-2): p. 143-149.

41. Almenningen, A., O. Bastiansen, and T. Montzfeldt, *Reinvestigation of the structure.* Acta Chemica Scandinavika, 1969. **23**: p. 2848-2864.

42. Jonsson, P.G., *Hydrogen bond studies. XLIV. Neutron diffraction study of acetic acid.* Acta Cryst. , 1970. **B27**: p. 893-898.

43. Colomban, P., M. Pham-Thi, and A. Novak, *Vibrational study of structure and phase transitions in caesium hydrogen selenate ($CsHSeO_4$).* Journal of Molecular Structure, 1987. **161**(0): p. 1-14.

44. Merle, R. B., Chisholm, C. R. I., Boysen, D. A. & Haile, S. M., *Instability of Sulfate and Selenate Solid Acids in Fuel Cell Environments.* Energy & Fuels, 2002. **17**(1): p. 210-215.

45. Friesel, M., A. Lundén, and B. Baranowski, *Bulk phase transitions of cesium hydrogen sulphate initiated by surface processes, grinding or external pressure.* Solid State Ionics, 1989. **35**(1-2): p. 91-98.

46. Belushkin, A. V., Adams, M. A., Hull, S. & Shuvalov, L. A., *P-T phase diagram of $CsHSO_4$. Neutron scattering study of structure and dynamics.* Solid State Ionics, 1995. **77**: p. 91-96.

47. Kamazawa, K., Harada M., Ikedo, Y., Sugiyama J., Tyagi M. and Matsuo, Y., *Long Range Proton Diffusive Motion of $CsHSO_4$ and $CsHSeO_4$: High Energy Resolution Quasielastic Neutron Scattering of Superprotonic Conductors.* J. Phys. Soc. Jpn., 2010. **79**: p. 7.

48. Norby, T., M. Friesel, and B.E. Mallander, *Proton and deuteron conductivity in $CsHSO_4$ and $CsDSO_4$ by in situ isotopic exchange.* Solid State Ionics, 1995. **77**: p. 105-110.

49. Ortiz, E., Vargas, R.A. and Mellander, B.E., *Phase behaviour of the solid proton conductor $CsHSO_4$.* Journal of Physics: Condensed Matter, 2006. **18**(42): p. 9561.

50. Ponomareva, V. and G. Lavrova, *Factors affecting the hydrogen reduction kinetics of $CsHSO_4$.* Inorganic Materials, 2009. **45**(1): p. 85-89.

51. Haile, D.A.B.a.S.M., *High-Temperature Behavior of CsH_2PO_4 under Both Ambient and High Pressure Conditions.* Chem. Mater., 2003. **15**: p. 727.

52. Li, Z. and T. Tang, *High-temperature thermal behaviors of XH_2PO_4 (X = Cs, Rb, K, Na) and LiH_2PO_3.* Thermochimica Acta, 2010. **501**(1-2): p. 59-64.

53. Taninouchi, Y.-k., Uda, T., Awakura, Y., Ikeda, A. & Haile, S. M., *Dehydration behavior of the superprotonic conductor CsH_2PO_4 at moderate temperatures: 230 to 260 ºC.* Journal of Materials Chemistry, 2007. **17**(30): p. 3182-3189.

54. Baranov, A.I., V.P. Khiznichenko, and L.A. Shuvalov, *High temperature phase transitions and proton conductivity in some kdp-family crystals.* Ferroelectrics, 1989. **100**(1): p. 135-141.

55. Romain, F. and A. Novak, *Raman study of the high-temperature phase transition in CsH_2PO_4.* Journal of Molecular Structure, 1991. **263**: p. 69-74.

56. Boysen, D. A., Uda, T., Chisholm, C. R. I. & Haile, S. M., *High-Performance Solid Acid Fuel Cells Through Humidity Stabilization.* Science, 2004. **303**(5654): p. 68-70.

57. Rapoport, E., J.B. Clark, and P.W. Richter, *High-pressure phase relations of RbH_2PO_4, CsH_2PO_4, and KD_2PO_4.* Journal of Solid State Chemistry, 1978. **24**(3-4): p. 423-433.

58. Park, J.-H., *Possible origin of the proton conduction mechanism of CsH_2PO_4 crystals at high temperatures.* Physical Review B, 2004. **69**(5): p. 054104.

59. Botez, C.E., Martinez, H., Tackett, R.J., *High-temperature crystal structures and chemical modifications in RbH_2PO_4.* Journal of Physics: Condensed Matter, 2009. **21**(32): p. 325401.

60. Vijayakumar, M., A.D. Bain, and G.R. Goward, *Investigations of Proton Conduction in the Monoclinic Phase of RbH_2PO_4 Using Multinuclear Solid-State NMR.* The Journal of Physical Chemistry C, 2009. **113**(41): p. 17950-17957.

61. Li, Z. and T. Tang, *High-temperature dehydration behavior and protonic conductivity of RbH_2PO_4 in humid atmosphere.* Materials Research Bulletin, 2010. **45**(12): p. 1909-1915.

62. Boysen, D. A., Haile, S. M., Liu, H. & Secco, R. A., *Conductivity of Potassium and Rubidium Dihydrogen Phosphates at High Temperature and Pressure.* Chemistry of Materials, 2004. **16**(4): p. 693-697.

63. Ortiz, E., Vargas, R. A., Cuervo, G., Mellander, B. E. & Gustafson, J., *On the high-temperature phase transition of RbH_2PO_4 - A polymorphic transition?* Journal of Physics and Chemistry of Solids, 1998. **59**(6-7): p. 1111-1117.

64. Botez, C. E., Carbajal, D., Adiraju, V. A. K., Tackett, R. J. & Chianelli, R. R., *Intermediate-temperature polymorphic phase transition in KH_2PO_4: A synchrotron X-ray diffraction study.* Journal of Physics and Chemistry of Solids, 2010. **71**(11): p. 1576-1580.

65. Subramony, J.A., S. Lovell, and B. Kahr, *Polymorphism of Potassium Dihydrogen Phosphate.* Chemistry of Materials, 1998. **10**(8): p. 2053-2057.

66. Lee, K.-S., Moon, J., Lee, J. & Jeon, M., *High-temperature phase transformations in LiH_2PO_4 and possible solid-state polymerization.* Solid State Communications, 2008. **147**(1-2): p. 74-77.

67. Park, J.-H., *Separation of surface and bulk electrical conductivity in KH_2PO_4 and KH_2AsO_4 crystals at high temperatures.* Solid State Communications, 2002. **123**(6-7): p. 291-294.

68. Chen, R. H., Yen, C.-C., Shern, C. S. & Fukami, T., *Impedance spectroscopy and dielectric analysis in KH_2PO_4 single crystal.* Solid State Ionics, 2006. **177**(33-34): p. 2857-2864.

69. Muroyama, H., Kudo, K., Matsui, T., Kikuchi, R. & Eguchi, K., *Electrochemical properties of MH_2PO_4/SiP_2O_7-based electrolytes (M = alkaline metal) for use in intermediate-temperature fuel cells.* Solid State Ionics, 2007. **178**(27-28): p. 1512-1516.

70. Jung Kweon, J., Won Lee, K., Eui Lee, C., Lee, K.-S. & Jo, Y. J., *Impedance spectroscopy of the superprotonic conduction in LiH_2PO_4.* Applied Physics Letters, 2012. **101**(1): p. -.

71. Jung Kweon, J., Won Lee, K., Eui Lee, C. & Lee, K.-S., *Nuclear magnetic resonance study of the superprotonic conduction in LiH_2PO_4.* Applied Physics Letters, 2011. **98**(26): p. 262903-262903-3.

72. Clearfield, A., *Inorganic ion exchangers with layered structures.* Annual reviews material science, 1984. **14**: p. 205.

73. Park, Y.-I., J.-D. Kim, and M. Nagai, *High proton conductivity in ZrP-PTFE composites.* Journal of Materials Science Letters, 2000. **19**(19): p. 1735-1738.

74. Anilkumar, G. M., Nakazawa, S., Okubo, T. & Yamaguchi, T., *Proton conducting phosphated zirconia-sulfonated polyether sulfone nanohybrid electrolyte for low humidity, wide-temperature PEMFC operation.* Electrochemistry Communications, 2006. **8**(1): p. 133-136.

75. Alberti, G., Costantino, U., Casciola, M., Ferroni, M., Massinelli, L. and Staiti, P., *Preparation, characterization and proton conductivity of titanium phosphate sulfophenylphosphonate.* Solid State Ionics, 2001. **145**(1-4): p. 249-255.

76. Hogarth, W.H.J., et al., *Proton conduction mechanism and the stability of sol-gel titanium phosphates.* Solid State Ionics, 2007. **177**(39-40): p. 3389-3394.

77. Gridnev, S.A., Kravchenko, S.A., *Elastic and inelastic properties of CsH_2AsO_4 at high pressures and temperatures.* Ferroelectrics, 1998. **214**: p. 317.

78. Hart, S., Richter, P. W., Clark, J. B. & Rapoport, E., *Phase transitions in CsH_2AsO_4 at high pressures and temperatures.* Journal of Solid State Chemistry, 1981. **37**(3): p. 302-307.

79. Vargas, R. A., Torijano, E., Diosa, J. E. & Mellander, B. E., *On the high temperature phase behaviour of $NH_4H_2AsO_4$.* Solid State Ionics, 1999. **125**(1-4): p. 187-192.

80. Jaouadi, K., Zouari, N., Mhiri, T. & Giorgi, M., *Synthesis, structural study and thermal behaviour of a new superprotonic compound: $Cs_2(HSeO_4)(H_2AsO_4)$.* Physics Procedia, 2009. **2**(3): p. 1185-1194.

81. Amri, M., Zouari, N., Mhiri, T., Pechev, S., Gravereau, P. and Von Der Muhll, R., *Structural, vibrational and dielectric properties of new potassium hydrogen sulfate arsenate: $K_4(SO_4)(HSO_4)_2(H_3AsO_4)$.* Journal of Physics and Chemistry of Solids, 2007. **68**(7): p. 1281-1292.

82. Andrei, B.Y., *Composite materials with ionic conductivity: from inorganic composites to hybrid membranes.* Russian Chemical Reviews, 2009. **78**(11): p. 1013.

83. Uvarov, N.F. and P. Vaněk, *Stabilization of New Phases in Ion-Conducting Nanocomposites.* Journal of Materials Synthesis and Processing, 2000. **8**(5): p. 319-326.

84. Maier, J., *Ionic conduction in space charge regions.* Progress in Solid State Chemistry, 1995. **23**(3): p. 171-263.

85. Uvarov, N.F., *Composite Solid Electrolytes*, in *Solid State Electrochemistry II*. 2011, Wiley-VCH Verlag GmbH & Co. KGaA. p. 31-71.

86. Uvarov, N.F., *Ionics of nanoheterogeneous materials.* Russian Chemical Reviews, 2007. **76**: p. 415.

87. Ponomareva, V. and G. Lavrova, *Controlling the proton transport properties of solid acids via structural and microstructural modification.* Journal of Solid State Electrochemistry, 2010. **15**(2): p. 213-221.

88. Boysen, D. A., Chisholm, C. R. I., Haile, S. M. & Narayanan, S. R.., *Polymer Solid Acid Composite Membranes for Fuel-Cell Applications.* Journal of The Electrochemical Society, 2000. **147**(10): p. 3610-3613.

89. Andronie, A., Morozan, A., Nastase, N., *$CsHSO_4$/Nanooxide Polymer Membranes for Fuel Cell*, in *Functionalized Nanoscale Materials, Devices and Systems*, A. Vaseashta and I.N. Mihailescu, Editors. 2008, Springer Netherlands. p. 415-418.

90. Ponomareva, V.G. and G.V. Lavrova, *Influence of dispersed TiO_2 on protonic conductivity of $CsHSO_4$.* Solid State Ionics, 1998. **106**(1-2): p. 137-141.

91. Ponomareva, V.G. and E.S. Shutova, *High-temperature behavior of CsH_2PO_4 and CsH_2PO_4-SiO_2 composites.* Solid State Ionics, 2007. **178**(7-10): p. 729-734.

92. Ponomareva, V. G., Uvarov, N. F., Lavrova, G. V. & Hairetdinov, E. F., *Composite protonic solid electrolytes in the $CsHSO_4$-SiO_2 system.* Solid State Ionics, 1996. **90**(1-4): p. 161-166.

93. Otomo, J., Ishigooka, T., Kitano, T., Takahashi, H. & Nagamoto, H., *Phase transition and proton transport characteristics in CsH_2PO_4/SiO_2 composites.* Electrochimica Acta, 2008. **53**(28): p. 8186-8195.

94. Chisholm, R.I., Boysen, A., Papandrew, A.B., Zecevic, S., Cha, S-Y., Kenji, Á.V. Sasaki, A., Giapis, K.P. and Haile, S.M., *From Laboratory Breakthrough to Technological Realization: The Development Path for Solid Acid Fuel Cell.* The Electrochemical Society, Fall 2009. Interface.

95. Matsui, T., Kukino, T., Kikuchi, R. & Eguchi, K., *Composite effects of silicon pyrophosphate as a supporting matrix for $CsH_5(PO_4)_2$ electrolytes at intermediate temperatures.* Electrochimica Acta, 2006. **51**(18): p. 3719-3723.

96. Matsui, T., Muroyama, H., Kikuchi, R. & Eguchi, K., *ChemInform Abstract: Development of Novel Proton Conductors Consisting of Solid Acid/Pyrophosphate Composite for Intermediate-Temperature Fuel Cells.* ChemInform, 2011. **42**(17): p. no-no.

97. T. Matsui, T.K., R. Kikuchi, and K. Eguchi, *Intermediate temperature fuel cells employing CsH_2PO_4/SiP_2O_7-based composite electrolytes.* Journal of the Electrochemical Society, 2006. **153**(2): p. A339.

98. Ponomareva, V., E. Shutova, and G. Lavrova, *Electrical conductivity and thermal stability of $(1-x)CsH_2PO_4/xSiP_yO_z$ (x=0.2-0.7) composites.* Inorganic Materials, 2008. **44**(9): p. 1009-1014.

99. Li, Z., *Impedance analysis and protonic conduction mechanism in RbH_2PO_4/SiO_2 composite systems.* Electrochimica Acta, 2010. **55**(24): p. 7298-7304.

100. Li, Z. and W. Chan, *Phase transition of RbH_2PO_4 and its composite with SiO_2 studied by thermal analysis.* Journal of Thermal Analysis and Calorimetry, 2011. **104**(2): p. 585-592.

101. Costamagna, P., Yang, C., Bocarsly, A. B. & Srinivasan, S., *Nafion® 115/zirconium phosphate composite membranes for operation of PEMFCs above 100 ºC.* Electrochimica Acta, 2002. **47**(7): p. 1023-1033.

102. Alberti, G., Casciola, M., Cavalaglio, S. & Vivani, R., *Proton conductivity of mesoporous zirconium phosphate pyrophosphate.* Solid State Ionics, 1999. **125**(1-4): p. 91-97.

103. Alberti, G., Casciola, M., Costantino, U., Peraio, A. & Montoneri, E., *Protonic conductivity of layered zirconium phosphonates containing $-SO_3H$ groups. I. Preparation and characterization of a mixed zirconium phosphonate of composition $Zr(O_3PR)_{0.73}(O_3PR')_{1.27}\cdot nH_2O$, with $R=-C_6H_4-SO_3H$ and $R' = -CH_2-OH$.* Solid State Ionics, 1992. **50**(3-4): p. 315-322.

104. Alberti, G., Casciola, M., Palombari, R. & Peraio, A., *Protonic conductivity of layered zirconium phosphonates containing $-SO_3H$ groups. II. Ac conductivity of zirconium alkyl-sulphophenyl phosphonates in the range 100 - 200°C, in the presence or absence of water vapour.* Solid State Ionics, 1992. **58**(3-4): p. 339-344.

105. Alberti, G. and M. Casciola, *Layered $metal^{IV}$ phosphonates, a large class of inorgano-organic proton conductors.* Solid State Ionics, 1997. **97**(1-4): p. 177-186.

106. Alberti, G., Casciola, M., Pica, M., Tarpanelli, T. and Sganappa, M., *New preparation methods for composite membranes for medium temperature fuel cells based on precursor solutions of insoluble inorganic compounds.* Fuel Cells, 2005. **5**(3): p. 366-374.

107. Casciola, M. and Costantino, U., *Relative humidity influence on proton conduction of hydrated pellicular zirconium phosphate in hydrogen form.* Solid State Ionics, 1986. **20**(1): p. 69-73.

108. Stein, E.W., A. Clearfield, and M.A. Subramanian, *Conductivity of group IV metal sulfophosphonates and a new class of interstratified metal amine-sulfophosphonates.* Solid State Ionics, 1996. **83**(1-2): p. 113-124.

109. Sunarso, J., Chen, C- Y., Tran, T. A., Wong, M. S. and Diniz Da Costa, J. C., *Proton conductive composite membranes.* International Journal of Nanotechnology,, 2007. **45**: p. 597.

110. Kim, Y. S., Wang, F., Hickner, M., Zawodzinski, T. A. & McGrath, J. E., *Fabrication and characterization of heteropolyacid ($H_3PW_{12}O_{40}$)/directly polymerized sulfonated poly(arylene ether sulfone) copolymer composite membranes for higher temperature fuel cell applications.* Journal of Membrane Science, 2003. **212**(1-2): p. 263-282.

111. Ramani, V., H.R. Kunz, and J.M. Fenton, *Investigation of Nafion®/HPA composite membranes for high temperature/low relative humidity PEMFC operation.* Journal of Membrane Science, 2004. **232**(1-2): p. 31-44.

112. Helen, M., B. Viswanathan, and S.S. Murthy, *Synthesis and characterization of composite membranes based on α-zirconium phosphate and silicotungstic acid.* Journal of Membrane Science, 2007. **292**(1-2): p. 98-105.

113. Kim, H. J., Chu, Y. H., Moon, J. H., Han, H. S. & Shul, Y. G., *Preparation of Heteropoly Acid Entraped in Nano Silica Matrix.* Molecular Crystals and Liquid Crystals, 2001. **371**: p. 131 - 134.

114. Ramani, V., H.R. Kunz, and J.M. Fenton, *Stabilized heteropolyacid/Nafion® composite membranes for elevated temperature/low relative humidity PEFC operation.* Electrochimica Acta, 2005. **50**(5): p. 1181-1187.

115. Krishnan, P., J.-S. Park, and C.-S. Kim, *Preparation and characterization of proton-conducting sulfonated poly(ether ether ketone)/phosphatoantimonic acid composite membranes.* European Polymer Journal, 2007. **43**(9): p. 4019-4027.

116. Deniard-Courant, S., Piffard, Y., Barboux, P. & Livage, J., *Relative humidity influence on the water content and on the protonic conductivity of the phosphatoantimonic acids $H_nSb_nP_2O_{3n+5}$, xH_2O (n = 1, 3, 5).* Solid State Ionics, 1988. **27**(3): p. 189-194.

117. Matsui, T., Kazusa, N., Kato, Y., Iriyama, Y., Abe, T., Kikuchi, K. and Ogumi, Z., *Effect of pyrophosphates as supporting matrices on proton conductivity for NH_4PO_3 composites at intermediate temperatures.* Journal of Power Sources, 2007. **171**(2): p. 483-488.

118. Hibino, T., Jin, Y., Lee, B., *Development and application of SnP_2O_7 based proton conductors to intermediate temperature fuel cells.* Journal of the Japan Petroleum Institute, 2010. **53**(1): p. 12.

119. Nagao, M., Takeuchi, A., Heo, P., Hinino, T. Sano, M., Tomita, A.,, *A proton conducting In^{3+} doped SnP_2O_7 electrolyte for intermediate temperature fuel cells.* Electrochemical and Solid-State Letters, 2006. **9**(3): p. A105.

120. Genzaki, K., Heo, P., Sano, M. & Hibino, T., *Proton Conductivity and Solid Acidity of Mg-, In-, and Al-Doped SnP_2O_7.* Journal of The Electrochemical Society, 2009. **156**(7): p. B806-B810.

121. Jin, Y., Y. Shen, and T. Hibino, *Proton conduction in metal pyrophosphates (MP_2O_7) at intermediate temperatures.* Journal of Materials Chemistry, 2010. **20**(30): p. 6214-6217.

122. Chen, X., Wang, C., Payzant, E. A., Xia, C. & Chu, D. , *An oxide-ion and proton co-ion conducting $Sn_{0.}9In_{0.1}P_2O_7$ electrolyte for intermediate temperature fuel cells.* Journal of electrochemical society, 2008. **115**(12): p. B1264.

123. Jin, Y.C., M. Okada, and T. Hibino, *A comparative study of Pt/C cathodes in $Sn_{0.9}In_{0.1}P_2O_7$ and H_3PO_4 ionomers for high-temperature proton exchange membrane fuel cells.* Journal of Power Sources, 2011. **196**(11): p. 4905-4910.

124. Heo, P., Shibata, H., Nagao, M., Hibino, T. & Sano, M., *Performance of an Intermediate-Temperature Fuel Cell Using a Proton-Conducting $Sn_{0.9}In_{0.1}P_2O_7$ Electrolyte.* J. Electrochem. Soc. **153**.

125. A. Tomita, N.K., T. Kamiya, M. Nagao, T. Hibino, *Intermediate-temperature proton conduction in Al^{3+} doped SnP_2O_7.* Journal of the Electrochemistry Society, 2007. **154**(2): p. B1265-B1269.

126. Sun, X., Wang, S., Wang, Z., Ye, X., Wen, T. and Huang, F., *Proton conductivity of CeP_2O_7 for intermediate temperature fuel cells.* Solid State Ionics, 2008. **179**(21-26): p. 1138-1141.

127. Li, Y., Kunitake, T., Aoki, Y. & Muto, E., *Efficient, Anhydrous Proton-Conducting Nanofilms of Y-Doped Zirconium Pyrophosphate at Intermediate Temperatures.* Advanced Materials, 2008. **20**(12): p. 2398-2404.

128. Iwahara, H., *Proton conducting ceramics and their applications.* Solid State Ionics, 1996. **86-88**(Part 1): p. 9-15.

129. Uda, T. and S.M. Haile, *Thin-Membrane Solid-Acid Fuel Cell.* Electrochemical and Solid-State Letters, 2005. **8**(5): p. A245-A246.

130. Louie, M.W., K. Sasaki, and S. Haile, *Towards Understanding Electrocatalysis in CsH_2PO_4-Based Fuel Cells: Platinum and Palladium Thin Film Electrodes.* ECS Transactions, 2008. **13**(28): p. 57-62.

CHAPTER 3

EXPERIMENTAL METHODS

In this chapter, the methodology used for the characterisation of materials is explained. The fundamentals of every technique used for the physico-chemical as well as the electrochemical analysis of samples and the equipment used are described. The analysis of the results obtained by these techniques will be further discussed in following chapters.

3.1 Physico-chemical methods

3.1.1 Powder X-Ray Diffraction (P-XRD)

Powder X-ray diffraction analysis is a robust technique able to provide a rapid determination of the number of crystalline phases of a sample, providing that minerals are present at a level of 2 % wt. or above. It was used to characterise the crystallographic structure and to confirm the identities of the synthesised crystalline phosphate-based solid acids *(see Chapters 4 and 5)*. The crystallography of catalysts was also analysed by this technique *(see Chapter 6)*. These measurements were carried out by the Chemical and Materials Analysis group (ACMA) of the department of Chemical Engineering and Advanced Materials (CEAM) in Newcastle University. The instrument used was a PANalytical X'Pert Pro Multipurpose Diffractometer (MPD), fitted with an X'Celerator and a secondary monochromator. The X'Celerator was an ultra-fast X-ray detector with RTMS (Real Time Multiple Strip) technology to collect X-rays diffracted from the sample over a range of 2θ angles. All scans were carried out in continuous mode using the X'Celerator RTMS detector.

For data acquisition a Philips PW3040/60 X-ray generator was used with a Cu anode of 40 kV and 40 mA to produce Cu-Kα radiation with a wavelength of 1.54180 Å. The data was collected over a 2θ range of 5 to 90° with a step size of 0.0334°2θ and a nominal time per step of 150 s.

Phase identification was carried out by means of the X'Pert accompanying program High Score Plus and the results were compared with the International Crystallographic

Diffraction Database (ICDD). The minimum crystallite size of the compounds was calculated using Scherrer equation (equation 3.1) [1]:

$$\tau = \frac{K\lambda}{\beta' \cos\theta} \tag{3.1}$$

where τ is the minimum crystallite size (Å), K the shape factor (K = 0.9 Å, assuming spherical crystallites), λ the X-Ray wavelength (Å), β' is the instrument broadening (radians) and θ the Bragg angle (radians).

Semi-quantitative Relative Intensity Ratio (RIR) method was used to estimate the mass ratio of different phases within a sample. This method consists in the comparison of the integrated intensities of the diffraction peaks from each of the phases in order to estimate the mass ratio between them [2]. These measurements were carried out using PANalytical X'Pert software.

Sample preparation

The samples were maintained in the oven at 80 °C for 24 h prior to the analysis to avoid any adsorbed humidity due to the hygroscopic nature of the powders. Approximately 10 mg samples were ground for 5 min in an agate mortar to eliminate possible agglomerates and to homogenise the sample and then packed into the sample holder. The measurements were performed using a rotating sample stage to achieve homogeneous results. The compounds were characterised in ambient conditions of temperature (~20 °C) and pressure (~1 atm).

3.1.2 Environmental Scanning Electron Microscopy (E-SEM)

Environmental scanning electron microscopy is an ideal tool for observing the surface shape and morphology of samples. It was used to characterise the morphology of the solid acid powders and to measure their particle size *(see Chapter 4)*. Surface and cross-section morphology of composite membranes was also analysed using this technique *(see Chapter 5)*. The samples were scanned by an electron beam and the signal produced by the interaction with the surface was measured by a detector. The analysis of the secondary electrons of the samples allowed producing a topographic image of the samples. These measurements were carried out by the Chemicals and Materials Analysis group (ACMA) of the department of Chemical Engineering and Advanced Materials (CEAM) in

Newcastle University. The E-SEM micrographs were recorded using a FEI XL30 ESEM-FEG (Environmental Scanning Electron Microscope-Field Emission Gun) in low vacuum mode at 10 -15 kV.

Sample preparation

Solid acid powder samples were dried in an oven for 24 h at 80 °C to avoid moistening. They were ground in an agate mortar for 5 min to homogenise and to avoid agglomerates. The sample was placed on an aluminium holder and coated by sputtering with a layer of gold of few nanometres thickness to allow a clear image of the sample. The composite membranes were placed on an aluminium holder with both sides facing the top. The cross section of the membrane was also analysed. To obtain a non-deformed image of the cross section of the membranes a fragile fracture was carried out by placing the membrane into liquid N_2 for 1 min and breaking it with two tweezers.

3.1.3 Energy Dispersive X-ray Spectroscopy (EDS)

Energy dispersive X-ray spectroscopy is a technique use for the elemental characterisation of a sample. Samples were exposed to a beam of charged particles and the X-ray emissions generated by the sample were analysed by an X-ray detector. CsH_2PO_4-doped PBI membranes were analysed by this technique in order to study the interaction between both materials *(see Chapter 5)*. These measurements were carried out by the Chemicals and Materials Analysis group (ACMA) of the department of Chemical Engineering and Advanced Materials (CEAM) in Newcastle University. The elemental line-scan analysis of the samples was carried out using a FEI XL30 ESEM-FEG (Environmental Scanning Electron Microscope-Field Emission Gun) with a Rontec microanalysis system attached and the software used was called Quantax. The measurements were done in low vacuum at 20 kV.

Sample preparation

A fragile fracture of the membrane was carried out by placing the membrane into liquid N_2 for 1 min and breaking it with two tweezers and the cross section was determined by E-SEM to allow the line-scan analysis.

3.1.4 Thermo-gravimetric Analysis (TGA)

Thermo-gravimetric analysis is a technique used for thermal characterisation, where the mass of a sample is monitored as a function of temperature or time as it is subjected to a controlled temperature program in a controlled atmosphere. It was used to measure the mass loss of the synthesised solid acid powders *(see Chapter 4)*. The analysis was made in the department of Chemical Engineering and Advanced Materials (CEAM) of Newcastle University using a PerkinElmer STA600 analyser. The analysis was made under inert atmosphere (He) with a gas flow rate of 30 ml min^{-1} and in a temperature range from 50 °C to 600 °C with a thermal slope of 5 °C min^{-1}. The mass of the samples was ca. 100 mg before the analysis.

Sample preparation

Powdered solid acids were ground in an agate mortar for 5 min and placed in a ceramic crucible. All samples were dried in the oven for 24 h at 80 °C prior to the experiment to avoid any adsorbed humidity.

3.1.5 Differential Scanning Calorimetry (DSC)

Differential scanning calorimetry is a technique used for thermal characterisation where the difference in the amount of heat required to increase the temperature of a sample and reference is measured as a function of temperature. It measures how the heat capacity (C_p) of a material is changed by temperature. A sample of known mass is heated or cooled and the changes in its heat capacity are tracked as changes in the heat flow. This technique was used for the detection of transitions like melts, phase changes or decomposition in the synthesised solid acids *(see Chapter 4)*. The analysis was made in the department of Chemical Engineering and Advanced Materials (CEAM) of Newcastle University using a PerkinElmer STA600 analyser. The analysis was made under inert atmosphere (He) with a gas flow rate of 30 ml min^{-1} and in a temperature range from 50 °C to 600 °C with a thermal slope of 5 °C min^{-1}. The mass of the samples was ca. 100 mg before the analysis.

Sample preparation

Powdered solid acids were ground in an agate mortar for 5 min and placed in a ceramic crucible. All samples were dried in the oven for 24 h at 80 °C prior to the experiment to avoid any absorbed humidity.

3.1.6 Solid state Nuclear Magnetic Resonance (ss-NMR) Spectroscopy

Solid state nuclear magnetic resonance spectroscopy is an analytical technique used to characterise physical and chemical properties of atoms or molecules in a material. It is based on a phenomenon occurring in the nuclei of an atom when it is subjected to a static magnetic field and then exposed to a second oscillating magnetic field. By this technique analysis on the nuclei of atoms are performed and the chemical environment of specific nuclei is deduced from the information obtained. It was used to study phosphate condensation on the heat-treated CsH_2PO_4 samples *(see Chapter 5)*. Solid state ^{1}H and ^{31}P NMR analyses were performed with a Varian VNMRS 400 WideBore solid state NMR spectrometer with a Varian 3.2 mm T3 probe and 3.2 mm zirconia rotor. This analysis was made in the department 'Chimie Moléculaire et Organisation du Solide' of the 'Institut Charles Gerhardt Montpellier, CNRS-UM2', France.

Sample preparation

Powdered and fibre CsH_2PO_4 were ground in an agate mortar for 5 min and placed in the NMR holder. All samples were dried in the oven for 24 h at 80 °C prior to the experiment to avoid any adsorbed humidity.

3.1.7 Mechanical properties

The mechanical properties of the fabricated composite membranes were characterised by measuring their tensile strength. The tensile properties indicate how the material reacts to forces being applied in tension. A tensile test is a fundamental mechanical test where a carefully prepared specimen is loaded in a very controlled manner while measuring the applied load and the elongation of the specimen over some distance.

Tensile tests were used to determine the modulus of elasticity, or *Young's modulus (Y)*, which describes tensile elasticity, that is, the tendency of an object to deform along an axis when opposing forces are applied along that same axis. It is defined as the ratio of tensile stress to tensile strain and calculated from the slope of its stress/strain curve in the elastic deformation region (figure 3.1). In this linear region, the line obeys the relationship defined as Hooke's Law where the ratio of stress to strain is a constant.

The point of the curve where the stress/strain line relationship deviates from the straight line is known as the *Yield strength point*. After this point the strain increases faster than the

stress, and some permanent deformation occurs and the material will not return to its original unstressed condition when the load is removed.

The *ultimate tensile strength (UTS)* is the maximum stress level reached in a tension test. It represents the strength of a material to withstand external forces without breaking. On the stress/strain curve the UTS is the highest point of the line.

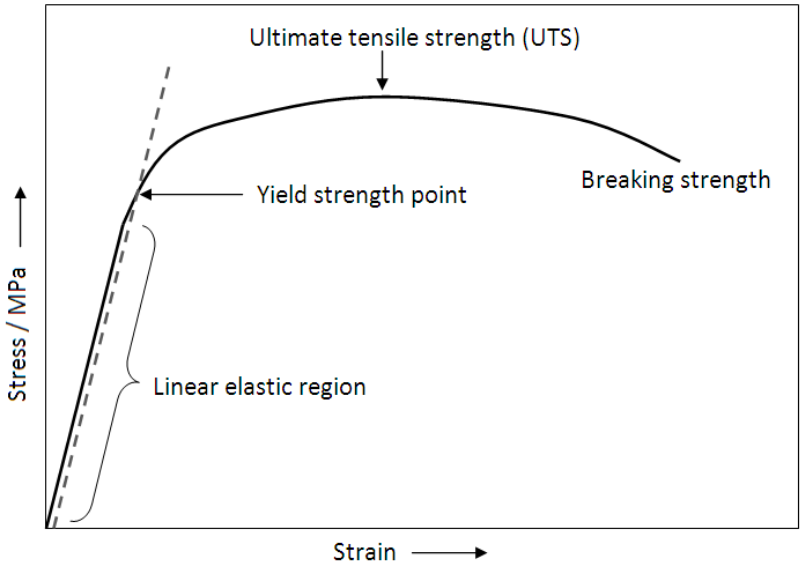

Figure 3.1. Schematic representation of a stress/strain curve.

These experiments were carried out in a Tinius Olsen device H25KS with a 100 N load. 1 mm s^{-1} speed was applied until specimen break took place. Horizon software was used in the experiments. The above mentioned parameters were calculated for each of the composite membranes fabricated *(see Chapter 5)*.

Sample preparation

Composite membranes were cut in 5 × 1 cm strips. The thickness of each sample was measured prior to the experiment using a standard micrometre.

3.1.8 Electrospinning

Electrospinning is a technique used to produce polymeric or hybrid fibres in the micrometre to nanometre scale [3, 4]. The principle of this technique is to apply a high potential to a drop of a polymer solution, such that the repulsive electrical forces overcome the surface tension of the drop. A charged jet of the solution is then ejected onto a

grounded collector allowing the evaporation of the solvent and the formation of solid thin fibres. The shape of the polymer solution droplet changes when the potential is applied, resulting in a characteristic shape known as the *Taylor Cone*. The electrospinning device comprised a high voltage power supply and a syringe pump to control the feed rate of solution to the syringe (figure 3.2).

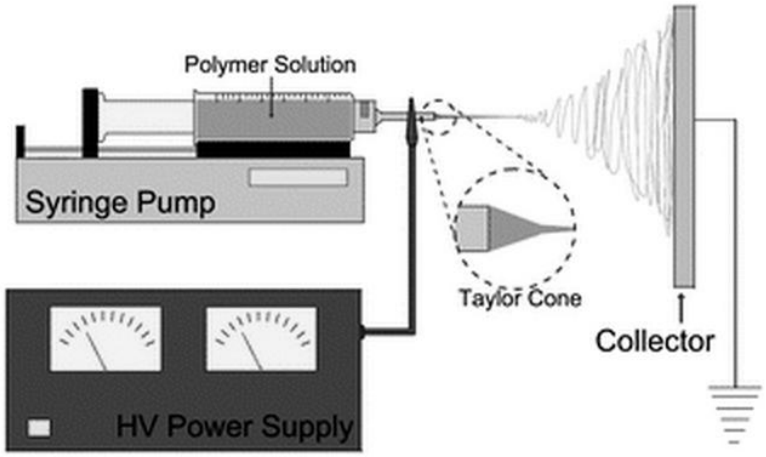

Figure 3.2. Schematic diagram of the electrospinning device [4].

This technique was used to produce CsH_2PO_4 fibres and to develop a new method to fabricate phosphate-based solid acid proton conducting membranes *(see Chapter 5)*. CsH_2PO_4 was electrospun by the electrospinning device onto a grounded collector covered by an aluminium foil. The output solution rate of the needle was 0.3 ml h^{-1} and the distance of the needle from the target and the potential applied were 10 cm and 15 kV respectively.

Sample preparation

The methodology used for sample preparation for the electrospinning of the partially dehydrated CsH_2PO_4 is explained in section 5.1.

3.2 Electrochemical methods

3.2.1 Electrochemical Impedance Spectroscopy (EIS)

Electrochemical impedance spectroscopy is a method used to characterise the electrical properties and determine parameters associated with electrochemical interface and bulk of

materials. The principle of this technique is to measure the response of a system to an applied sinusoidally varying alternating voltage at a range of frequencies. Impedance analysis of ionic solids identifies the elementary process such as, bulk conduction, ionic transport, grain boundary conduction and the electrode-electrolyte interface process in the measured frequency domain. It is a non-destructive technique and also can provide the dynamic properties to understand the microscopic nature of the proton conducting materials [5].

The proton conductivity of the solid acids was measured using EIS. The EIS experiment involved applying a small sinusoidal voltage perturbation (20 mV) to the system in a broad range of frequencies (between 1 Hz and 500 kHz) and measuring the resulting current with the phase angle. Using this data, the real (Z') and imaginary (Z'') impedances were calculated and plotted against each other in what is called Nyquist impedance spectra (figure 3.3). The value corresponding to the ionic resistance of the electrolyte ($R_{electrolyte}$) was calculated from the intercept of the spectrum with the real axis.

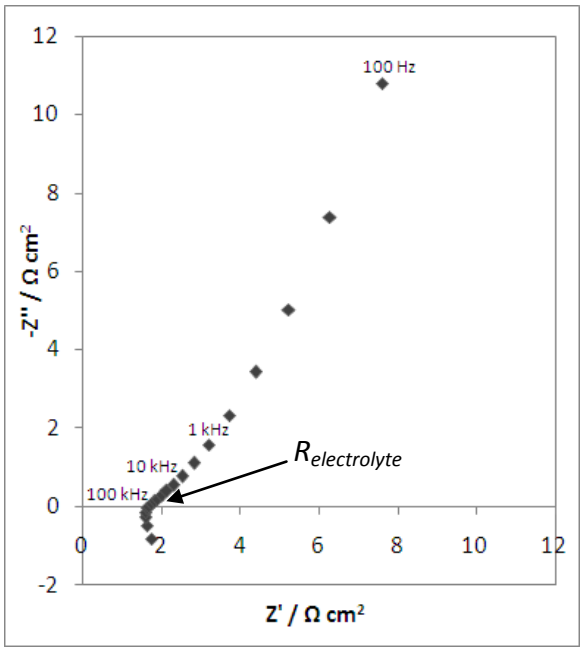

Figure 3.3. Nyquist plot of a 300 µm thickness CsH_2PO_4 pellet at 250 ºC.

Considering the calculated resistance and the distance between the electrodes and cross-section area, conductivity of the material was calculated using equation 3.2. Stabilising time of 20 min was left before measuring each point. All the measurements were made under water saturated N_2 stream with a gas flow rate of 50 ml min^{-1} and the cell temperature was varied in the range of 50 to 300 °C.

$$\sigma = \frac{d}{R\,A} \tag{3.2}$$

where σ is the proton conductivity (S cm^{-1}), d represents the distance between electrodes (cm), R the resistance (Ω) and A is the cross-section area (cm^2).

Due to the heterogeneity of some of the composite membranes, in-plane and through-plane conductivity measurements were carried out in these samples. In-plane measurements were carried out placing the same side of the membrane in a four platinum electrode cell (figure 3.9) while for through-plane conductivity the electrolysis tubular cell (figure 3.10) with one electrode on each side of the membrane was used. This way the anisotropic behaviour of the proton conduction in the cast composite membranes was studied.

Sample preparation

Pellets of the solid acids with a diameter of 1.8 cm were prepared by pressing the powder at 7 × 10^3 kg cm^{-2} and ca. 18 °C for 30 min. These pellets were prepared with 300 mg powder and thickness of ca. 300 μm in order to maintain enough mechanical strength and avoid pellet cracking in the conductivity cell. Pellets were sandwiched between two 1.5 cm diameter carbon papers (Freudenberg H2315-I2-C8, with gas diffusion layer) to provide better contact in the electrolyte/electrode interface. Measurements were carried out in the tubular electrolysis cell shown in figure 3.10 with an Ar flow of 50 ml min^{-1} passing through a temperature controlled water saturator. Torque was applied by applying 2.5 atm air pressure to the compression piston. The composite membranes were cut in 1 × 5 cm sized strips. The samples were placed in the conductivity cell shown in figure 3.9 and the cell was sealed by applying a 2 N m torque using a torque wrench of 0 to 5 N m range.

3.2.2 Cyclic Voltammetry (CV)

Cyclic voltammetry is one of the most important and widely used methods for electrochemical studies of a system, providing information about thermodynamic and kinetics of redox processes of electroactive species, adsorption and coupled chemical reactions. The obtained voltammograms in which the current is monitored as a function of applied potential is informative concerning the oxidation and reduction reactions from which the required information can be acquired. In cyclic voltammetry, the potential/time waveform is based on sweeping potential at a constant rate between initial and final

potentials (E_1 and E_2) which is known as the forward scan. Then the potential can be swept back to the initial potential (from E_2 to E_1) in the backward scan, as shown in figure 3.4.

Cyclic voltammetry was performed in this research to address the effect of different aqueous electrolytes in the electrochemical active surface (EAS) of platinum and iridium oxide and to identify the redox processes taking place at different potentials *(see Chapter 6)*. These experiments were carried out in a standard three electrode cell (figure 3.8). CVs were also performed to characterise the electrodes of the single-cell electrolysis system (figure 3.10) and estimate catalyst utilisation with a solid state electrolyte *(see Chapter 7)*.

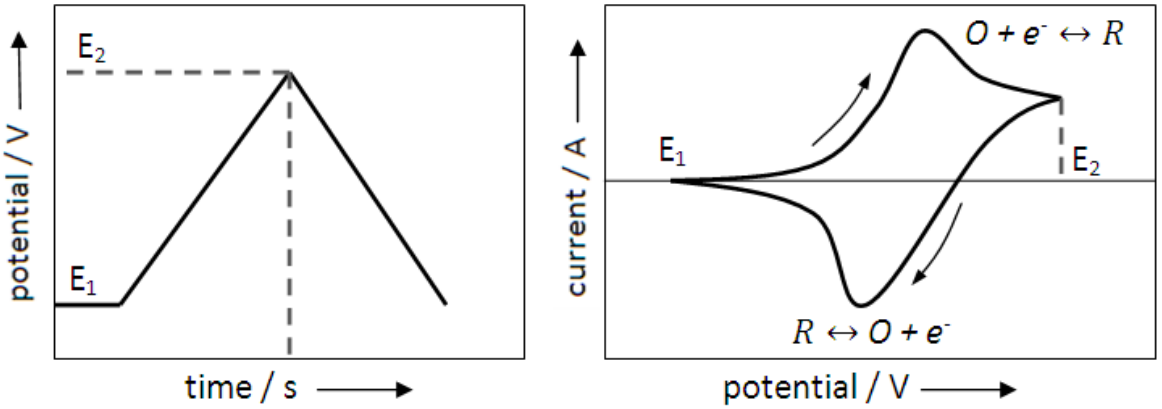

Figure 3.4. (a) cyclic potential sweep, (b) resulting cyclic voltammogram.

ESA values of iridium oxide are commonly given by charge units (mC cm^{-2}) calculated by the area integration of the cyclic voltammograms in the 0 – 1.4 V region [6-8]. In the case of platinum, a well-established technique to calculate the EAS is to integrate the charge of the proton desorption peak (Q_H) obtained in the range of 0 – 0.4 V [9-11]. At this potential range the proton attached to the surface of the Pt desorbs giving an anodic current in form of a peak. The value of this coulombic charge is directly proportional to the area of catalyst active in the electrochemical half-reaction as showed in equation 3.3.

$$EAS_{CV} = \frac{Q_H}{[Pt] \times 0.21} \tag{3.3}$$

where Q_H represents the charge for hydrogen desorption (mC cm^{-2}), $[Pt]$ the platinum loading (mg cm^{-2}) and 0.21 (mC cm^{-2}) represent the charge required to desorb a monolayer of H_2 on bright Pt [12, 13].

Sample preparation

Due to the variety of methods and electrodes prepared for both, half-cell and electrolysis cell experiments, the sample preparation methods are explained in detail in the experimental sections of Chapters 6 and 7.

3.2.3 Linear Sweep Voltammetry (LSV)

Linear sweep voltammetry follows the same principle as cyclic sweep voltammetry where only the forward sweep is monitored (figure 3.4). Quasi-steady linear sweep voltammograms (or polarisations) were performed in both aqueous media (three electrode cell, figure 3.8) and in solid state (tubular electrolysis cell, figure 3.10) in order to determine the activity and stability of the system towards water splitting reaction. Quasi-steady polarisation curves were carried out in the potential range of 1.0 – 2.0 V at a scan rate of 1 mV s^{-1} in all experiments. In the obtained curves the losses arising from the ohmic resistance of the system (iR_A), ionic from the electrolyte and electric from the system, and the kinetic losses produced by the anode (η_{An}) and cathode (η_{Cath}) are included (figure 3.5). The effect of these processes was separately analysed in order to determine the contribution of each of them to the overall performance of the system.

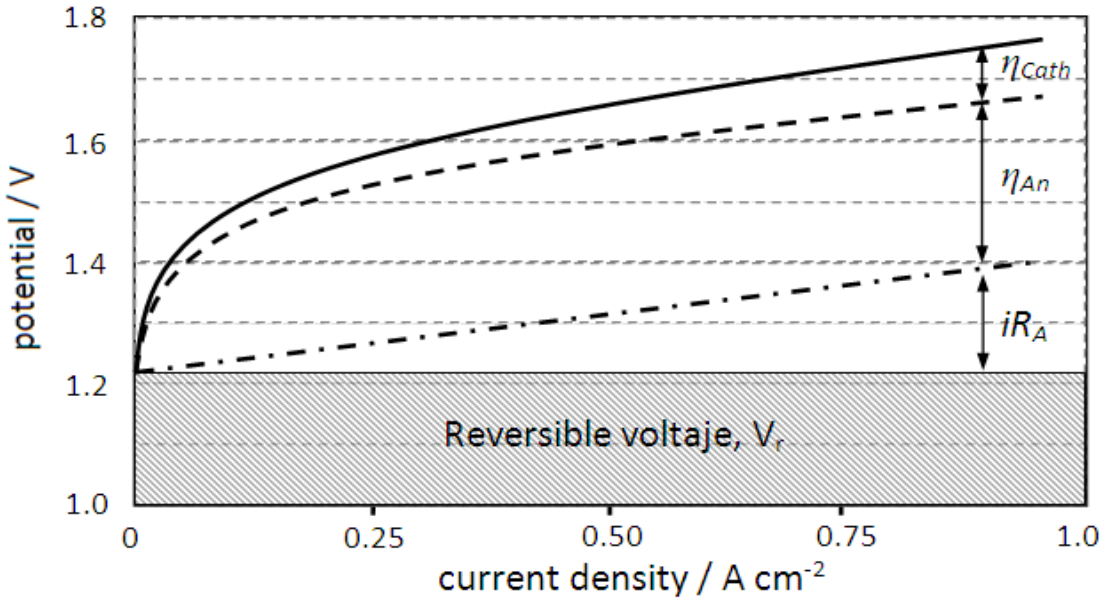

Figure 3.5. Standard polarisation curve of an electrolysis system showing the reversible voltage (v_r), ohmic losses (iR_A) and anode and cathode overpotentials (η).

The effect of the ***ohmic resistance of the system (iR_A)*** was determined by electrochemical impedance spectroscopy (section 3.2.1). The contribution of the ohmic resistance arises mainly from the protonic resistance provided by the electrolyte. It was calculated for the aqueous electrolyte in half-cell studies *(see Chapter 6)* and for the solid electrolyte in the single-cell electrolysis characterisation *(see chapter 7)*.

The contribution of the ***kinetic losses produced in the cathode (η_{Cath})*** was calculated for the single-cell electrolysis system *(see Chapter 7)*, corresponding to the hydrogen evolution reaction (HER). Hydrogen pump polarisations were carried out in order to determine the overpotential provided by the cathode kinetics in the electrolysis cell. These measurements were carried out feeding 50 ml min^{-1} H_2 gas to the counter (and reference) electrode and 50 ml min^{-1} N_2 gas to the working electrode and then polarising the system from 0 to 350 mV. The hydrogen is oxidised in the counter electrode to protons and electrons; protons travel through the electrolyte and electrons through the external circuit to meet in the working electrode, where protons are reduced to hydrogen gas. The electrolysis cell shown in figure 3.10 was used for these experiments.

The linear sweeps obtained were corrected for the iR_A and η_{Cath} in order to determine the ***kinetic losses produced in the anode (η_{An})***, corresponding to the oxygen evolution reaction (OER). The activity of IrO_2 towards OER was calculated by determining the current density obtained at different overpotentials. The kinetic parameters corresponding to this reaction (Tafel slope, b, exchange current density, j_0, and activation energy, E_a) were calculated as explained in section 3.2.3.1.

Sample preparation

Due to the variety of methods and electrodes prepared for both, half-cell and single-cell electrolysis experiments, the sample preparation methods are explained in detail in the experimental section of Chapters 6 and 7.

3.2.3.1 Calculation of the kinetic parameters

During the linear sweeps the electrocatalytic process is dominated by two main processes; (1) charge-transfer, where the exchange of electrons between the electrode and the electrolyte is the limiting step and (2) mass-transport, where the process is controlled by the diffusion of species. In order to study the electrocatalytic activity of the catalyst and

calculate pure kinetic parameters, the region where the process is controlled by charge-transfer must be determined.

This is the initial region of the polarisation curve where the relation of the exchange of electrons with the surface of the electrode and the potential applied is exponential, (region I, figure 3.6). During the rest of the curve, region II of figure 3.6, both processes will take place at the same time, being the limiting step a balance between electron transfer in the interface electrode/electrolyte and the diffusion of reactants and products (and the species taking place in the reaction mechanism, i.e. H^+) from the active sites of the electrocatalyst [14, 15].

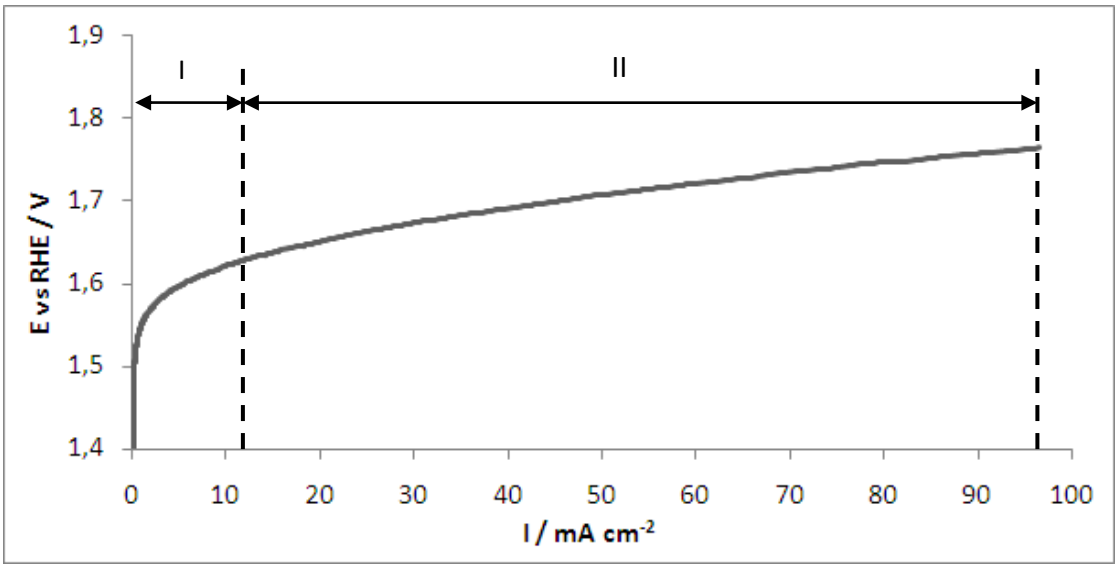

Figure 3.6. Polarisation curve of IrO_2 in 5.15M H_3PO_4 at 80 °C, scan rate 1 mV s^{-1}.

The reversible potential, E_{rev}, is the potential before polarising the system, where no net current flows, and which can be calculated by Nerst equation (equation 3.4).

$$E_{rev} = E^0_{rev} + \frac{2.3RT}{nF} log \frac{[Ox]^n}{[Re]^n} \quad (3.4)$$

where R represents the ideal gas constant (8.314 J mol^{-1} K^{-1}), n the number of electrons taking place in the reaction and F represents the Faradaic constant (96495 C mol^{-1}). As the concentration of oxidised and reduced species in the system is difficult to determine experimentally, the reversible potential can also be calculated from the thermodynamic parameters of the reaction:

$$E_{rev} = -\frac{\Delta G_R}{nF} \tag{3.5}$$

where ΔG_R (kJ mol^{-1}) stands for the Gibbs free energy of reaction. For any given temperature ΔG_R can be calculated from reaction 3.6, where the enthalpy and entropy of reaction (ΔH_R, ΔS_R) will be temperature dependent as stated in reactions 3.7 and 3.8.

$$\Delta G_R = \Delta H_R - T\Delta S_R \tag{3.6}$$

$$\Delta H_R = H^0 - R\int_{298K}^{T} C_p dT \tag{3.7}$$

$$\Delta S_R = S^0 - R\int_{298K}^{T} \frac{C_p}{T} dT \tag{3.8}$$

where H^0 (kJ mol^{-1}) and S^0 (kJ mol^{-1} K^{-1}) represent the standard enthalpy and entropy and C_p (kJ mol^{-1}) the temperature dependant heat transfer coefficient. At the reversible potential the system is in a dynamic equilibrium where oxidation and reduction processes happen at the same rate. The sum of these cathodic and anodic currents equal to zero and their magnitude, both the same in absolute values, equals to the so-called *exchange current (i_0).*

$$i = i_{anode} + i_{cathode} = 0 \tag{3.9}$$

$$i_0 = |i_{anode}| = |i_{cathode}| \tag{3.10}$$

i_0 is a kinetic parameter which describes how fast the electrochemical reaction happens when the system is at equilibrium and is thus directly related to the ability for charge transfer in the electrode/electrolyte interface [14].

When the system is polarised to more positive potentials an anodic current is generated by the OER and the cathodic parameter in Butler-Volmer equation (equation 3.11) disappears, leading to the so-called Tafel equation (equation 3.12) [16].

$$i = i_0^{\frac{\alpha_a nF}{RT}\eta - \frac{\alpha_c nF}{RT}\eta} \tag{3.11}$$

$$\log i = \log i_0 + \frac{\alpha_a nF}{RT}\eta \quad \rightarrow \quad \eta = a + b\ \log i \tag{3.12}$$

where η is the overpotential (the difference between the applied potential and the E_{rev}), meaning how far is the system from equilibrium, b stands for the *Tafel slope* $\left({}^{2.3RT}/_{\alpha_a nF}\right)$ and a equals $\left({}^{2.3RT\log i_0}/_{\alpha_a nF}\right)$ It is possible to measure experimentally the exchange current (i_0) and Tafel slope (b) by plotting the logarithmic current vs. applied potential (or overpotential), known as Tafel plot (figure 3.7).

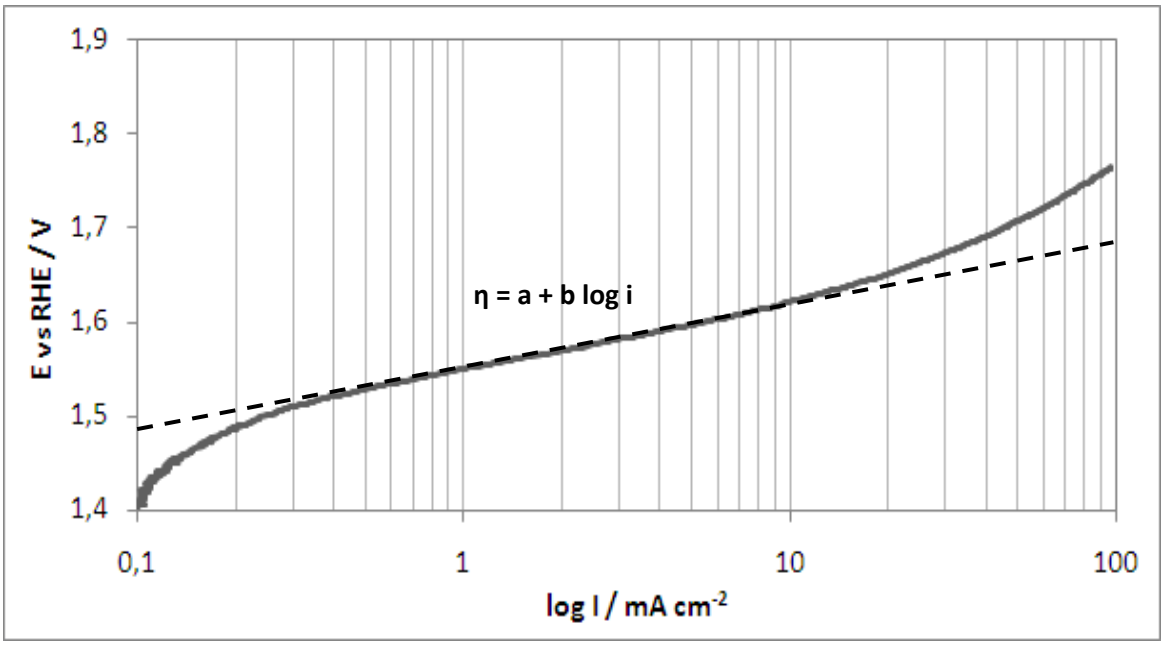

Figure 3.7. Tafel plot of IrO_2 in 5.15M H_3PO_4 at 80 °C, scan rate 1 mV s^{-1}.

The charge transfer process occurs where the linear region of the polarisations is distinguished. The slope of the linear region is b and the interception where the extrapolation of the linear region meets the E_{rev} (η = 0) is the value where i = i_0.

The *activation energy* is the minimum energy required for the electrochemical process to occur. It can be calculated from the dependence if i_0 with temperature, following Arrhenius law (equations 3.13 and 3.14).

$$i_0 = i^{\frac{-E_a}{RT}} \tag{3.13}$$

$$\log i_0 = \log i - \frac{E_a}{2.3RT} \tag{3.14}$$

where E_a represents the activation energy (kJ mol^{-1}) of the electrochemical reaction. This parameter is calculated experimentally by calculating the slope of the line in the so-called Arrhenius plot; that is log i_0 vs. T^{-1}.

3.2.4 Electrochemical cells

Three different electrochemical cells were used in this research; (1) a standard jacketed three electrode cell for catalyst characterisation studies, (2) a four electrode cell for in-plane conductivity measurements of composite membranes and (3) a tubular electrolysis cell for electrolysis studies and trough-plane conductivity measurements of pellets and membranes.

The three electrode cell consisted in a 100 ml capacity glass cell (figure 3.8). It was jacketed for a temperature controlled performance using a standard water bath. The reference electrode used was Ag/AgCl electrode (BASi), glassy carbon electrode (BASi) with 0.07 cm^2 area or a gold electrode with 0.154 cm^2 were used as working electrode and a platinised titanium mesh with 2.5 × 2 cm as counter electrode. N_2 was bubbled continuously in the solution to maintain the system deoxygenated. The cell was connected to a Sycopel Scientific Ministat potentionstat (Model 256D Metered Ministat) to perform the linear and sweep voltammetry experiments.

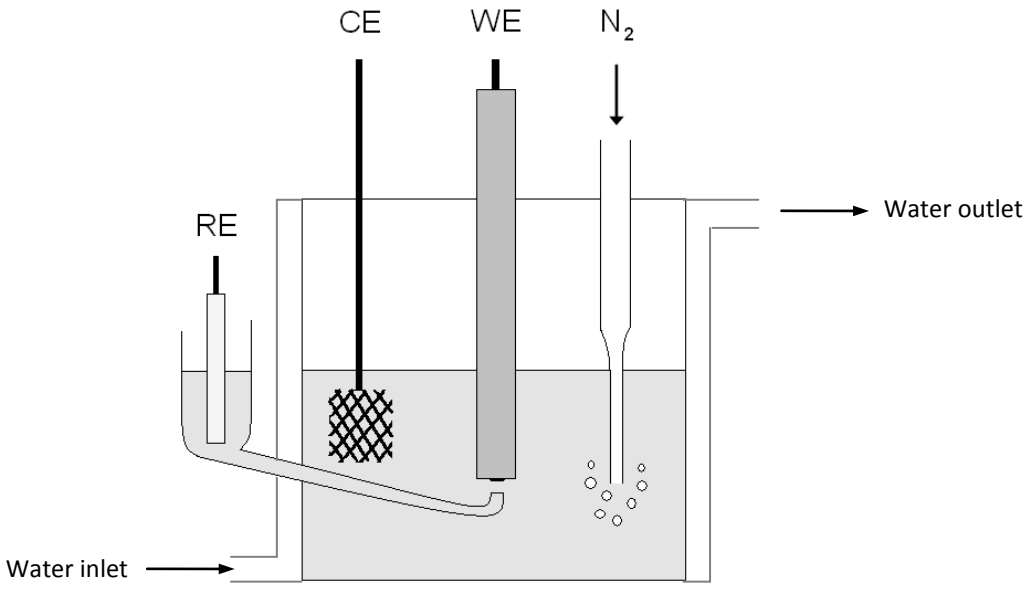

Figure 3.8. Schematic diagram of the three electrode half-cell, showing the reference electrode (RE), counter electrode (CE) and working electrode (WE).

The four electrode cell used for in-plane conductivity measurements is shown in figure 3.9. Four equally spaced platinum foils act as the electrodes in contact with the measured material. Two of the electrodes were used to current flow while the other two were used to

measure the voltage drop of the system. 50 ml min^{-1} Ar was passed through a temperature controlled water saturator and then fed to the gas chamber of the cell, in contact with the Pt electrodes. All gas feeding tubes were heated to avoid water condensation in the system. The cell was connected to a frequency response analyser (PSM1735 Multimeter analyser with a Newton 4th Ltd. Impedance Analysis Interface) to perform impedance measurements.

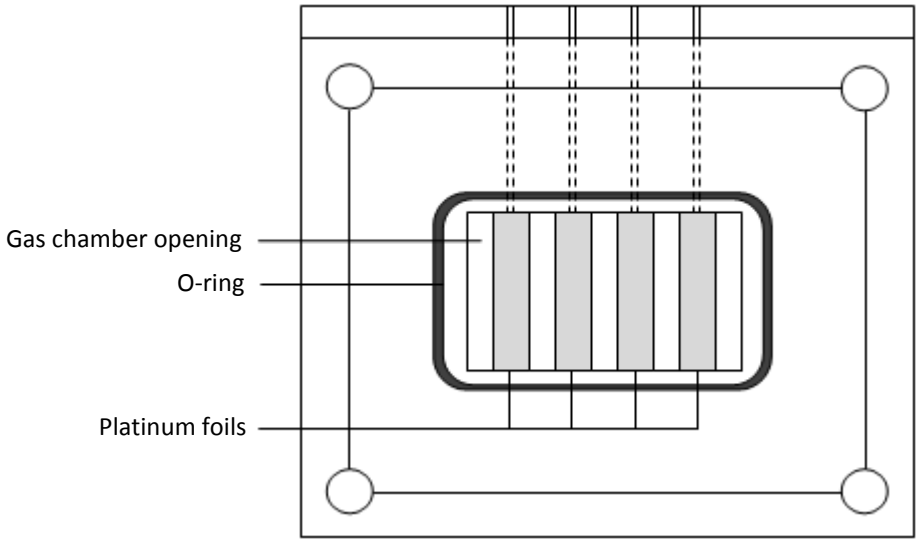

Figure 3.9. Schematic drawing of proton conductivity cell for in-plane conductivity measurements.

Electrolysis studies and through-plane impedance measurements were carried out in the tubular cell shown in figure 3.10. The sample (either pellet or membrane) was placed in the sample holder (figure 3.10-b) between two titanium rods with gas inlet and outlet. A spiral channelling was mechanised at the end of the titanium rods to distribute the gases uniformly. The ends of the rods were gold coated to avoid any corrosion issues. A thermocouple was fitted in the gas channel of one of the rods in close contact with the measured sample. The titanium rods were embedded in two ceramic tubes and everything clamped together by a cylindrical heater. Torque to the system was provided by a pressurised piston in the edge of one of the titanium rods. The pressure range was 0 – 5 atm. All gas feeding tubes were heated to avoid water condensation in the system. Electrolysis studies were performed using an EG&G Princeton scanning potentiostat model 362. For EIS measurements the cell was connected to a frequency response analyser (PSM1735 Multimeter analyser with a Newton 4th Ltd. Impedance Analysis Interface). The electrical resistance provided by the system was measured at different piston pressures and subtracted from the impedance resistance measured (figure A-1, appendix A).

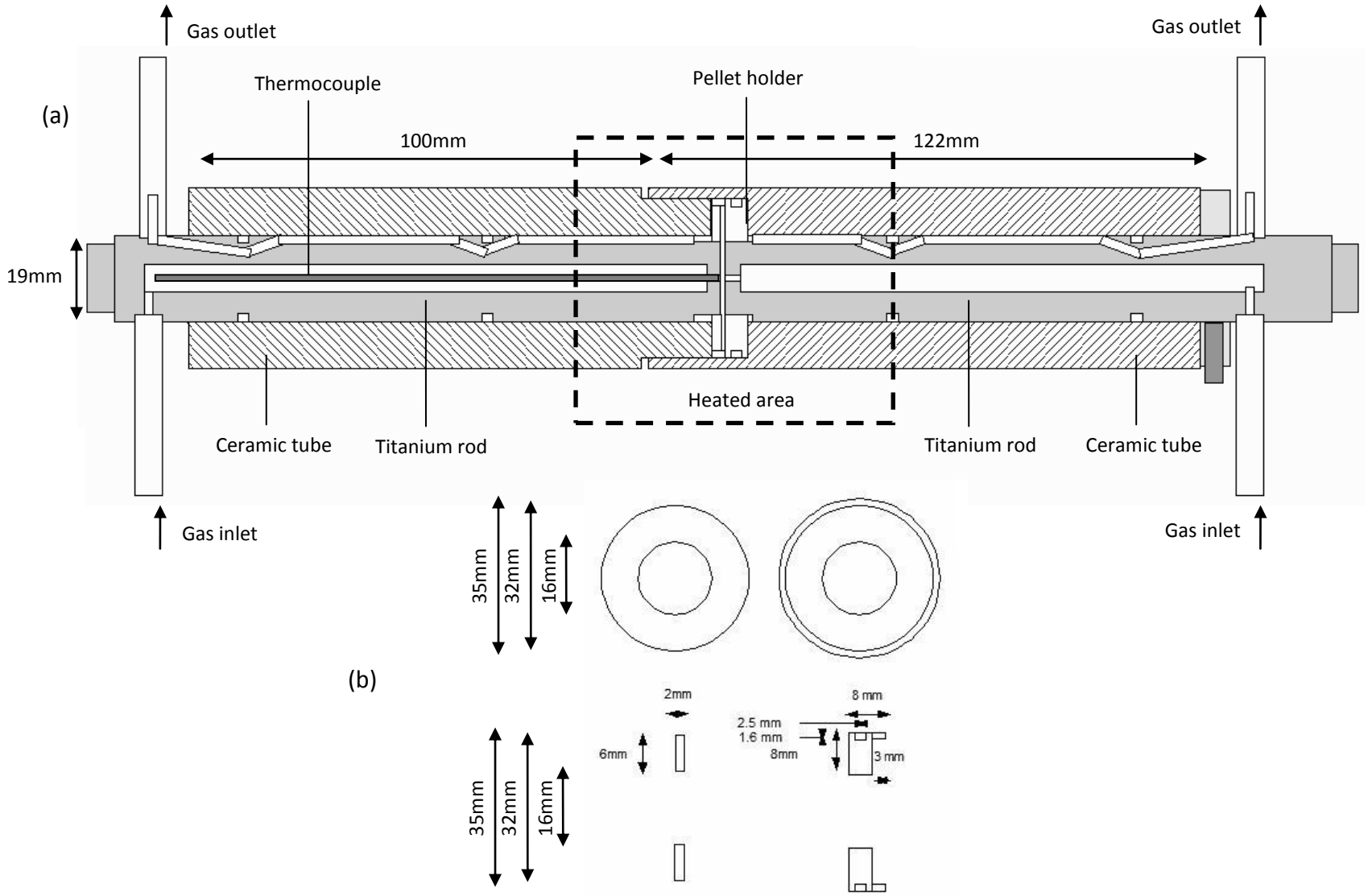

Figure 3.10. Schematic drawing of (a) electrochemical tubular cell and (b) sample holder.

3.3 References

1. Pecharsky, V., Zavalij, P., *Fundamentals of Powder Diffraction and Structural Characterization of Materials*. 2009, 2nd edition: Springer.
2. Chung, F.H., *Quantitative interpretation of X-ray diffraction patterns of mixtures. II. Adiabatic principle of X-ray diffraction analysis of mixtures.* Journal of Applied Crystallography, 1974. **7**(6): p. 526-531.
3. Huang, Z.-M., Zhang, Y.Z., Kotaki, M., and Ramakrishna, S., *A review on polymer nanofibers by electrospinning and their applications in nanocomposites.* Composites science and technology, 2003. **63**(15): p. 2223-2253.
4. Cavaliere, S., Subianto, S., Savych, I., Jones, D. J., and Rozière, J., *Electrospinning: designed architectures for energy conversion and storage devices.* Energy & Environmental Science, 2011. **4**(12): p. 4761-4785.
5. Barsoukov, E. and J.R. Macdonald, *Impedance spectroscopy: theory, experiment, and applications*. 2005: Wiley. com.
6. Juodkazytė, J., Šebeka, B., Valsiunas, I., and Juodkazis, K., *Iridium anodic oxidation to Ir (III) and Ir (IV) hydrous oxides.* Electroanalysis, 2005. **17**(11): p. 947-952.
7. Felix, C., Maiyalagan, T., Pasupathi, S., Bladergroen, B., & Linkov, V., *Synthesis, characterisation and evaluation of IrO_2 based binary metal oxide electrocatalysts for oxygen evolution reaction.* International Journal of Electrochemical Science, 2012. **7**: p. 12064-12077.
8. Burke, L.D., Whelan , D.P., *A voltammetric investigation of the charge storage reactions of hydrous iridium oxide layers.* J Electroanal Chem., 1984. **162**: p. 121-141.
9. Perez, J., E.R. Gonzalez, and E.A. Ticianelli, *Oxygen electrocatalysis on thin porous coating rotating platinum electrodes.* Electrochimica Acta, 1998. **44**(8–9): p. 1329-1339.
10. Deepalochani, B.K., *Performance of Platinum Black and Supported Platinum Catalysts in a Direct Methanol Fuel Cell* Int. J. Electrochem. Sci., 2009. **4**: p. 386-395.
11. McBreen, J., *Voltammetric Studies of Electrodes in Contact with Ionomeric Membranes.* Journal of The Electrochemical Society, 1985. **132**(5): p. 1112-1116.
12. Trasatti, S. and Petrii, O.A., *Real surface area measurements in electrochemistry.* Pure Appl. Chem., 1991. **63**(5): p. 711-734.
13. Dongping Zhan, J.Velmurugan, M.V. Mirkin, *Adsorption/Desorption of Hydrogen on Pt Nanoelectrodes:Evidence of Surface Diffusion and Spillover.* J Am Chem Soc., 2009. **131**(41): p. 14756-14760.
14. Miles, M.H., Kissel, G., Lu, P. W. T. and Srinivasan, S., *Effect of Temperature on Electrode Kinetic Parameters for Hydrogen and Oxygen Evolution Reactions on Nickel Electrodes in Alkaline Solutions.* Journal of The Electrochemical Society, 1976. **123**(3): p. 332-336.
15. Krishtalik, L.I., *Kinetics and mechanism of anodic chlorine and oxygen evolution reactions on transition metal oxide electrodes.* Electrochimica Acta, 1981. **26**(3): p. 329-337.
16. Song, C. and J. Zhang, *Electrocatalytic Oxygen Reduction Reaction*, in *PEM Fuel Cell Electrocatalysts and Catalyst Layers*, J. Zhang, Editor. 2008, Springer London. p. 89-134.

CHAPTER 4

SYNTHESIS AND CHARACTERISATION OF PHOSPHATE-BASED SOLID ACIDS

In this chapter the physico-chemical and electrochemical characterisation of phosphate-based solid acids was carried out and the stability in terms of thermal decomposition and water solubility addressed. Structure and morphology in terms of crystallite and particle sizes were examined by P-XRD and E-SEM and thermal stability in terms of dehydration was studied by TGA-DSC analysis in the temperature range of 50 – 600 °C. The dependency of proton conductivity on temperature was determined by EIS in order to study the so-called 'superprotonic phase transition' exhibited by these materials. The effect of humidification on the stability of CsH_2PO_4 was further analysed in order to address the humidity conditions required for a stable performance of this material in the electrolysis system.

4.1 Introduction

Great effort has been made in material science in order to develop new materials to allow increasing the operating temperature of proton exchange membrane fuel cells (PEMFC) and water electrolysers (PEMWE) [1-4]. The increase in the operating temperature reduces the electric energy demand and enhances the kinetics of the electrochemical reactions and the catalyst tolerance to CO poisoning. Water management in these devices is also greatly simplified when operating above 100 °C [5].

The electrolyte is the main cause of the temperature restriction due to the water boiling point. Nafion®, a perfluorosulfonated chained polymer, which is the state-of-the-art electrolyte membrane used in these electrochemical devices, loses its proton conductivity in the absence of liquid water [6]. It has been therefore an extent research in material science in order to find or develop materials which can conduct protons at temperatures higher than 100 °C; that is, in the absence of liquid water. Although there is knowledge of high temperature proton conductors in the range of 500 – 800 °C [7], few possibilities of proton conducting materials in the medium temperature range (100 – 300 °C) where

operating conditions are much more favourable from an engineering point of view, have been found [1, 8, 9]. Phosphoric acid-doped polymers have been the most promising electrolytes for medium temperatures [10, 11], but still many problems have to be overcome, ca. slow electrode kinetics [12, 13] or durability issues caused by membrane mechanical degradation and phosphoric acid leaching [14, 15]. Solid acids have attracted great interest the last decade due to their high proton conductivity (10^{-2} - 10^{-3} S cm^{-1}) at the intermediate temperature range (150 - 300 °C) [16, 17]. Their proton conductivity mechanism is believed to be driven by proton hopping, also known as 'Grotthuss mechanism' [4, 18]. These inorganic salts are usually composed by an alkali-metal as the positive ion and one (or more) kind of the following anion groups; sulphates, selenates, phosphates and arsenates.

In this chapter the synthesis and characterisation of phosphate-based solid acids is investigated. Five different materials of the alkali-metal family, MH_2PO_4 (M = Cs, Rb, K, Li and NH_4) were synthesised and their properties investigated. The effect of humidification in the stability of CsH_2PO_4 was further analysed in order to determine the suitability of this material as electrolyte in PEM water electrolysers.

4.2 Experimental

The synthesis of phosphate-based solid acids, MH_2PO_4 (M = Cs, Rb, K, Li), was carried out by combining each starting reagent Cs_2CO_3 (Aldrich, 99.0%), Rb_2CO_3 (Alfa-Aesar, 99.8%), K_2CO_3 (Alfa-Aesar, 99.0%), Li_2CO_3 (Sigma-Aldrich, 99.0%) and H_3PO_4 (Sigma-Aldrich, ACS > 85% wt. aq. solution) in a molar ratio of 1:2 (equation 4.1).

$$M_2CO_3 + 2H_3PO_4 \rightarrow 2MH_2PO_4 + H_2O + CO_2 \quad (4.1)$$

The reaction was carried out in aqueous solution at ~18 °C and 1 atm. In the case of LiH_2PO_4, KH_2PO_4 RbH_2PO_4 and CsH_2PO_4 polycrystalline powders were obtained by drop wise addition of 1.5 M solid acid aqueous solution into 250 ml methanol. Single crystals were grown by the slow evaporation of water at ambient conditions (~18 °C, 1 atm) from 3.0 M aqueous solution of each solid acid. Sample verification was carried out by Powder X-Ray Diffraction analysis (P-XRD) at ~20 °C and 1 atm. Granular $(NH_4)H_2PO_4$ was obtained from commercial source (Sigma-Aldrich, 98.0%). Polycrystalline powder of this compound was obtained by drop wise addition of 1.5 M aqueous solution into 250 ml

acetone and single crystals by the slow evaporation of 3.0 M aqueous solution at ambient conditions (~18 °C, 1 atm). All the samples were dried in an oven at 80 ºC for 24 h to avoid moistening. Pellets of all materials were fabricated by pressing the grounded powder at 7×10^3 kg cm^{-2} at room temperature for 30 min. Pellets were approximately 300 µm thick (although exact thickness was measured for each one of the samples) and 1.8 cm diameter.

The crystallographic properties of the samples were characterised by Powder X-Ray Diffraction (P-XRD) and morphology by Environmental Scanning electron microscopy (E-SEM). The thermal stability of the samples was analysed by Thermo-Gravimetric Analysis (TGA) and Differential Scanning Calorimetry (DSC) and their proton conductivity measured by Electrochemical Impedance Spectroscopy (EIS). All these methods are more extensibly explained in chapter 3.

4.3 Characterisation of phosphate-based solid acids

4.3.1 Crystallographic structure and morphology

Phosphate-based solid acids were characterised by P-XRD in order to verify the successful synthesis of the compounds and study their crystallographic structure. The spectrum of each of the synthesised powders matches with the data provided by the International Crystallographic Diffraction Database (ICDD). By Scherrer equation (equation 3.1, Chapter 3) the crystallite size of the compound was calculated using the three most characteristic peaks of each spectrum.

All the solid acid compounds exhibited an average crystallite size of the same range, between 60 and 90 nm diameter, assuming spherical crystallites. LiH_2PO_4 exhibits the highest crystallite size while KH_2PO_4 showed the smallest, while Rb, Cs and NH_4-based dihydrogen phosphates exhibited sizes in between. The specifications and crystallographic data of these compounds is summarised in table 4.1. It has been reported by several authors how the crystal structure of these materials changes at higher temperatures, when they undergo a structural solid phase transition to proton conducting materials [19-22].

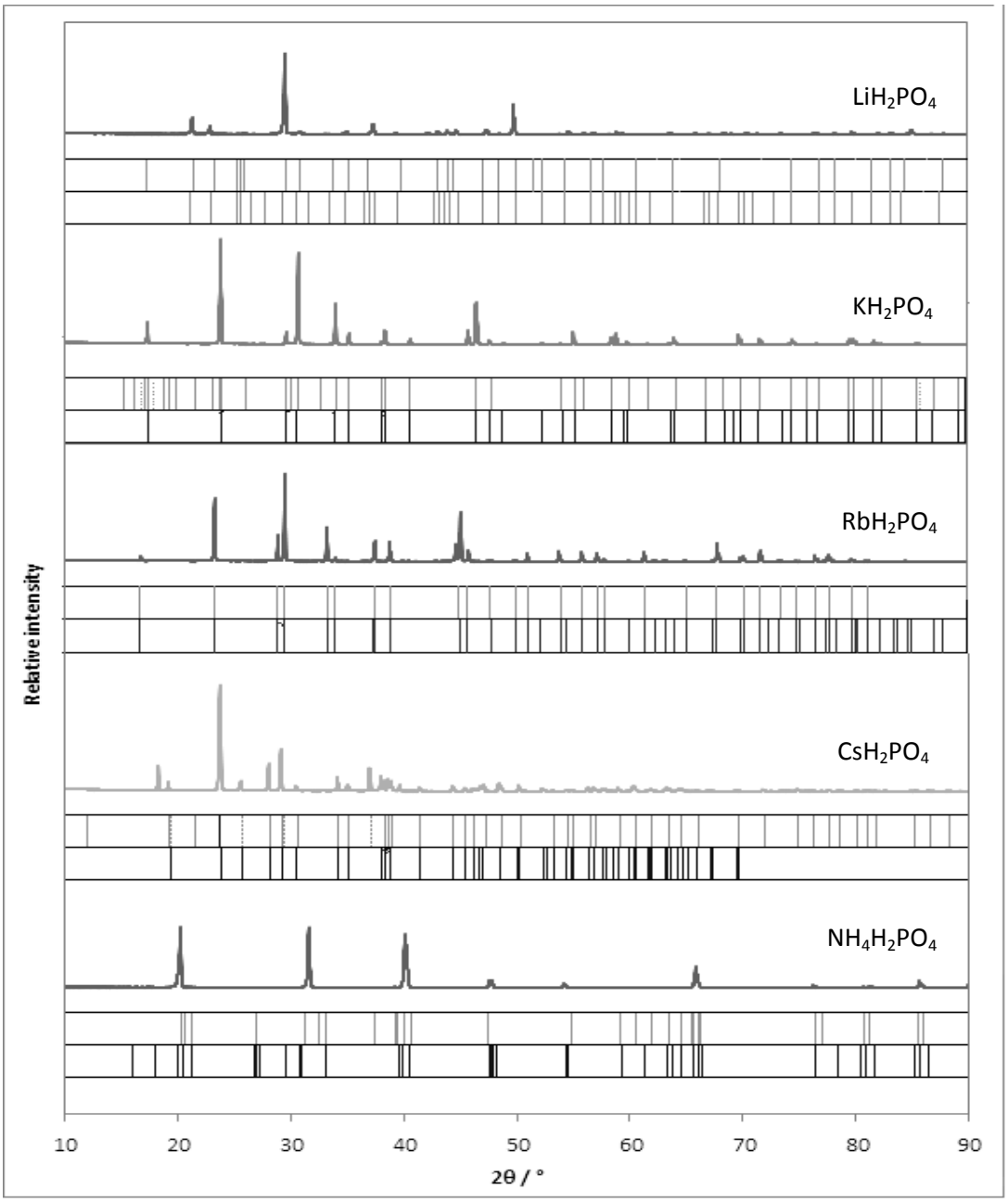

Figure 4.1. P-XRD spectra of polycrystalline powder of phosphate-based solid acids at room temperature and atmospherical pressure.

Table 4.1. Crystallographic data of solid acids at ~ 18 °C.

Material	**Card-number / ICDD**	**Crystal system**	**Crystallite size / nm**
LiH_2PO_4	00-021-498	Orthorhombic	89.5
KH_2PO_4	00-035-0807	Tetragonal	60.7
RbH_2PO_4	00-034-0074	Tetragonal	64.9
CsH_2PO_4	01-035-0746	Monoclinic	68.3
$NH_4H_2PO_4$	00-006-0125	Tetragonal	80.3

The particle size is an important parameter to take into account in inorganic proton conductors. In order to use this type of materials as an electrolytic media for proton conduction they are commonly subjected to high pressures in order to fabricate a dense pellet. The particle size and distribution affects the density and homogeneity of this pellet by the effect of the grain boundary. Besides as it will be explained further, particle size has an effect in material dehydration rate by effect of the surface area. It is also an important variable to study in both electrode and composite membrane fabrication, where smallest particles are commonly preferred. The preference to smaller particles arises from three main reasons; (1) small particle size would increase the surface area to volume ratio allowing a better triple phase boundary in the electrode when the powder is used as ionomer (2) smaller particles are commonly easier fused together by pressure and more dense pellets without grain boundary can be fabricated and (3) smaller particles produce a better colloidal dispersion of the powder into a polymer solution allowing a more homogeneous casting of a polymeric/inorganic composite membrane (*see Chapter 5*).

In order to study the morphology and particle size, further characterisation of the solid acids was carried out by E-SEM. The precipitation of the solid polycrystalline powders was carried out in various solvents; acetone, 1, 2 – propanol, ethanol and methanol in order to study its effect on the particle size. Powders precipitated into methanol (acetone in the case of $NH_4H_2PO_4$) exhibited in general the smallest particle size and thus, only those results are discussed in this chapter.

The E-SEM micrographs show the morphology and particle size of the polycrystalline powders. The particle size distribution of the solid acid powders was calculated by the analysis of three different regions of the micrographs with a sample size of 300 points and is shown in figure 4.3.

LiH_2PO_4 showed the smallest particle sized powder with an average of 400 nm. KH_2PO_4 exhibited the highest particle size of 30 µm average of clearly defined and very well dispersed monolithic morphology particles. Rb and Cs-based dihydrogen phosphates powders showed a similar smooth-edge particle shape with an average of 2 and 4 µm respectively, although CsH_2PO_4 had a much higher particle size distribution. $NH_4H_2PO_4$ exhibited 5 µm average particle size although bigger particles as high as 50 µm were also spotted.

A particle is considered a sum of crystallites arranged together. Considering spherical units, an estimation of the agglomerated number of crystallites to form a particle was carried out. This calculation was done considering the mean size of the particle size distribution of each compound (table 4.2).

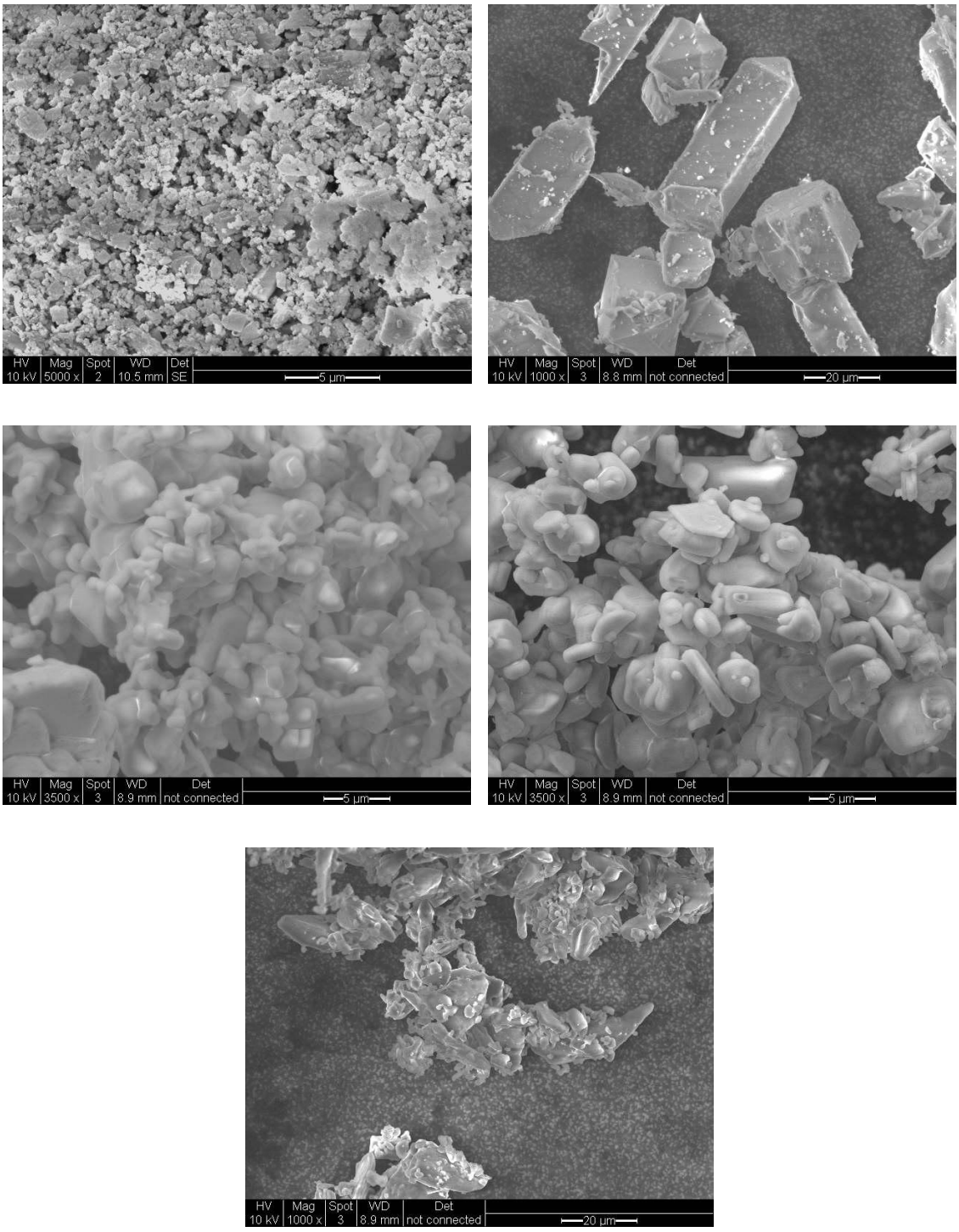

Figure 4.2. E-SEM images of (a) LiH_2PO_4 (b) KH_2PO_4 (c) RbH_2PO_4 (d) CsH_2PO_4 and (e) $NH_4H_2PO_4$ powders precipitated into methanol (and acetone).

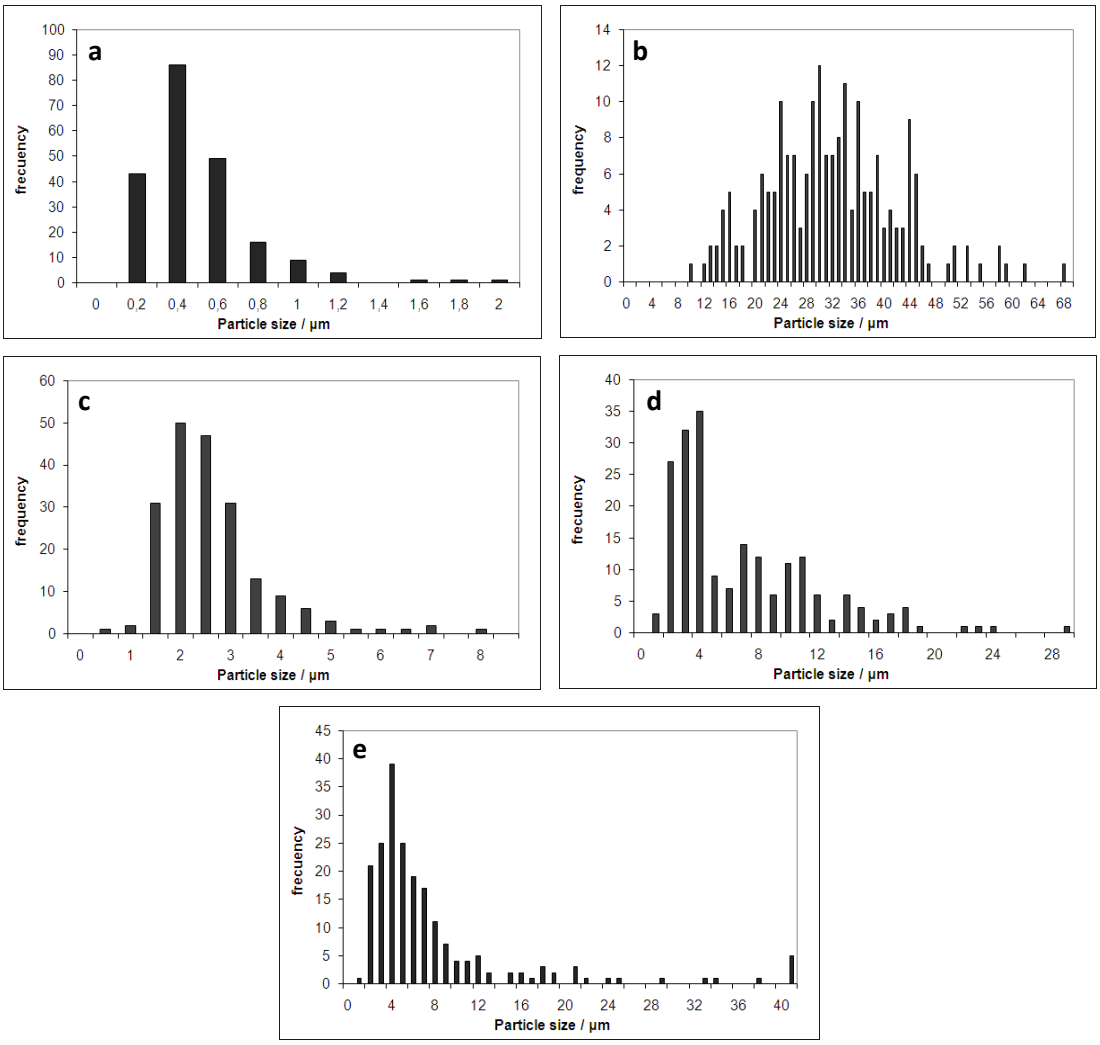

Figure 4.3. Particle size distribution of polycrystalline (a) LiH_2PO_4 (b) KH_2PO_4 (c) RbH_2PO_4 (d) CsH_2PO_4 and (e) $NH_4H_2PO_4$

Table 4.2. Particle and crystallite size of phosphate-based solid acids.

Material	Crystallite size / nm	Mean particle size / µm	N° of crystallites per particle
LiH_2PO_4	89.5	0.40	4.44
KH_2PO_4	60.7	30	494
RbH_2PO_4	64.9	2	30.8
CsH_2PO_4	68.3	4	50.6
$NH_4H_2PO_4$	80.3	5	62.3

The particle size distribution of these compounds obtained by precipitation into methanol has not been previously studied by other research groups and therefore no consistent data to compare is available in literature. Few SEM micrographs of CsH_2PO_4 [23] and RbH_2PO_4 [24] polycrystalline powders precipitated by this method were found in the literature and analysed in order to compare to the results obtained in this research. Cs and Rb salts show mean particle sizes of ca. 5 and 4 μm respectively and smooth edged morphology, which are slightly higher but in close agreement to the results obtained. *Ahn. et al.* reported a polyol precipitation method which affects the morphology of CsH_2PO_4 powder, being able to obtain plate and rod like particles over the micron-size [25]. Authors suggested that preferred orientations of the crystals are responsible of the different morphologies obtained. A few reports on the fabrication of CsH_2PO_4 nanoparticles are reported using different surfactants where particles in the nanometric size were obtained [26-28]. The problems exhibited by this method are the difficulty of eliminating the surfactants after the fabrication and the low physical stability of the nanoparticles caused by their high hygroscopicity; they adsorb atmospheric humidity and they dissolve together into bigger particles. This nanoparticle fabrication method was tried in this research but no successful results were obtained.

4.3.2 Proton conductivity

The most characteristic property of this family of solid acids is their transition to proton conductors at the medium temperature range. Proton conductivity at a certain temperature is enhanced by two to three orders of magnitude placing them as potential materials as intermediate temperature electrolytes. This transition is noticed in many of the studied (di)hydrogen sulphates, selenates, arsenates or phosphates [16, 17]. It is explained by two theories; (1) solid-state phase transition [29, 30] or (2) material dehydration [31, 32].

The first one of these theories, proposed by *Baranov et al.*, states that these materials undergo a polymorphic transition in their crystal structure which is responsible for the high proton conductivity [29]. They proposed that the mechanism for proton conductivity after this polymorphic transition is carried by proton hopping or 'Grotthuss mechanism', where occupation of the interstitial proton site is possible and the proton migration from one oxygen atom of the phosphate group to another is accompanied by the formation of a new hydrogen bond. KH_2PO_4 was reported to undergo a structural change from tetragonal to monoclinic symmetry at 187 °C [29] accompanied by an increase in proton conductivity of

approximately two orders of magnitude. Same tetragonal to monoclinic transitions was reported for RbH_2PO_4 at 86 °C although this material undergoes another phase transition to a yet unclear structure of superprotonic phase at 285 °C [24]. CsH_2PO_4 undergoes a monoclinic to cubic structural transition at 231 °C accompanied by an increase of three orders of magnitude in proton conductivity [33].

The second theory states that the high proton conductivity exhibited by these materials at the medium temperature range in caused by a dehydration/polymerisation reaction [20]. The water produced by this reaction would be responsible for proton conductivity in the lattice of the crystals by vehicle mechanism. In this case water would act as a proton solvent producing hydronium ions, H_3O^+, allowing proton conduction in the grain boundary of the material.

EIS is the most commonly used technique to measure transport properties such as protonic conductivity [34]. In figure 4.4 the transition to proton conducting materials of the synthesised solid acids measured by this technique is shown. All samples were characterised in humidified conditions (RH = 3.0 %) to avoid any dehydration of the materials above their transition temperature [21, 24, 35, 36].

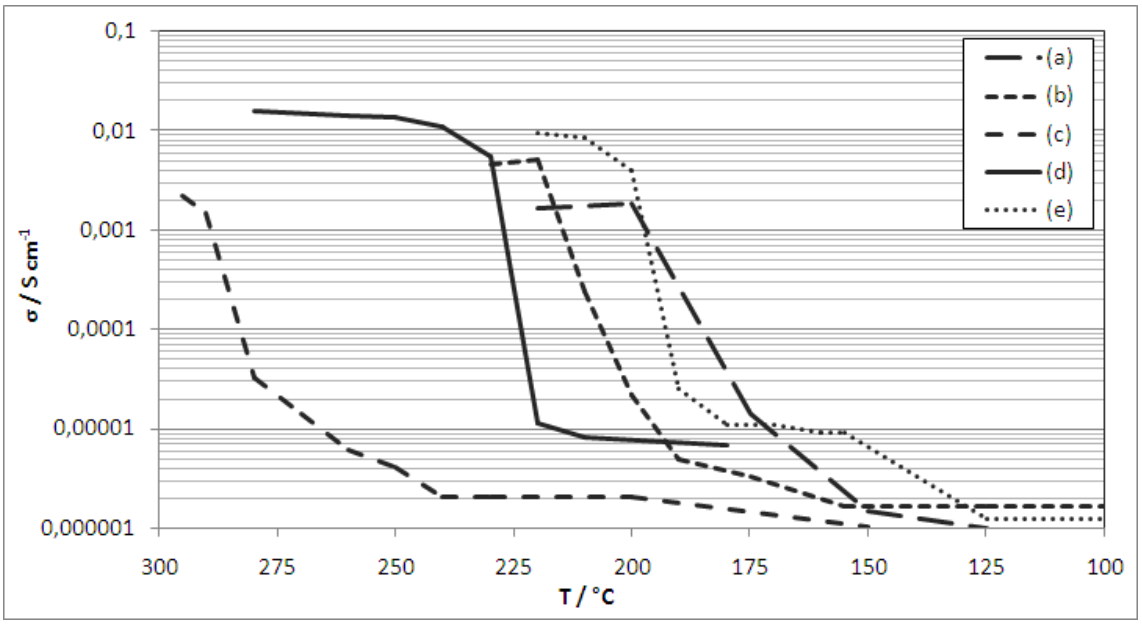

Figure 4.4. Temperature dependence of the protonic conductivity of (a) LiH_2PO_4 (b) KH_2PO_4 (c) RbH_2PO_4 (d) CsH_2PO_4 and (e) $NH_4H_2PO_4$

All materials show a sharp increase in their conductivity at a certain temperature. LiH_2PO_4 reached a maximum proton conductivity of 2×10^{-3} S cm^{-1} at 200 °C in contrast to the high

conductivity value of 10 S cm^{-1} reported by *Lee et al.* [21]. Same conductivity value was achieved for RbH_2PO_4 at a much higher temperature of 285 °C which is in good agreement with the 10^{-2} S cm^{-1} value reported by *Li et al.* [37]. KH_2PO_4 and $NH_4H_2PO_4$ showed a maximum conductivity of 5×10^{-3} and 9×10^{-3} S cm^{-1} at 210 and 200 °C, respectively. Measured conductivity values for these two compounds are one and two orders of magnitude higher respectively than those results reported by other authors [29, 38, 39]. The conductivity of $NH_4H_2PO_4$ dropped considerably with time, which is attributed to the decomposition of this compound to ammonia and phosphoric acid, as explained later in this chapter. CsH_2PO_4 shows the highest conductivity among the other solid acids, reaching values over 10^{-2} S cm^{-1} at temperatures higher than 230 °C. This temperature transition and conductivity results are in good agreement with other reported values which are in the range of 8×10^{-3} to 2.2×10^{-2} S cm^{-1} [17, 18, 40]. CsH_2PO_4 also remains stable in the broadest temperature range, 230 – 280 °C, before it melts. This makes the cesium-based solid acid the most interesting material for application as electrolyte and its proton conducting behaviour is therefore further studied in this research. The maximum proton conductivity and transition temperature values of all the studied phosphate based solid acids are tabulated in table 4.3.

Table 4.3. Proton conductivity and transition temperature of phosphate based solid acids.

Material	**Proton conductivity** σ **/ S** cm^{-1}	**Transition temperature** T_t **/ °C**
LiH_2PO_4	2.0×10^{-3}	200
KH_2PO_4	5.0×10^{-3}	210
RbH_2PO_4	2.0×10^{-3}	285
CsH_2PO_4	1.5×10^{-2}	230
$NH_4H_2PO_4$	9.0×10^{-3}	200

Impedance analysis by Nyquist plot, figure 4.5, shows the difference on the spectrum of CsH_2PO_4 at temperatures lower and higher than 230 °C. At 200°C the spectra exhibits a single arc that extends to the origin at high frequencies and intercepts the real axis at lower frequencies. This intercept point corresponds to the dc conductivity of the electrolyte. A resistance value of approximately 3500 Ω cm^2 is exhibited by the non-conducting pellet,

which considering the 300 µm thickness of it lead us to conductivity value of approximately 8×10^{-6} S cm^{-1}. The value of the intercept and consequently the size of the semicircle decreases when the temperature is increased from 100 to 230 °C meaning that the protonic conductivity increases slightly in that temperature range as seen in figure 4.4. At temperatures higher than 230 °C however, the impedance spectra changes drastically to a straight line where no arc is shown. The resistance measured from the system is between 2 and 3 Ω cm^2 at 250 °C, which leads to values over 10^{-2} S cm^{-1}. This value is obtained from the high frequency intercept with the real axis corresponding to the dc conductivity of the electrolyte.

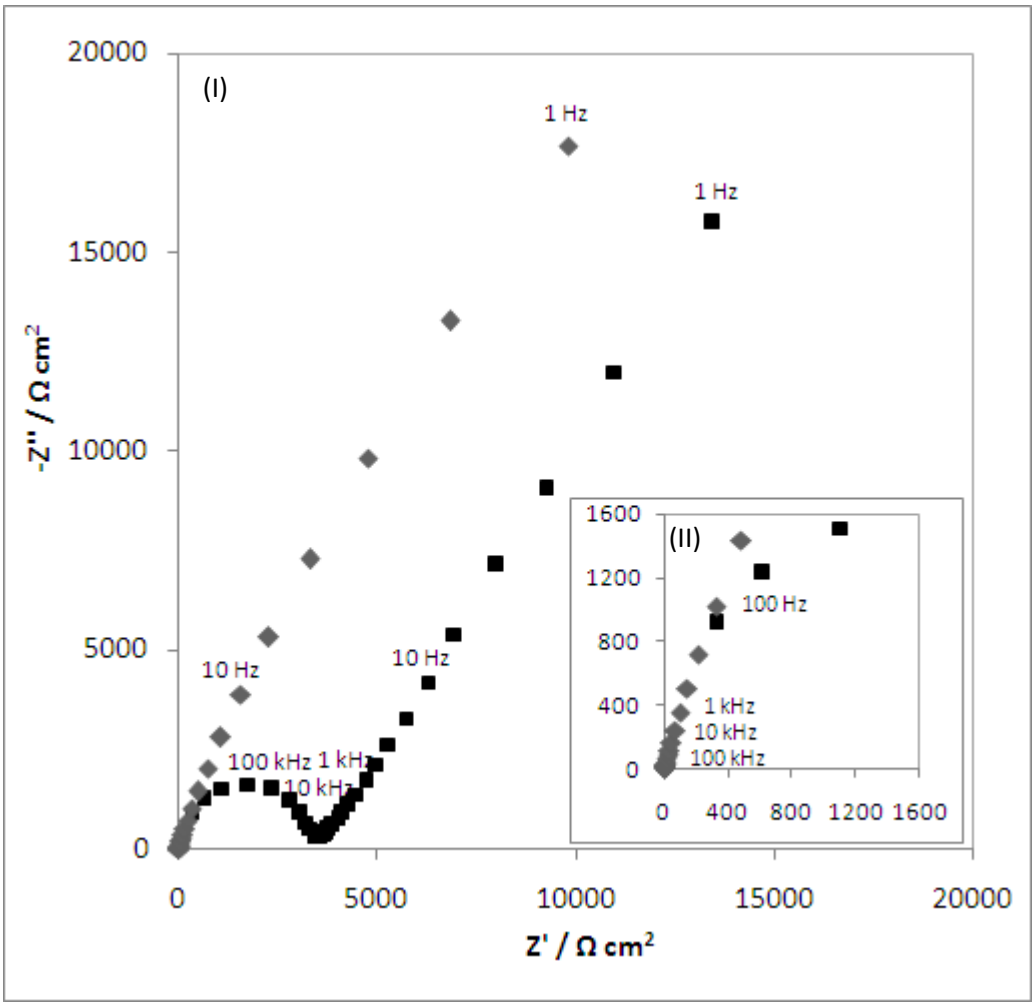

Figure 4.5. (I) Nyquist plot of the EIS spectra of CsH_2PO_4 at (■) 200 °C and (♦) 250 °C. (II) Inset of the high frecuency region.

Conductivity values at the low temperature range, below 230 °C, differs between samples and it is attributed to residual surface water present in the grain boundary regions of the polycrystalline material [18]. This residual water in the grain boundary would partially

dissolve the solid acid and generate protonated water molecules, H_3O^+, that would be responsible of proton transport by vehicle mechanism. The slight increase in proton conductivity with temperature at temperatures below 230 °C is attributed to a faster diffusion of the hydronium ions. At temperatures higher than 230 °C, according to many authors, the proton conduction mechanism changes drastically to the so-called 'Grotthuss mechanism' where protons are able to 'hop' from a phosphate group to another allowing much higher proton conduction within the material. At temperatures higher than 280 °C the melting of the pellet causes short-circuits in the system. Although the melting point of CsH_2PO_4 is reported to be much higher, ca. 345 °C [41], the humidity has a strong influence on it, and the operating temperature range at the relative humidity needed to avoid dehydration of the material *(see section 4.3.1)*, is reduced to 230 – 280 °C.

This material also exhibits a clear hysteresis in proton conductivity between heating and cooling cycles (figure 4.6). Some defend this hysteresis is caused by the difference in the activation energy required for the solid state transition in both cooling and heating cycles and it is therefore considered as an indicator of the phase-transition theory to a proton conducting state [18]. Others defend that the dehydration reaction happening over their transition temperature remains happening at some extent in the cooling cycle causing this hysteresis [32].

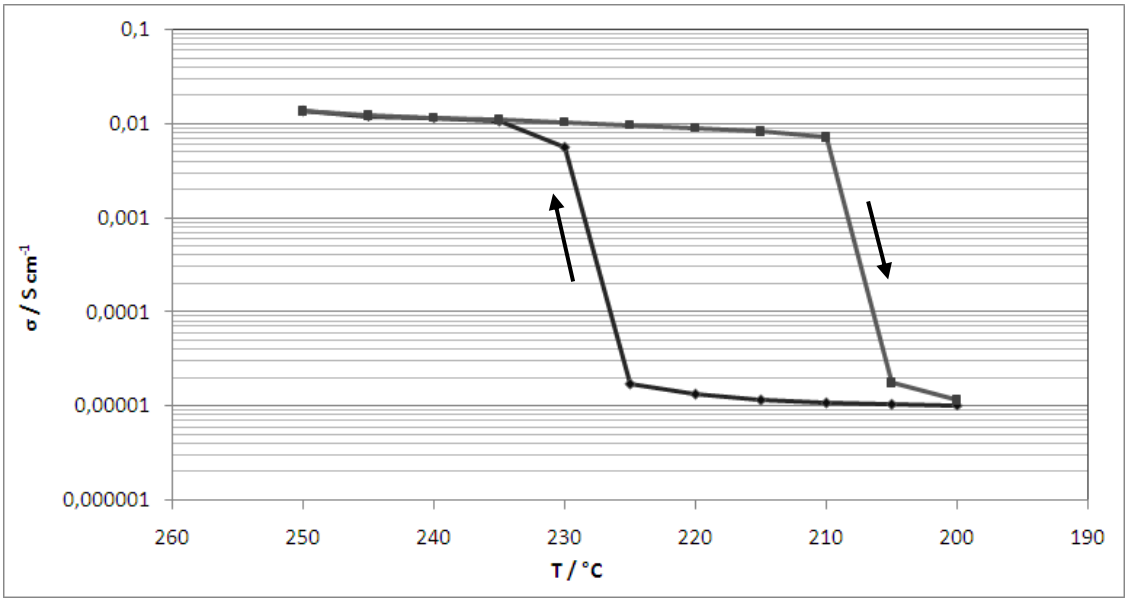

Figure 4.6. Temperature dependence of the protonic conductivity of CsH_2PO_4. The hysteresis between the heating and cooling cycle is shown.

The hysteresis region of CsH_2PO_4 was found to be unstable with time. Proton conductivity measurements were performed at different times maintaining the temperature of the system at temperatures between 230 - 215 °C in the cooling cycles. The proton conductivity in this hysteresis region tends to decrease to its original value with rates of approximately one order of magnitude every two hours (measured at 220 °C). This can be explained by either a low stability of the proton conducting crystal structure at this temperature range or by a continuous decrease of the dehydration reaction rate. The author in this study is inclined to believe the first of both options, as dehydration should stop at temperatures below ca. 230 °C [35] showing a much faster decrease in the reaction rate. Either way the temperature range for stable operating conditions is limited to temperatures higher than 230 °C.

4.4 Physical and chemical stability

The high proton conductivity exhibited by this family of solid acids makes them potentially useful electrolytes in PEM electrochemical devices [42]. However, the physico-chemical stability of these materials in the intermediate temperature range where they exhibit this property must be addressed. Two main issues could affect the integrity of the materials at these conditions; water solubility and dehydration. The big amounts of water fed into a PEM water electrolyser, even as steam at T > 100 °C, could partially (or totally) dissolve the electrolyte and produce gas crossover or electric shortcuts through it. This would cause a gradual decrease on the performance until a failure of the system.

CsH_2PO_4 has been proved to be the most conductive material of this family over the widest temperature range (230 – 280 °C) which placed it as the most interesting material to focus this study. Thermal stability of the phosphate-based soli acids in powder form was studied by TGA and DSC in order to address the rate of dehydration of the materials in the absence of humidification.

The stability of CsH_2PO_4 in pellet form under different humidification conditions was also carried out in order to study the conditions to prevent dehydration as well as the reversibility of it. Electrochemical impedance spectroscopy was used to measure the resistance of a CsH_2PO_4 pellet over 24 h tests. The resistance measured would be directly related to the degree of dehydration of the material as well as to the dissolution of the pellet. Samples were also characterised by E-SEM in order to address the physical integrity of the pellet before and after the experiments.

4.4.1 Thermal stability

The thermal stability of these compounds is a key point to be studied. Their application at medium temperatures (150 - 300 °C) makes it necessary to study any material degradation around this range. As reported by various authors [24, 35, 43-45] these compounds undergo a dehydration reaction when they reach their transition temperature to proton conductors. This dehydration arises from the condensation reaction of dihydrogen phosphate groups to form pyro- and poly-phosphates until their total dehydration to meta-phosphates [35, 41], although as reported by *Osterheld et al*. [46], many kinds of different condensed species of phosphates may be generated. In order to analyse this degradation process, thermo-gravimetric analysis coupled with differential scanning calorimetry (TGA-DSC) was carried out (figure 4.7).

The mass loss obtained for Li, K, Rb and Cs dihydrogen phosphates follow the same tendency. They start dehydrating at temperatures close to their transition temperature to proton conductors and they show two main different slopes in the dehydration rate. These data is in good agreement with results provided by other authors [21, 24, 41, 44] where the two slopes regarded in the mass loss profile of these solid acids are attributed to different steps in the dehydration mechanism. The first one would correspond to the condensation of phosphates to the formation of half-dehydrated compound or pyro-phosphate ($MH_2P_2O_7$) and the second to the formation of the totally dehydrated meta-phosphate (MPO_3) (equations 4.3 – 4.4) [35, 41].

$$MH_2PO_4 \rightarrow M_2H_2P_2O_7\,(s) + H_2O\,(g) \qquad (4.3)$$

$$M_2H_2P_2O_7 \rightarrow MPO_3\,(s) + H_2O\,(g) \qquad (4.4)$$

The mass loss start is accompanied by a well-defined endothermic peak which some attribute to the solid state phase transition enthalpy [29, 35] and others to the enthalpy of the dehydration reaction [31, 32]. The total loss is in very good agreement with the total theoretical loss calculated, considering all the mass loss produced by dehydration, this is, to the intrinsic water in the dihydrogen phosphate structure. The onset dehydration temperature and total mass loss of each compound in the 50 to 600 °C temperature range, compared to the theoretical mass loss expected is shown in table 4.4.

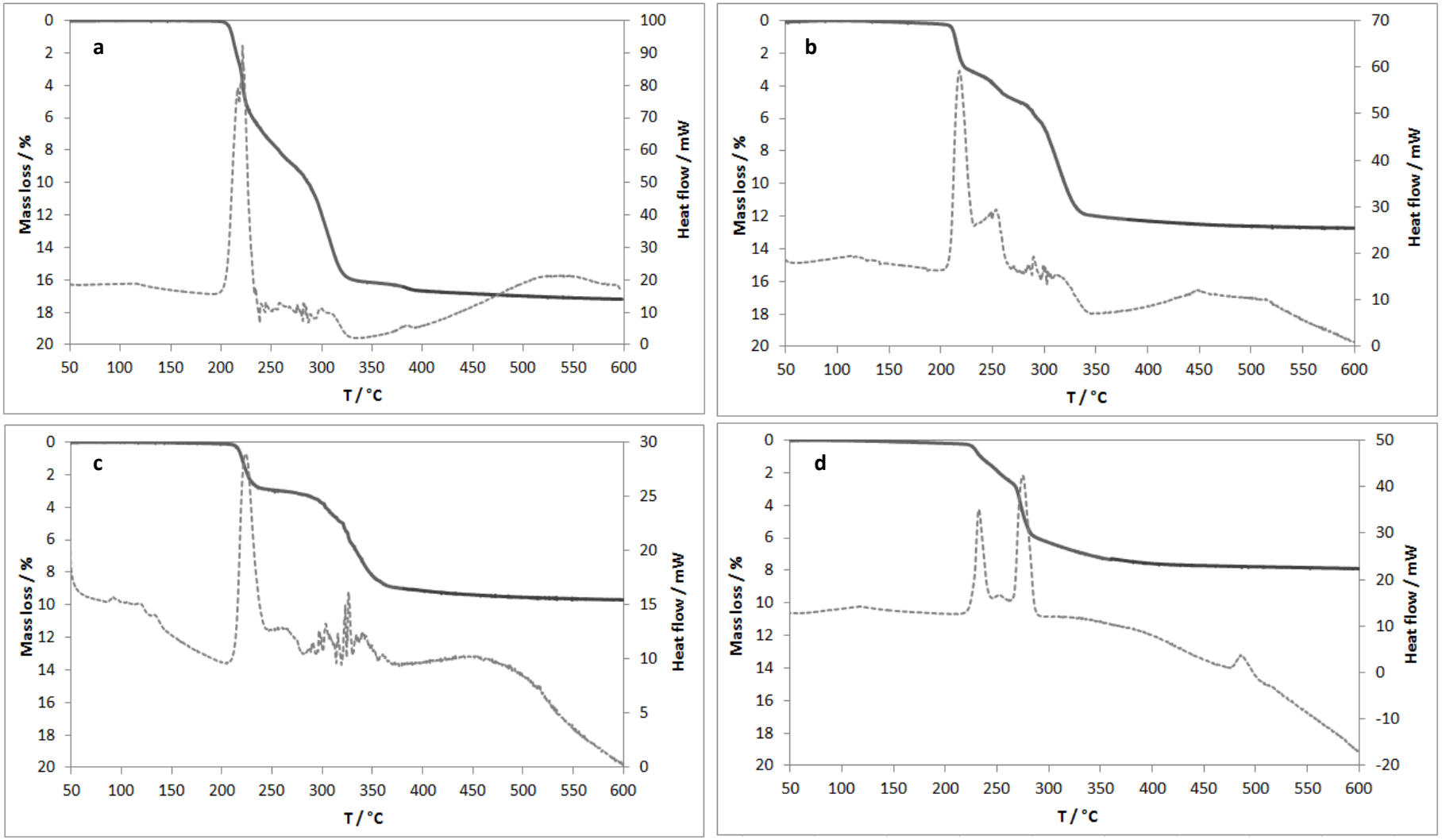

Figure 4.7. TGA and DSC analysis of (a) LiH_2PO_4 (b) KH_2PO_4 (c) RbH_2PO_4 (d) CsH_2PO_4 at 5 °C min^{-1}.

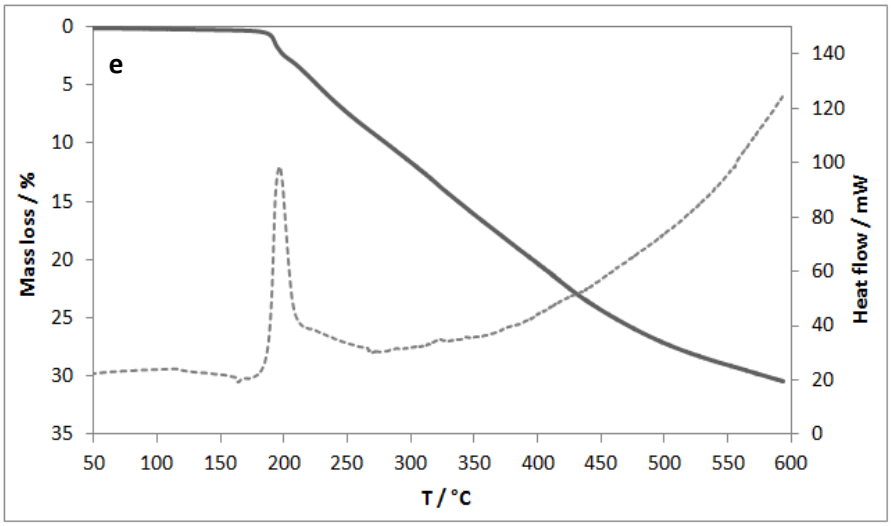

Figure 4.8. TGA and DSC analysis of (e) $NH_4H_2PO_4$ at 5 °C min^{-1}

Table 4.4. Dehydration mass loss of phosphate-based solid acids.

Material	Theoretical mass loss / %	Real mass loss / %	Dehydration onset temp. / °C
LiH_2PO_4	17.3	17.2	205
KH_2PO_4	13.2	12.5	208
RbH_2PO_4	9.9	9.5	210
CsH_2PO_4	7.8	7.6	228
$NH_4H_2PO_4$	15.6	33.5	182

In the case of $NH_4H_2PO_4$, a different profile of mass loss following a continuous slope is regarded in contrast with the rest of phosphate-based solid acids. Many authors attribute this mass loss to a degradation of the compound by the decomposition to ammonia and phosphoric acid (equation 4.5) [39, 47].

$$NH_4H_2PO_4 \rightarrow NH_3\,(g) + H_3PO_4\,(l) \qquad (4.5)$$

The results obtained in this study show a clear endothermic peak at the same temperature the mass loss starts. This is attributed to the enthalpy of reaction 4.5. and the continuous linear mass loss in the TGA plot to a combined mass loss of the produced NH_3 and the dehydration of the produced H_3PO_4 [48]. The theoretical total mass loss of the material

considering these two effects is of approximately 35 % which is in better agreement with the results obtained. Some authors defend that the continuous mass loss is attributed to a simultaneous decomposition and condensation of ammonium phosphates and that direct dehydration of $NH_4H_2PO_4$ can only happen in presence of a NH_3 atmosphere [45].

It was proposed that the dehydration process of phosphate solid acids is also related to the particle size of the polycrystalline powder. *Li et al.* [24] reported that RbH_2PO_4 particles tend to dehydrate in the outer shell part of the particles reaching eventually the core of the particles, as shown in the diagram in figure 4.9. This, in combination with the two-step the dehydration process proposed earlier, would explain the different rates shown in the mass loss curves. We consider that this model can be applied to all the solid acids studied here, with exception of $NH_4H_2PO_4$.

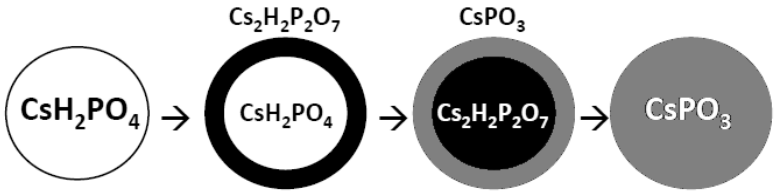

Figure 4.9. Schematic model of the dehydration process proposed by *Li et al.* [24] applied to CsH_2PO_4.

To verify the particle size effect on dehydration of these materials, TGA results obtained for polycrystalline powder and single crystals of CsH_2PO_4 were compared and the effect of dehydration rate addressed.

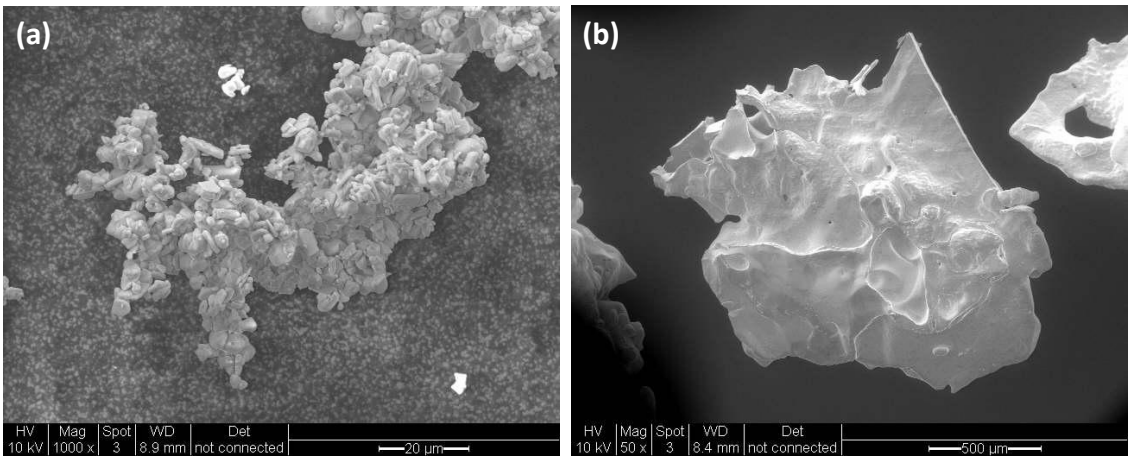

Figure 4.10. E-SEM micrographs of (a) polycrystalline CsH_2PO_4 and (b) single crystals of CsH_2PO_4.

The difference in particle size between both structures of the same material is of ×100 to ×1000 (figure 4.10). Thermal analysis plotted in figure 4.11 shows that polycrystalline powder (a) dehydrates at a considerably faster rate that single crystals. In figure 4.12. however, DSC spectra show that the endothermic peak corresponding to both dehydration steps occur at the same temperature.

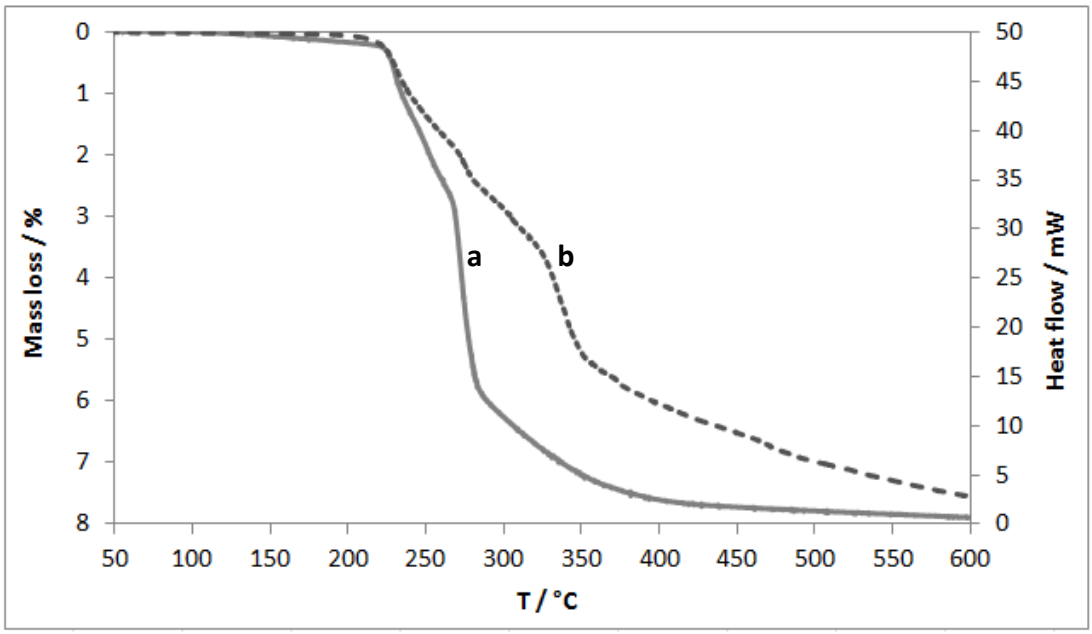

Figure 4.11. TGA of (a) polycrystalline CsH_2PO_4 and (b) single crystals CsH_2PO_4 at 5 °C min^{-1}.

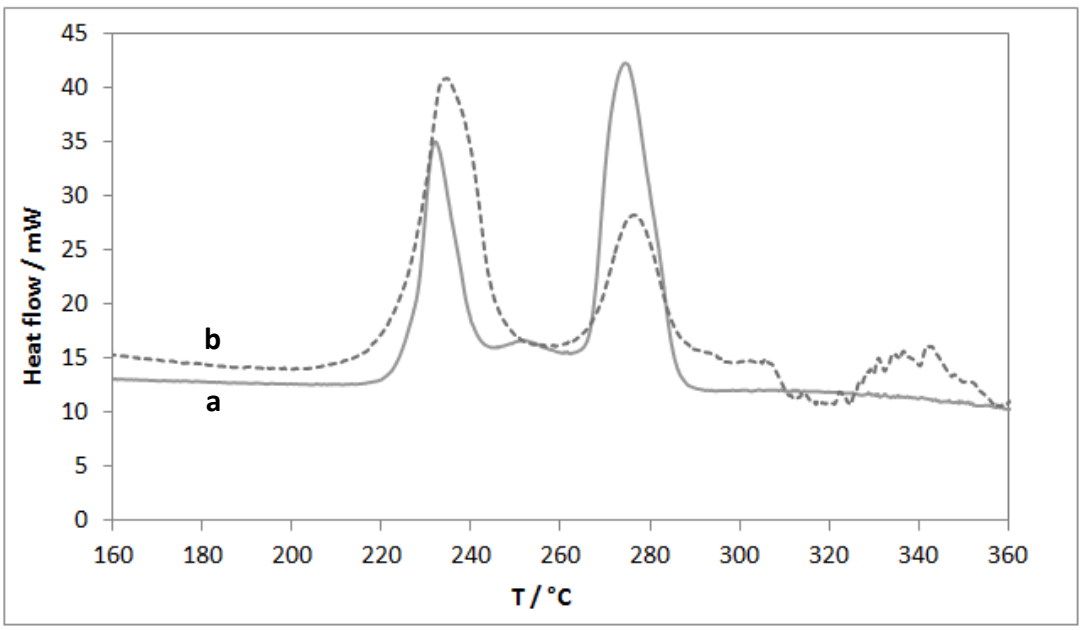

Figure 4.12. DSC of (a) Polycrystalline CsH_2PO_4 and (b) single crystals CsH_2PO_4 at 5 °C min^{-1}.

The two-step dehydration/condensation process proposed before is therefore consistent with the data obtained and the mass loss of the material is attributed only to water loss. This dehydration, as will be explained in further analysis, can be avoided by supplying humidification to the system [35].

The stability of CsH_2PO_4 under real operating conditions of a PEM water electrolyser was addressed. Avoiding the dehydration of the solid acid is a key issue for a successful application of this material as electrolyte in these devices. Proton conductivity loss to values under 10^{-2} S cm^{-1} would generate high ohmic resistance in the system considering the high thickness required, >300 µm, for a mechanically stable pellet.

4.4.2 The effect of humidification on the stability of CsH_2PO_4

Condensation of phosphates is a well-known phenomenon where the constituent water of the acidic groups is lost when temperature is increased. This process is found in a wide range of phosphate-based materials varying the condensation/dehydration onset temperature from one material to another. As already proven in this chapter, phosphate condensation in CsH_2PO_4 starts at a temperature of ca. 230 °C, curiously similar to its proton transition temperature. At this conditions, and in absence of humidity, the hydrogen-bonded dihydrogen phosphate chains of this material lose its constituent water condensating the phosphate groups into pyro- and polyphosphates ($CsH_xP_yO_z$) until its total dehydration to cesium metaphosphate ($CsPO_3$) (reactions 4.3 and 4.4) [35, 41, 46].

The loss of constituent water from the dihydrogen phosphate chain, and the consequent loss of proton bonds, causes a decrease in the proton conductivity of the material. A simple model for phosphate condensation is shown in figure 4.13. The 'proton hopping' or 'Grotthuss' conduction mechanism explained before *(see Chapter 2)* [4], can no longer work when dehydration takes place. In order to avoid this reaction, humidification in the system must be carefully controlled at all times.

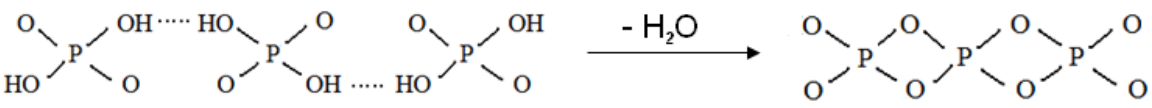

Figure 4.13. Simple model of phosphate condensation.

In order to study the suitability of CsH_2PO_4 as proton conducting electrolyte in PEM water electrolysis systems, the stability of this material at different humidification rates was addressed. The minimum humidification required to avoid dehydration above 230 °C as well as the physical stability in terms of material dissolution at high humidification rates were studied.

The value of water partial pressure (P_{H2O}) provided to the system was controlled by passing the feeding gas (Ar) through a temperature-controlled water saturator. The relative humidity in the system was calculated by equation 4.6.

$$\% RH = \frac{P_{H_2O}}{P^*_{H_2O}} \times 100 \qquad (4.6)$$

where P_{H2O} (atm) describes the water partial pressure in the feeding gas and P^*_{H2O} (atm) the saturation water partial pressure at a given temperature. At temperatures higher than 100 °C the relative humidity drops exponentially if the system is not overpressured. In figure 4.14 the relative humidity dependence on the temperature of the system is plotted and the operating region of the system (T > 230 °C) highlighted. The maximum relative humidity possible to achieve at 235 °C (and atmospheric pressure) is 3.5 %, which is obtained by heating the water saturator to its maximum temperature, 99 °C.

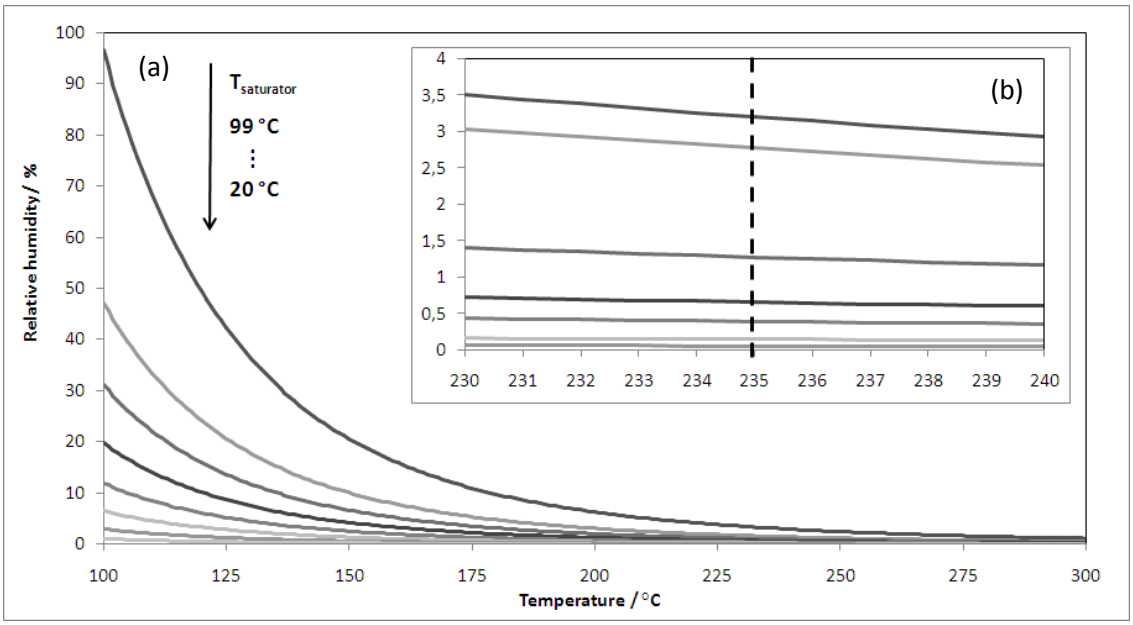

Figure 4.14. % RH vs. temperature diagram at atmospheric pressure and (a) 100 – 300 ºC, (b) 230 – 240 ºC.

The system was operated at 235 °C (over its phase transition temperature to proton conductive state) and the humidification conditions applied are those summarised in table 4.5. The water vapour pressure at 235 ºC is 32.1 atm. The resistance of the CsH_2PO_4 pellets was measured by EIS and monitored for 24 h in order to study the loss in proton conductivity of the material. The cell where these experiments were carried out is shown in figure 3.10. The results obtained are plotted in figure 4.15.

Table 4.5. Humidification conditions of the system.

$T_{saturator}$ / °C	P_{H2O} / atm	$RH_{(Tcell = 235\ °C)}$ / %
99	0.97	3.21
70	0.31	1.04
60	0.20	0.66
50	0.12	0.40
40	0.06	0.21
20	0.02	0.06

The minimum humidification rate required in the system to avoid dehydration of CsH_2PO_4 is 0.12 atm of water partial pressure (0.40 % RH in the cell), which is in good agreement with the results obtained by *Otomo et al.* [49] and *Haile et al.*[35]. At higher humidification rates the conductivity of the material remains stable but at lower rates however, material dehydration, driven by self-condensation of phosphate groups [46], causes a gradual decrease in the proton conductivity of the material. At humidification rates of 0.06 and 0.02 atm P_{H2O} the conductivity loss starts at 0 and 2 h and the rate is of approximately one order of magnitude every 24 h and 12 h, respectively. At the highest humidification rate provided to the system, 0.97 atm (3.21 % RH in the cell), proton conductivity of CsH_2PO_4 remains stable.

Otomo et al. reported comparable results in terms of stability of CsH_2PO_4 under similar humidification rates [50] although the stable behaviour of the pellet at the minimum humidification to avoid dehydration, determined as P_{H2O} = 0.12 atm in this study, was not reported. In addition, they reported a much more drastic conductivity drop for low humidity rates, decreasing by 2 or 3 orders of magnitude in the first minutes. This difference is explained by the experimental conditions; in this study samples were

stabilised at 0.30 atm P_{H2O} prior to experiment and thus residual water adsorbed in the grain boundary of the material would have an effect in the proton conductivity making the drop gradual. This is assuming that in the results reported by *Otomo et al.* no initial humidification was provided. This positive effect of adsorbed water can also be noticed by the slightly higher conductivity shown at the highest humidity ratio, which can also be seen in their results, and is even more noticeable at low proton conducting conditions, below 230 °C [18].

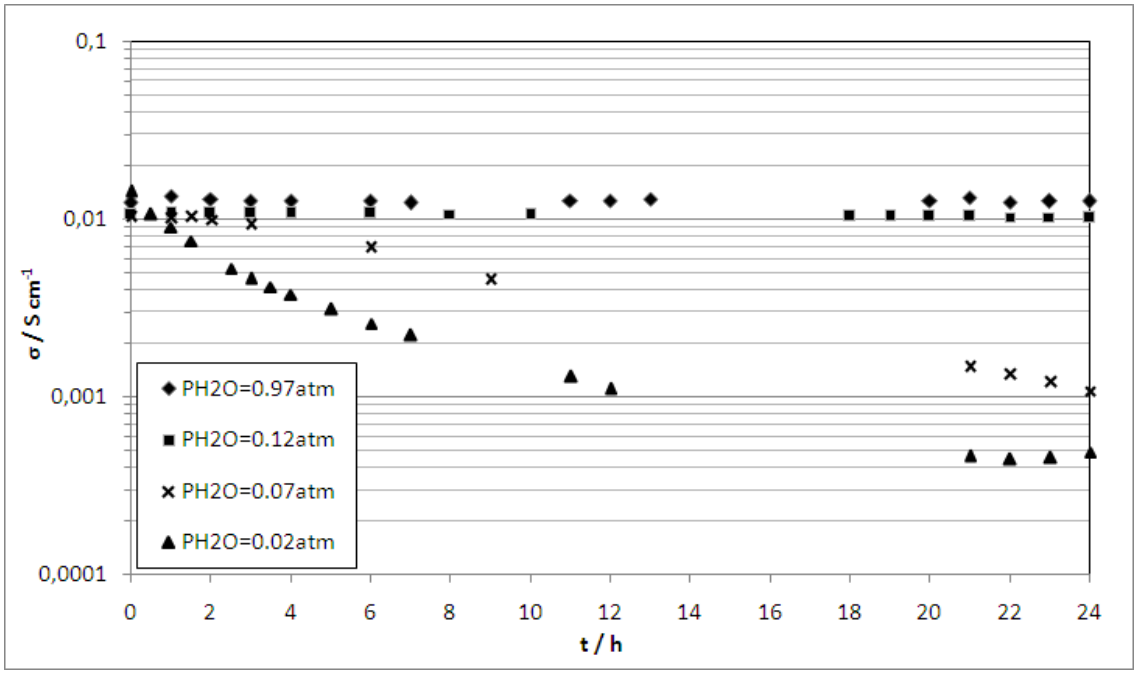

Figure 4.15. Time dependence of the protonic conductivity of CsH_2PO_4 at atm. pressure and 235 °C.

In terms of material dissolution, the resistance provided by the electrolyte is expected to decrease due to a thinning of the pellet, and CsH_2PO_4 is therefore considered stable at high humidification rates and suitable for electrolysis application. This conclusion is complemented by E-SEM characterisation of samples before and after the tests. As shown in figure 4.16 in the cross-section micrographs of pellets, the samples subjected to low humidification rates (figures c and d) show considerable porosity. This is attributed to water release in gas form caused by dehydration of the material. The water vapour bubbles generated in this process produce holes in the bulk of the pellet providing it with substantial porosity. In figure 4.16 (b) the micrograph of high humidification rate sample is shown where the unchanged integrity of the pellet is patent.

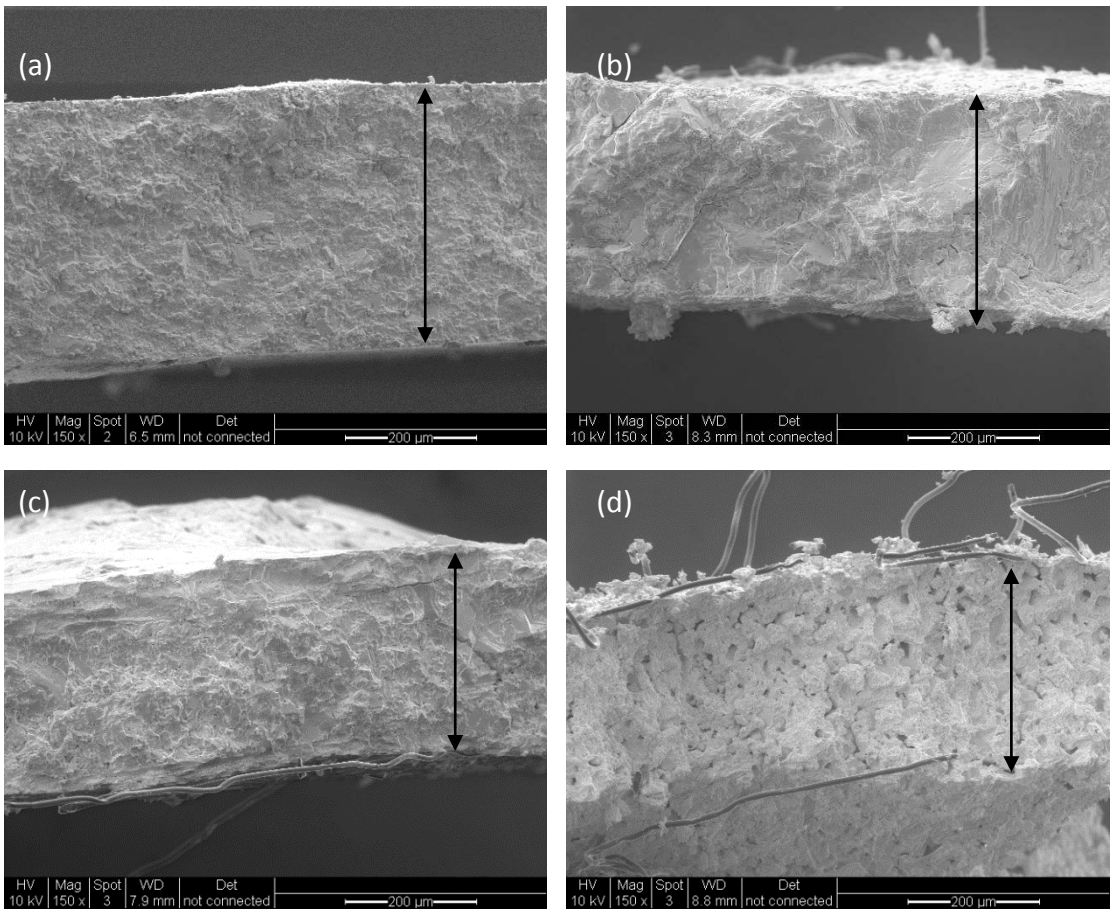

Figure 4.16. SEM micrographs of (a) new pellet and after stability test at (b) P_{H2O}= 0.97 atm, (c) P_{H2O}= 0.07 atm and (d) P_{H2O}= 0.02 atm.

The effect of the humidification rate in the reversibility of the dehydration reaction of CsH_2PO_4 was also studied. For this purpose, various experiments were carried out where the material was deliberately subjected to dehydration either by dry gas or low humidification gas. Then the system was provided with humidified gas in order to study the rate of rehydration (hydrolysis of condensed phosphates) at different humidification conditions. The proton conductivity of the samples was again measured in order to monitor the dehydration/rehydration reactions in the material. *Otomo et al*. were the only group reporting the reversibility of CsH_2PO_4 in terms of proton conductivity [49]. They reported that providing 0.30 atm of water partial pressure to the system after brief dehydration the material recovered its initial proton conductivity. They did not study however the minimum humidification rate required to trigger rehydration. The next experiments reported address the minimum humidification required for this purpose and the response time of the system to the changes in humidification.

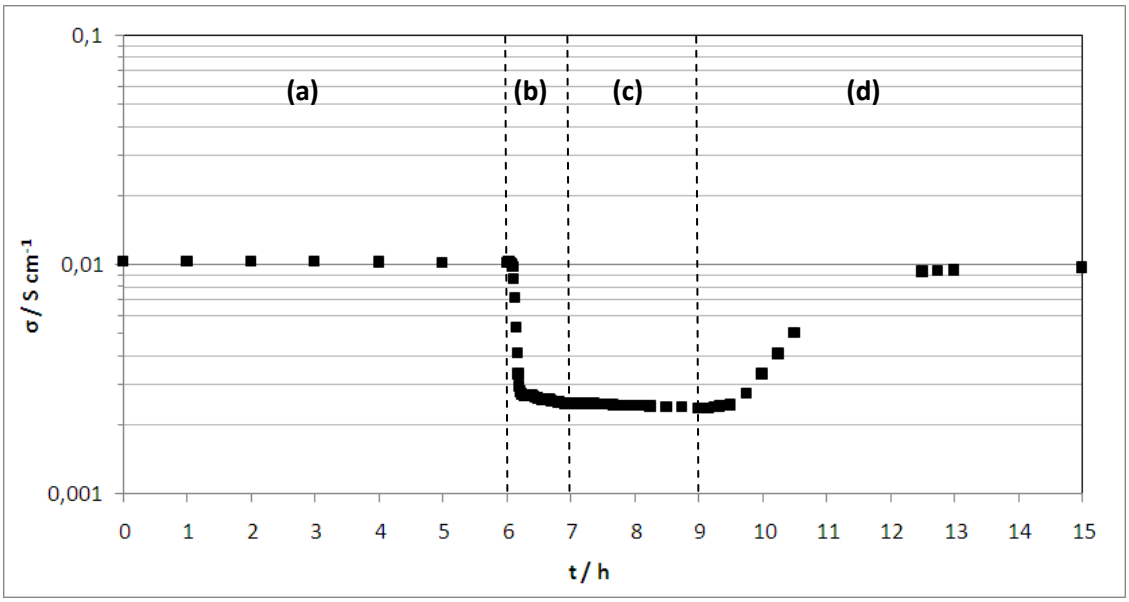

Figure 4.17. % RH vs. temperature diagram at atmospheric pressure.

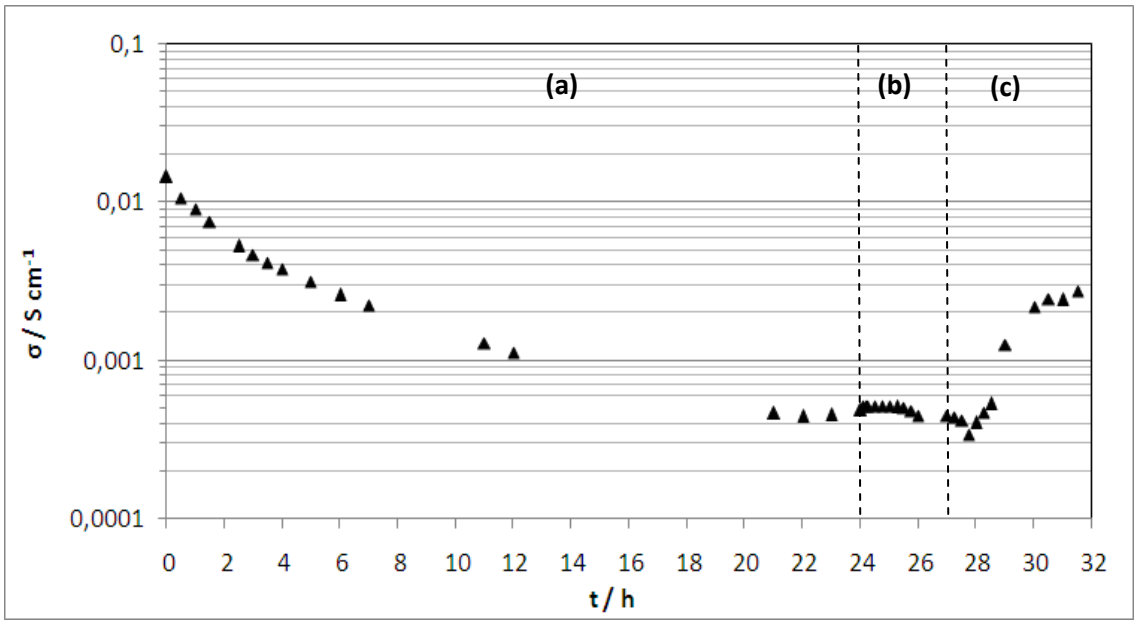

Figure 4.18. % RH vs. temperature diagram at atmospheric pressure.

In figure 4.17 four different regions are highlighted corresponding to different humidification rates of the feeding gas. During the first six hours, *region a*, the sample was stabilised at 0.12 atm water partial pressure showing a constant proton conductivity of 10^{-2} S cm^{-1}. After the stabilisation time dry gas was supplied to the system for one hour, *region b*, where a significant sharp decrease in proton conductivity is seen followed by a stabilisation region to values of approximately 2.5×10^{-3} S cm^{-1}. In *region c*, humidification of P_{H2O} = 0.12 atm was again provided to the system to induce rehydration

of the material, but as it is shown, no increase in conductivity happened. This means that although a humidification rate of P_{H2O} = 0.12 atm can avoid dehydration, it is not enough to promote the reaction in the opposite direction. In *region d* humidification was increased to P_{H2O}= 0.97 atm causing, after 30 min stabilisation time, a gradual increase in proton conductivity to almost a total recovery (97 %). These 30 minutes is the time the system needed to respond to the change and stabilise to the given humidification rate.

In figure 4.18, a similar experiment is shown where a CsH_2PO_4 pellet was stabilised at 0.02 atm of water partial pressure for 24 h, *region a,* and then humidification of P_{H2O} = 0.20 atm, *region b,* and P_{H2O} = 0.31 atm, *region c,* were provided by increasing the temperature in the water saturator. 0.31 atm of water partial pressure is the minimum humidification required to induce a rehydration of the material at this temperature. It can be concluded that higher humidification rates are therefore needed to rehydrate CsH_2PO_4, P_{H2O} > 0.31 atm, than to avoid dehydration, P_{H2O} > 0.12 atm.

4.5 Conclusions

The investigation and development of intermediate temperature proton conducting materials is a key issue to allow rising the operating temperature of PEM electrochemical devices. In this chapter the synthesis of phosphate-based solid acids was carried out and their properties in terms of structure, morphology and proton conductivity studied. The effect of material dehydration at the intermediate temperature range induced by phosphate condensation was addressed and the physical and chemical stability of CsH_2PO_4 under operating temperature and humidification conditions analysed.

All phosphate-based solid acids exhibited a clear transition to proton conductors in the intermediate temperature range. Maximum values of proton conductivity over 10^{-2} S cm^{-1} were obtained for CsH_2PO_4 at temperatures between 230 and 280 °C.

A significant mass loss takes place close to transition temperatures when no humidification is provided, which is attributed to dehydration for all cases except of $NH_4H_2PO_4$, where chemical decomposition to ammonia and phosphoric acid is assumed. Although it is reported that no water is required for proton transport in these materials, in real operating conditions water must be provided to the system in order to maintain proton conductivity and material stability.

CsH_2PO_4 shows good stability in terms of water solubility at high humidification rates and dehydration was proved to be avoided when $P_{H2O} > 0.120$ atm is applied to the system. Rehydration of the material, this is, hydrolysis of condensed phosphates, can be carried out at $P_{H2O} > 0.313$ atm being the rehydration rate faster at higher water partial pressures. Higher humidification rates are therefore needed to trigger rehydration than to avoid dehydration.

These results place CsH_2PO_4 as a promising proton conductor material for PEM fuel cells and electrolysers. The inorganic nature of this material however, requires high thickness pellets to be fabricated, ca. 300 μm, and used as electrolytes. Different approaches to reduce the thickness of the electrolyte and thus, the ohmic resistance of the system are proposed in Chapter 5.

4.6 References

1. Scott, K., C. Xu, and X. Wu, *Intermediate temperature proton-conducting membrane electrolytes for fuel cells*. Wiley Interdisciplinary Reviews: Energy and Environment, 2013: p. n/a-n/a.
2. Paschos O, K.J., Stimming U, Maglia F., *A review on phosphate based, solid state, protonic conductors for intermediate temperature fuel cells.* J Phys Condens Matter., 2011. **23**(23).
3. Lee SY, O.A., Kanno M, Nakamoto H, Yasuda T, Watanabe M., *Non-humidified intermediate temperature fuel cells using protic ionic liquids.* J Am Chem Soc., 2010. **132**(28): p. 9764-73.
4. Tolchard, J., *Electrolytes / Solid: Protons*, in *Encyclopedia of Electrochemical Power Sources*, J. Garche, Editor. 2009, Elsevier: Amsterdam. p. 188-195.
5. Barbir, F., *PEM Fuel Cells, Theory and Practice*. 2005, Amsterdam: Elsevier. 456.
6. Mauritz, K.A., Moore R.B., *State of understanding of nafion.* Chemical reviews, 2004. **104**: p. 4535−4585.
7. Kreuer, K.D., *Proton conducting oxides.* Annual Review of Materials Research, 2003. **33**: p. 333-359.
8. Colomban, P., *Proton Conductors: Solids, Membranes and Gels - Materials and Devices*. 1992, New York: Cambridge University.
9. Knauth, P., Di Vona M.L., *Solid State Proton Conductors: Properties and Applications in Fuel Cells*. 2012, UK: John Wiley & Sons. Ltd.
10. Berning, T., Kongstein, O.E., Borresen, B., Seland, F., Tunold, R., *Polymer electrolyte fuel cells based on phosphoric acid doped polybenzimidazole (PBI) membranes.* Energy, 2007. **32**: p. 418-422.
11. Daletou, M.K., N. Gourdoupi, and J.K. Kallitsis, *Proton conducting membranes based on blends of PBI with aromatic polyethers containing pyridine units.* Journal of Membrane Science, 2005. **252**(1–2): p. 115-122.
12. Jalani, N.H., Ramani, M., Ohlsson, K., Buelte, S., Pacifico, G., Pollard, R. and Datta, R., *Performance analysis and impedance spectral signatures of high temperature PBI–phosphoric acid gel membrane fuel cells.* Journal of Power Sources, 2006. **160**(2): p. 1096-1103.
13. Mamlouk, M. and K. Scott, *The effect of electrode parameters on performance of a phosphoric acid-doped PBI membrane fuel cell.* International Journal of Hydrogen Energy, 2010. **35**(2): p. 784-793.
14. Li, Q., Rudbeck, H. C., Chromik, A., Jensen, J. O., Pan, C., Steenberg, T. and Kerres, J., *Properties, degradation and high temperature fuel cell test of different types of PBI and PBI blend membranes.* Journal of Membrane Science, 2010. **347**(1–2): p. 260-270.
15. Lobato, J., Cañizares, P., Rodrigo, M.A. and Linares, J.J., *Improved polybenzimidazole films for H_3PO_4-doped PBI-based high temperature PEMFC.* Journal of Membrane Science, 2007. **306**(1–2): p. 47-55.
16. Goñi-Urtiaga, A., D. Presvytes, and K. Scott, *Solid acids as electrolyte materials for proton exchange membrane (PEM) electrolysis: Review.* International Journal of Hydrogen Energy, 2012. **37**(4): p. 3358-3372.
17. Haile, S.M., Boysen, D.A., Chisholm C.R.I. and Merle R.B., *Solid acids as fuel cell electrolytes.* Nature, 2001. **410**.

18. Haile SM, Sasaki K, Boysen DA, Uda T., *Solid acid proton conductors: from laboratory curiosities to fuel cell electrolytes.* Faraday Discuss., 2007. **134**: p. 17-39.

19. Botez, C.E., Botez, C. E., Carbajal, D., Adiraju, V. A., Tackett, R. J. and Chianelli, R. R., *Intermediate-temperature polymorphic phase transition in KH_2PO_4: A synchrotron X-ray diffraction study.* Journal of Physics and Chemistry of Solids, 2010. **71**(11): p. 1576-1580.

20. Ortiz, E., Vargas, R. A., & Mellander, B. E., *On the high-temperature phase transition of RbH_2PO_4 - A polymorphic transition?* Journal of Physics and Chemistry of Solids, 1998. **59**(6-7): p. 1111-1117.

21. Lee, K. S., Moon, J., Lee, J., & Jeon, M., *High-temperature phase transformations in LiH_2PO_4 and possible solid-state polymerization.* Solid State Communications, 2008. **147**(1-2): p. 74-77.

22. Lee, K.-S., *Hidden nature of the high-temperature phase transitions in crystals of KH_2PO_4-type : Is it a physical change ?* Journal of Physics and Chemistry of Solids, 1996. **57**(3): p. 333-342.

23. Chen, X., Wang, C., Payzant, E. A., Xia, C., & Chu, D., *An Oxide Ion and Proton Co-Ion Conducting $Sn_{0.9}In_{0.1}P_2O_7$ Electrolyte for Intermediate-Temperature Fuel Cells.* Journal of The Electrochemical Society, 2008. **155**(12): p. B1264-B1269.

24. Li, Z. and T. Tang, *High-temperature dehydration behavior and protonic conductivity of RbH_2PO_4 in humid atmosphere.* Materials Research Bulletin, 2010. **45**(12): p. 1909-1915.

25. Ahn, Y. S., Mangani, I. R., Park, C. W., & Kim, J., *Study on the morphology of CsH_2PO_4 using the mixture of methanol and polyols.* Journal of Power Sources, 2006. **163**(1): p. 107-112.

26. Telila, H., Mamo, T., Hernandez-Sanchez, R., *The Fabrication of Nanoparticle CsH_2PO_4 Electrolyte for Fuel Cell Applications.* Caltech Undergraduate Research Journal 2009. **Winter**: p. 32-39.

27. Hosseini, S., Daud, W., Badiei, M., Amir, A., Kadhum, H., Mohammad, A.B., *Effect of surfactants in synthesis of CsH_2PO_4 as protonic conductive membrane* Bull. Mater. Sci., 2011. **34**(4): p. 759-765.

28. Hosseini, S., Mohamad, A. B., Kadhum, A. H., & Wan Daud, *Thermal analysis of CsH_2PO_4 nanoparticles using surfactants CTAB and F-68.* Journal of Thermal Analysis and Calorimetry, 2010. **99**(1): p. 197-202.

29. Baranov, A.I., V.P. Khiznichenko, and L.A. Shuvalov, *High temperature phase transitions and proton conductivity in some kdp-family crystals.* Ferroelectrics, 1989. **100**(1): p. 135-141.

30. Plakida, N.M., *Theory of superionic phase transition in $CsHSO_4$.* American Institute of Physics, 1984. **41**(3): p. 114-116.

31. Ortiz, E., Vargas, R.A.,Mellander, B.E., *On the high-temperature phase transitions of some KDP-family compounds: a structural phase transition? A transition to a bulk-high proton conducting phase?* Solid State Ionics, 1999. **125**(1): p. 177-185.

32. Park, J.-H., *Possible origin of the proton conduction mechanism of CsH_2PO_4 crystals at high temperatures.* Physical Review B, 2004. **69**(5): p. 054104.

33. Bronowska, W. and A. Pietraszko, *X-ray study of the high-temperature phase transition of CsH_2PO_4 crystals.* Solid State Communications, 1990. **76**(3): p. 293-298.

34. Gomadam, P.M. and J.W. Weidner, *Analysis of electrochemical impedance spectroscopy in proton exchange membrane fuel cells.* International Journal of Energy Research, 2005. **29**(12): p. 1133-1151.

35. Taninouchi, Y.K., Uda, T., Awakura, Y., Ikedab A. and Haile, S.M., *Dehydration behavior of the superprotonic conductor CsH_2PO_4 at moderate temperatures: 230 to 260 ºC.* J. Mater. Chem. , 2007. **17**: p. 3182-3189.

36. Ikeda A., *Examination of the superprotonic transition and dehydration behavior of $Cs_{0.75}Rb_{0.25}H_2PO_4$ by thermogravimetric and differential thermal analyses.* Solid State Ionics, 2010. **181**: p. 193-196.

37. Li, Z., *Impedance analysis and protonic conduction mechanism in RbH_2PO_4/SiO_2 composite systems.* Electrochimica Acta, 2010. **55**(24): p. 7298-7304.

38. Freeda, T.H. and Mahadevan, C., *Electrical conductivity measurements on gel grown KDP crystals added with some ammonium compounds.* Bulletin of Materials Science, 2000. **23**(4): p. 335-340.

39. Kubasova, L.V., *Polyphosphoric Acids and Their Ammonium Salts.* Russian Chemical Reviews, 1971. **40**(1): p. 1.

40. Sugahara, T., Hayashi, A., Tadanaga, K., & Tatsumisago, M., *Characterization of proton conducting $CsHSO_4$–CsH_2PO_4 ionic glasses prepared by the melt-quenching method.* Solid State Ionics, 2010. **181**(3–4): p. 190-192.

41. Taninouchi, Y. K., Hatada, N., Uda, T., & Awakura, Y., *Phase Relationship of CsH_2PO_4 – $CsPO_3$ System and Electrical Properties of $CsPO_3$.* Journal of The Electrochemical Society, 2009. **156**(5): p. B572-B579.

42. Chisholm, C., Boysen, D.A., Papandrew, A.B., Zecevic, S., Cha, S., and K.J. Sasaki, Varga, A., Giapis, T.P., Haile, S.M., *From Laboratory Breakthrough to Technological Realization: The Development Path for Solid Acid Fuel Cells.* The Electrochemical Society, 2009. Interface (Fall).

43. Ikeda, A. and S.M. Haile, *The thermodynamics and kinetics of the dehydration of CsH_2PO_4 studied in the presence of SiO_2.* Solid State Ionics, 2012. **213**(0): p. 63-71.

44. Choi, B.-K., *High temperature phase transitions and thermal decomposition of KH_2PO_4 crystals.* Journal of Physics and Chemistry of Solids, 1995. **56**(8): p. 1023-1030.

45. Galwey, A.K., Brown, M.E., *Thermal Decomposition of Ionic Solids: Chemical Properties and Reactivities* 1999, Amsterdam. Elsevier. 567.

46. Osterheld, R.K. and L.F. Audrieth, *Polymerization and Depolymerization Phenomena in Phosphate–Metaphosphate Systems at Higher Temperatures. Condensation Reactions Involving the Potassium Hydrogen Orthophosphates.* The Journal of Physical Chemistry, 1952. **56**(1): p. 38-42.

47. Guerrant, G.O. and D.E. Brown, *Thermal Stability, Thermal Decomposition of High-Analysis Fertilizers Based on Ammonium Phosphate.* Journal of Agricultural and Food Chemistry, 1965. **13**(6): p. 493-497.

48. Chen, R. H., Yen, C. C., Shern, C. S., & Fukami, T., *Studies of high-temperature phase transition, electrical conductivity, and dielectric relaxation in $(NH_4)H_2PO_4$ single crystal.* Journal of Applied Physics, 2005. **98**(4): p. 044104.

49. Otomo, J., Tamaki, T., Nishida, S., Wang, S., Ogura, M., Kobayashi, T. and Takahashi, H. ., *Effect of water vapor on proton conduction of cesium dihydrogen phosphate and application to intermediate temperature fuel cells.* Journal of Applied Electrochemistry, 2005. **35**(9): p. 865-870.

50. tomo, J., Minagawa, N., Wen, C. J., Eguchi, K., & Takahashi, H., *Protonic conduction of CsH_2PO_4 and its composite with silica in dry and humid atmospheres.* Solid State Ionics, 2003. **156**(3–4): p. 357-369.

CHAPTER 5

FABRICATION OF CsH_2PO_4 - BASED PROTON CONDUCTING MEMBRANES

In this chapter different approaches to build thin membranes based on CsH_2PO_4 are proposed. The methodology of each fabrication technique is explained and the membrane characterisation results presented in terms of morphology, composition, proton conductivity and tensile strength. Five membrane fabrication methods are proposed in this section; (1) casting of CsH_2PO_4/polymer membranes, (2) CsH_2PO_4-doped polymeric membranes, (3) glass-fibre reinforced membranes, (4) electrospinning of CsH_2PO_4 fibre mat and (5) casting of partially polymerised CsH_2PO_4. The maximum proton conductivity achieved was 8×10^{-3} S cm^{-1} at 250 °C by the glass-reinforced membranes.

5.1 Introduction

The main characteristic of PEM water electrolysis over other electrolysis systems is the use of a solid electrolyte. It reduces the volume of the cell and provides the system with several advantages such as a more portable design with high energy density. The modular nature of PEM electrolysers gives the possibility of a delocalised fuel production (energy storage in form of H_2) in order to build a decentralised energy production system *(see Chapter 1)* [1, 2]. The electrolyte of the electrolyser cell needs to fulfil several specifications in order to be applicable in a real system. It must have high proton conductivity and low electrical conductivity, high chemical and thermal stability and it has to act as an effective separator with good mechanical strength and low permeability to gases. Perfluorosulfonic acid polymers (i.e. Nafion®) are the state-of-the-art electrolytes used for this application fulfilling all the specifications listed above. However, these polymers need liquid water in their structure in order to conduct protons and they are therefore limited to operating temperatures below 100 °C. In order to increase the operating temperature of PEM electrolysers, CsH_2PO_4, from the phosphate solid acid family, is proposed in this research as an alternative proton conducting solid electrolyte. CsH_2PO_4 has been reported as a promising proton conducting material to be used in intermediate temperature fuel cells [3]. At temperatures higher than 230 °C, this material undergoes a structural change providing

it with high proton conductivity (1.5×10^{-2} S cm^{-1}) which makes it desirable to use as electrolyte in intermediate temperature electrochemical devices, i.e. water electrolysers.

Commonly, electrolytes of these phosphate salts are fabricated by unaxially compressing the polycrystalline powder at high pressures to form a dense pellet. The inorganic nature of the material provides the pellet fabricated by this method with very brittle properties and therefore high thickness is needed in order to fabricate a mechanically stable electrolyte. The pellet must be able to support the stresses generated in the electrolysis cell, by temperature and pressure gradients for instance. *Uda et al.* [4] reported the fabrication of a membrane electrode assembly (MEA) using a CsH_2PO_4 pellet as thin as 25 µm supported on a porous stainless steel electrode. The extremely low thickness of the electrolyte provides their fuel cell system with relatively low ohmic resistance (~ 150 mΩ cm^2) and maximum single cell power densities of 415 mW cm^{-2} at 240 °C. In this research the same methodology was tried in order to build a thin supported pellet, however no successful results were obtained as the electrolytes did not have enough mechanical stability and electric short-circuits and high gas permeability were caused by pellet cracking.

Although a few short durability test are reported for the system mentioned above, the long-term durability of this system is an issue that should be better addressed, not only in stable operating conditions (at a fixed potential), but also in start-stop cycles were stresses arisen from cooling and heating the system could affect the integrity of such thin and brittle electrolyte. In this research, the minimum thickness achieved for a stable, self-supported pellet was found to be ca. 300 µm, which considering the proton conductivity of this material would provide the electrolysis cell with a minimum resistance of ca. 1.5 Ω cm^2. This high resistance would generate high ohmic losses lowering the overall performance of the system. Different approaches for electrolyte fabrication are therefore required. Many authors reported that the addition of several oxides (i.e. SiO_2, TiO_2) to a solid acid powder provides it with slightly higher proton conductivity (ca. 3×10^{-2} S cm^{-1}) by the creation of a new conducting phase and enhanced mechanical stability, although no data of the latter is provided [5-7]. The resulting material is an inorganic powder which is also compressed into thick pellets (ca. 400 µm) to use as electrolyte. Although proton conductivity is increased the resistance provided by the electrolyte would still be too high because of the high thickness required. *Bocchetta et al.* reported the fabrication of a porous alumina membrane (50 µm) filled with CsH_2PO_4 for application in a fuel cell [8]. They proposed these membranes as low temperature PEM electrolytes and claim that the interaction

between the alumina membrane and the solid acid creates a new proton conducting phase at room temperature. The solubility of CsH_2PO_4 in condensed water is an issue that should be addressed in that case, as it would affect the durability of the system. *Boysen et al.* reported the fabrication of composite membranes as thin as 5 – 20 µm by the casting of a sulfate-based solid acid ($CsHSO_4$) with polyvinylidene difluoride (PVDF) [9]. This method provided membranes with a maximum conductivity of 5.6×10^{-3} S cm^{-1} for a 20 µm thickness membrane at 150 °C. An addition of 20 % wt. of polymer lowered the conductivity of the solid acid by approximately half an order of magnitude.

Although few attempts to fabricate solid acid-based composite membranes have been carried out, it still remains as a challenge to make this material applicable in a real electrochemical system. Next, five different fabrication methods to build thin membranes based on CsH_2PO_4 are proposed.

5.2 Membrane fabrication methods

The fabrication methods reported in this research include doping of basic polymers (imidazole and pyridine-based polymers) by acid/base interaction with CsH_2PO_4, the addition of a stable polymer as a binder and the addition of glass fibres as a reinforcement for CsH_2PO_4 and two methods based on a partial dehydration/polymerisation of CsH_2PO_4; casting of a partially polymerised CsH_2PO_4 membrane and the fabrication of a highly interconnected CsH_2PO_4 – fibre mat by electrospinning.

5.2.1 Casting of CsH_2PO_4/polymer composite membranes

In order to provide mechanical stability to a CsH_2PO_4-based membrane, a polymer was added as a binder. The polymer used, *poly-[2,2'-m-(phenylene)-5,5'-bibenzimidazole]* (PBI), was chosen due to its high chemical and thermal stability at the intermediate temperature range of 230 – 300 °C. This high stability is provided by the strong intermolecular bonds of the aromatic bi-benzimidazole structure (figure 5.1).

The low price and the availability of this polymer, because of its use as phosphoric acid-doped electrolyte in fuel cells, made it desirable to use in the fabrication of composite membranes.

The addition of a polymer to the CsH_2PO_4-based membrane would help bind the solid acid particles together providing the composite membrane with higher mechanical stability enabling the fabrication of thin membranes.

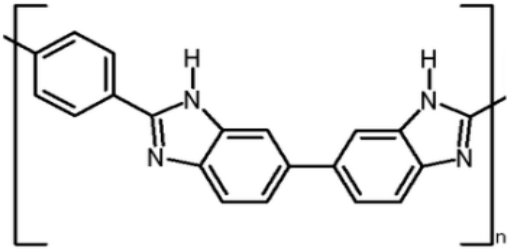

Figure 5.1. Chemical structure of poly-[2,2'-m-(phenylene)-5,5'-bibenzimidazole] (PBI).

Experimental

Poly-[2,2'-m-(phenylene)-5,5'-bibenzimidazole] (PBI) (Between Lizenz GmbH) with a $M_w = 10^6$ g mol^{-1} was dissolved in dimethyl acetamide (DMAc) using a sealed teflon vessel and heating it in a microwave for 1 min at 400 W for 6 to 8 times. 5 and 10 % wt. PBI solution in DMAc were prepared. The resulting solutions were centrifuged in order to eliminate non-dissolved rests of PBI. The exact concentrations of the solutions were determined by casting a known volume of the PBI solution into a membrane and weighing it afterwards.

The synthesis of CsH_2PO_4 was carried out as explained in section 4.2. The powder was precipitated by spraying the reaction solution into methanol in order to achieve a more homogeneous particle size distribution of the CsH_2PO_4 particles.

In order to fabricate composite membranes, the required amounts of polycrystalline powder of CsH_2PO_4 were added to PBI solution and mechanically stirred for 2 h. The dispersion was then placed in an ultrasonic bath for 15 min and casted onto a 5 × 5 cm glass plate at 75 °C for 6 h. The resulting composite membrane was pealed from the glass plate using methanol and then dried in the oven at 80 °C for 24 h.

Composite membranes with weight percentages of CsH_2PO_4 of 75, 80, 85, 90 and 95 % wt. were fabricated using 5 and 10 % wt. PBI solutions. The two different PBI solution concentrations were used to analyse the influence of the viscosity on the dispersion of CsH_2PO_4 particles in solution. The thickness of the membranes varied between 25 and 150 µm and was controlled by the amount of material used in their fabrication.

5.2.2 CsH_2PO_4 – doped polymeric membranes

Doping of a basic polymer with an acid is a methodology used to fabricate proton conducting membranes for intermediate temperature fuel cells. The most common example is the doping of PBI with phosphoric acid. The imidazole groups of the chemical structure of PBI, due to their basic nature, creates bonds with the phosphoric acid by acid/base interaction providing the polymer with a high loading of acid in its structure. The phosphoric acid acts as a proton carrier within the membrane providing it with high proton conductivity (3 - 5 × 10^{-2} S cm^{-1}) at temperatures as high as 180 °C [10, 11]. Pyridine based polymers (Advent TPS®) are also doped with phosphoric acid in order to provide the membrane with high proton conductivity and to use in intermediate temperature fuel cells as electrolyte [12]. The chemical structure of the pyridine based aromatic polyether of Advent TPS® polymer is shown in figure 5.2. In the case of this polymer, pyridine groups act as the basic agents allowing the doping of the polymeric membrane with an acid. The main characteristics of both polymers are displayed in table 5.1.

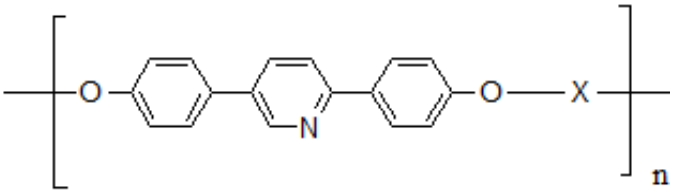

Figure 5.2. Chemical structure of pyridine-based Advent TPS® polymer.

Table 5.1. Physico-chemical properties of PBI and Advent TPS® membranes.

Properties	**Advent TPS®** [13]	**PBI** [11, 14, 15]
T_g / °C	250 - 255	425 - 435
$T_{decomposition}$ (5% weight loss) / °C	415	700
Maximum tensile strength (non-doped) / Mpa	74 ± 4	125 ± 25
Maximum tensile strength (H_3PO_4-doped) / Mpa	12 ± 2	15 ± 4
Proton conductivity (H_3PO_4-doped) / S cm^{-1}	8 × 10^{-2}	5 × 10^{-2}

In this research both polymers, PBI and Advent TPS®, were used in their membrane form in order to get doped by CsH_2PO_4. The basic groups of both polymers, imidazole and

pyridine respectively, would interact by an acid/base interaction with the solid acid building hydrogen bonds as they do with phosphoric acid and allowing the doping of the membrane with CsH_2PO_4.

Experimental

PBI membranes were fabricated by casting a 10 % wt. PBI solution in DMAc onto a 5 × 5 cm glass plate at 75 °C for 8 h. Membranes with thickness of 10 - 20 µm were fabricated. Advent TPS® membranes were purchased (Advent Technologies) with thickness of 75 µm.

Membranes were immersed in a 6.5 M saturated water solution of CsH_2PO_4 and kept at 85 °C for 6 days to allow the acid/base interaction between both materials. Membranes were also immersed in melted CsH_2PO_4 at 300 °C for 2 and 4 h with the same purpose. 100 ml min^{-1} humid N_2 (P_{H2O} = 0.95 atm) was provided to the system to avoid dehydration of CsH_2PO_4. The resulting membranes were washed in methanol and dried in an oven at 80 °C overnight.

5.2.3 Glass fibre reinforced membranes

In this method the addition of glass fibres to CsH_2PO_4 in order to build a stable and thin pellet with improved mechanical properties was studied. The presence of glass fibres in a compressed CsH_2PO_4 structure would help to distribute the stresses and enable the fabrication of thinner pellets with less brittle characteristics. Glass fibre filters were used in order to provide an interconnected fibre-mat structure and they were filled with CsH_2PO_4 in order to provide proton conductivity to the composite. The high thermal stability of the glass fibre filters made them desirable to use with this purpose. Specifications of the glass fibre filters used in this research are summarised in table 5.2.

Experimental

Binder-free glass fibre filters (Millipore®, type 1) were placed in 5.0 cm diameter petri dish and volumes of 1, 1.5, 2 and 3 ml of CsH_2PO_4 saturated solution at room temperature (C = 4.4 M) were added. The samples were dried in an oven at 80 °C for 5 h and then pressed between two teflon sheets at 7×10^3 kg cm^{-2} at room temperature for 30 min. The thickness of the resulting composite membranes was between 100 and 200 µm depending on the amount of CsH_2PO_4 solution added.

Table 5.2. Specifications of Milipore® type 1 glass-fibre filters.

Chemical composition	Glass fibre (without binder)
Maximum Operating Temperature / °C	500
Pore size / µm	1.6
Wettability	Hydrophilic
Filter Diameter / mm	47
Porosity / %	90

5.2.4 Electrospinning of CsH_2PO_4 fibre mat

In this section a new fabrication method of a composite membrane based on the electrospinning of CsH_2PO_4 is proposed. Electrospinning is a technique used to produce polymeric or hybrid fibres in the micrometre to nanometre scale [16, 17] *(see section 3.1.8).* A CsH_2PO_4 solution in water cannot be electrospun because of the low viscosity and charging of the solution when a high voltage is applied. The addition of a carrier polymer to the solution could provide a way to electrospin CsH_2PO_4 fibres but this would imply further treatment of the produced fibres to eliminate the polymer, either thermally or by washing. This step would affect the integrity of the fibres in terms of morphology and composition. For this reason a different method to electrospun CsH_2PO_4, based on the condensation of phosphates, was developed.

CsH_2PO_4, as the majority of the phosphate-based solid acids, undergoes a dehydration/polymerisation reaction over its so-called superprotonic phase transition temperature (reactions 4.3 - 4.4). By this reaction the material loses its constituent water, generating longer chains of condensed phosphates leading to the formation of pyro- and poly-phosphates ($CsH_xP_yO_z$) until its complete dehydration to cesium metaphosphate ($CsPO_3$).

When this polymerised material is dissolved in water it gives a transparent viscous solution. The viscosity of this solution allows it to be electrospun in the absence of any carrier polymer or additive making it possible to generate pure inorganic fibres of this salt in one step. This method is proposed for the fabrication of a dense highly interconnected CsH_2PO_4 fibre-mat. The later addition of a polymer to this mat in order to provide good

mechanical properties and occlude porosity would lead to a new fabrication method of a medium temperature proton conducting membrane.

Experimental

Polycrystalline powder of CsH_2PO_4 was heat-treated to induce the dehydration reaction. The conditions of the thermal treatment are displayed in table 5.3. These treatment conditions were chosen as they induced the lowest degree of dehydration needed to electrospin CsH_2PO_4 into fibres. The resulting partially polymerised CsH_2PO_4 powder (CDP_p) was dissolved in DI water to a concentration of 2.25 g ml^{-1}. This concentration provided suitable viscosity to the solution in order to be electrospun. The solution of CDP_p was then electrospun by the electrospinning device (figure 3.2, chapter 3) onto a grounded collector covered by an aluminium foil in the conditions displayed in table 5.4.

Table 5.3. Heat treatment conditions

Temperature / °C	300
Heating rate / °C min^{-1}	10
Time / h	3

Table 5.4. Electrospinning conditions

Potential / kV	15
Distance / cm	10
Rate solution / ml h^{-1}	0.3

Fibre-mats where kept in a 50 % RH atmosphere for 7 days ($CDP_{f\text{-}RH}$) to allow the rehydration of the fibres to the initial CsH_2PO_4. No higher relative humidity was used because the electrospun fibre would dissolve.

5.2.5 Casting of partially polymerised CsH_2PO_4

The same principle of phosphate condensation used for the fabrication of electrospun CsH_2PO_4 fibres was used to fabricate cast membranes of partially polymerised CsH_2PO_4. The loss of the constituent water of this salt upon heat treatment generates longer chains of phosphates providing the material with a more polymeric nature. The resulting material, unlike pure CsH_2PO_4, can be casted into self-supported membranes as thin as 25 µm. Although the mechanical properties of the material are improved by this process proton conductivity is partially lost. A compromise between both properties is therefore required in order to build a mechanically stable proton conducting membrane for application in a PEMWE. The heat treatment conditions used in this method were the minimum time and

temperature conditions to induce the dehydration degree needed for a successful casting of a membrane. Less time or temperature dehydration processes did not generate enough phosphate condensation to allow casting the material into a self-supported membrane.

Experimental

CsH_2PO_4 was heat treated in the conditions displayed in table 5.3. The resulting partially dehydrated material (CDP_p) was dissolved in DI water in a concentration of 5.0 mg ml^{-1}. The solution was stirred until complete dissolution and placed in the ultrasonic bath for 1 h in order to eliminate any air bubbles retained in the viscous solution. Membranes were casted onto 5 × 5 cm glass plates at 80 °C for 6 h until all water was evaporated and pealed with methanol. The resulting samples were dried in an oven at 80 °C for 24 h. The thickness of the membranes was controlled by the volume of solution used in the casting.

5.3 Characterisation of membranes

Membranes fabricated by the five different methods described above were characterised in terms of composition, morphology, proton conductivity and tensile strength. These characteristics define the potential of the membranes for application as electrolytes in a PEMWE.

5.3.1 Composition

The chemical composition of membranes fabricated by membrane doping with CsH_2PO_4, electrospinning and casting of partially dehydrated CsH_2PO_4 was further analysed. These methods are based on the chemical modification of materials by acid/base interaction and dehydration of CsH_2PO_4 respectively. Characterisation of the chemical composition of the final materials was therefore carried out.

5.3.1.1 Doping level of CsH_2PO_4/polymer membranes

The CsH_2PO_4 doping level of the membranes was calculated by measuring the weight before and after the doping process and applying equation 5.1. All weights were measured after drying the membranes in the oven at 80 °C for 24 h to eliminate the contribution of water uptake to the total weight of the doped membranes. The solid acid doping level (x)

of the membranes was calculated as the molar number of CsH_2PO_4 per repeat unit of polymer, calculated by equation 5.1. Doping level results are reported in table 5.5.

$$Doping\ level\ (x) = \frac{(m_{doped} - m_{undoped})/M_{CsH_2PO_4}}{m_{undoped}/M_{Polymer}} \quad (5.1)$$

where, m_{doped} and $m_{undoped}$ are the weight of the doped and non-doped membranes and $M_{CsH2PO4}$ and $M_{polymer}$ represent the molecular weight of CsH_2PO_4 and of a repeat unit of the polymer, respectively.

Table 5.5. CsH_2PO_4 doping level of Advent TPS® and PBI membranes**.**

Conditions		**x / mol CsH_2PO_4 polymer unit^{-1}**	
		Advent TPS®	**PBI**
6.5 M CsH_2PO_4 sol. T = 85 °C t = 6 days		0	0.22
Melted CsH_2PO_4 T = 300 °C	t = 2 h	-	0.74
	t = 4 h	-	0.68

PBI membranes got a 0.22 doping level when a saturated solution of CsH_2PO_4 was used and values close to 0.70 in pure melted CsH_2PO_4. This doping corresponds to the amount of solid acid interacting with the imidazole groups by hydrogen bonding. Advent TPS® membranes showed no difference in their weight before and after doping in a saturated solution of CsH_2PO_4. The difference in the doping level on both types of membranes is attributed to the slightly higher alkalinity of the imidazole groups of PBI (pK_a = 5.5) to the pyridine groups of Advent TPS® (pK_a = 5.2) [11, 18]. Advent TPS® membranes showed chemical instability when melted CsH_2PO_4 was used as the doping medium. The resulting membranes changed their colour from yellow to black and lost their mechanical stability breaking into many pieces and making the weight measurement after the doping process not possible. This loss in mechanical stability is attributed to the chemical degradation of the polymer under the conditions applied.

The low doping levels obtained by these methods are attributed to a poor acid/base interaction caused by the low acidity of CsH_2PO_4. The pH of saturated solution of

CsH_2PO_4 solution was experimentally measured at different temperatures (figure 5.3). A constant pH value of 4.63 was measured at all temperatures. The low acidity of the CsH_2PO_4 solution, also expected in pure melted CsH_2PO_4, does not provide enough protons to the medium and therefore hydrogen bonding between the basic groups of the polymer and the solid acid is limited.

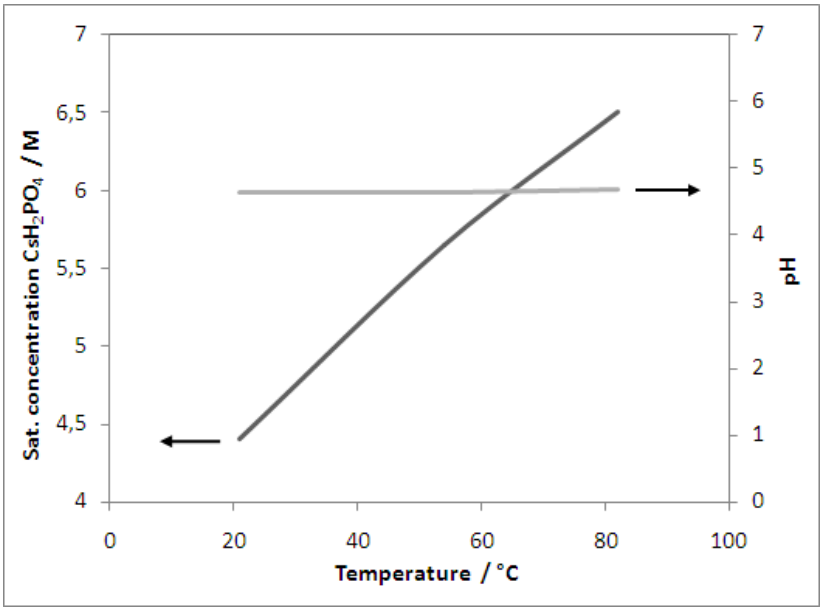

Figure 5.3. Saturation concentration and pH dependency on temperature of CsH_2PO_4 solution.

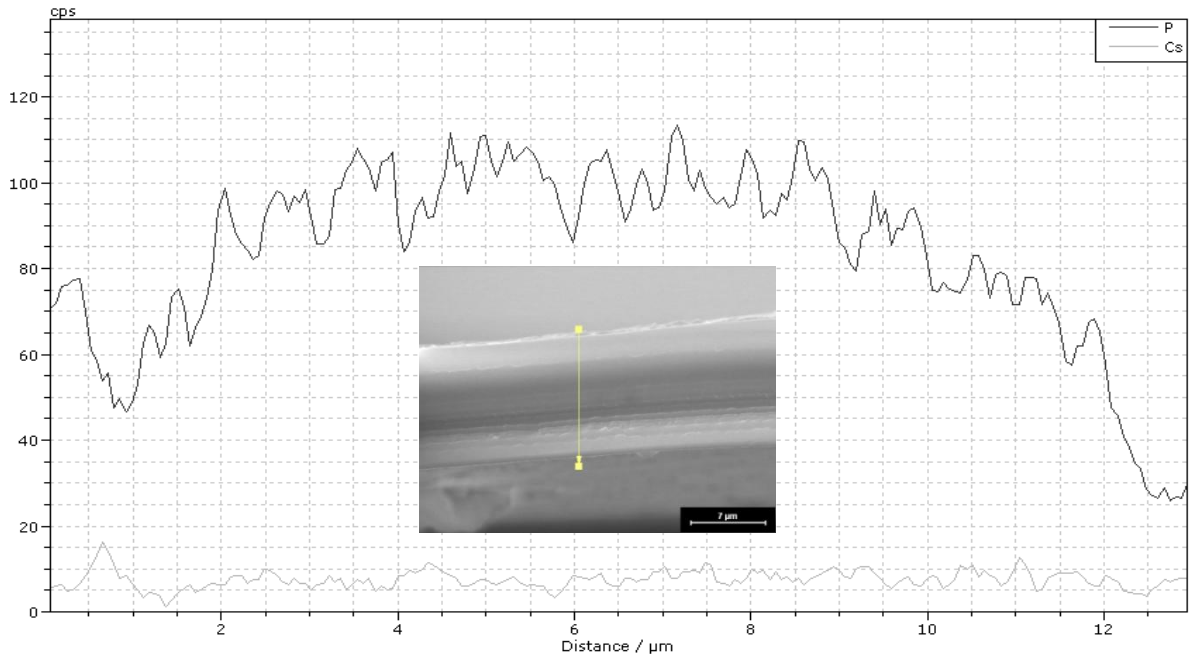

Figure 5.4. EDS analysis of the cross section of CsH_2PO_4-doped PBI membrane (T = 300 °C, t = 2 h).

PBI membranes doped in melted CsH_2PO_4 were analysed by EDS in order to study the distribution of the solid acid in the thickness of the polymeric membrane. The profile of P and Cs elements in their cross section line was analysed (figure 5.4). Phosphorous was more abundant than cesium along the entire cross section line analysed. This was attributed to a higher interaction of the benzimidazole groups with the disassociated $H_2PO_4^-$ ions rather than the exchange of the proton of the benzimidazole group with large size Cs^+ ion. The amount of phosphorous is lower in the edges of the membrane which could be caused by the washing up carried out with methanol after the doping process.

5.3.1.2 Phosphate condensation and CsH_2PO_4 fibre composition

The chemical structure of partially polymerised CsH_2PO_4 used in the casting and electrospinning methods was studied. The structure of fibrous CsH_2PO_4 (CDP_f) and rehydrated CsH_2PO_4 fibres ($CDP_{f\text{-}RH}$) was analysed by P-XRD and ^1H and ^{31}P MAS NMR. P-XRD spectra of these materials are shown in figure 5.5.

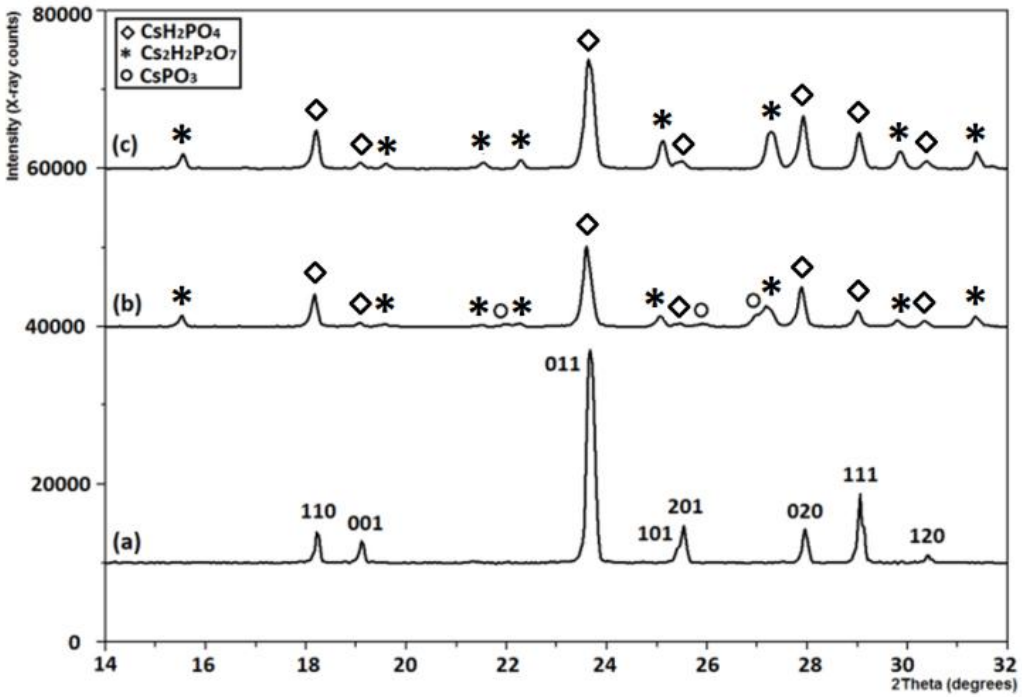

Figure 5.5. P-XRD patterns in the 2θ range of 14-32° of (a) CsH_2PO_4 (b) CDP_f and (c) $CDP_{f\text{-}RH}$.

The first pattern (figure 5.5-a) shows the typical diffraction peaks corresponding to the room temperature monoclinic structure of CsH_2PO_4, with a B21/m space group and lattice parameters a = 4.8725 Å, b = 6.3689 Å and c = 15.0499 Å [19].

In pattern (b), corresponding to CDP_f, the main peaks of the initial CsH_2PO_4, marked with '◊', are still visible although they generally show lower intensity. New diffraction peaks attributed to formation of a new phase of partially polymerised CsH_2PO_4, cesium pyrophosphate ($Cs_2H_2P_2O_7$) [20-22], are shown and marked with '*'. The positions are in good agreement with the diffraction peaks reported in the ICDD for this material (card number: 45-619). This phase presents an orthorhombic structure with lattice parameters *a* = 4.571 Å, *b* = 8.150 Å and *c* = 11.405 Å [23]. The presence of three low intensity peaks marked with 'o' suggests further polymerisation to cesium metaphosphate ($CsPO_3$) [21], of monoclinic structure and lattice parameters *a* = 12.744 Å, *b* = 4.344 Å and *c* = *6.829* Å [23]. These peaks do not closely correspond to patterns reported in the ICDD for $CsPO_3$ (card number: 45-617) probably because they correspond to a different degree of condensation of phosphates [24]. It is worth noting that the left hand limb at 25.9° was described as an unknown phase diffraction peak by *Taninouchi et al* [21].

In diffraction pattern (c), corresponding to rehydrated electrospun fibres ($CDP_{f\text{-}RH}$), all the diffraction peaks corresponding to CsH_2PO_4 and $Cs_2H_2P_2O_7$ are observed, meaning that cesium pyrophosphate does not hydrolysed to the initial CsH_2PO_4 in the conditions applied. Nevertheless, the peaks corresponding to further polymerised species disappeared, which means that those species hydrolysed in these conditions. According to these diffraction patterns, in CDP_f a mixture of partially dehydrated/polymerised ($Cs_2H_2P_2O_7$) and bulk (CsH_2PO_4) material coexist, although few low intensity peaks corresponding to further dehydrated species were also observed.

Considering CsH_2PO_4 and $Cs_2H_2P_2O_7$ as the major coexisting phases in the CsH_2PO_4 fibres, a semi-quantitative Relative Intensity Ratio (RIR) method was used to estimate the mass ratio of each of the phases in the samples [25]. The values obtained for a mass ratio of phases CsH_2PO_4:$Cs_2H_2P_2O_7$ were 69:31% for CDP_f and 71:29% for $CDP_{f\text{-}RH}$. This suggest that, although a few condensed phosphate species appear to hydrolyse, most of them remain stable at the conditions applied, which are thermodynamically more favourable for rehydration than the temperature and relative humidity conditions of an intermediate temperature electrochemical device.

Figure 5.6 shows the ^{31}P MAS NMR spectra of (a) bulk CsH_2PO_4 (b) CDP_p (c) CDP_f and (d) $CDP_{f\text{-}RH}$. The first spectrum presents a single sharp resonance with a chemical shift at -5.39 ppm which corresponds to the phosphorous of the dihydrogen phosphate group. This resonance appears also in the spectra of figure 5.6 (b), (c), (d), indicating that dihydrogen

phosphate groups are conserved in the material after partial polymerisation and electrospinning to CsH_2PO_4 fibres. In the spectrum of CDP_p six resonances with different chemical shifts are observed at -5.39, -6.52, -7.14, -9.14, -21.08 and -22.80 ppm corresponding to different degrees of condensation of the phosphate groups. All these signals are also visible, although with lower intensity, in the spectrum of CDP_f. The lower intensity is explained by the partial rehydration of the material when dissolving it in water to prepare the electrospinning solution. In the spectrum of CDP_f, after conditioning at 50 % RH for 7 days, the resonances with chemical shifts at -6.65 and -9.20 disappear, which was attributed to the partial hydrolysis of the condensed phosphate species.

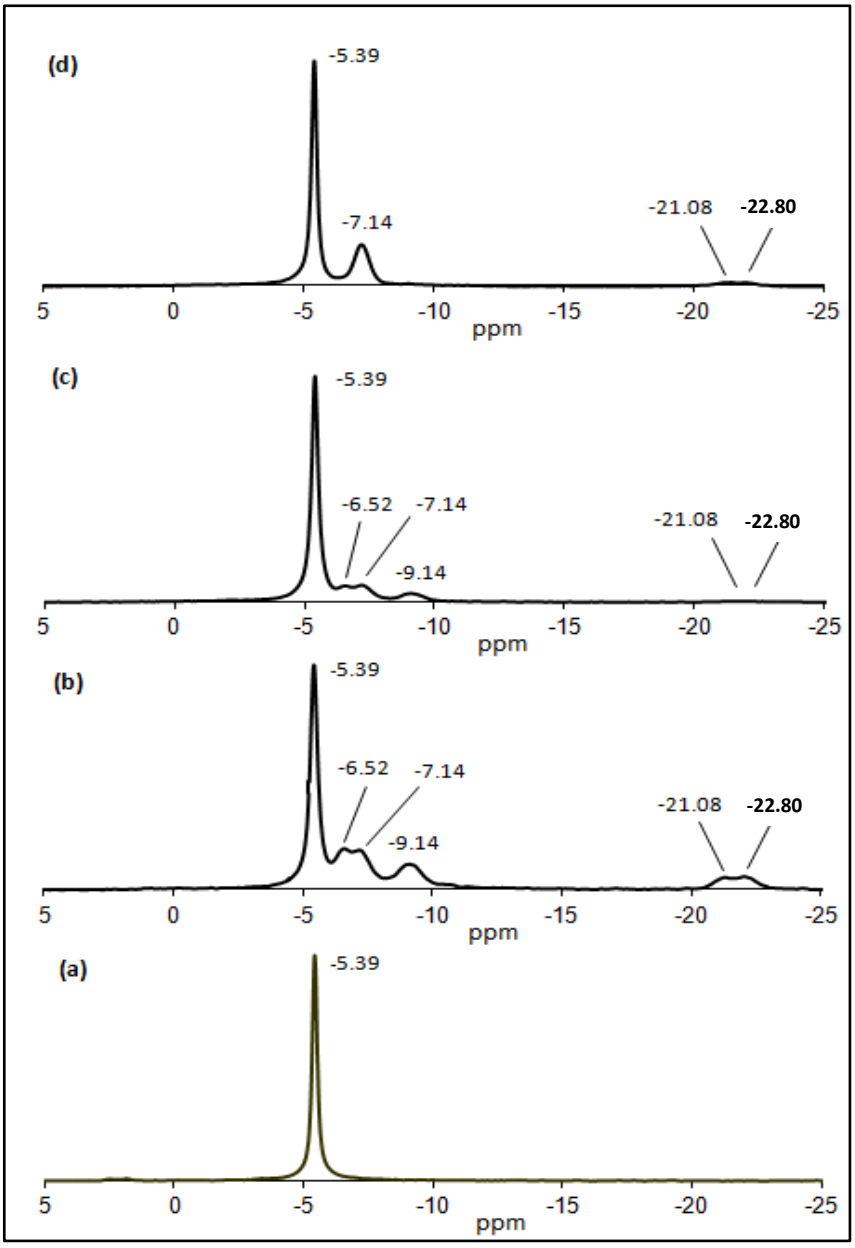

Figure 5.6. ^{31}P MAS NMR spectra of (a) pure CsH_2PO_4 (b) CDP_p (c) CDP_f and (d) $CDP_{f\text{-}RH}$

^{1}H NMR spectra of bulk CsH_2PO_4 is shown figure 5.7-a. Two resonances with chemical shifts at 14.47 and 10.96 ppm are observed. These peaks correspond to the two crystallographically distinct hydrogen atoms of the dihydrogen phosphate group [26-28]. In the case of the ^{1}H NMR spectra of CDP_f (fig. 5.7-b), the same two resonances are observed with a small negative shift of approximately 0.50 ppm placing them at 13.92 and 10.55 ppm. The presence of the two same resonances in the electrospun fibres confirms that the initial bulk CsH_2PO_4 type environment of hydrogen remains in the structure of the electrospun fibres.

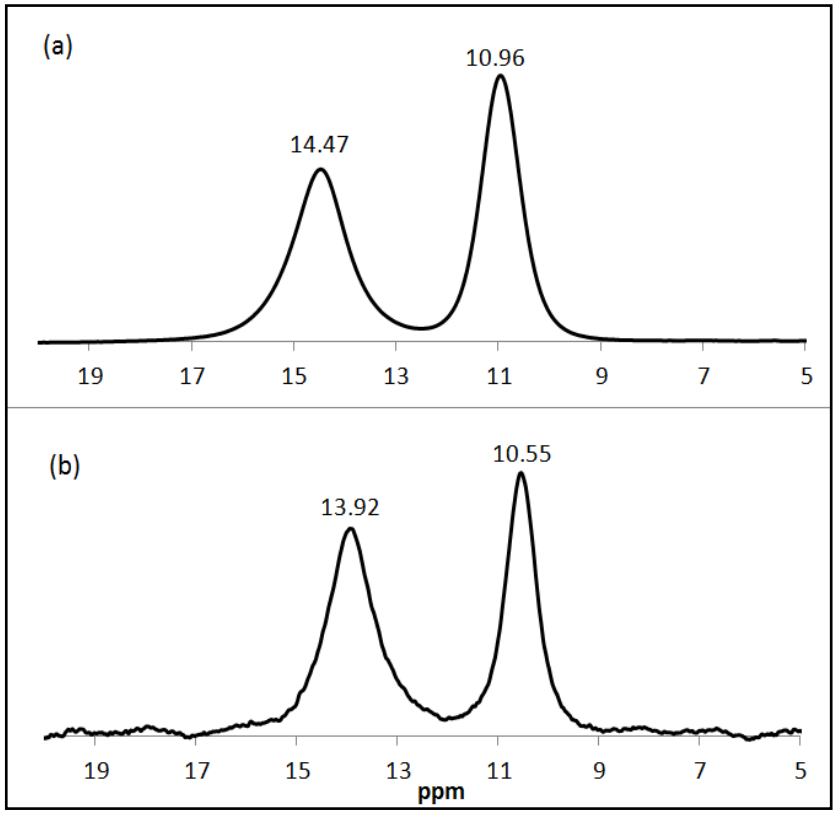

Figure 5.7. ^{1}H MAS NMR spectra of (a) bulk CsH_2PO_4 and (b) CDP_f

5.3.2 Morphology

The morphology of CsH_2PO_4 based membranes was studied by E-SEM. Top, bottom and cross section images of the membranes were obtained, as shown in figure 5.8. The homogeneity of the membranes in terms of CsH_2PO_4 distribution and thickness was studied.

The distribution of CsH_2PO_4 particles in membranes fabricated by the casting of CsH_2PO_4/polymer method is a fundamental issue. In this method PBI was used as

polymeric binder to keep the CsH_2PO_4 particles together and to provide enough mechanical strength to allow fabricating thin membranes (< 50 µm).

Membranes fabricated with CsH_2PO_4 weight percentages higher than 75 % were not mechanically stable and tend to break in the pealing process after casting. The distribution of CsH_2PO_4 particles in the membrane was not homogeneous due to the precipitation of particles on the bottom of the membrane during the casting process. This effect was more noticeable in membrane fabricated using 5 % wt. PBI solution because of its lower viscosity.

This precipitation caused an excess of PBI on the top side of the membrane which creates a non proton conducting polymeric layer. This two-layered membrane structure is not desirable as the top PBI layer would act as an isolating layer when using it as proton conducting electrolyte. E-SEM micrographs of a composite membrane with 75 % wt. of CsH_2PO_4 are shown in figure 5.8.

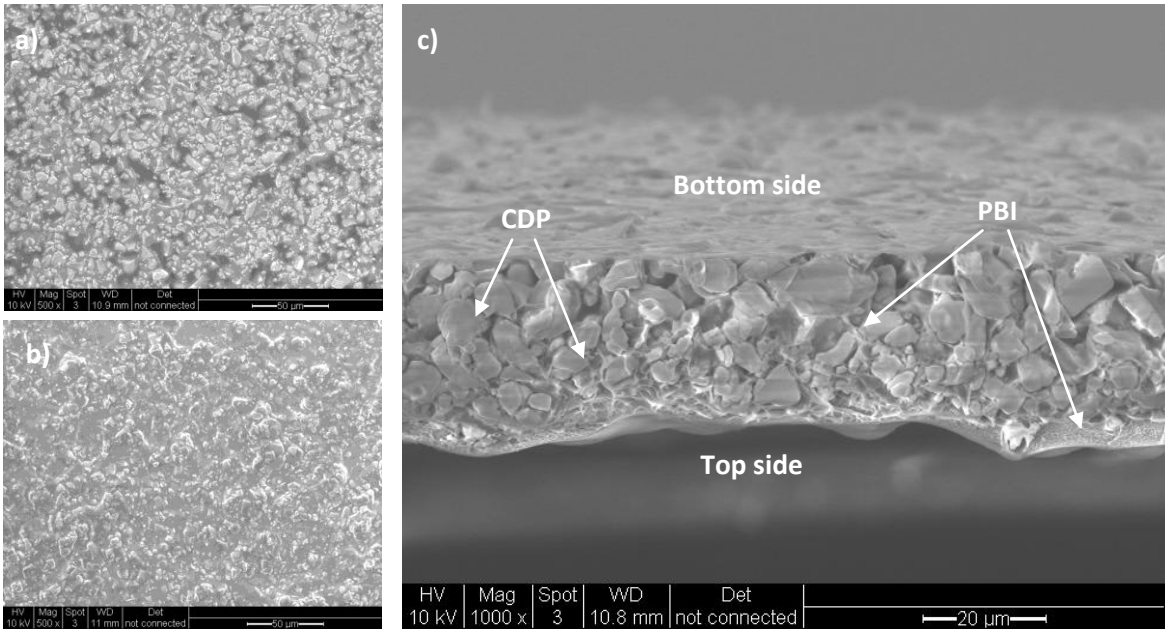

Figure 5.8. E-SEM images of $CDP_{0.75}/PBI_{0.25}$ composite membrane. (a) bottom side (b) top side (c) cross section

Membranes fabricated by glass fibre reinforcing method were characterised in terms of porosity (density) and fibre distribution in the CsH_2PO_4 matrix. 2 ml of saturated solution of CsH_2PO_4 was found to be the optimum amount of solid acid to fill the glass fibre filter (figure 5.9). Lower volumes did not fill completely the filter whereas higher volumes created an excess of CsH_2PO_4 on the top of the membrane which cracked and detached from it.

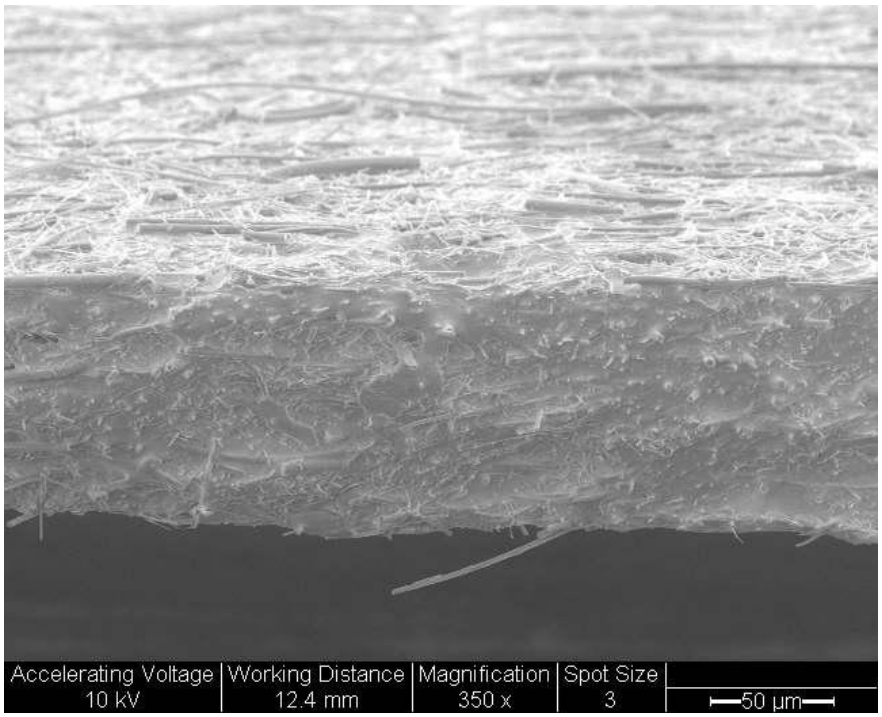

Figure 5.9. E-SEM cross section image of glass fibre reinforced CsH_2PO_4 composite membrane.

The high pressure applied fused the CsH_2PO_4 crystals creating a dense and continuous solid acid phase between both sides of the membrane. This continuous phase is fundamental in order to have proton conducting paths between both electrodes in an electrolysis cell.

Membranes fabricated by electrospinning were characterised by E-SEM in order to study the morphology of the fabricated CsH_2PO_4 fibres, the densification of the fibre mat and the distribution of the polymer added to the mat to occlude the porosity of the resulting membrane. Figure 5.10 shows the E-SEM micrographs of CsH_2PO_4 fibres.

The distribution of fibre diameter of CDP_f, calculated by the analysis of three different regions of the mat surface with a sample size of 300 points, follows a normal distribution having its maximum at 1.25 μm, as shown in figure 5.11. The majority of the fibres are of sizes in the range 0.5 - 2 μm, although some thicker fibres are also visible. These thick fibres are formed by the instabilities occurring in the Taylor cone during the electrospinning process [29] *(see section 3.1.8).*

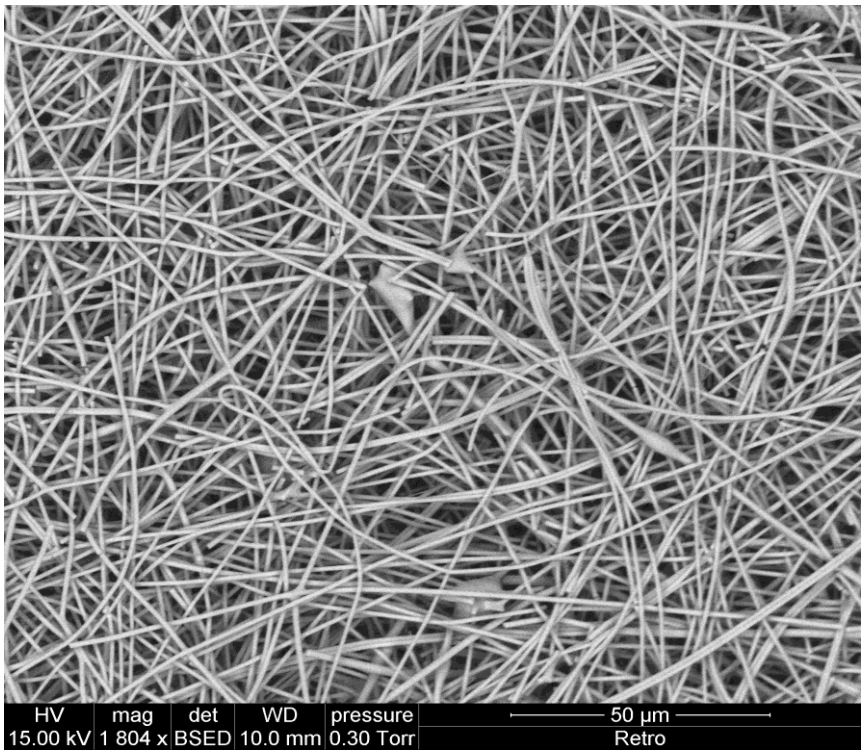

Figure 5.10. E-SEM image of electrospun CsH_2PO_4 fibres.

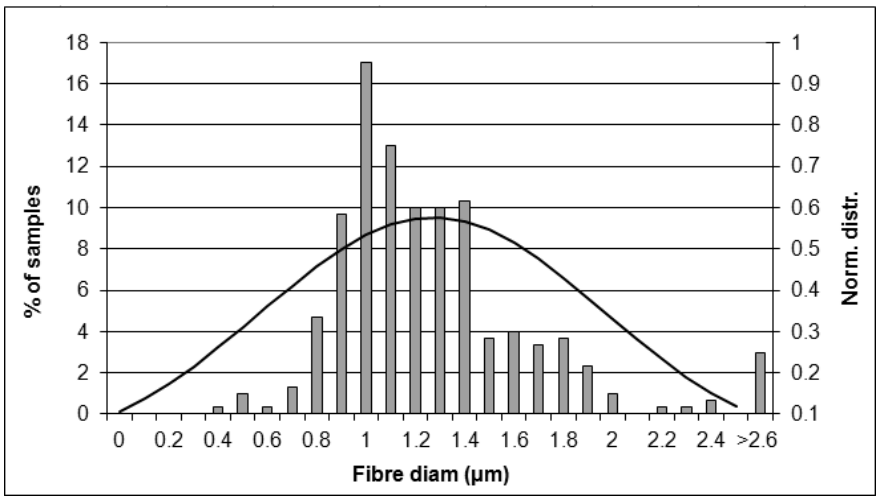

Figure 5.11. Diameter size distribution of CDP_f

CsH_2PO_4 fibres fabricated by electrospinning onto the static target produce a 'cotton-wool-like' mat. This mat was pressed to densify it, and thus to reduce its porosity, using pressures from 0.5 to 4 tonne at room temperature and for 1 min each sample. In figure 5.12 E-SEM micrographs of the fibre mat after densification at 2 and 4 tonne are shown. A pressure of 2 tonne (figure 5.12-a) was chosen as the optimum value as it provided the highest porosity reduction while maintaining integrity of the fibres. At pressures higher than 4 tonne, fibres fused together, becoming a brittle pellet (figure 5.12-b). The thickness

of the fibre mat is easily controlled by the time of electrospinning and densification pressure.

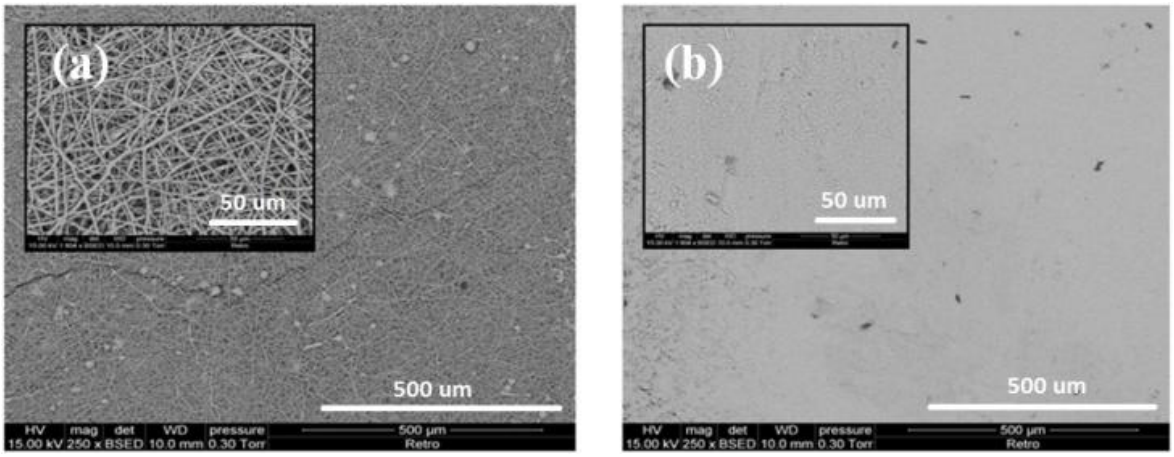

Figure 5.12. E-SEM micrographs (x250 and x1800) of densified CDP_f mats at (a) 2 tonne and (b) 4 tonne

PBI was added to the fiber mat in order to provide the membrane with higher mechanical strength and to occlude the porosity. Unlike in the CsH_2PO_4/polymer casting method, where discrete particles of the solid acid get isolated by a polymer layer, the highly interconnected mat of CsH_2PO_4 fibres fabricated by electrospinning would provide enough percolation degree in the CsH_2PO_4 phase allowing proton conducting paths along the thickness of the membrane.

The addition of polymer creates a similar problem as the CsH_2PO_4/polymer casting method, which is the creation of an isolating PBI layer on top of the membrane due to an excess of PBI solution. Low volumes of PBI solution did not occlude the porosity of the fibre mat and slightly higher volumes provide an excess of polymer. In figure 5.13 the polymeric layer created on the top of the fibre mat is shown. It was not possible for the author to fabricate a non porous membrane without the existence of this layer.

Membranes fabricated by the casting of partially polymerised CsH_2PO_4 were also characterised by E-SEM in order to determine the homogeneity of the thickness and the porosity. In this method, as well as in the electrospinning method, CsH_2PO_4 was subjected to a heat treatment in order to induce a partial polymerisation of the material. Figure 5.14 shows E-SEM micrographs of CsH_2PO_4 and CDP_p.

The as-prepared CsH_2PO_4 (figure 5.14-a) exhibited smooth particles on its surface with an average diameter size of 8 µm. After the polymerisation step (figure 5.14-b) particles fused

together forming agglomerates of diameter >50 µm which appeared to form an extended structure in three dimensions.

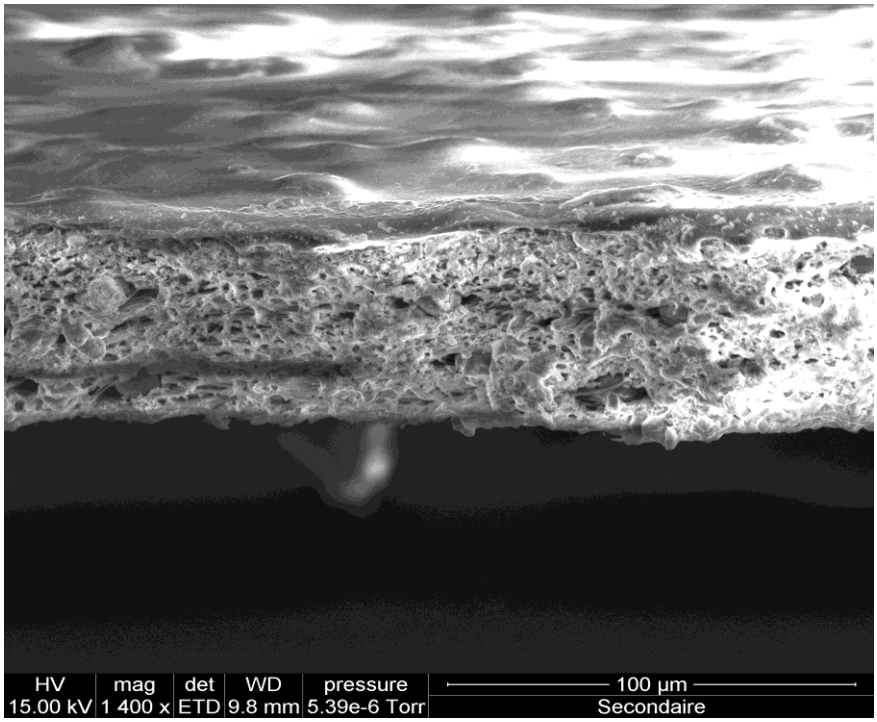

Figure 5.13. E-SEM cross section micrographs of CDP_f mat with PBI polymer.

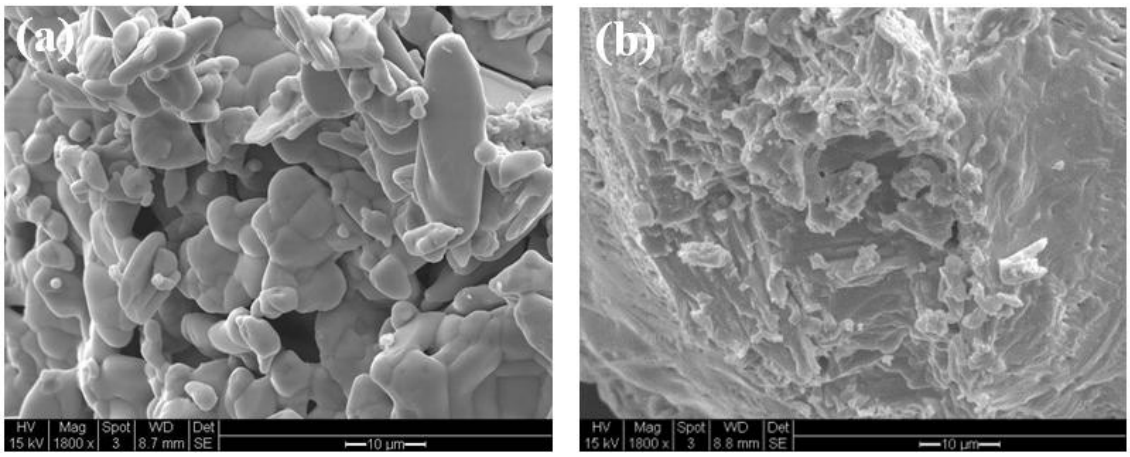

Figure 5.14. E-SEM micrographs of (a) CsH_2PO_4 powder and (b) CDP_p powder.

Casted membranes of partially polymerised CsH_2PO_4 were fabricated with thickness between 25 and 200 µm. The top side of these membranes showed an uneven surface morphology. No porosity or holes caused by bubbles in the casting solution were seen in the E-SEM micrographs of these membranes, as shown in figure 5.15.

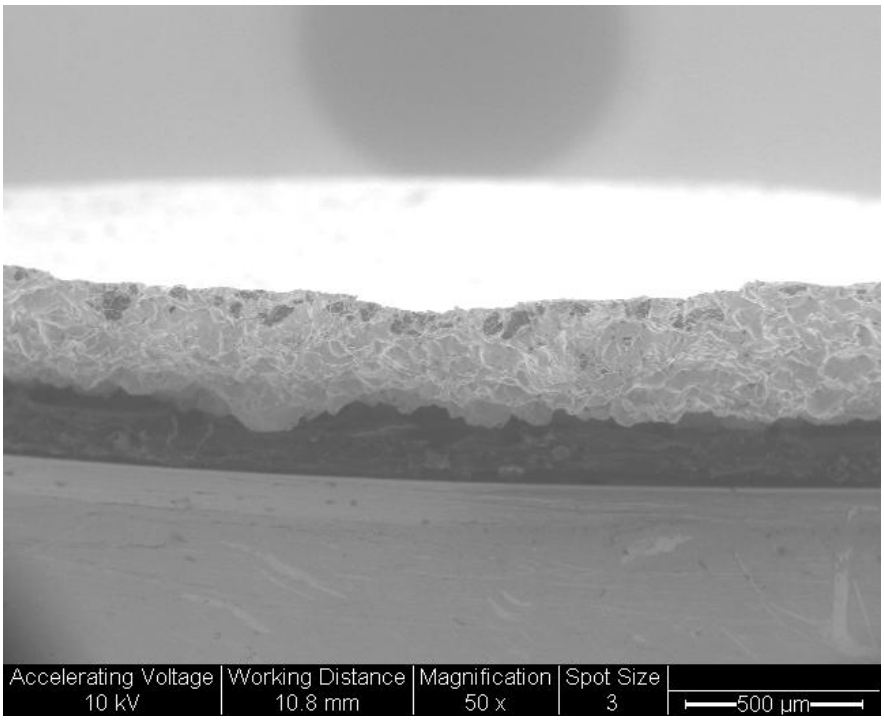

Figure 5.15. E-SEM cross section micrograph of a casted membrane of partially polymerised CsH_2PO_4.

5.3.3 Proton conductivity

Proton conductivity is one of the most important characteristics an electrolyte must fulfil in order to be applied in a PEMWE. The electrolyte must exhibit the maximum proton conductivity and the minimum thickness possible in order to minimise the ohmic losses in the system.

Pure CsH_2PO_4 exhibits proton conductivity over 10^{-2} S cm^{-1} at temperatures higher than 230 °C, but due to its brittle mechanical properties high thickness pellets (> 300 µm) must be fabricated. The maximum proton conductivity any membrane based on CsH_2PO_4 would exhibit would not be over the above mentioned value and therefore the only approach to minimise the resistance of the electrolyte is based in the fabrication of thinner membranes.

The maximum though-plane proton conductivity obtained from each of the composite membranes fabricated by the methods explained in this chapter at 200 – 250 °C temperature range is shown in figure 5.16. Results are compared to the conductivity of a pure CsH_2PO_4 pellet.

The lowest proton conductivity was exhibited by membranes fabricated by CsH_2PO_4-doped PBI membranes. The conductivity of all membranes fabricated by this method was in the range of 10^{-7} S cm^{-1} regardless of the doping conditions. In figure 5.12-c the

conductivity of PBI membrane doped at 300 °C for 2 h in melted CsH_2PO_4 is shown. This low conductivity values proof that the maximum doping level achieved by this method, 0.74 mol CsH_2PO_4 PBI unit^{-1}, is not enough solid acid uptake to provide the membrane with proton conducting paths. In H_3PO_4-doped PBI membranes the doping level is in the range of 5 - 15 mol H_3PO_4 PBI unit^{-1} [30, 31], which is a mixed contribution of phosphoric acid chemically bonded to the PBI basic groups and free phosphoric acid. In order to have a successful CsH_2PO_4-doped PBI membrane considerably higher doping levels should be achieved which in this research was not experimentally possible because of the low acidity of CsH_2PO_4 and thus, low acid/base interaction.

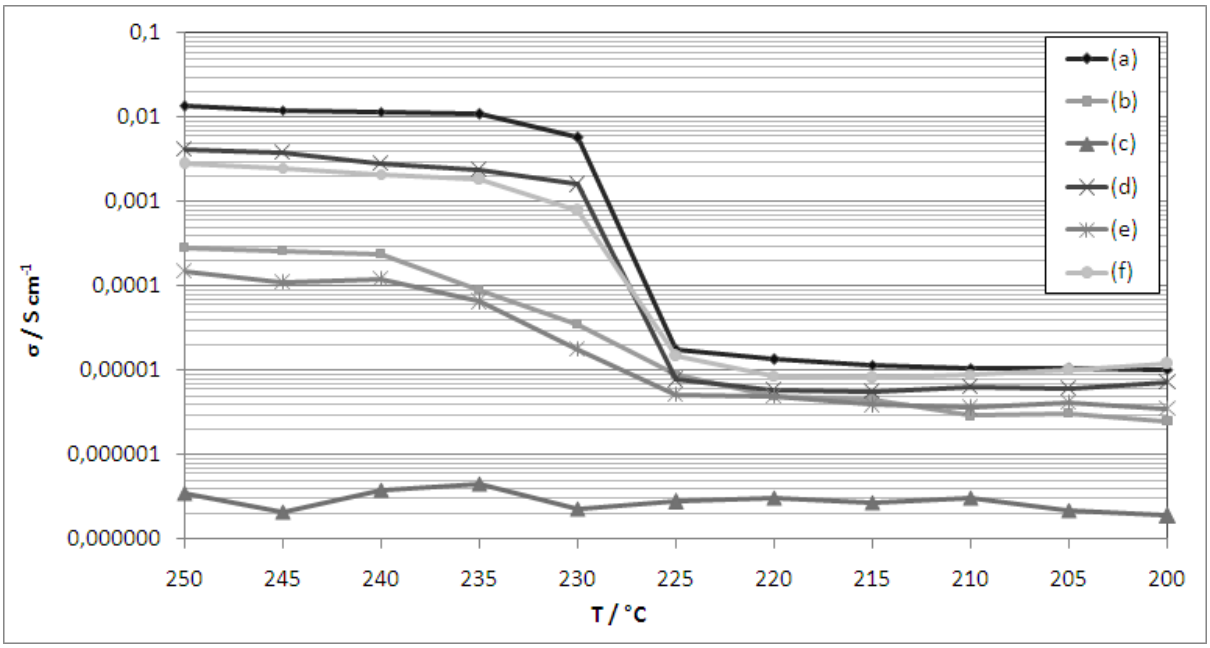

Fig. 5.16. Effect of temperature in the protonic conductivity of (a) CsH_2PO_4 pellet (b) $CDP_{0.75}/PBI_{0.25}$ membrane by casting of PBI/polymer method (c) CsH_2PO_4 doped PBI membrane (doped in melted CsH_2PO_4 for 2 h) (d) glass fibre reinforced membrane (e) electrospun membrane (with polymer) and (f) partially dehydrated CsH_2PO_4 membrane fabricated by casting.

Membranes obtained by casting of CsH_2PO_4/polymer method, where PBI was used as binder to build a thin membrane, exhibited a maximum through-plane proton conductivity of 3×10^{-4} S cm^{-1} at 250 °C. In figure 5.12-b the temperature dependence on the proton conductivity of $CDP_{0.75}/PBI_{0.25}$ composite membrane is shown. Proton conductivity of membranes with lower amount of polymer is not shown as they were not mechanically stable and the pealing process after casting was not possible. The loss in conductivity compared to pure CsH_2PO_4, approximately 2 orders of magnitude, was attributed to the

formation of a PBI layer on top of the membrane and to the isolation of the discrete particles of CsH_2PO_4 by a thin PBI layer. In this fabrication method, where CsH_2PO_4 powder is dispersed into a PBI solution and then casted, PBI acts as a binder as well as an insulator. In order to address the contribution of the PBI layer formed on top of the membrane by an excess of polymer solution to the overall resistance of the membrane, in-plane and through-plane conductivity measurements were carried out. Results of both measurements for a $CDP_{0.75}/PBI_{0.25}$ composite membrane are shown in figure 5.17.

In plane measurements were carried out in the bottom side of the composite membrane, where no PBI layer was formed. Figure 5.17 shows the contribution of the PBI layer formed on the top of the membrane to the overall resistance lowering the conductivity by almost 1 order of magnitude from in-plane to through-plane. Although this polymeric layer increases the resistance of the membrane the in-plane conductivity (ca. 10^{-3} S cm^{-1}) is still 1 order of magnitude lower than pure CsH_2PO_4. This loss in conductivity is attributed to the formation of a thin PBI layer between the particles of the solid acid. This polymeric layer in the grain boundary of CsH_2PO_4 increased the resistance for proton conduction from particle to particle; no continuous CsH_2PO_4 phase is achieved by this method.

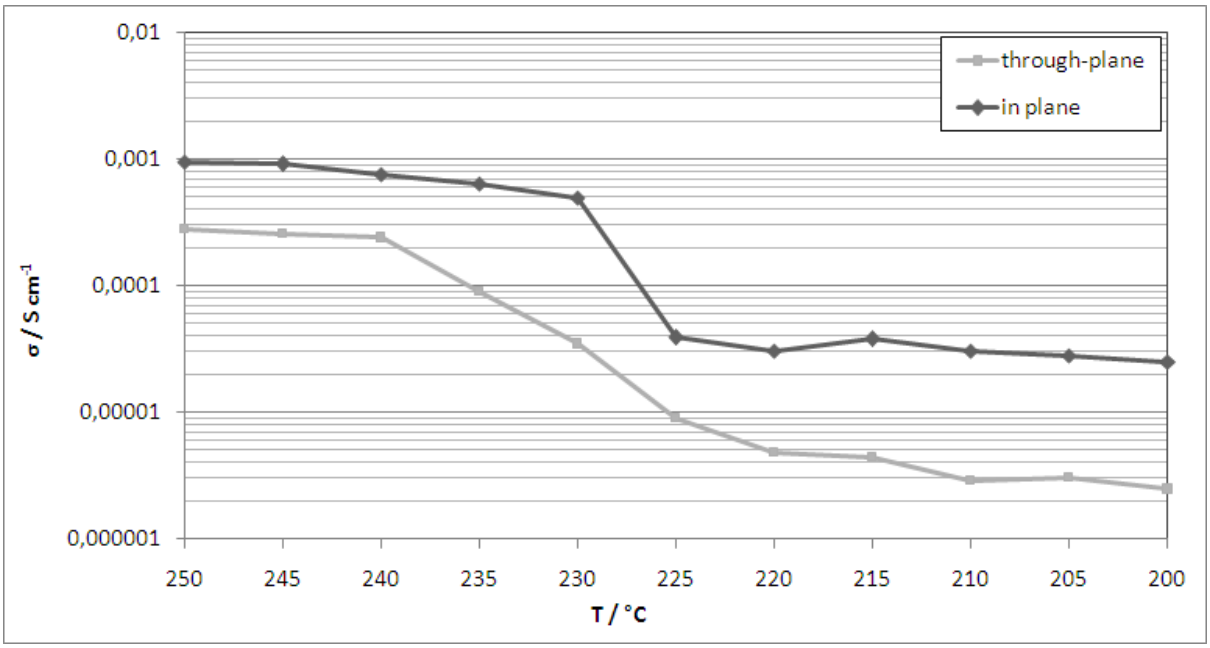

Fig. 5.17. Effect of temperature in the in-plane and through-plane protonic conductivity of $CDP_{0.75}/PBI_{0.25}$ composite membrane.

In order to avoid the isolation effect of discrete CsH_2PO_4 particles by PBI, another membrane fabrication method by the electrospinning of CsH_2PO_4 is proposed. A highly

interconnected fibre mat of CsH_2PO_4 was fabricated as the backbone of the membrane and then the porosity of the mat occluded by the addition of PBI. The interconnected fibre backbone would provide enough proton conducting paths with good percolation degree within the composite membrane structure.

The conductivity of CsH_2PO_4 fibres compressed in pellet form was measured in order to address the loss in conductivity caused by the partial dehydration of CsH_2PO_4. The fibres (CDP_f) exhibited a maximum proton conductivity of 8×10^{-3} S cm^{-1} at 250 °C. However, once PBI was added to the fibre mat the conductivity of the membrane decreased to 1.5×10^{-4} S cm^{-1}. Values are shown in figure 5.18. This loss in conductivity is once again attributed to the formation of an isolating PBI layer on top of the composite membrane (figure 5.13).

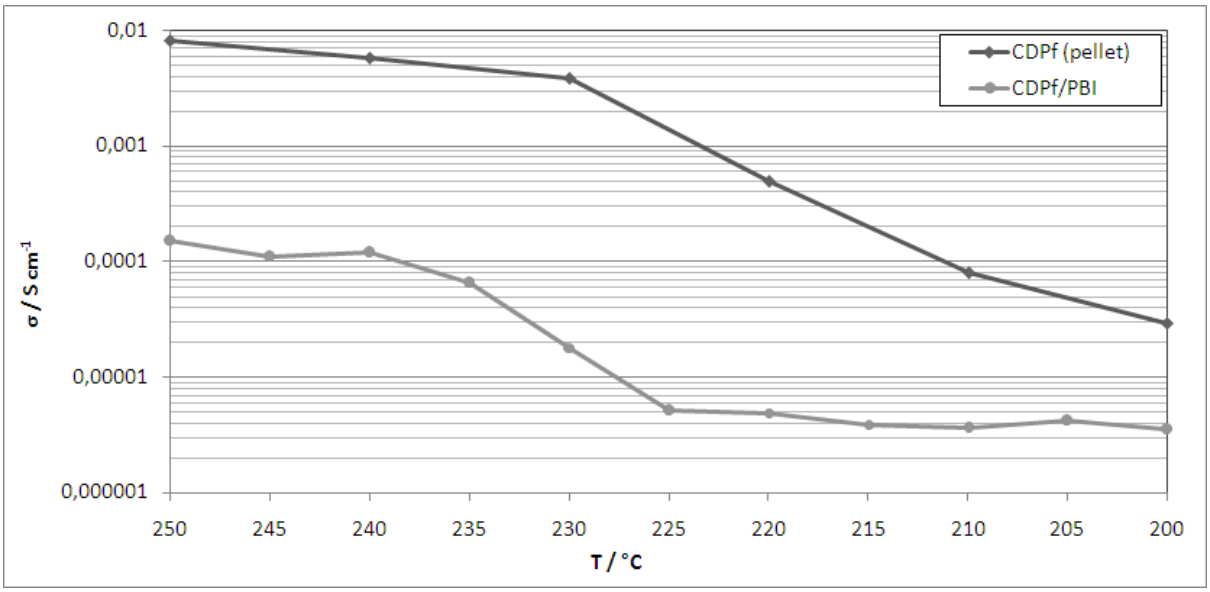

Fig. 5.18. Effect of temperature in the through-plane protonic conductivity of a pellet of CsH_2PO_4 fibres (CDP_f) and electrospun fibre mat of CsH_2PO_4 with PBI (CDP_f/PBI).

The solution of partially polymerised CsH_2PO_4 was also directly casted into membranes without any additive. The maximum proton conductivity exhibited by this type of membranes was 3×10^{-3} S cm^{-1}. The conductivity of the cast membrane was compared to those of the partially polymerised powder in pellet form (figure 5.19). Although both materials exhibit similar proton conductivity at 250 °C the profile of each of them varies considerably at the range of temperatures measured. The difference in the proton conduction is attributed to the rehydration of partially polymerised CsH_2PO_4. The profile shape of the cast CDP_p membrane is very similar to that of the initial non-dehydrated

material, with a notorious increase in the proton conductivity at 230 °C. This was attributed to a partial rehydration of CsH_2PO_4 when the casting solution (in H_2O) was prepared. When the proton conductivity of the material is measured just after the dehydration process, a different profile with a more gradual increase was seen. This slightly higher conductivity at lower temperatures could be attributed to a higher adsorption of water which helped the proton conduction in the material.

Although the proton conductivity of membranes fabricated by this method was almost one order of magnitude lower than that of pure CsH_2PO_4, it is worth mentioning that this methodology allowed fabricating very thin membranes which would help to lower the ohmic resistance of the system. In order to equal the resistance provided by a 300 µm CsH_2PO_4 pellet, 2.0 Ω cm^{-2}, membranes fabricated by this method should not have thicknesses higher than 60 µm.

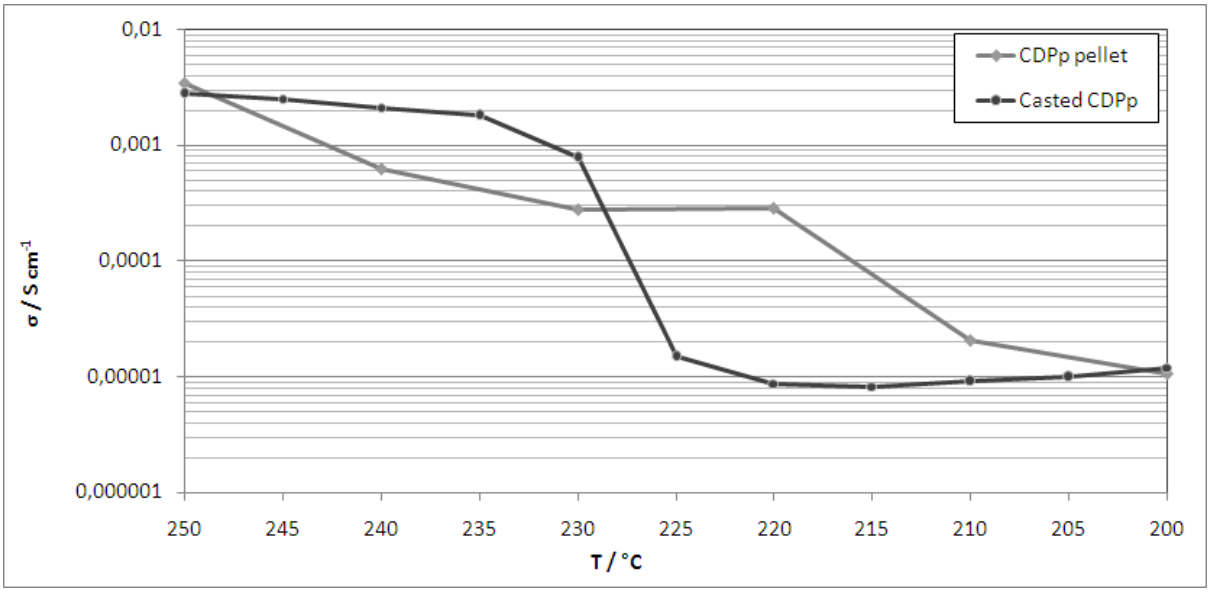

Fig. 5.19. Effect of temperature in the through-plane protonic conductivity of a pellet of partially polymerised CsH_2PO_4 (CDP_p pellet) and membrane fabricated by casting of partially polymerised CsH_2PO_4 (casted CDP_p).

The highest proton conductivity was achieved by glass fibre reinforced membranes. The addition of an interconnected mat of glass fibres provides the composite membrane with less brittle characteristics and therefore thinner membranes (100 – 200 µm) could be fabricated. The maximum proton conductivity exhibited by these membranes is 4×10^{-3} S cm^{-1} at 250 °C as shown in figure 5.16, although values as high as 8×10^{-3} S cm^{-1} at 275 °C were recorded. This high conductivity and the possibility of reducing the thickness of

the pellet make this a potentially useful membrane fabrication method. Nonetheless, membrane thicknesses lower than 80 μm are required in order to fabricate an electrolyte with resistance lower than 1 Ω cm^{-2}.

5.3.4 Tensile strength

In order to assess the mechanical properties of the composite membranes fabricated, their tensile strength was measured. The effect of polymer and glass-fibre addition to the inorganic salt and the partial polymerisation effect on the mechanical properties of the membrane were studied in terms of tensile strength. All composite membranes were compared to a pure PBI casted membrane. Tensile data about pure CsH_2PO_4 pellet was not possible to be obtained due to the high brittleness of the sample. The tensile stress vs. strain curves of the fabricated membranes are shown in figure 5.16 and the Young modulus and maximum stress summarised in table 5.6.

In figure 5.16-I, the tensile strength properties of a pure non-doped PBI membrane is compared to the fabricated CsH_2PO_4-based membranes. The mechanical strength towards tensile stress is significantly higher in the pure PBI membrane, exhibiting a maximum stress of 4460 N cm^{-2} and a Young modulus of 0.93 GPa. These results are in good agreement to those reported for pristine PBI membranes, being in the maximum stress in the range of 7.5 – 15 × 10^3 N cm^{-2} and Young modulus of 1 – 1.5 GPa [14, 30].

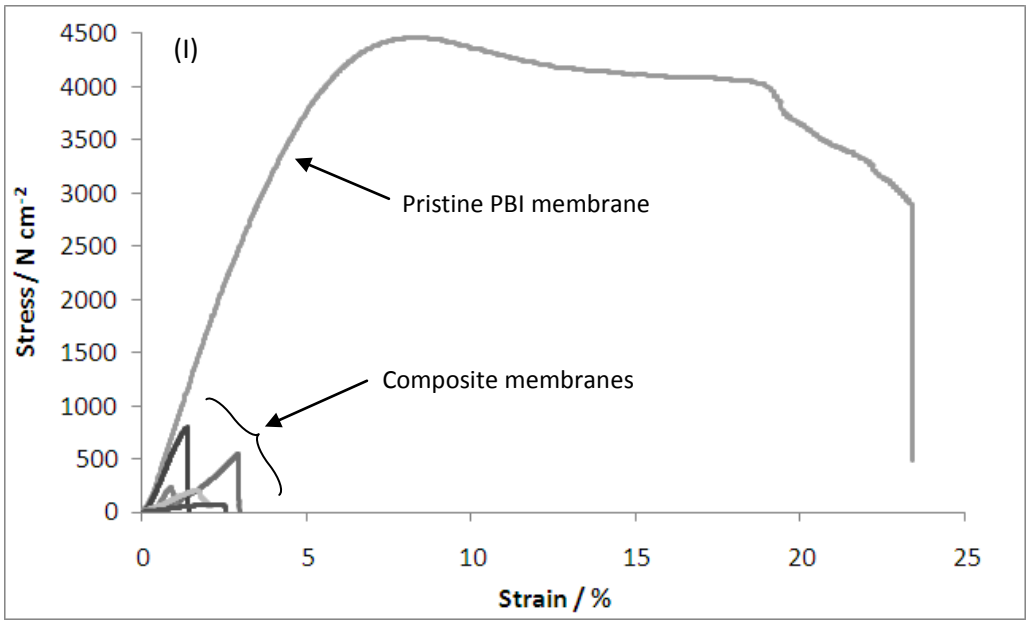

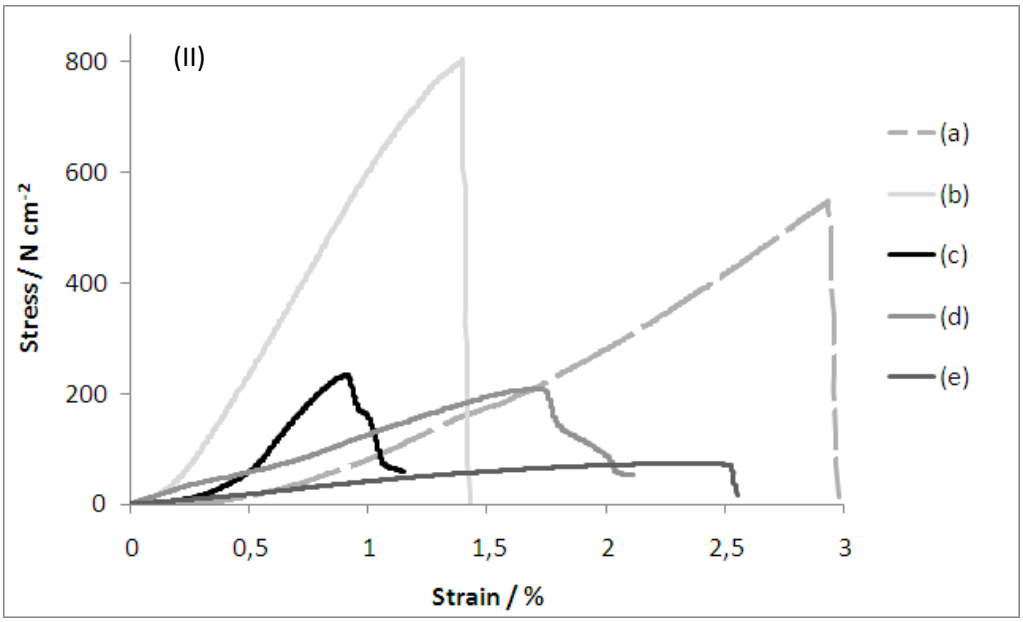

Fig. 5.20. (I) Tensile stress vs. strain comparison between a casted pure PBI membrane and the fabricated composite membranes. (II) Tensile stress vs. strain comparison between (a) $CDP_{0.75}/PBI_{0.25}$ and (b) $CDP_{0.66}/PBI_{0.33}$ membranes by casting of PBI/polymer method (c) electrospun membrane with PBI (d) glass fibre reinforced membrane (e) partially dehydrated CsH_2PO_4 membrane fabricated by casting.

Table 5.6. Mechanical properties of CsH_2PO_4-based composite membranes**.**

Membrane	**Mechanical parameters**	
	Young modulus / GPa	**UTS / N cm^{-2}**
Casting of pure PBI	0.93	4460
Casting of $CDP_{0.66}$ / $PBI_{0.33}$	0.73	804
Casting of $CDP_{0.75}$ / $PBI_{0.25}$	0.18	547
Electrospun / PBI	0.24	227
Glass-fibre reinforced	0.14	209
Partially dehydrated	0.13	74

The maximum tensile stress supported by the rest of the composite membranes was significantly lower to that exhibited by pristine PBI. CsH_2PO_4/PBI cast membrane with 33% wt. of polymer exhibited the highest maximum stress (804 N cm^{-2}) and Young modulus (0.73 GPa) of all composite membranes. Then CsH_2PO_4/PBI cast membrane with 25% PBI and the electrospun membrane with PBI showed considerably lower values

because a lower amount of polymer in the membrane. Lastly, glass-fibre reinforced membrane and cast of partially dehydrated CsH_2PO_4 membrane exhibited similar values of Young modulus, ca. 0.14 GPa, and maximum stress of 209 and 74 N cm^{-2}, respectively.

The mechanical properties towards tensile strength of the composite membranes exhibited relatively low values, comparing to those of pristine PBI. Nevertheless, it has to be stressed that the membranes fabricated by the proposed methods exhibited more ductile properties than the pure CsH_2PO_4 pellet. The decrease in the brittleness of the membranes, comparing to that of pure CsH_2PO_4, makes the composite membranes easily handled and assembled into a electrochemical cell.

5.4 Conclusions

The difficulty of fabricating a thin membrane of CsH_2PO_4 is an important issue in order to apply this material as a proton conducting electrolyte in electrochemical systems. In this chapter, five different methods were proposed for the fabrication of CsH_2PO_4-based composite membranes; (1) casting of CsH_2PO_4/polymer membrane, (2) CsH_2PO_4-doped polymeric membrane, (3) glass-fibre reinforced membranes, (4) electrospinning of CsH_2PO_4 fibre mat and (5) the casting of partially polymerised CsH_2PO_4.

Physico-chemical characterisation of membranes was carried out and the morphology and homogeneity of the different membranes reported. Minimum thickness membranes were obtained by the casting of CsH_2PO_4/PBI membranes, as thin as 25 μm. P-XRD and ss-NMR results revealed that the heat treated CsH_2PO_4, used in methods relying on its partial polymerisation, methods (4) and (5), various phases coexist, being the initial proton conducting phase still present in the structure of the material. The partially polymerised CsH_2PO_4 exhibited a maximum conductivity of 3×10^{-3} S cm^{-1} at 250 °C.

Membranes fabricated by the glass-fibre reinforced method exhibited the highest proton conductivity, 8×10^{-3} S cm^{-1} at 275 °C. All methods using polymer as a binder, doped membrane or to occlude porosity, methods (1), (2) and (4), show low proton conductivity, $< 3 \times 10^{-4}$ S cm^{-1}, caused by the isolating properties of the polymer and low acid uptake. Membranes fabricated by the casting of partially polymerised CsH_2PO_4 exhibited a maximum conductivity value of 2×10^{-3} S cm^{-1} at 250 °C.

The mechanical properties of the composite membranes in terms of tensile stress were significantly lower than those obtained for pure PBI polymeric membrane. Nevertheless, although the mechanical properties of the pure CsH_2PO_4 pellet could not be measured because of its high brittleness, the fabricated composite membranes exhibited more ductile properties which made them easy to handle and to assemble in the electrochemical cell.

In conclusion, glass-fibre reinforcing was considered as the most promising method for CsH_2PO_4–based membrane fabrication, because of mainly its high proton conductivity and mechanical stability.

5.5 References

1. Grigoriev, S., V. Porembsky, and V. Fateev, *Pure hydrogen production by PEM electrolysis for hydrogen energy.* International Journal of Hydrogen Energy, 2006. **31**(2): p. 171-175.
2. Saxe, M. and P. Alvfors, *Advantages of integration with industry for electrolytic hydrogen production.* Energy, 2007. **32**(1): p. 42-50.
3. Haile, S. M., Chisholm, C. R., Sasaki, K., Boysen, D. A., & Uda, T., *Solid acid proton conductors: from laboratory curiosities to fuel cell electrolytes.* Faraday discussions, 2007. **134**: p. 17-39.
4. Uda, T. and S.M. Haile, *Thin-membrane solid-acid fuel cell.* Electrochemical and Solid-State Letters, 2005. **8**(5): p. A245-A246.
5. Li, Z. and W.E. Chan, *Phase transition of RbH_2PO_4 and its composite with SiO_2 studied by thermal analysis.* Journal of thermal analysis and calorimetry, 2011. **104**(2): p. 585-592.
6. Otomo, J., Ishigooka, T., Kitano, T., Takahashi, H., & Nagamoto, H., *Phase transition and proton transport characteristics in CsH_2PO_4/SiO_2 composites.* Electrochimica Acta, 2008. **53**(28): p. 8186-8195.
7. Ponomareva, V., E. Shutova, and G. Lavrova, *Electrical conductivity and thermal stability of $(1- x)\ CsH_2PO_4/xSiP_yO_z$ $(x= 0.2–0.7)$ composites.* Inorganic Materials, 2008. **44**(9): p. 1009-1014.
8. Bocchetta, P., R. Ferraro, and F. Di Quarto, *Advances in anodic alumina membranes thin film fuel cell: CsH_2PO_4 pore-filler as proton conductor at room temperature.* Journal of Power Sources, 2009. **187**(1): p. 49-56.
9. Boysen, D. A., Chisholm, C. R., Haile, S. M., & Narayanan, S. R., *Polymer solid acid composite membranes for fuel-cell applications.* Journal of the Electrochemical Society, 2000. **147**(10): p. 3610-3613.
10. Ma, Y. L., Wainright, J. S., Litt, M. H., & Savinell, R. F., *Conductivity of PBI membranes for high-temperature polymer electrolyte fuel cells.* Journal of the Electrochemical Society, 2004. **151**(1): p. A8-A16.
11. Mamlouk, M. and K. Scott, *Phosphoric acid-doped electrodes for a PBI polymer membrane fuel cell.* International Journal of Energy Research, 2011. **35**(6): p. 507-519.
12. Pefkianakis, E. K., Deimede, V., Daletou, M. K., Gourdoupi, N., & Kallitsis, J. K., *Novel Polymer Electrolyte Membrane, Based on Pyridine Containing Poly(ether sulfone), for Application in High-Temperature Fuel Cells.* Macromolecular Rapid Communications, 2005. **26**(21): p. 1724-1728.
13. Gourdoupi, N., Geormezi, M., Kallitsis, J. K., Stolten, D., & Grube, T., *High Temperature PEM FCs Based on Advent TPS® Technology.* Report Nr.: Schriften des Forschungszentrums Jülich/Energy & Environment, 2010.
14. He, R., Li, Q., Bach, A., Jensen, J. O., & Bjerrum, N. J., *Physicochemical properties of phosphoric acid doped polybenzimidazole membranes for fuel cells.* Journal of Membrane Science, 2006. **277**(1): p. 38-45.
15. Rikukawa, M. and K. Sanui, *Proton-conducting polymer electrolyte membranes based on hydrocarbon polymers.* Progress in Polymer Science, 2000. **25**(10): p. 1463-1502.
16. Cavaliere, S., Subianto, S., Savych, I., Jones, D. J., & Rozière, J., *Electrospinning: designed architectures for energy conversion and storage devices.* Energy & Environmental Science, 2011. **4**(12): p. 4761-4785.

17. Huang, Z. M., Zhang, Y. Z., Kotaki, M., & Ramakrishna, S., *A review on polymer nanofibers by electrospinning and their applications in nanocomposites.* Composites Science and Technology, 2003. **63**(15): p. 2223-2253.

18. Fieser, L.F. and M. Fieser, *Reagents for organic synthesis*. Vol. 2. 1967: John Wiley & Sons.

19. Nelmes, R.J., Choudhary, R.N.P., *Structural studies of the monoclinic dihydrogen phosphates: II. A neutron-diffraction study of TlH_2PO_4.* Solid State Commun., 1978. **26**: p. 823.

20. Ortiz, E., R.A. Vargas, and B.E. Mellander, *On the high-temperature phase transitions of some KDP-family compounds: a structural phase transition? A transition to a bulk-high proton conducting phase?* Solid State Ionics, 1999. **125**(4): p. 177-185.

21. Taninouchi, Y. K., Uda, T., Awakura, Y., Ikeda, A., & Haile, S. M., *Dehydration behavior of the superprotonic conductor CsH_2PO_4 at moderate temperatures: 230 to 260 ºC.* Journal of Materials Chemistry, 2007. **17**(30): p. 3182-3189.

22. Taninouchi, Y., Hatada, N., Uda, T. and Awakura, Y., *Phase Relationship of CsH_2PO_4–$CsPO_3$ System and Electrical Properties of $CsPO_3$.* Journal of The Electrochemical Society, 2009. **156**(5): p. B572-B579.

23. Bronowska, V., *Structural phase transitions and chemical transformations of CsH_2PO_4 crystals.* International Centre for Diffraction Data, JCPDS, 1997.

24. Lee, K.-S., *Hidden nature of the high-temperature phase transitions in crystals of KH_2PO_4-type : Is it a physical change ?* Journal of Physics and Chemistry of Solids, 1996. **57**(3): p. 333-342.

25. Chung, F.H., *Quantitative interpretation of X-ray diffraction patterns of mixtures. II. Adiabatic principle of X-ray diffraction analysis of mixtures.* J. Appl. Cryst. , 1974. **7**: p. 526-531.

26. Traer, J. W., Soo, K. J., Vijayakumar, M., & Goward, G. R., *Elucidating the Time Scale and Geometry of Phosphate and Phosphonate Rotation in Solid Acid Electrolytes Using Multinuclear NMR.* The Journal of Physical Chemistry C. **115**(13): p. 6064-6072.

27. Haile, S.M., H. Liu, and R.A. Secco, *High-Temperature Behavior of CsH_2PO_4 under Both Ambient and High Pressure Conditions.* Chemistry of Materials, 2003. **15**(3): p. 727-736.

28. Yamada, K., Sagara, Y., Yamane, Y., Ohki, H., Okuda, T., *Superprotonic conductor CsH_2PO_4 studied by ^{1}H, ^{31}P NMR and X-ray diffraction.* Solid State Ionics, 2004. **175**: p. 557-562.

29. Reneker, D. H., Yarin, A. L., Zussman, E., & Xu, H., *Electrospinning of Nanofibers from Polymer Solutions and Melts.* Advances in applied mechanics, 2007. **41**: p. 43.

30. Qingfeng, L., H.A. Hjuler, and N.J. Bjerrum, *Phosphoric acid doped polybenzimidazole membranes: Physiochemical characterization and fuel cell applications.* Journal of Applied Electrochemistry, 2001. **31**(7): p. 773-779.

31. Shen, C. H., Jheng, L. C., Hsu, S. L. C., & Wang, J. T. W., *Phosphoric acid-doped cross-linked porous polybenzimidazole membranes for proton exchange membrane fuel cells.* Journal of Materials Chemistry, 2011. **21**(39): p. 15660-15665.

CHAPTER 6

THE EFFECT OF THE ELECTROLYTE ON THE CATALYTIC ELECTROCHEMICAL ACTIVE SURFACE (EAS) AND OXYGEN EVOLUTION REACTION (OER)

In this chapter the effect of the electrolytic media on the electrochemical active surface (EAS) of IrO_2 and Pt black was studied. The activity of IrO_2 as oxygen evolution reaction catalyst in CsH_2PO_4 saturated solution was also addressed and compared to its performance in H_3PO_4 and H_2SO_4 solutions. IrO_2 showed poor activity towards OER in CsH_2PO_4 solution which was mainly attributed to the low acidity of the electrolyte (pH = 4.63) and to anion adsorption in the catalyst caused by the high phosphate concentration.

6.1 Introduction

The nature of the electrolyte plays an important and significant role in the activity of a catalyst towards any electrochemical reaction [1-4]. The presence of different ionic species, pH or viscosity for instance, would affect the performance of a catalyst in terms of catalyst deactivation, reaction mechanism or diffusion of reactants and products. All these parameters will have a great impact on the overall performance of any electrocatalyst for a given reaction.

In the case of PEM water electrolysers, although both hydrogen and oxygen evolution reactions take place at the same time, it is the latter (OER) that attracts more interest as it is the slowest, limiting reaction of the system. RuO_2 is proved to be the most active catalyst for OER in acidic media although its poor stability leads IrO_2 as the state-of-the-art catalyst for this reaction in these electrochemical devices. Nevertheless, a significant effort is being made by the research community in order to develop new catalyst with improved activity and stability as well as reduced cost [5-10].

In this research the effect of the electrolyte on the OER rate of IrO_2 was studied for H_3PO_4, H_2SO_4 and CsH_2PO_4 solutions. In addition, the impact of these electrolytes on the electrochemical active surface (EAS) of IrO_2 and Pt was reported.

6.2 Experimental

Pt black (Alfa-Aesar) and IrO_2 (Sigma-Aldrich) catalyst were purchased from commercial sources. These are the same catalyst used for the electrolysis studies carried out in chapter 7. Both Pt and IrO_2 catalyst inks were prepared by dispersing 50 mg of catalyst in 1ml N-Methyl-2-pyrrolidone (NMP). 20 % wt. polyvinylidene fluoride (PVDF) was added as a binder in order to help the catalyst stick to the electrode and avoid catalyst detachment during experiments.

Samples for ESA calculation were prepared by micro-pipetting 3 µl ink dispersion onto a glassy carbon electrode (BASi) with 0.07 cm^2 area. Samples for OER studies were prepared by micro-pipetting 4 µl ink dispersion onto a gold electrode with 0.154 cm^2 area. Catalyst loadings were 2.14 and 1.30 mg cm^{-2}, respectively. All inks were sonicated for 30 min before depositing onto the electrode. Electrodes were placed in the oven at 80 °C overnight to dry the samples.

Saturated solution of CsH_2PO_4 at 40 °C (5.15 M) was prepared by dissolving 120 g CsH_2PO_4 *(see Chapter 4.2 for synthesis method)* in 100 ml DI water. Same concentration (5.15 M) solutions of H_3PO_4 (Sigma-Aldrich, >85 % wt.) and H_2SO_4 (Sigma-Aldrich, 95-98 %) were prepared by mixing the required amounts of acids with DI water.

The experiments were carried out in a standard jacketed half-cell configuration (figure 3.8) at temperatures between 40 and 80 °C, controlled by a water bath. N_2 gas was bubbled in the solution in all experiments in order to maintain the solution deoxygenated.

6.3 Electrochemical Active Surface (EAS)

The amount of catalyst active in an electrochemical reaction is dependent on the accessibility of the active sites of that catalyst to the reactants and the ability of it to release the products. In the case of a PEM water electrolyser, hydrogen evolution reaction (HER) in the cathode and oxygen evolution reaction (OER) in the anode (equations 1.4 – 1.5) will take place. This means that for both electrodes protonic and electric conducting paths must exist for the reaction to happen as well as physical paths to allow the access and release of gases. The sites of the electrode where all these conditions meet is the so-called *triple phase boundary* [11, 12]. The amount of catalyst in this boundary will lead to the calculation of the electrochemical active surface (EAS).

6.3.1 Pt black and IrO_2 ESA determination by P-XRD

The EAS of a catalyst can be estimated from the average crystallite size calculation using the Scherrer equation (equation 3.1) using the data obtained from the P-XRD spectra. Assuming spherical crystallites and knowing the density value of the material, a ratio of area per mass unit can be calculated. In figure 6.1 the P-XRD spectra of commercially available Pt black and IrO_2 are plotted.

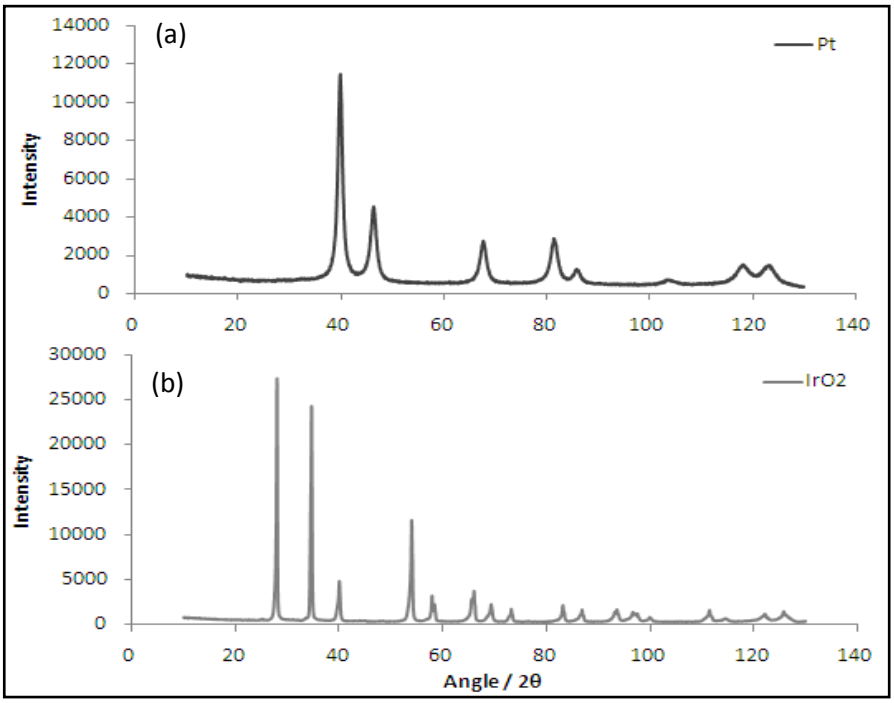

Figure 6.1. P-XRD spectra of (a) Pt black and (b) IrO_2 at 25 ºC and 1 bar.

The three most characteristic diffraction peaks of both materials (39.7°, 46.0° and 67.4° 2θ for Pt and 28.0°, 34.7° and 54.0° 2θ for IrO_2) were used in the crystallite size calculation by Scherrer equation (equation 3.1). The value of EAS_{XRD} is an estimation assuming that all the area of the catalyst is active and available for the reaction. Although in a real electrochemical system these conditions are not fulfilled, it provides an estimation of the catalyst % utilisation.

Table 6.1. Pt black and IrO_2 crystallographic properties.

Catalyst	**ρ / g cm^{-3}**	**Crystallite size / nm**	**EAS_{XRD} / m^2 g^{-1}**
Pt black	21.4	6.9	40.5
IrO_2	11.6	31.6	16.3

6.3.2 Pt black ESA determination by cyclic voltammetry

A real estimation of the EAS of an electrode can be determined by the calculation of the charge obtained by cyclic voltammetry (CV) in a half cell *(see section 3.2.2)* [13]. Pt black and IrO_2 were characterised by this technique in concentrated solutions (5.15 M) of H_3PO_4, H_2SO_4 and CsH_2PO_4 in order to study the effect of the electrolyte on the EAS of the catalysts. Experiments at a range of temperatures (40 – 80 °C) and scan rates (20 – 200 mV s^{-1}) were carried out to investigate the impact of these variables. For every sample 10 cycles were performed, which was enough to obtain stable and reproducible results.

Figure 6.2 depicts a standard CV of platinum black in 5.15 M H_3PO_4 using 20 mV s^{-1} sweep rate. In this voltammogram four main regions can be differentiated, all of them corresponding to different electrochemical processes happening at a given potential [14]; H_2 desorption (a) and adsorption (b) onto the platinum surface and Pt oxidation (c) and reduction (d). At potentials lower than 0 V (vs. SHE) H_2 evolution starts (I) while O_2 evolution starts at potential higher than 1.23 V (II). At the linear region between 0.4 – 0.8 V no electrochemical process take place, this is where only the charging of the double layer of the electrode occurs.

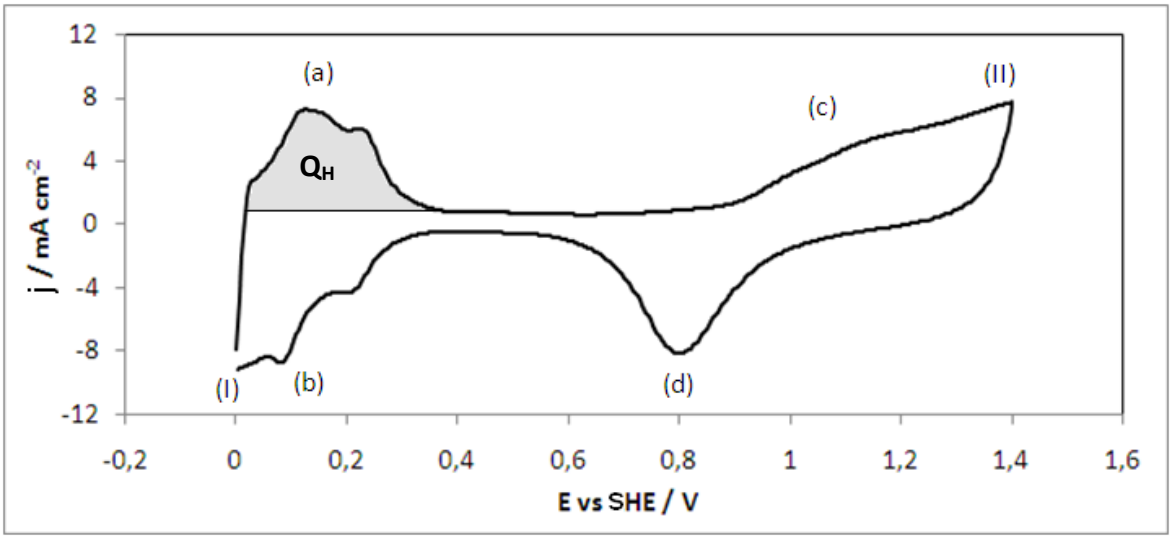

Figure 6.2. Cyclic voltammogram of Pt black in 5.15M H_3PO_4 at 20 mV s^{-1} sweep rate (cycle nº 10) and 40 ºC with the proton desorption area (Q_H) highlighted.

In the case of Pt, a well-established technique to calculate the EAS is to integrate the charge of the proton desorption peak (Q_H) obtained in the range of 0 – 0.4 V [15-17]. At this potential range, the proton attached to the surface of the Pt desorbs giving an anodic

current in form of a peak. The value of this coulombic charge is directly proportional to the area of catalyst active in the electrochemical half-reaction as showed in equation 3.3 *(see Chapter 3)*. The contribution of the double layer charge, although relatively small for Pt black samples, was subtracted for all EAS_{CV} calculations. Figure 6.3 shows the effect of the temperature on the EAS_{CV} of Pt black in the three different acidic electrolytes. All CV of Pt in different electrolytes at 50 mV s^{-1} are shown in figure A-2 *(appendix A)*.

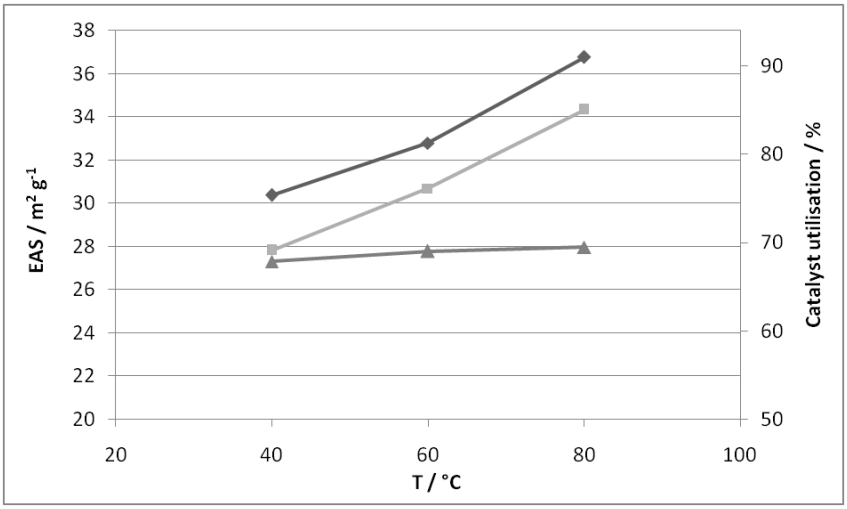

Figure 6.3. Pt black EAS_{CV} dependency on temperature in 5.15M (♦) H_2SO_4, (■) H_3PO_4 and (▲) CsH_2PO_4 aqueous solutions at 50 mV s^{-1} scan rate.

As seen in figure 6.3, the EAS of Pt black increases significantly in H_2SO_4 and H_3PO_4, 20 and 24 % respectively, when the temperature increases from 40 to 80 °C. In the case of CsH_2PO_4 a very mild increase of 2.4 % between 40 and 80 °C is noticed in the EAS_{CV} values. These results suggest that the EAS_{CV} is related to the pH as at higher proton concentration higher values were obtained. Lower pH values provide higher proton concentration and conductivity to the solution providing better access of the protons to the catalyst sites. Higher temperatures would also enhance proton diffusion in solution increasing the access of protons to these sites.

It has been suggested that anion adsorption onto the catalyst surface also affects the EAS, being phosphate anions more strongly adsorbed than sulphates and thereby showing higher active area in H_2SO_4 solution [18-21]. The catalyst utilisation value, obtained from the relation between calculated ESA_{XRD} and ESA_{CV} is also plotted in figure 6.3, being ca. 70 % for CsH_2PO_4 at all temperatures and as high as 85 and 91 % for H_3PO_4 and H_2SO_4 at 80 °C, respectively. Not much data is reported for Pt black utilisation in three electrode cell

configuration in acidic media. In the case of carbon supported platinum catalyst values, around 50 % were reported [22], although a high dispersion of values in catalyst utilisation are also reported (ca. 20 – 100 %) [16]. The high utilisation values obtained in this study are attributed to the absence of carbon as catalyst support, as well as to the much bigger particle size of Pt black compared to Pt/C. It is worth noting that although catalyst utilisation in Pt black seems high the absolute values of ESA are considerably smaller than carbon supported platinum, which is mostly caused by bigger and less dispersed crystallites.

6.3.3 IrO_2 ESA determination by cyclic voltammetry

IrO_2 has been long studied as an OER electrocatalyst for several electrochemical processes, including PEM electrolysis. As reported by many authors [23-26], iridium, as many other metals, forms hydrous oxide films when it is subjected to positive potential sweeps, leading, by the interaction with the ions in solution (i.e. H^+, OH^-), to oxide layers with properties differing to those of anhydrous oxides. The main difference arising from anhydrous and hydrous metal oxide films is that the latter shows a much higher degree of dispersion (less compact films) making the oxide layer considerably less dense.

Iridium undergoes several oxidation processes before reaching a stable and active state towards OER [24]. In these processes the oxidation state of the iridium ion changes by a simultaneous transfer of electrons and protons to keep the electroneutrality of the hydrous oxide film. The insertion of these ionic species in the oxide layer generates a so-called charge storage phenomenon in the material which can be studied by voltammetric techniques and can be related, for instance, to the hydrous oxide film thickness and composition. The anodic and cathodic currents generated by the redox processes of iridium are shown as oxidation and reduction peaks in the cyclic voltammograms. These redox couples have been extensively studied in order to identify the specific oxidation/reduction processes occurring and the species and charges involved in them. The main redox processes identified and agreed by most authors are Ir^{III}/Ir^{IV} and Ir^{IV}/Ir^{VI} couples taking place at potentials of ca. 1.0 V and 1.4 V (vs. SHE), respectively. The basic reaction for these processes is usually written as follows [18]:

$$IrO_x(OH)_y + \delta H^+ + \delta e^- \leftrightarrow IrO_{x-\delta}(OH)_{y+\delta} \quad (6.1)$$

Burke et al. [24] modelled the reaction corresponding to the Ir^{III}/Ir^{IV} couple considering the hydrous composition of the oxide as shown in equation 6.2 and in terms of structure in equation 6.3.

$$2\,[\,IrO_2(OH)_2 \cdot 2H_2O\,]^{2-} + 2e^- \leftrightarrow [Ir_2O_3(OH)_3 \cdot 3H_2O\,]^{3-} + 3OH^- \qquad (6.2)$$

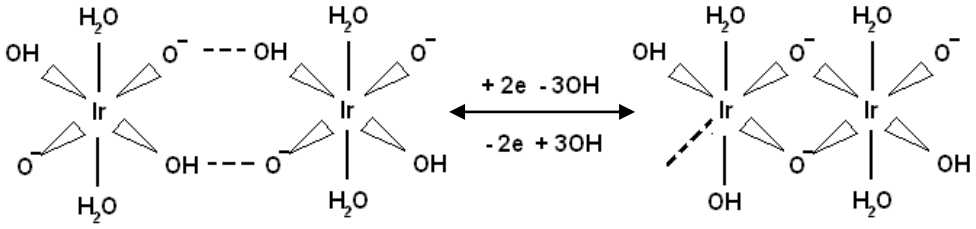

(6.3)

Both 6.1 and 6.2 equations define the same redox process yielding the same chemical species. Equation 6.3 helps to understand the nature and composition of this type of hydrous oxide and the charge storage phenomenon arising from this process.

Figure 6.4 shows the standard CV of IrO_2 obtained in 5.15 M H_3PO_4 at 20 mV s^{-1} sweep rate. In this case the voltammogram shows the anodic and cathodic currents generated by the solid sate redox transitions of iridium (a-b and c-d). At potentials lower than 0 V (vs. SHE) H_2 evolution starts (I) while O_2 evolution starts at potential higher than 1.23 V (II).

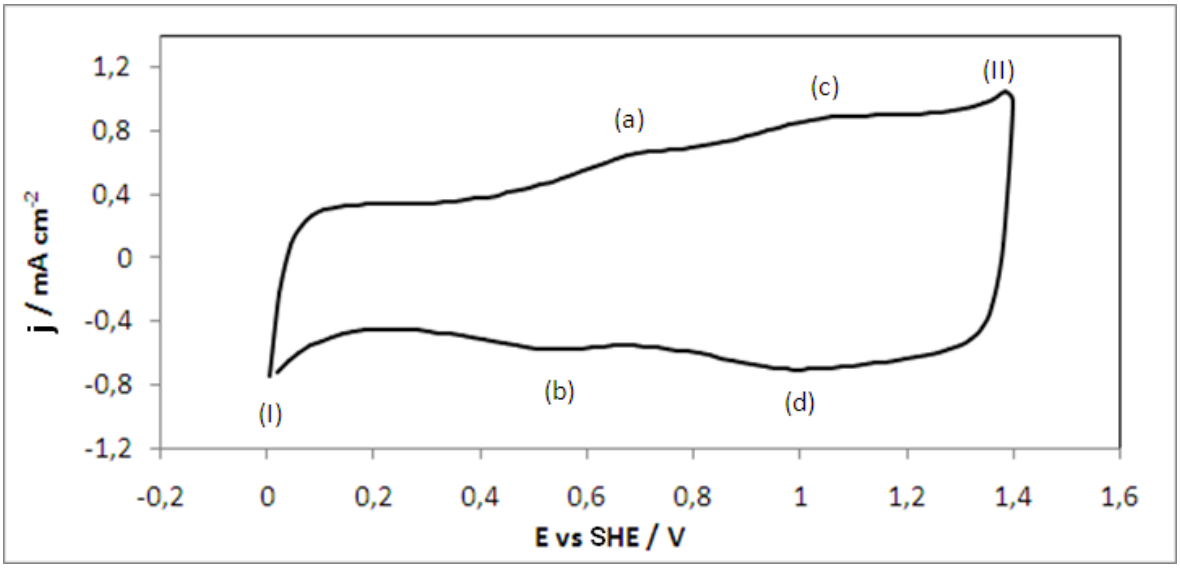

Figure 6.4. Cyclic voltammogram of IrO_2 in 5.15M H_3PO_4 at 80 °C and 50 mV s^{-1} sweep rate (cycle nº 10).

The redox couple situated at ca. 1.0 - 1.1 V (c-d) corresponds, in good agreement with other authors, to the Ir^{III}/Ir^{IV} transition, which is often clearly seen in iridium

voltammograms. The other redox couple situated at ca. 0.6 – 0.7 V is often reported as a pre-peak or shoulder. *Juodkazyte et al.* [27] attributed this peak to the transition of Ir/Ir^{III} in deoxygenated solutions following the reaction in equation 6.4. *Mozota et al.* [28] reported that the location and shape of this peak is greatly influenced by the nature of the ions in solution which agrees with the results obtained in this study (figure 6.5).

$$Ir + 3H_2O \leftrightarrow Ir(OH)_3 + 3H^+ + 3e^- \quad (6.4)$$

Unlike platinum, the pseudocapacitive behaviour caused by the implication of H^+ in the redox transitions of iridium makes it complicated to relate the charge to the surface area of electrochemically active catalyst. For this reason ESA_{CV} values of IrO_2 are commonly given by charge units (mC cm^{-2}) calculated by the area integration of the cyclic voltammograms in the 0 – 1.4 V region [24, 27, 29]. The obtained charge is dependent on the scan rate of the sweep (figure 6.5). Rest of CVs, at different temperatures are shown in figures A.3 – A.5 *(appendix A)*.

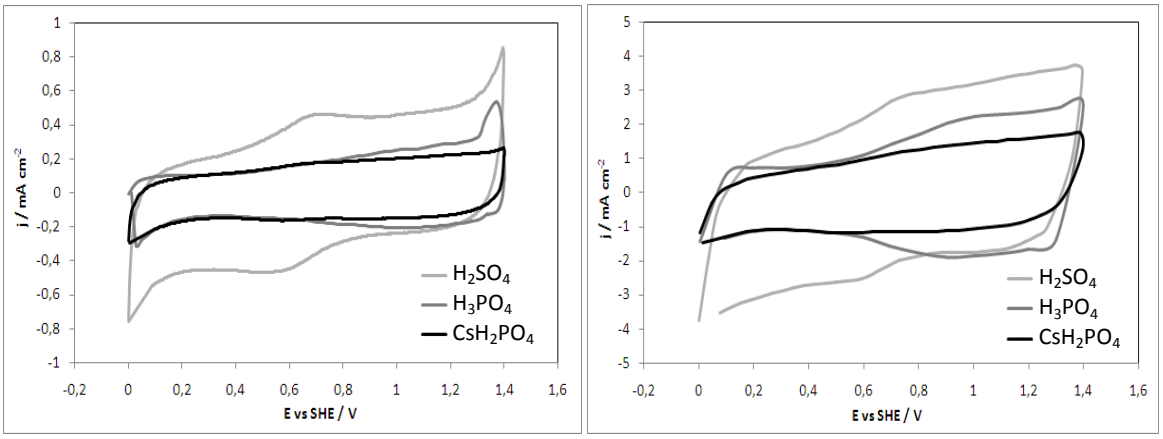

Figure 6.5. Cyclic voltammograms of IrO_2 in the three aqueous electrolytes at 20 mV s^{-1} (left) and 200 mV s^{-1} (right) sweep rate (40 °C) (cycles nº 10).

As seen in figure 6.5, the shape of the cyclic voltammograms changes considerably in the different electrolytes. In the case of H_2SO_4, the first redox couple at 0.6 – 0.7 V is easily recognised at all scan rates while the second couple at 1.0 – 1.1 V is slightly seen, only at high scan rates. The CVs of H_3PO_4 and CsH_2PO_4 electrolytes show very similar shape in the first half of the scan (0 – 0.6 V), however, in the second half the charge produced by the redox transitions is higher in H_3PO_4 which is more evident at higher scan rates. The oxygen evolution peak is not seen at high scan rates because of the masking effect of the double layer charge. Further oxidation step of iridium, Ir^{IV}/Ir^{VI}, is reported by several

authors to take place at higher potentials [23, 24, 31, 33]. This oxidation process will be further investigated in section 6.4.

The hydrogen evolution peak noticed at potentials close to 0 V suggests that the iridium oxide is at least partially reduced to metallic iridium, since hydrogen is not easily adsorbed onto an oxide surface [30, 31]. However, *Boodts et al.* suggested [32] and other authors agreed [33] that the oxide surface is never reduced to the metallic compound and therefore no bulk reduction of the catalyst takes place.

The dependency of the charge on the sweep rate is believed to be related to the existence of two regions on the catalyst surface; a region which protons can easily access (outer region) and another region where the accessibility for proton is lower (inner region) [34]. For this reason the total charge (q_T) can be related to the sum of the inner (q_{in}) and outer charge (q_{out}) as shown in equation 6.5.

$$q_T = q_{in} + q_{out} \tag{6.5}$$

At low scan rates the total charge dominates the process, while at high scan rates, as protons do not have enough time to intercalate into the oxide, it is the outer charge that dominates. In order to calculate the outer parameter, the charge obtained by the integration of the voltammogram (q) vs. the inverse of the square root of the scan rate ($v^{-1/2}$) is plotted and the obtained curve extrapolated to zero. For the total charge, the straight line obtained by plotting q^{-1} vs. $v^{1/2}$ is extrapolated to zero. All values are plotted in figure A.6, appendix A.

The summary of the effect of the electrolyte on the EAS values of Pt black and IrO_2 is shown in table 6.2. The amount of electrochemically active sites in these catalysts is affected by the anion nature and concentration in solution, being phosphate the anion with higher influence in the EAS loss and CsH_2PO_4 the solution where both catalysts show the lowest EAS. An increase in temperature influenced positively the EAS in all cases presumably caused by a better diffusion of species (i.e. H^+) at higher temperatures, as well as thermodynamically more favourable condition for anion desorption at higher temperatures. According to *Burke et al.* [24] the pH would also have an effect in the redox processes of hydrous metal oxides, i.e. iridium oxide, in other way. They suggested that as pH is increased, the equilibrium represented by equation 6.1 would be shifted to the left and the metal ion activity, and therefore its redox peak charge, would be reduced. This

would also explain the lowering tendency of the total charge of IrO_2 with increasing the pH. Generally, the charge data obtained for IrO_2 is lower than results provided by other authors, where values of 140 mC cm^{-2} were reported [29]. This is mainly attributed to the synthesis method used, which affects the particle size and consequently the ESA. As protons are involved in the oxidation steps of iridium (reaction 6.1), the oxidation and reduction peaks of the redox couple shift with the different pH of the electrolyte. The charge of these peaks is also dependant on the pH, as proton adsorption would be function of proton concentration in solution.

Table 6.2. Summary of EAS and charge values of Pt black and IrO_2 in 5.15M H_2SO_4, H_3PO_4 and CsH_2PO_4 at 40, 60 and 80 ºC.

Electrolyte	**Temperature / °C**	**Pt black EAS / m^2 g^{-1}**	**IrO_2**		
			Total charge / mC cm^{-2}	**Inner charge / mC cm^{-2}**	**Outer charge / mC cm^{-2}**
H_2SO_4	40	30.4	76.9	66.8	10.1
	60	32.8	76.9	62.1	14.9
	80	36.8	62.5	50.3	12.2
H_3PO_4	40	27.8	30.3	15.9	14.4
	60	30.7	38.5	30.2	8.2
	80	34.3	46.6	36.2	10.4
CsH_2PO_4	40	27.3	28.6	21.8	6.7
	60	27.8	30.3	20.3	10.0
	80	28.0	31.2	20.6	10.6

6.4 Oxygen evolution reaction (OER)

In PEM water electrolysis most of the losses limiting the electrochemical performance of the system arise from the overpotential generated in the anode, where the oxygen evolution reaction (OER) takes place [35]. The mechanism of this electrocatalytic reaction is much slower than the mechanism of the hydrogen evolution reaction (HER) taking place in the cathode, for this reason it is considered as the limiting reaction in the system and thus it has been the focus of much more extensive research [36-39].

The compatibility of the catalyst and the environment in which OER takes place is key issue for a successful electrocatalytic performance. In this section, the catalytic activity towards OER of commercially available IrO_2 catalyst in the presence of a saturated solution of CsH_2PO_4 (5.15 M) was studied. In order to address the effect of the pH and anion presence in solution, the same experiments were reported in the same concentration of H_3PO_4 and H_2SO_4 solutions and diluted (0.10 M) H_2SO_4 solution.

The two above-mentioned variables, pH and anion presence, are proved to place a great influence in the OER. On one hand, the acidity of the electrolyte would favour a certain mechanism driven by the concentrations, and therefore diffusion, of H^+ and OH^- species in the reaction media [40]. On the other hand, the anions of the electrolyte have a tendency to adsorb in the electrocatalyst surface which can lead to the deactivation of the active sites responsible for the reaction [21, 41].

6.4.1 OER characterisation by linear sweep polarisations

In order to study the OER in IrO_2 electrocatalyst quasi-steady polarisation curves (1 mV s^{-1} scan rate) were carried out at a range of temperatures (40 – 80 °C) for each electrolyte. 5 cycles were performed for all samples in order to obtain stable reproducible results.

All OER polarisation curves show a considerable hysteresis between the forward and backward scan as shown in figure 6.6. The difference shown in the activity of the electrocatalyst could be explained by two main reasons; (1) the blockage of active sites by the formation of O_2 bubbles on the surface of the electrode, or (2) partial deactivation of the catalyst by further oxidation of IrO_2 at high potentials to less active oxidation states [42]. Catalyst detachment is not considered to be the reason for this hysteresis as when the linear sweep is repeated at the same temperature the forward scan shows the same values

as before. The potential detachment of catalyst from the electrode surface was also monitored by integrating the area of the cyclic voltammetry curve before and after the linear sweep experiment series. The measured area did not show any significant decrease in charge, which suggests that no significant amount of IrO_2 was detached from the electrode surface by O_2 bubbling. It is therefore suggested that IrO_2 undergoes further oxidation at high potentials that affects its performance towards OER.

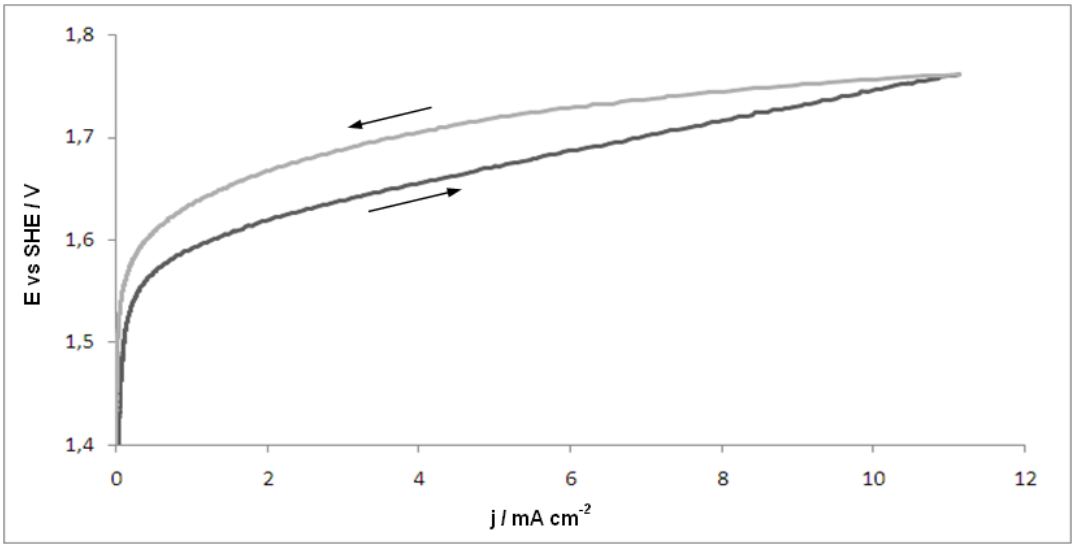

Figure 6.6. Hysteresis of the polarisation cycle nº 5 for IrO_2 in 5.15M CsH_2PO_4 at 40 °C, scan rate 1 mV s^{-1}.

The loss of activity due to hysteresis for all electrolytes at different temperatures was calculated and shown in figure 6.7. For both H_3PO_4 and H_2SO_4 concentrated solutions the activity loss between both cycles decreases with temperature whereas in CsH_2PO_4 and diluted H_2SO_4 solutions the loss keeps relatively constant at the range of temperatures used. The linear sweeps used in this study were the last forward scan (cycle nº 5) for all experiments in order to eliminate the hysteresis effect in the data analysis.

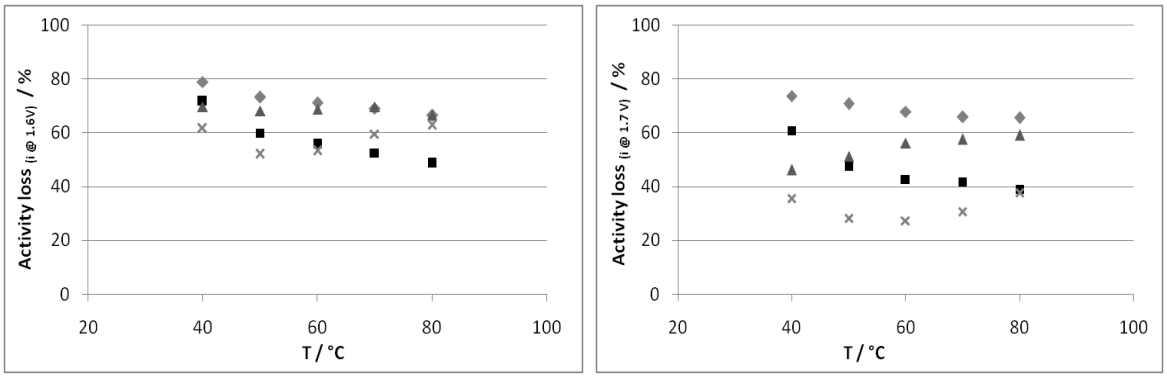

Figure 6.7. % loss in activity at 1.6 V (left) and 1.7 V (right) at different temperatures measured from the hysteresis of the polarisation cycles of 5.15 M (♦) H_3PO_4, (■) H_2SO_4, (▲) CsH_2PO_4 and (×) 0.10 M H_2SO_4.

6.4.2 iR and pH effect of the electrolyte on the OER activity of IrO_2

In the case of this study four different acid solutions were used as electrolyte; a saturated solution at 40 °C of CsH_2PO_4 (5.15 M), same concentration H_3PO_4 and H_2SO_4 solutions, and diluted (0.10 M) H_2SO_4 solution to match the same pH of concentrated H_3PO_4 solution. In all polarisations the effect of the pH and the ohmic resistance (iR) of the solutions must be addressed in order to have comparable results in different electrolytes.

The difference in pH between the electrolytes is caused by the difference in the proton concentration of the solutions. As protons are involved in the OER, the reversible potential of this reaction will shift by 59 mV per pH unit at 25 °C according to Nernst equation (equations 6.6 – 6.8), which would increase at higher temperatures.

$$E = E^0 + \frac{2.3RT}{nF} log \frac{[H^+]_{pH=0}}{[H^+]_{pH=1}} \tag{6.6}$$

$$log \frac{[H^+]_{pH=0}}{[H^+]_{pH=1}} = \log \frac{1}{0.1} = \log 10 = 1 \tag{6.7}$$

$$E = E^0 + \frac{2.3RT}{nF} = E^0 + 0.059_{25°C}\ (V) \tag{6.8}$$

The pH values for all four solutions were theoretically determined using the acidic constants of the acids (k_a) which determine the degree of disassociation of the acid into protons and anions. The values obtained were in good agreement with the potential shift measured in the H_2 evolution peak of the cyclic voltammograms of Pt electrode for H_2SO_4 and H_3PO_4 acids. In the case of CsH_2PO_4 the theoretical value calculated from the acidic constant of $H_2PO_4^-$ ion differs significantly from the values obtained by an standard pH-meter as well as from the HER potential shift on Pt electrode. All these values are shown in table 6.3.

The pH of both H_3PO_4 and H_2SO_4 solutions is very acidic due to the high degree of disassociation of these acids and the consequent high concentration of protons (hydronium ions in solution, H_3O^+). In the case of CsH_2PO_4 solution, although still acidic, the pH value is considerably higher. The first disassociation step of this salt liberates no protons ($CsH_2PO_4 \rightarrow Cs^+ + H_2PO_4^-$) and therefore just the diprotic ($H_2PO_4^-$) and triprotic (HPO_4^{-2}) acid (both very weak) will donate protons to the solution.

Table 6.3. pH values of the electrolytes obtained by theoretical calculation (pH_{th}), potential shift from HER in Pt (pH from E_{shift}) and measured by standard pH-meter (pH_{meas}).

Electrolyte	**pH_{th}**	**pH from E_{shift}**	**pH_{meas}**
H_2SO_4 (5.15 M)	-1.01*	-0.86	0.25
H_2SO_4 (0.10 M)	0.71*	-	0.48
H_3PO_4 (5.15 M)	0.71*	0.73	0.53
CsH_2PO_4 (5.15 M)	3.25	4.63*	4.71

* These values were used for pH-correct the OER linear sweeps.

The concentration of the anions in solution was calculated by the acidic constants which measure the degree of disassociation of the acids to protons and the conjugate anions. In case of CsH_2PO_4 a total disassociation of the salt is considered and the measured pH value of 4.63 was used to calculate the HPO_4^{-2} and PO_4^{-3} species` concentration. The anion concentrations for each electrolyte are summarised in table 6.4.

Table 6.4. Anion concentration in the aqueous electrolytes.

Electrolyte	**$[HSO_4^-]$ / M**	**$[SO_4^{-2}]$ / M**	**$[H_2PO_4^-]$ / M**	**$[HPO_4^{-2}]$ / M**	**$[PO_4^{-3}]$ / M**
H_2SO_4 (5.15 M)	-	5.15	-	-	-
H_2SO_4 (0.10 M)	-	0.10	-	-	-
H_3PO_4 (5.15 M)	-	-	0.19	1.1×10^{-4}	7.2×10^{-9}
CsH_2PO_4 (5.15 M)	-	-	5.15	2.3×10^{-5}	1.6×10^{-9}

iR measurements of the acidic solutions were carried out by electrochemical impedance spectroscopy (EIS) in order to correct the OER polarisations for the ohmic losses generated by the aqueous electrolyte. The high acidity of both concentrated H_3PO_4 and H_2SO_4 (5.15 M) make the solutions very conductive, hence the iR contribution is considerably low at the current densities obtained, 74 and 153 mΩ cm^2 respectively at 40 °C. In the case of diluted H_2SO_4 (0.10 M), the resistance of the solution shows a considerably higher value of 617 mΩ cm^2 attributed to the low concentration of the acid, and consequently proton concentration in solution. The impedance spectra of CsH_2PO_4 solution was corrected for the contribution of Cs^+ ion conduction in solution. In order to address the real iR

contribution arisen from H^+ conduction in this electrolyte, another experiment was run where the electrolyte was placed in a cell between two Pt coated (1.0 mg Pt cm^{-2}) gas diffusion electrodes (GDE) and a polarisation was recorded where H_2 evolution and H_2 oxidation took place in each of the electrodes (figure A.7, appendix A). As the kinetics of these reactions in Pt are very fast it is easy to recognise the iR contribution of H^+ conductivity by measuring the slope of the ohmic region line of the polarisation (R = E/I). The ratio used for the correction of the CsH_2PO_4 solution impedance spectrum between the total conductivity measured by EIS and proton conductivity was 2.44. In figure 6.8 Nyquist plot show the iR contribution of each electrolyte to the system. Values shown for CsH_2PO_4 solution were corrected for Cs^+ ion contribution.

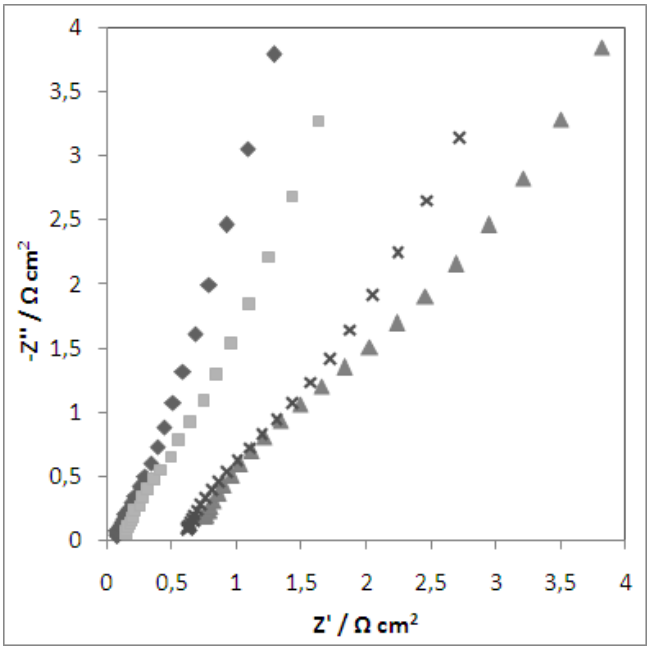

Figure 6.8. Nyquist plot of the half-cell showing the iR contribution of 5.15 M (♦) H_2SO_4, (▫) H_3PO_4, (▲) CsH_2PO_4 and (×) 0.10 M H_2SO_4 at 40 °C.

As proton conductivity, like most species' diffusion, is enhanced by increasing the temperature, the resistance of the system at different temperatures was measured. The obtained data is plotted in figure 6.9. The cell resistance in the case of diluted and concentrated H_2SO_4 and concentrated H_3PO_4 shows a moderate decrease when increasing the temperature of the system from 40 to 80 °C, while in the case of CsH_2PO_4 the cell resistance is decreased by approximately 35 %. It is worth mentioning that unlike what would be expected, the resistance of the solution to H^+ conduction is not linearly related to the pH value, i.e. to the H^+ concentration in solution. In case of the same pH solutions of

5.15 M H_3PO_4 and 0.10 M H_2SO_4 the resistance of the solution is increased by ca. four times and in the case of 5.15 M CsH_2PO_4 solution, with a very low proton concentration, the resistance is similar to that of the diluted H_2SO_4. This suggests that the water and the anionic species in solution interact with H^+ in different ways affecting its diffusion through the solution. This could be explained by different 'proton carrier clusters' in each of the solutions.

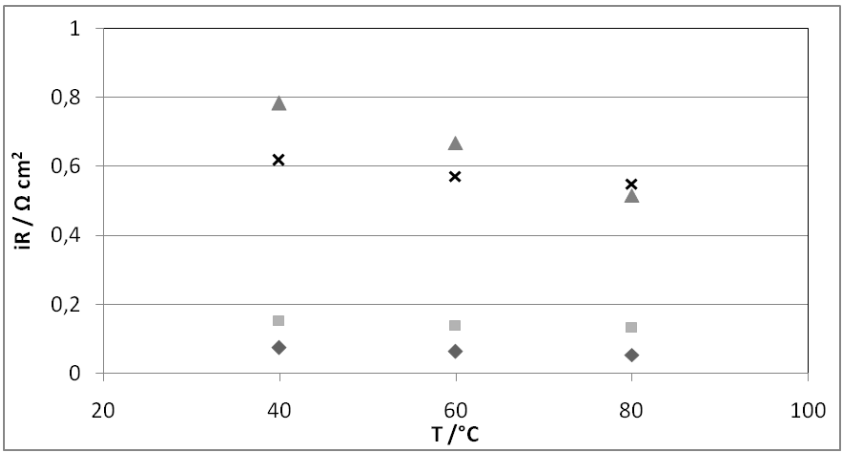

Figure 6.9. Resistance of the system at different temperature for 5.15 M (♦) H_2SO_4, (■) H_3PO_4, (▲) CsH_2PO_4 and (×) 0.10 M H_2SO_4.

The pH and iR-corrected linear sweeps of IrO_2 in the four electrolyte solutions at 80 °C are shown in figure 6.10 and the activity of IrO_2 in the temperature range of 40 - 80 °C at 1.6 and 1.7 V is plotted in figure 6.13. The electro-catalytic performance of IrO_2 changes considerably in different environments, which is attributed to two main variables; (1) pH and (2) anion adsorption onto the catalyst. The rest of the polarisations at 40 – 70 ºC are shown in figures A.8 – A.11, appendix A.

The performance of the catalyst is clearly related to the proton concentration in solution as seen in figure 6.11. The worst performance was obtained in concentrated CsH_2PO_4 solution (5.15 M) where the pH value is high (pH = 4.63), meaning a very low proton concentration. In the case of concentrated H_3PO_4 (5.15 M) and diluted H_2SO_4 (0.10 M), both with the same pH value of 0.714, the polarisations show approximately the same slope and for the concentrated H_2SO_4 solution (5.15 M), with the lowest pH value (pH = -1.0), the slope of the linear sweep is clearly improved. As protons are involved in the oxygen evolution reaction mechanism (see equations 6.9 - 6.11) as well as in the oxidation process of iridium (equation 6.1), the difference in pH would affect the rate of reaction caused by the availability of protons to the catalytic sites.

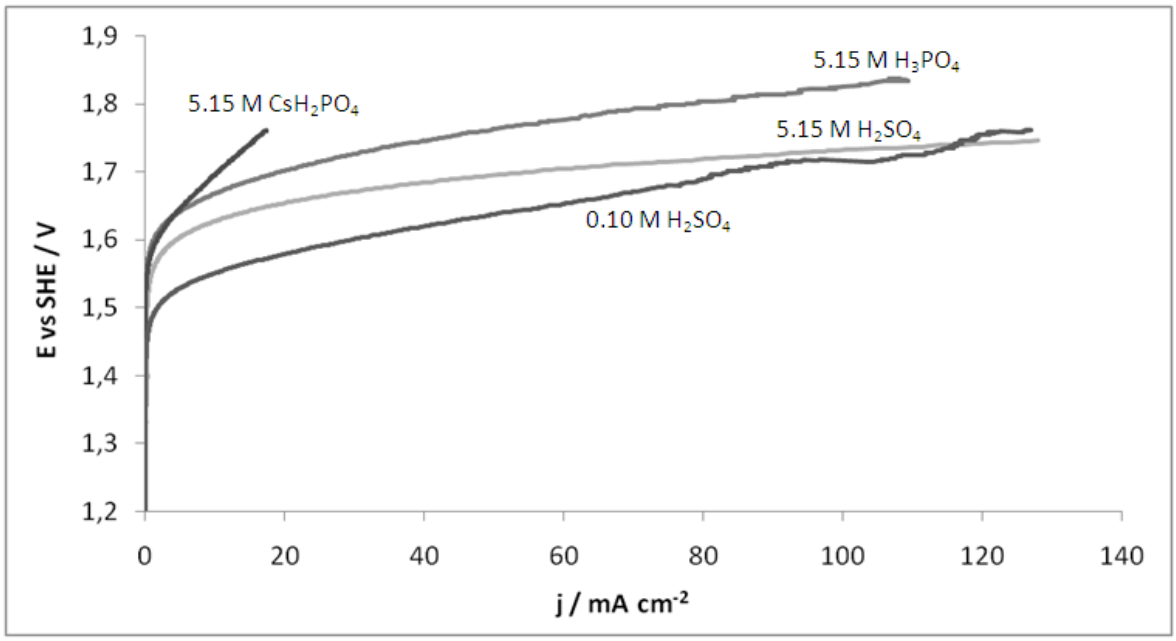

Figure 6.10. Linear sweep voltammograms for OER of IrO_2 in different electrolytes at 80 °C and 1 mV s^{-1} (cycle nº 5).

The effect of the pH in the oxidation potential is given in the Pourbaix diagram of Ir - H_2O system (figure 6.11) [42]. Here, the dependence of the different oxidation state transitions of Ir in the wide range of pH is plotted. For the oxidation steps of Ir^0/Ir^{III} and Ir^{III}/Ir^{IV} the above mentioned 59 mV per pH unit relationship is considered, whereas for Ir^{III}/Ir^{VI} and Ir^{IV}/Ir^{VI} oxidation steps 98.5 and 118 mV per pH unit were considered, respectively. The difference in slopes arises from the stoichiometric relation of Ir and protons in the oxidation reaction. Other authors [43] included the effect of current density of the system in the relation between potential and pH for IrO_2. This way in addition to the thermodynamic parameters considered in the Pourbaix diagram, kinetic considerations were included. All these studies confirm that the proton concentration in the electrolyte will affect the oxidation state of the iridium surface at a given potential and current density, influencing the activity of the iridium oxide towards OER.

Although the performance of the electrocatalyst has been shown to be related to the pH, the anion concentration in solution also seems to have an important effect in the onset potential (E_{onset}) for OER. For concentrated and diluted H_2SO_4 solutions, where the SO_4^{2-} anion concentration is 5.15 and 0.10 M respectively, the E_{onset} shifts by approximately 80 mV. This suggests that a high concentration of anions favours anion adsorption onto the catalyst surface lowering the exchange current density (rate of reaction at equilibrium) and thus generating an overpotential in the OER onset. The E_{onset} for concentrated H_3PO_4 and

CsH_2PO_4 solutions is higher than for H_2SO_4 as phosphate anions are known to adsorb more strongly than sulphate anions on the catalyst surface [21], creating an even higher overpotential. For both H_3PO_4 and CsH_2PO_4 solutions the onset potential is very similar suggesting that the 0.193 M $H_2PO_4^-$ anion concentration in 5.15 M H_3PO_4 solution (table 6.4) is enough to saturate the catalyst surface with phosphate groups.

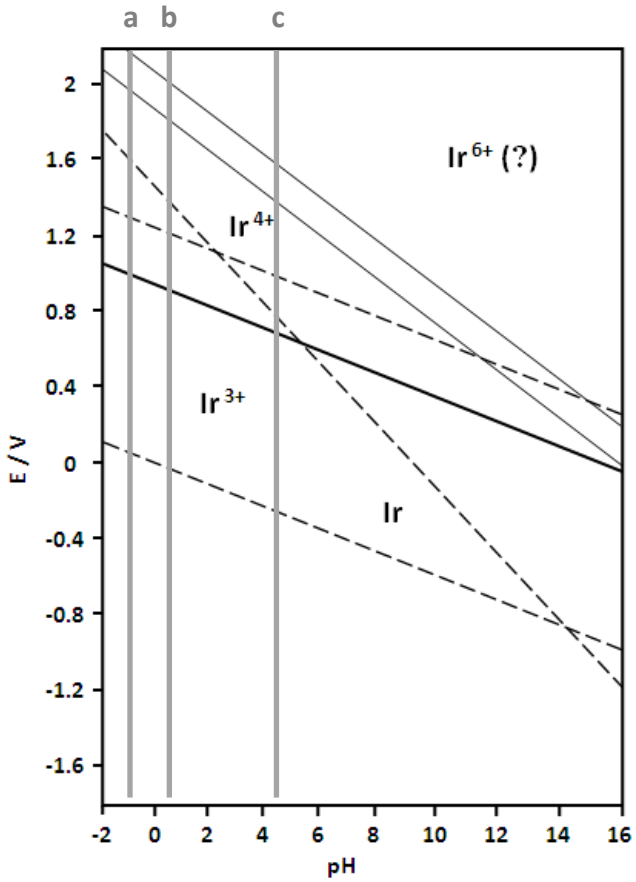

Figure 6.11. Pourbaix diagram of Ir-H_2O system at 25 °C [42]. Vertical lines pointing the pH of (a) 5.15M H_2SO_4, (b) 5.15 M H_3PO_4 and 0.10M H_2SO_4 and (c) 5.15M CsH_2PO_4.

The effect of temperature in the electrocatalytic performance, as shown in figure 6.12, is not the same for the different electrolytes. At moderate potentials (1.60 V) the activity of both concentrated H_3PO_4 and H_2SO_4 acids and CsH_2PO_4 solution remains constant at all temperatures. This suggests that there is not an obvious improvement in the reaction kinetics when temperature increases, which could be related to catalyst deactivation by anion adsorption. These are not the results expected as the anion desorption is usually an endothermic process and thus it should be favoured by increasing temperature [44]. It is thereby suggested that the temperature window used in these experiments is not wide enough to significantly affect this process. The activity of diluted H_2SO_4 improves by 65 %

with temperature increase of 40 °C but it is worth pointing out that, as the onset potential in this case is considerably lower, the measurement is no longer made on a purely kinetic region, and therefore this improvement could be driven by better ion diffusion. At higher potentials (1.70 V), the electrocatalytic activity is significantly improved by approximately 60 % by increasing the temperature from 40 to 80 °C in the case of both concentrated and diluted H_2SO_4 solutions. In the case of H_3PO_4 and CsH_2PO_4 solutions the improvement in activity is much more modest, being approximately 30 % for both systems. At this potential a mixed effect region is considered were kinetic and mass transport contributions take place and therefore a mass transport improvement due to a higher temperature is considered. Although a first thought might be to relate a better performance to higher proton conductivity, it is shown in figure 6.9 that the most significant decrease in resistance is shown in CsH_2PO_4 solution which shows a very moderate improvement in activity. It is therefore suggested that the activity improvement is related to the diffusion of the conjugated anions (SO_4^{2-} and $H_2PO_4^-$) in solution which agrees with the similar behaviour of both sulphate and phosphate-based solutions.

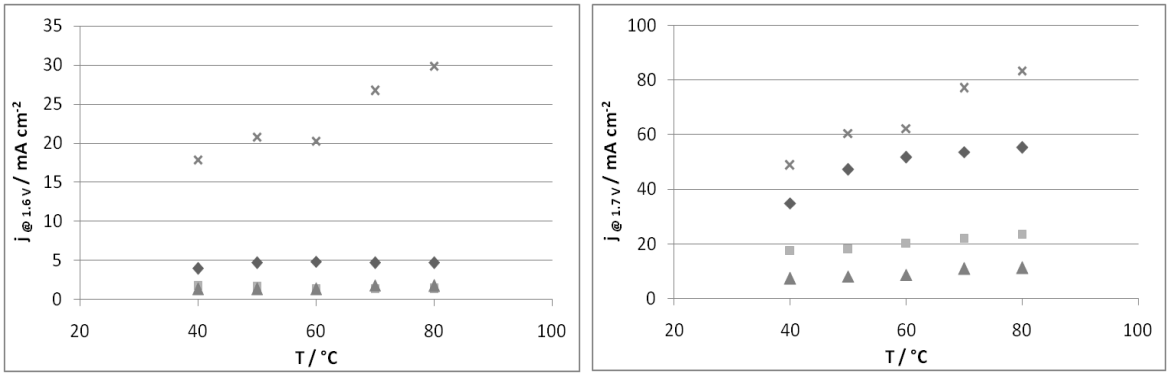

Figure 6.12. Electro-catalytic activity of IrO_2 for OER at 1.6 V (left) and 1.7 V (right) in 5.15 M (♦) H_2SO_4, (■) H_3PO_4, (▲) CsH_2PO_4 and (×) 0.10 M H_2SO_4.

6.4.3 Effect of the electrolyte in the kinetic parameters and reaction mechanism

The kinetic parameters for oxygen evolution were calculated in order to address the different processes happening in each electrolyte (i.e. catalyst oxidation/reduction, anion adsorption/desorption) and the limiting steps of the oxygen evolution reaction mechanism at the different pH and anion concentrations.

Although many reaction mechanisms are proposed for OER [40, 45], the following is generally accepted for metal oxide electrocatalysts in acidic media:

$$S + H_2O \rightarrow S\text{–}OH_{ads} + H^+ + e^- \quad (6.9)$$

$$S - OH_{ads} \rightarrow S\text{–}O_{ads} + H^+ + e^- \quad (6.10)$$

$$2S\text{–}O_{ads} \rightarrow 2S + O_2 \quad (6.11)$$

where S represents active site of the oxide electrocatalyst and OH_{ads} and O_{ads} stand for adsorbed hydroxyl species and adsorbed oxygen atoms, respectively. The first two steps of this mechanism involve a charge transfer where the formation of adsorbed hydroxyl species on the active site and the deprotonation of the species take place, respectively. In the last step an oxygen molecule is formed giving place to two free active sites of electrocatalyst [46].

From the Tafel plots (E vs. log j) of the linear sweeps of IrO_2 in the different electrolytes three different linear regions were identified; a low overpotential (Tafel 1), a moderate overpotential (Tafel 2) and a high overpotential region (Tafel 3). In figure 6.13 the three regions in the case of IrO_2 in 5.15 M CsH_2PO_4 solution are shown.

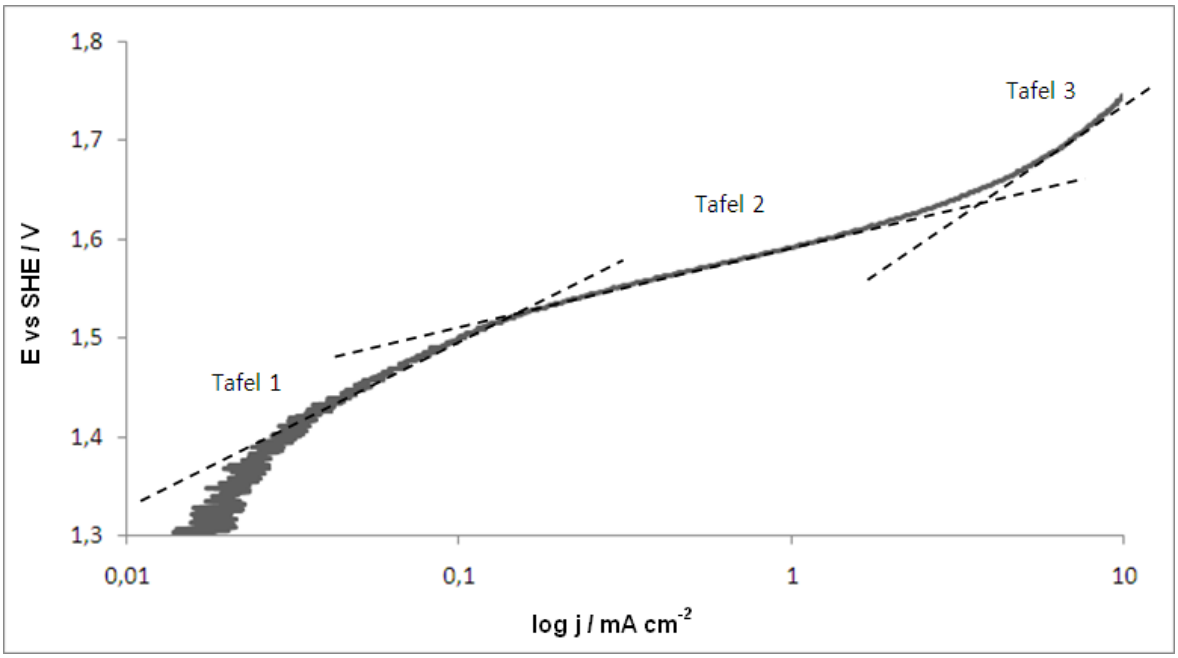

Figure 6.13. E vs. log j plot of IrO_2 in 5.15 M CsH_2PO_4 solution at 40 °C where three different Tafel regions are differentiated; low overpotential (Tafel 1), moderate overpotential (Tafel 2) and high overpotential (Tafel 3) region (sweep rate = 1mV s^{-1}).

Low overpotential region (Tafel 1)

The first Tafel region at the low overpotential is clearly seen in the different four electrolytes at 40 °C. At higher temperatures this region tend to lose linearity because of

the appearance of an oxidation peak in the 1.35 – 1.40 V range (figure 6.15). The presence of this peak is attributed to the potential cycling of the samples from 1.10 to 1.80 V, as at the backward scans, a peak corresponding to the reduction couple of iridium was found. Although the temperature is not thought to be responsible for the appearance of the peaks, it affects the potential in which the reduction/oxidation peaks appear, reducing their potential difference at higher temperature. This can be seen and follows the same trend in all samples of H_2SO_4 and H_3PO_4 solutions. In figure 6.14 this effect is shown for 5.15 M H_2SO_4 samples.

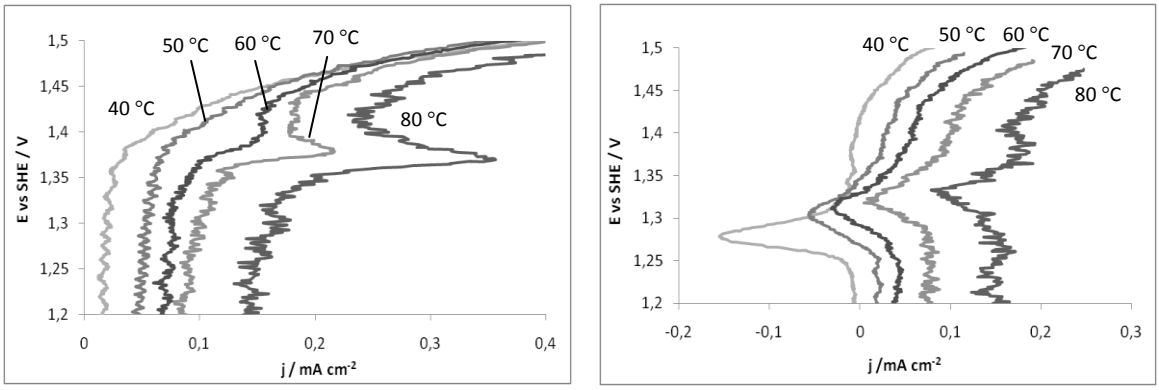

Figure 6.14. Effect of temperature (40 to 80 °C) on the oxidation peak (left) and reduction peak (right) of IrO_2 in 5.15 M H_2SO_4 (scan rate = 1 mV s^{-1}).

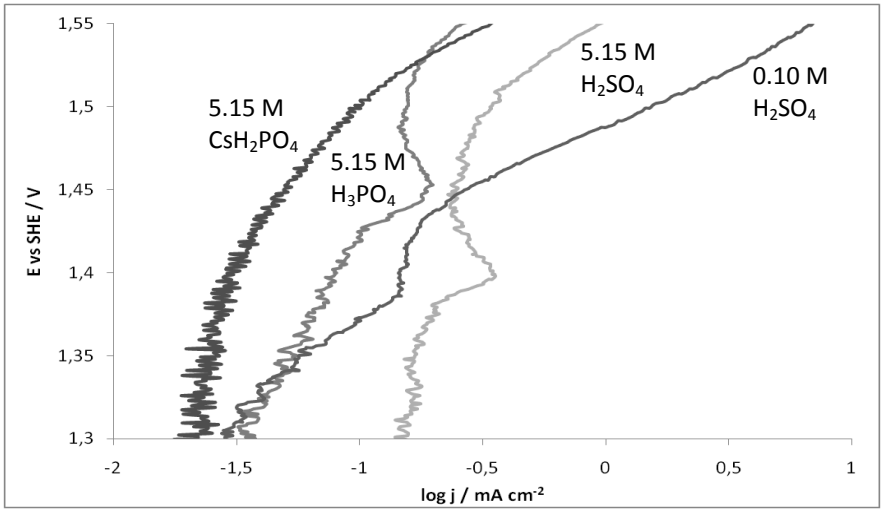

Figure 6.15. Ir oxidation peak at 80 °C in the four different electrolytes.

In the case of CsH_2PO_4 solution no reduction or oxidation peaks were seen in this potential range, as shown in figure 6.15. Although a significant negative shift in the reduction potential of iridium is expected by the difference in pH as stated in the Pourbaix diagram (figure 6.11), the linear sweeps were already pH-corrected and therefore the oxidation peak

should not be hidden by the potential shift. This might be explained by a different pH dependence of the redox transition potential from the Nernstian relationship of 59 mV pH unit^{-1} [24, 27, 42] (equation 6.8) as will be discussed later. The absence of the oxidation peak in CsH_2PO_4 solution could also be attributed to small charge of the oxidation process caused by the low proton concentration.

As shown in figure 6.16 and table 6.5, the Tafel slopes and the potential region in which the linearity is seen at 40 °C differ considerably between the four electrolytes. In the case of sulphuric acid solutions the Tafel slope increases from 100 to 123 mV dec^{-1} when the concentration is increased from 0.10 to 5.15 M and for both phosphate solutions, H_3PO_4 and CsH_2PO_4, the Tafel slope shows a value of approximately 160 mV dec^{-1}. The charge transfer coefficient was calculated from the Tafel slopes, corresponding presumably to an oxidation step of iridium to a more active state towards OER. The exchange current densities show higher values in sulphuric acid solutions which can be attributed to a weaker adsorption of the sulphate species comparing to that of phosphates. The adsorption of anions onto the catalyst active sites would, as stated before, partially inhibit the reaction at equilibrium lowering the j_0 values.

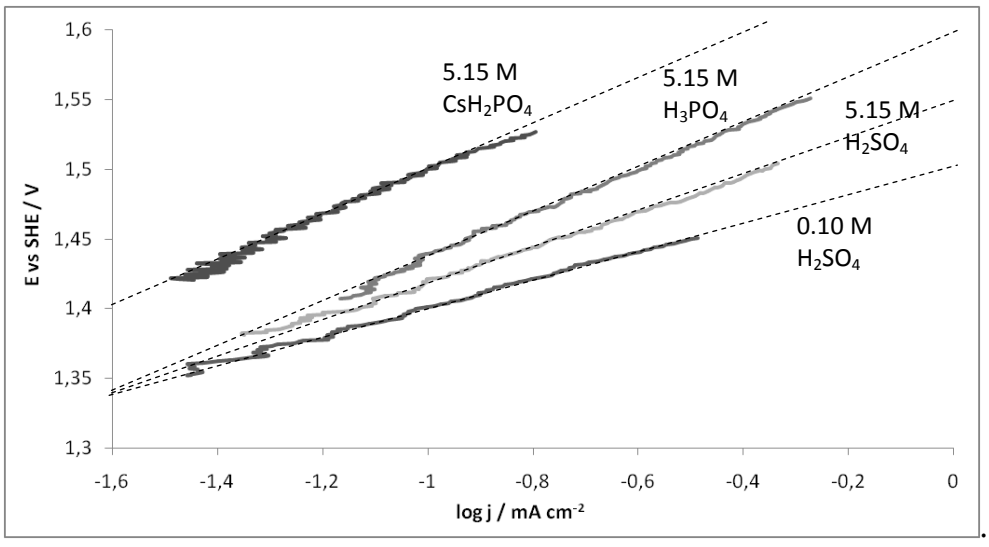

Figure 6.16. Tafel slopes of IrO_2 at low overpotential in different electrolytes at 40 °C (scan rate = 1 mV s^{-1}).

This low overpotential region is therefore attributed to an oxidation step of iridium to a more active oxidation state towards OER, presumably Ir^{IV} / Ir^{VI}. *Burke et al.* [24] identified a redox peak by cyclic voltammetry in 1.0 M H_2SO_4 at similar potentials, ca. 1.40 V. Several other authors also reported this redox couple, generally identified by cyclic voltammetry, at similar potentials, between 1.30 – 1.50 V [31, 40]. In the Pourbaix

diagram of Ir – H_2O system (figure 6.11) the unusual pH dependence on the potential of this process is shown, which agrees with many other authors [24, 31, 40, 42]. It is stated that not only the pH dependence differs from the Nernstian relation, being in this case 118 mV pH unit^{-1}, but it also would be affected by the composition of the oxide layer, i.e. the concentration of oxidised iridium species. According to these authors the potential difference arises from the more acidic character of the produced oxide because of the increased charge density around the metal ion. It is also mentioned that at higher pH values, the oxidation reaction (equation 6.1) is shifted to the left, hindering the oxidation process to some extent.

Table 6.5. Kinetic parameters of IrO_2 at the low overpotential range at 40 °C.

Electrolyte	**Tafel slope (b) / mV dec^{-1}**	**Charge transfer coefficient (α)**	**Exchange current density (j_0)* / mA cm$^{-2}_{XRD}$**	**Overpotential (η) / mV**
H_2SO_4 (5.15 M)	123	0.50	1.22×10^{-5}	160 – 280
H_2SO_4 (0.10 M)	100	0.64	7.97×10^{-6}	140 – 230
H_3PO_4 (5.15 M)	159	0.41	2.17×10^{-5}	200 – 330
CsH_2PO_4 (5.15 M)	162	0.42	9.50×10^{-6}	210 – 300

** j_0 values normalised to the surface area of IrO_2 obtained from P-XRD (see table 6.1)*

Moderate overpotential region (Tafel 2)

At the moderate potential range a clearly defined Tafel region (Tafel 2, figure 6.13) is seen in all electrolytes and temperatures. Tafel slopes in 5.15 M H_2SO_4, H_3PO_4 and CsH_2PO_4 show values of approximately 75 mV dec^{-1} at most temperatures and 65 mV dec^{-1} in the case of 0.10 M H_2SO_4 (figure 6.17) which is in good agreement with the results reported by other authors for OER for IrO_2 in acid solutions at this potential range [23, 25, 47].

All Tafel slopes remain relatively constant at different temperatures (figure 6.18, left) which suggests that the temperature range used does not affect significantly the process happening at the moderate potential range (1.45 – 1.65 V). Values close to 1 were obtained for the charge transfer coefficient (figure 6.18, right).

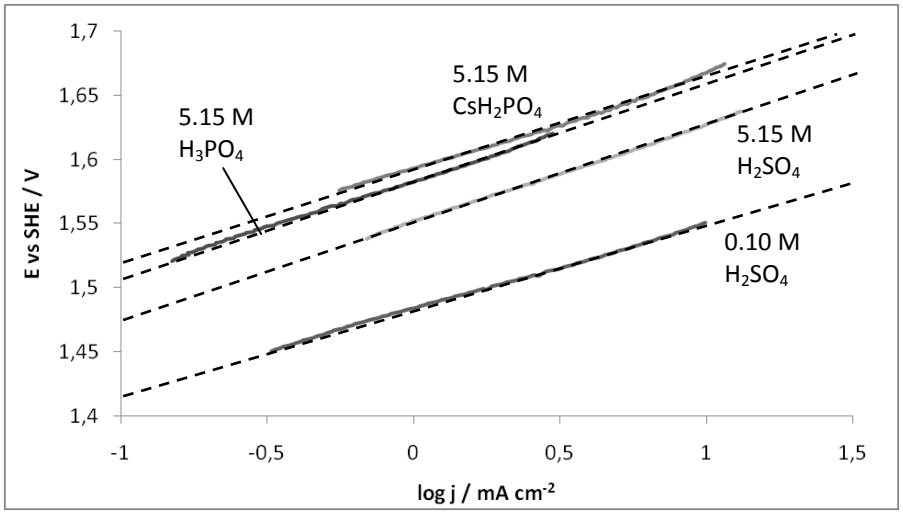

Figure 6.17. Tafel slopes of IrO_2 at moderate overpotential in different electrolytes at 80 °C (scan rate = 1 mV s^{-1}).

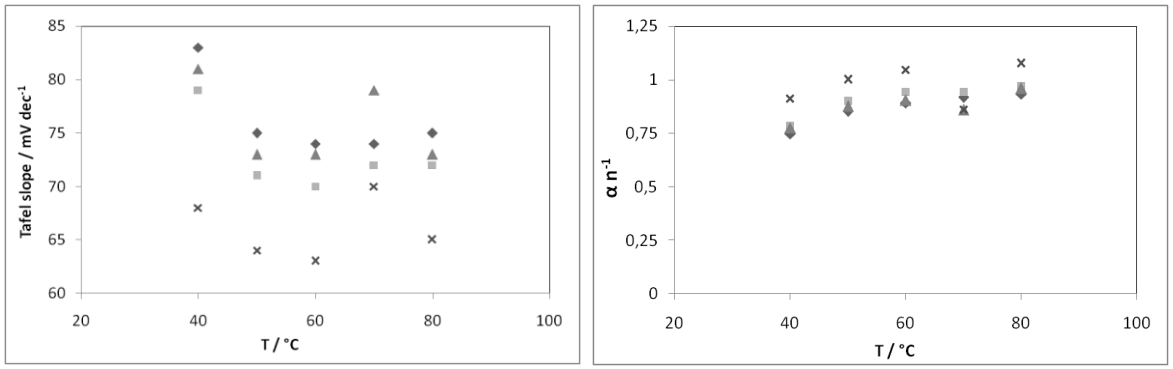

Figure 6.18. Tafel slope (left) and charge transfer coefficient (right) dependence on temperature for IrO_2 at moderate overpotential in 5.15 M (♦) H_2SO_4, (■) H_3PO_4, (▲) CsH_2PO_4 and (×) 0.10 M H_2SO_4.

Tafel slope values of ca. $\left(\frac{2RT}{3F}\right)$ have been reported for iridium oxide at the moderate overpotential in acidic solutions, which are in good agreement with the values obtained in this research. This Tafel slope value is attributed to the second step in the reaction mechanisms being the rate determining step (equation 6.10). Nevertheless high dispersion in the Tafel slopes have been reported for this moderate overpotential region, varying from ca. 40 to 90 mV dec^{-1} (at 25 ºC) [23,48,54].

Gottesfeld et al. [23] proposed that the Tafel slope for this process depends on the oxide layer thickness of the catalyst, varying between 50 and 90 mV dec^{-1} (at room temperature) from a thick oxide layer (700 Å) to a thin anodised surface (10-20 Å). The change in the Tafel slope, according to the authors, is caused by the different affinity for oxygen intermediates (i.e. OH^-) of the oxide layers when the second step in the reaction

mechanisms ($S–OH_{ads} \rightarrow S–O_{ads} + H^+ + e^-$), where the hydroxyl consumption takes place releasing a proton and producing an adsorbed oxygen atom, is the rate determining step. At higher overpotentials their results show higher Tafel values, close to 150 mV dec^{-1} which according to them would correspond to the first step of the reaction mechanism ($S + H_2O \rightarrow S–OH^*_{ads} + H^+ + e^-$) being the rate determining step, where the hydroxyl group is adsorbed onto the catalyst surface. These results are in agreement with those obtained in this study as it will be explained later in this section. *Hu et al.* [48] proposed in a more recent study that the Tafel slope, when the first step of the mechanism is the rate determining step, exhibits values of 120 mV dec^{-1}, while in the case of the second step being the rate determining step, Tafel slope equals 40 mV dec^{-1}. They agreed with the influence of the oxide layer composition on Tafel slope and proposed that the intermediate values of Tafel slopes obtained, 60 mV dec^{-1}, are caused by a sub-mechanism on the first step, as shown in equations 6.12 and 6.13.

$$S + H_2O \rightarrow S–OH^*_{ads} + H^+ + e^- \quad (6.12)$$

$$S – OH^*_{ads} \rightarrow S – OH_{ads} \quad (6.13)$$

where the adsorption intermediates (i.e. $-OH^*_{ads}$ and $-OH_{ads}$) are the same chemical species with different energy states. They therefore concluded that the reaction at the moderate overpotential range is controlled by the first step in the reaction mechanism. *Miles et al.* [25] also reported a Tafel value of 80 mV dec^{-1} for IrO_2 in 1.0 M H_2SO_4, at a similar overpotential. *Burke et al.* [24] stressed the importance of the composition and thickness of the oxide layer; they suggested that if it becomes too thick the system could be limited by the electron transfer within the oxide layer instead of being limited by ion transfer. This effect, according to the authors, would affect the reaction rate and increase the Tafel slope value.

The exchange current densities (j_0) were calculated from the intersection of the Tafel slopes with the reversible potential, E_{rev}. Values of exchange current density were lower than those reported by *Miles et al.* [25] for a 1.0 M H_2SO_4 solution at the moderate overpotential region, which were in the range of 1.5×10^{-4} mA cm^{-2}. In this study j_0 exhibited values between 5.1×10^{-7} and 4.9×10^{-6} mA cm^{-2} showing the following trend at all temperatures, 0.10 M $H_2SO_4 \geq$ 5.15 M $H_2SO_4 >$ 5.15 M $CsH_2PO_4 \geq$ 5.15 M H_3PO_4. This variation in j_0 could be related to the adsorption of anions onto the catalyst surface as

phosphate ions are known to adsorb more strongly than sulphate ions. Anion adsorption would occlude active sites on the catalyst surface partially inhibiting the reaction at equilibrium and thus reducing the j_0. The charge transfer coefficient for IrO_2 in acidic solutions reported by *Miles et al.*, 0.82, is in good agreement with those obtained in this study (figure 6.18 - right).

The activation energy for the electrochemical process was calculated from the dependence if j_0 with temperature, following Arrhenius law (equations 3.13 - 3.14). In Figure 6.19 the Arrhenius plots for OER at the moderate overpotential region is shown.

The activation energies for this process in the different electrolytes varied between 39 and 23 kJ mol^{-1}, following the trend; 5.15 M H_3PO_4 > 0.10 M H_2SO_4 > 5.15 M CsH_2PO_4 > 5.15 M H_2SO_4. The E_a values obtained are approximately half of those reported by [21] for diluted H_2SO_4 and H_3PO_4 solutions. This difference could be related to the contribution of the anion adsorption/desorption process to the overall apparent E_a.

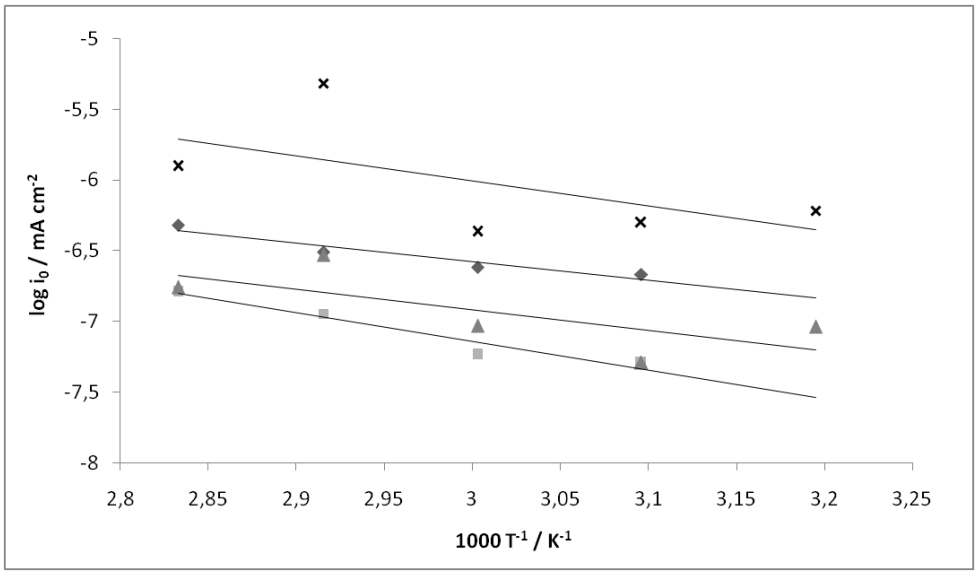

Figure 6.19. Arrhenius plots of for IrO_2 in 5.15 M (♦) H_2SO_4, (■) H_3PO_4, (▲) CsH_2PO_4 and (×) 0.10 M H_2SO_4.

High overpotential region (Tafel 3)

At the high overpotential region of the polarisation curves, potentials higher than 1.60 V for all electrolytes, another Tafel region is considered (Tafel 3, figure 6.13). This region, unlike the previous two (Tafel 1 and Tafel 2, figure 6.13), does not show a totally linear tendency which suggests that this cannot be considered as a pure kinetic region. Apart

from kinetic effect arising from the OER and the effect of the oxide layer characteristics formed at higher potentials, a mass transport contribution affected by presumably proton mass transport in the electrolyte should be considered. Protons are generated in the working electrode where OER takes place and consumed in the counter electrode, in the HER. At high overpotentials and high current densities the production/consumption of protons will create a proton concentration gradient in the electrolyte affecting the performance of the reaction. This local change of pH on the electrode surface would on one hand shift the reaction potential and on the other hand affect the OER by the diffusion of the species involved in the reaction [53].

In order to address the effect of the mass transport in this region of the linear sweeps, a simple correction based on Fick´s first law of diffusion was used (equation 6.14).

$$J = -D\frac{dC}{dx} \tag{6.14}$$

where J represents the flux density (mol m^2 s^{-1}), D stands for the diffusion coefficient of H^+ in the electrolyte solution (m^2 s^{-1}) and dC and dx represent the differential in concentration and position. Relating the molar flux to the current generated in the system we can calculate the theoretical value of the limiting current for each electrolyte.

$$J = \frac{j}{nF} = -D\left(\frac{dC}{dx}\right)_{x=0} \tag{6.15}$$

$$j_L = \frac{-DnF\Delta C_{H^+}}{\delta} \tag{6.16}$$

where j_L (mA cm^{-2}) represents the limiting current density of the system and δ (cm) the Nernst diffusion layer.

Considering a δ of 0.01 cm [49] for a non-stirred solution, and the diffusion coefficients found in the literature [50, 51] the limiting current for each system can be calculated. In the case of 5.15 M H_2SO_4, being a strong acid, the disassociation to protons is complete and therefore the high concentration of protons (pH = -1.0) is considered enough to avoid any effect in terms of proton mass transport and therefore, no mass transport correction was carried out. For 5.15 M H_3PO_4, although the proton concentration is much lower (pH = 0.714), the weak nature of the acid provides the solution with a high concentration of non-

disassociated H_3PO_4, which would act as a proton donor, bringing to equilibrium any localised pH gradient in the system. For this reason H_3PO_4 solution would neither be affected by proton mass-transport issues. This buffer effect of the phosphoric acid solution is also considered in the case of 5.15 M CsH_2PO_4 solution. Despite the low proton concentration of this solution (pH = 4.63), the non-disassociated $H_2PO_4^-$ and HPO_4^{2-} species in solution would act as proton donors maintaining the proton concentration constant in the solution and thus, countering any localised pH change in the proximity of the electrodes.

In the case of the 0.10 M H_2SO_4 solution however, the complete disassociation of the acid would provide a moderate proton concentration ($[H^+]$ = 0.20 M) which, using the above mentioned parameters, lead us to a j_L value of 135 mA cm^{-2}. Plotting E vs. $(j_L \times j)/(j_L - j)$ the effect of the mass transport is subtracted from the linear sweep lowering the Tafel slope from 315 to 144 mV dec^{-1} (figure 6.20).

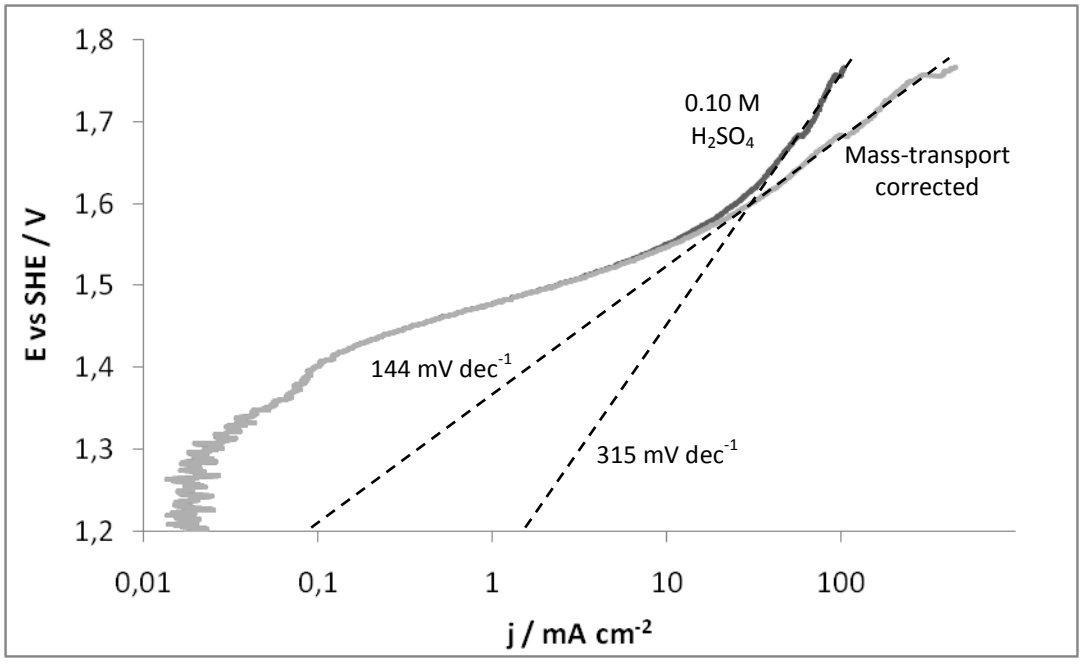

Figure 6.20. Proton mass transport correction at high overpotential in 0.10 M H_2SO_4 at 60 °C.

The Tafel slope values obtained for the four electrolytes at the temperature range 40 – 80 °C are shown in figure 6.22, left. The slope is clearly related to the pH of the solution, being at 80 °C, 107 mV dec^{-1} for 5.15 M H_2SO_4, 142 and 130 mV dec^{-1} for same pH 0.1 M H_2SO_4 and 5.15M H_3PO_4 solutions respectively and 212 mV dec^{-1} for CsH_2PO_4. This means that the proton concentration plays an important role in the OER in acidic media

improving the OER rate as the pH decreases. Tafel values obtained for H_2SO_4 and H_3PO_4 solutions were similar to those reported by *Gottesfeld et al.* and *Lyons et al.* for OER in 1.0 M H_2SO_4 at the high overpotential region [23,53], where Tafel slope equaled 120 and 150 mV dec^{-1}, respectively. Tafel slope values reported at the high overpotential region follow the general expression of $\left(\frac{2RT}{F}\right)$, which is atributted to the first step of the reaction mechanism, that is, the adsorption of OH^- species onto the catalyst, being the rate determining step ($S + H_2O \rightarrow S–OH_{ads} + H^+ + e^-$).

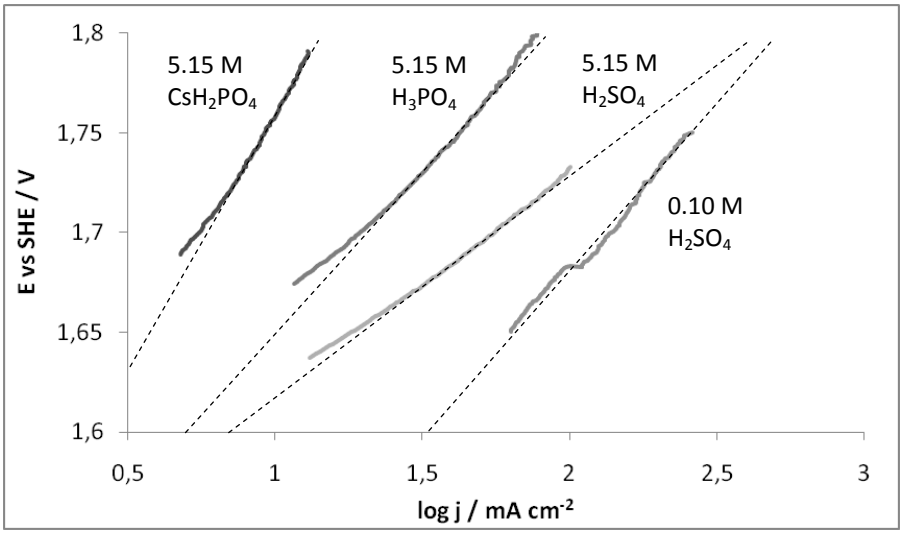

Figure 6.21. Tafel slopes of IrO_2 at high overpotential in different electrolytes at 80 °C.

The significantly high Tafel slope measured in the case of 5.15 M CsH_2PO_4 solution at high overpotentials suggests that the extremely low concentration of protons has negative effects on the oxygen evolution reaction. The effect of the low proton concentration on the formation of the active oxide species in the catalyst surface should be taken into account. As protons are involved in the oxidation step of iridium to an active oxidation state (presumably Ir^{VI}), such high pH would not provide enough proton concentration, changing the oxide layer characteristics to a less active oxide layer towards OER. In other words, as stated by *Burke et al.* [24], at high pH conditions the electro-oxidation reaction of iridium ($IrO_x(OH)_y$) would be shifted to the left (equation 6.1) and therefore the hydroxylic complex of iridium becomes more stable and the metal ion activity reduces. If this is so, the affinity of the oxide for hydroxyl groups would be different, affecting the rate of reaction. It is thereby proposed, that although protons are not believed to influence the performance in terms of mass transport in the current densities obtained, they have a

significant effect in the kinetics of iridium towards OER, affecting the properties of the surface oxide and therefore, reaction rate.

Burke et al. [24] also reported in their study a Tafel slope of ca. 200 mV dec^{-1} for OER in IrO_2 in 1.0 M H_2SO_4 solution, which they attributed to structural changes in the oxide layer as, according to them, no conventional principles of electrochemistry could explain such result. *Krishtalik* [55] reported high overpotential Tafel slope values in ruthenium-based anodes of 80 mV dec^{-1} at pH < 2, which would increase to values as high as 220 mV dec^{-1} at pH = 10 (which would again drop to 70 mV dec^{-1} at pH > 12). The increase in the slope was not attributed to a change of the limiting step of the unchanged mechanism but to a modification of the surface composition, affecting the interaction of the adsorbed intermediate species (i.e. OH_{ads}, O_{ads}) with the reactants. Several other authors reported high experimental values of Tafel slopes for OER (at room temperature) using different catalyst, such as, boron-doped diamond (b = 340 mV dec^{-1}) [56] or Ru-based perovskyte (b = 222 mV dec^{-1}) [57]. All these high experimental Tafel slope values were attributed to the different characteristics of the catalysts surface, affecting the affinity and coverage of the intermediate species taking place in the reaction mechanism. For other processes, such as the electro-oxidation of methanol by Pt-based catalyst, high Tafel values at the high overpotential region, between 230 – 270 mV dec^{-1}, were also reported [58]. They attributed the high values of Tafel slopes to the effect of the particle size and distribution, as these parameters play important roles in the oxidation of small organic molecules [59].

The increase in temperature decreased the Tafel slope value in all H_2SO_4 and H_3PO_4 solutions. In CsH_2PO_4 solution the Tafel slopes remained approximately at the same value. Charge transfer coefficients were calculated from Tafel slopes, being values close to 0.5 for all H_2SO_4 and H_3PO_4 solutions and 0.25 in the case of CsH_2PO_4 (figure 6.22 - right).

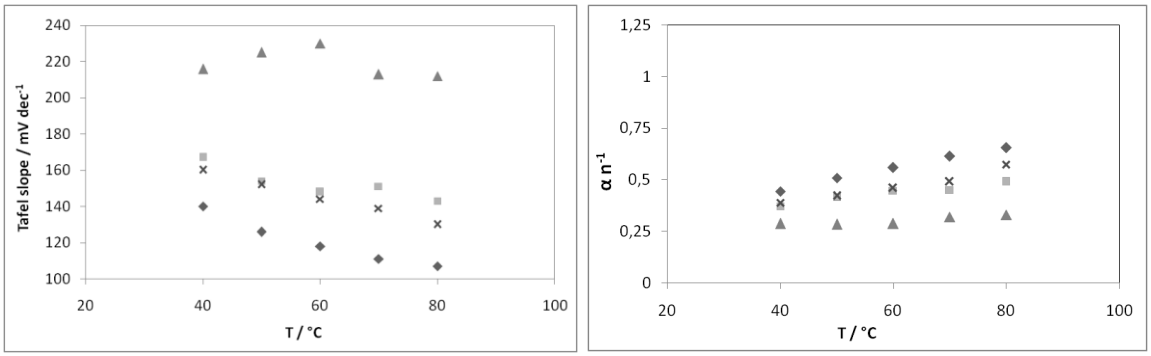

Figure 6.22. Tafel slope and charge transfer coefficient dependence on temperature for IrO_2 at high overpotential in 5.15 M (♦) H_2SO_4, (■) H_3PO_4, (▲) CsH_2PO_4 and (×) 0.10 M H_2SO_4.

The exchange current density values obtained were in the range of 2.8×10^{-5} and 5.0×10^{-4} mA cm^{-2} for all concentrated solutions and of approximately 2.0×10^{-2} mA cm^{-2} for the diluted H_2SO_4 solution. The difference in the j_0 values is attributed to the anion adsorption onto the catalyst surface. The difference in anion concentration may still affect the exchange current density in this high overpotential range, being the highest in dilute H_2SO_4, where the anion concentration is lower. The activation energy was calculated at the high overpotential range from the relation of the exchange current density with temperature (figure 6.23). The activation energies obtained for OER in the different electrolytes are the following; 12 kJ mol^{-1} in 5.15 M H_2SO_4, 13 kJ mol^{-1} in 5.15 M H_3PO_4, 15 kJ mol^{-1} in 5.15 M CsH_2PO_4 and 31 kJ mol^{-1} in 0.10 M H_2SO_4.

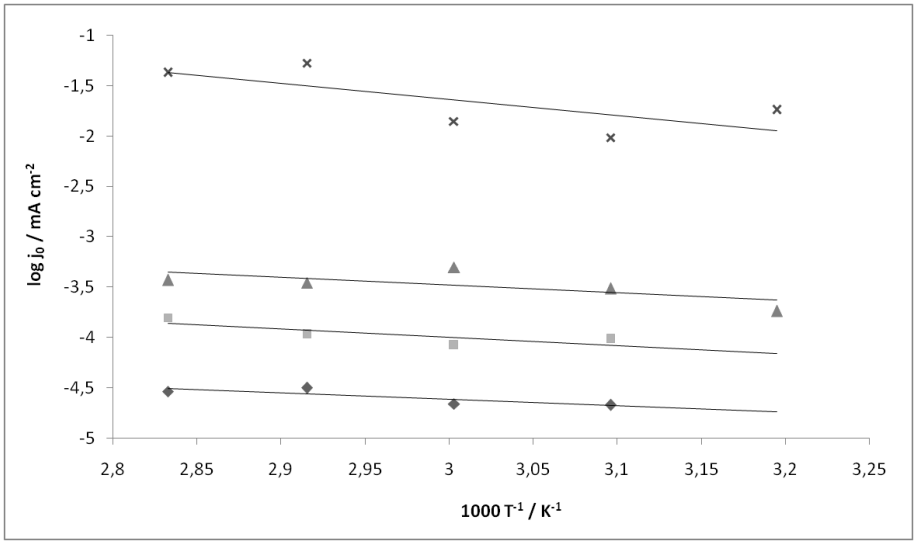

Figure 6.23. Arrhenius plots of for IrO_2 in 5.15 M (♦) H_2SO_4, (■) H_3PO_4, (▲) CsH_2PO_4 and (×) 0.10 M H_2SO_4.

The significantly low values obtained for E_a in all electrolytes, specifically in CsH_2PO_4 considering its low performance towards OER, suggest that the values do not correspond only to purely OER. Other processes occurring at the same potential, i.e. anion desorption or iridium oxidation could be affecting the overall apparent E_a lowering it to the values reported.

6.5 Conclusions

The effect of pH and anion concentration on the electrochemical active surface (EAS) of IrO_2 and Pt black was first addressed. H_2SO_4 was found to be the electrolyte where both catalysts show the highest EAS followed by H_3PO_4 and CsH_2PO_4. This suggests that anion adsorption onto the catalyst surface affects the amount of free catalyst and thus, the overall catalyst performance towards a given reaction. Lower pH values increase the integrated charge for both catalysts because of higher proton concentration and accessibility to the catalytic sites.

The performance of IrO_2 in saturated solution of CsH_2PO_4 shows a significantly low activity towards OER. The effect of pH and different anion nature (sulphates and phosphates) and concentration was addressed by comparing the results to the same concentration (5.15 M) H_2SO_4 and H_3PO_4 and diluted (0.10 M) H_2SO_4 solutions. Onset potential for IrO_2 in CsH_2PO_4 shows the highest overpotential of all electrolytes. This is attributed to the stronger adsorption of phosphates compared to sulphate anions and to the highest anionic concentration of all solutions. The shapes of the steady-state linear sweeps suggest that the activity of IrO_2 towards OER is strongly affected by the pH and thus the main reason of the poor performance on CsH_2PO_4 is caused by the high pH value of the solution (pH = 4.63).

The kinetic study of IrO_2 in the different electrolytes proves that the oxidation of iridium towards a more active oxidation state for OER take place before the actual reaction. This was concluded by noticing an oxidation peak at the low overpotential region in most electrolytes before OER was considered to start. At the moderate overpotential region a well defined Tafel region with slopes of ca. $\left(\frac{RT}{F}\right)$ was exhibited in all electrolytes and attributed to the second step of the reaction mechanism being the rate determining step (equation 6.10), where the release of a proton and an electron from the adsorbed hydroxyl group takes place. The high overpotential region of the polarisation, corrected for mass-transport contribution in the case of 0.10 M H_2SO_4, exhibited Tafel slope values of ca. $\left(\frac{2RT}{F}\right)$ for all H_2SO_4 and H_3PO_4 acid solution. This Tafel value is attributed to the first step of the reaction mechanism being the rate determining step (equation 6.9), where adsorption of the hydroxyl group onto the catalyst takes place. In CsH_2PO_4 saturated solution Tafel

slope values close to $\left(\frac{4RT}{F}\right)$ where measured. These high values are attributed to the difference in the oxide properties of iridium, suggesting that the pH of the CsH_2PO_4 solution is too high to provide enough protons to the iridium to create a hydrous oxide layer, active towards OER.

In conclusion, CsH_2PO_4 in solution is not a favourable electrolyte for IrO_2 towards OER. The low acidity inhibits the activity of the catalyst driven presumably by a change in the oxide layer thickness and composition, to a non-hydrated and less active oxide. The use of this material as solid state electrolyte in a PEM water electrolysis system is studied in Chapter 7.

6.6 References

1. Samaranayake, C.P. and S.K. Sastry, *Electrode and pH effects on electrochemical reactions during ohmic heating.* Journal of Electroanalytical Chemistry, 2005. **577**(1): p. 125-135.
2. Gómez-Marín, A.M. and J.M. Feliu, *Pt(111) surface disorder kinetics in perchloric acid solutions and the influence of specific anion adsorption.* Electrochimica Acta, 2012. **82**(0): p. 558-569.
3. Nylen, L., Behm, M., Cornell, A., & Lindbergh, G., *Investigation of the oxygen evolving electrode in pH-neutral electrolytes: Modelling and experiments of the RDE-cell.* Electrochimica Acta, 2007. **52**(13): p. 4513-4524.
4. Li, S., Chen, H. Y., Tang, M. C., Wei, W., Xia, W., Wu, Y. M. and Jiang, X., *Electrochemical behavior of lead alloys in sulfuric and phosphoric acid electrolyte.* Journal of power sources, 2006. **158**(2): p. 914-919.
5. Kadakia, K., *High performance fluorine doped (Sn,Ru)O_2 oxygen evolution reaction electro-catalysts for proton exchange membrane based water electrolysis.* Journal of power sources, 2014. **245**(0): p. 362-370.
6. Lee, W.H. and H. Kim, *Oxidized iridium nanodendrites as catalysts for oxygen evolution reactions.* Catalysis Communications, 2011. **12**(6): p. 408-411.
7. Li, G., Yu, H., Song, W., Wang, X., Li, Y., Shao, Z., & Yi, B., *Zeolite-templated $Ir_xRu_{1-x}O_2$ electrocatalysts for oxygen evolution reaction in solid polymer electrolyte water electrolyzers.* international journal of hydrogen energy, 2012. **37**(22): p. 16786-16794.
8. Ma, L., S. Sui, and Y. Zhai, *Preparation and characterization of Ir/TiC catalyst for oxygen evolution.* Journal of power sources, 2008. **177**(2): p. 470-477.
9. Ma, H., Liu, C., Liao, J., Su, Y., Xue, X., & Xing, W., *Study of ruthenium oxide catalyst for electrocatalytic performance in oxygen evolution.* Journal of Molecular Catalysis A: Chemical, 2006. **247**(1–2): p. 7-13.
10. Mamaca, N., Mayousse, E., Arrii-Clacens, S., Napporn, T. W., Servat, K., Guillet, N., & Kokoh, K. B., *Electrochemical activity of ruthenium and iridium based catalysts for oxygen evolution reaction.* Applied Catalysis B: Environmental, 2012. **111–112**(0): p. 376-380.
11. Wilson, M.S. and S. Gottesfeld, *Thin-film catalyst layers for polymer electrolyte fuel cell electrodes.* Journal of Applied Electrochemistry, 1992. **22**(1): p. 1-7.
12. O'Hayre, R., Barnett, D. M., & Prinz, F. B., *The triple phase boundary; a mathematical model and experimental investigations for fuel cells.* Journal of The Electrochemical Society, 2005. **152**(2): p. A439 - A444.
13. Trassatti, S. and Petrii, O.A., *Real surface area measurements in electrochemistry.* Pure Appl. Chem., 1991. **63**(5): p. 711-734.
14. Woods, R., *Electroanalytical chemistry: a series of advances*. 1976, New York: Dekker. 1-162.
15. Perez, J., E.R. Gonzalez, and E.A. Ticianelli, *Oxygen electrocatalysis on thin porous coating rotating platinum electrodes.* Electrochimica Acta, 1998. **44**(8–9): p. 1329-1339.
16. Deepalochani, B.K., *Performance of Platinum Black and Supported Platinum Catalysts in a Direct Methanol Fuel Cell* Int. J. Electrochem. Sci., 2009. **4**: p. 386-395.
17. McBreen, J., *Voltammetric Studies of Electrodes in Contact with Ionomeric Membranes.* Journal of The Electrochemical Society, 1985. **132**(5): p. 1112-1116.

18. Faguy, P. W., Markovic, N., Adzic, R. R., Fierro, C. A., & Yeager, E. B., *A study of bisulfate adsorption on Pt(111) single crystal electrodes using in situ Fourier transform infrared spectroscopy.* Journal of electroanalytical chemistry and interfacial electrochemistry, 1990. **289**(1–2): p. 245-262.

19. Ye, S., H. Kita, and A. Aramata, *Hydrogen and anion adsorption at platinum single crystal electrodes in phosphate solutions over a wide range of pH.* Journal of Electroanalytical Chemistry, 1992. **333**(1–2): p. 299-312.

20. Kamat, A., Herrmann, M., Ternes, D., Klein, O., Krewer, U., & Scholl, S., *Experimental Investigations into Phosphoric Acid Adsorption on Platinum Catalysts in a High Temperature PEM Fuel Cell.* Fuel Cells, 2011. **11**(4): p. 511-517.

21. Owe, L.-E., *Characterisation of Iridium Oxides for Acidic Water Electrolysis*, in *Department of Materials Science and Engineering*. 2011, Norwegian University of Science and Technology: Trondheim, Norway.

22. Mamlouk, M., *Investigation of high temperature polymer electrolyte membrane fuel cells*, in Chemical Engineering and Advanced Materials (2008), Newcastle University: Newcastle upon Tyne, thesis.

23. Gottesfeld, S. and S. Srinivasan, *Electrochemical and optical studies of thick oxide layers on iridium and their electrocatalytic activities for the oxygen evolution reaction.* Journal of electroanalytical chemistry and interfacial electrochemistry, 1978. **86**(1): p. 89-104.

24. Burke, L.D., Whelan , D.P., *A voltammetric investigation of the charge storage reactions of hydrous iridium oxide layers.* J Electroanal Chem., 1984. **162**: p. 121-141.

25. Miles, M. H., Klaus, E. A., Gunn, B. P., Locker, J. R., Serafin, W. E., & Srinivasan, S., *The oxygen evolution reaction on platinum, iridium, ruthenium and their alloys at 80 ºC in acid solutions.* Electrochimica Acta, 1978. **23**(6): p. 521-526.

26. Zerbino, J.O., Tacconi, NR. and A.J. Arva, *The Activation and Deactivation of Iridium Electrodes in Acid Electrolytes.* Journal of The Electrochemical Society, 1978. **125**(8): p. 1266-1276.

27. Juodkazytė, J., Šebeka, B., Valsiunas, I., & Juodkazis, K., *Iridium anodic oxidation to Ir (III) and Ir (IV) hydrous oxides.* Electroanalysis, 2005. **17**(11): p. 947-952.

28. Mozota, J. and B.E. Conway, *Surface and bulk processes at oxidized iridium electrodes I. Monolayer stage and transition to reversible multilayer oxide film behaviour.* Electrochimica Acta, 1983. **28**(1): p. 1-8.

29. Felix, C., Maiyalagan, T., Pasupathi, S., Bladergroen, B., & Linkov, V., *Synthesis, characterisation and evaluation of IrO_2 based binary metal oxide electrocatalysts for oxygen evolution reaction.* International Journal of Electrochemical Science, 2012. **7**: p. 12064-12077.

30. Slavcheva, E., Radev, I., Topalov, G., & Budevski, E., *Sputtered electrocatalysts for PEM electrochemical energy converters.* Electrochimica Acta, 2007. **53**(2): p. 362-368.

31. Wen, T.C. and C.C. Hu, *Hydrogen and Oxygen Evolutions on Ru-Ir Binary Oxides.* Journal of The Electrochemical Society, 1992. **139**(8): p. 2158-2163.

32. Boodts, J.C.F. and S. Trasatti, *Hydrogen evolution on iridium oxide cathodes.* Journal of Applied Electrochemistry, 1989. **19**(2): p. 255-262.

33. Cheng, J., Zhang, H., Ma, H., Zhong, H., & Zou, Y., *Study of carbon-supported IrO_2 and RuO_2 for use in the hydrogen evolution reaction in a solid polymer electrolyte electrolyzer.* Electrochimica Acta, 2010. **55**(5): p. 1855-1861.

34. Ardizzone, S., G. Fregonara, and S. Trasatti, *"Inner" and "outer" active surface of RuO_2 electrodes.* Electrochimica Acta, 1990. **35**(1): p. 263-267.

35. Compton, R.G., *Electrode Kinetics: Reactions*. Vol. 27. 1987: Elsevier. 367.

36. Reier, T., M. Oezaslan, and P. Strasser, *Electrocatalytic Oxygen Evolution Reaction (OER) on Ru, Ir, and Pt Catalysts: A Comparative Study of Nanoparticles and Bulk Materials.* ACS Catalysis, 2012. **2**(8): p. 1765-1772.

37. McCrory, C. C., Jung, S., Peters, J. C., & Jaramillo, T. F., *Benchmarking Heterogeneous Electrocatalysts for the Oxygen Evolution Reaction.* Journal of the American Chemical Society, 2013.

38. Doyle, R.L., Godwin, Ian J., Brandon, Michael P., Lyons, Michael E. G., *Redox and electrochemical water splitting catalytic properties of hydrated metal oxide modified electrodes.* Physical Chemistry Chemical Physics, 2013. **15**(33): p. 13737.

39. Gorlin, Y. and T.F. Jaramillo, *A Bifunctional Nonprecious Metal Catalyst for Oxygen Reduction and Water Oxidation.* Journal of the American Chemical Society, 2010. **132**(39): p. 13612-13614.

40. Matsumoto, Y. and E. Sato, *Electrocatalytic properties of transition metal oxides for oxygen evolution reaction.* Materials Chemistry and Physics, 1986. **14**(5): p. 397-426.

41. Zlotorowicz, A., *Electrocatalysts for medium temperature PEM water electrolysis*. 2013, NTNU. p. 144.

42. Pourbaix, M.a.Z., *Electrochemical Properties of the Platinum Metals.* Platinum Metals Rev., 1959. **3**(3): p. 100-106.

43. Minguzzi, A., Fan, F. R. F., Vertova, A., Rondinini, S., & Bard, A. J., *Dynamic potential–pH diagrams application to electrocatalysts for water oxidation.* Chemical Science, 2012. **3**(1): p. 217-229.

44. Walter, J., Weber, J.R., *Adsorption processes.* The University of Michigan, 1974: p. 375-392.

45. Bockris, J.M., *Kinetics of activation controlled consecutive electrochemical reactions: anodic evolution of oxygen.* The Journal of Chemical Physics, 1956. **24**: p. 817.

46. Song, S., Zhang, H., Ma, X., Shao, Z., Baker, R. T., & Yi, B., *Electrochemical investigation of electrocatalysts for the oxygen evolution reaction in PEM water electrolyzers.* international journal of hydrogen energy, 2008. **33**(19): p. 4955-4961.

47. Siracusano, S., Baglio, V., D'Urso, C., Antonucci, V., & Aricò, A. S., *Preparation and characterization of titanium suboxides as conductive supports of IrO_2 electrocatalysts for application in SPE electrolysers.* Electrochimica Acta, 2009. **54**(26): p. 6292-6299.

48. Hu, J. M., Zhang, J. Q., Meng, H. M., & Cao, C. N., *Microstructure, electrochemical surface and electrocatalytic properties of IrO_2+ Ta_2O_5 oxide electrodes.* Journal of materials science, 2003. **38**(4): p. 705-712.

49. John O'M. Bockris, Maria Gamboa-Aldecoa, *Modern Electrochemistry.* 2000. **2**: p. 1232-1236.

50. Leaist, D.G., *Diffusion in aqueous solutions of sulfuric acid.* Can. J. Chem., 1984. **62**: p. 1692-97.

51. Ruiz Bevia, F., J. Fernandez-Sempere, and N. Boluda-Botella, *Variation of phosphoric acid diffusion coefficient with concentration.* AIChE Journal, 1995. **41**(1): p. 185-189.

52. Bockris, J.M. and A.S. Huq, *The mechanism of the electrolytic evolution of oxygen on platinum.* Proceedings of the Royal Society of London. Series A. Mathematical and Physical Sciences, 1956. **237**(1209): p. 277-296.

53. Pletcher, D. and Sotiropoulos, S., *Hydrogen Adsorption-Desorption and Oxide Formation-Reduction on Polycrystalline platinum in Unbuffered Aqueous Solutions*. J. Chem. Soc. Faraday Trans., 1994, **90** (24): p. 3663-3668.

54. Lyons, M.E.G. and Floquet, S., *Mechanism of oxygen reactions at porous oxide electrodes. Part 2 – Oxygen evolution at RuO_2, IrO_2 and $Ir_xRu_{1-x}O_2$ electrodes in aqueous acid and alkaline solution.* Phys. Chem. Chem. Phys., 2011, **13**: p. 5314-5335.

55. Krishtalik, L.J., *Kinetics and mechanism of anodic chlorine and oxygen evolution reactions on transition metal oxide electrodes.* Electrochimica acta, 1980, **26**: p.329 – 337.

56. Kapałka, A., Fóti, G. and Comninellis, C., *Determination of the Tafel slope for oxygen evolution on boron-doped diamond electrodes.* Electrochemistry Communications, 2008, **10 (**4): p.607–610.

57. Chi, E-O., Kwon, Y-U and Mho, S-I., *Oxygen evolution reactioni at electrodes of single phase ruthenium oxides with perovskyte and pyrochlore structures,* Bull. Korean Chem. Soc., 1997, **18** (9): p. 972-976.

58. Gloaguen, F., Leger, J. -M. and Lamy, C., *Electrocatalytic oxidation of methanol on platinum nanoparticles electrodeposited onto porous carbon substrates*. Journal of applied electrochemistry, 1997, **20,** p: 1052-1060

59. Neto, A. O., Perez, J., Napporn, W. T., Ticianelli E.A. and Gonzalez, E. R., *Electrocatalytic oxidation of methanol: Study with Pt:Mo dispersed catalyst.* J. Braz. Chem. Soc., 2000, **11** (1).

CHAPTER 7

CsH_2PO_4 AS ELECTROLYTE IN INTERMEDIATE TEMPERATURE PROTON EXCHANGE MEMBRANE WATER ELECTROLYSIS (IT-PEMWE)

In this chapter the performance of CsH_2PO_4 as electrolyte in a solid electrolyte water electrolysis system is analysed. CsH_2PO_4 was used as a solid pellet and in glass fibre reinforced composite membrane form. Platinum-based cathodes were characterised by cyclic and linear sweep voltammetry in order to study the effect of platinum loading and CsH_2PO_4 loading required as ionomer in the electrode. Anode characterisation was performed by cyclic voltammetry and full electrolysis cell characterisation by linear sweep polarisations. Hydrogen and oxygen evolution reactions were analysed separately and their kinetic parameters calculated. The ohmic contribution of the electrolyte was determined by electrochemical impedance spectroscopy, measuring minimum resistances of ca. 1.5 and 1.0 Ω cm^{-2} for a pellet and a composite membrane, respectively. The maximum activity obtained for the electrolysis system using a CsH_2PO_4 pellet as electrolyte was 20 mA cm^{-2} at 1.90 V and 265 °C. The stability of the electrolyte under operating conditions was addressed for 48 h. Finally, a comparison between CsH_2PO_4–based fuel cell and electrolysis cell systems was carried out.

7.1. Introduction

Material research has focused on the development of intermediate temperature proton conductors, mostly for their application in PEM fuel cell systems. The intermediate temperature range (100 – 300 °C) provides the electrochemical system with numerous advantages such as, higher thermodynamic efficiency, faster kinetics and easier water management.

In 2001 *Sossina Haile's* group in Caltech, California, proposed solid acids as promising proton conductor materials [1] and few years later they developed an intermediate temperature fuel cell based on CsH_2PO_4 as electrolyte. The initial performance of 48.9 mW

cm^{-2} obtained for a H_2/O_2 fuel cell with a 280 µm CsH_2PO_4 pellet [2] was then greatly improved to 415 mW cm^{-2} by reducing the electrolyte thickness to 25 µm [3].

Water electrolysis is often regarded as the opposite principle of a fuel cell. While in a H_2/O_2 fuel cell hydrogen oxidation reaction (HOR) and oxygen reduction reaction (ORR) take place in the electrodes, in a water electrolysis hydrogen evolution reaction (HER) and oxygen evolution reaction (OER) take place; the same reactions but in opposite directions. For this reason, the promising results obtained for CsH_2PO_4-based PEMFC were also expected in an intermediate temperature PEMWE. The main difference of these two electrochemical systems is the material used in the oxygen electrode. While in PEMFC, carbon supported platinum is commonly used as catalyst on carbon paper/cloth gas diffusion layer (GDL) for the ORR, in PEMWE iridium oxide is used as OER catalyst and titanium foam/mesh as GDL or current collector. Carbon materials are not used in the anode of PEMWE in order to avoid its electrochemical oxidation at high potentials (equation 7.1) [4].

$$C + 2H_2O \leftrightarrow CO_2 + 4H^+ + 4e^- \qquad E_{SHE} = 0.207\ V \qquad (7.1)$$

The role of the electrolyte in both PEMFC and PEMWE systems is to conduct the produced protons between both electrodes, closing the electrochemical circuit. The conductivity and thickness of this electrolyte will provide the system with certain ohmic resistance, and thus, minimum thickness with a maximum conductivity is required for a successful operation. The environment provided by the electrolyte/catalyst interface in the electrode surface is equally relevant for a good electrochemical performance.

In chapter 6 the effect of a saturated aqueous solution of CsH_2PO_4 on the activity of IrO_2 as OER catalyst was studied. The system exhibited poor activity compared to that obtained in concentrated (and diluted) H_2SO_4 and H_3PO_4 acids. Three different Tafel slopes were identified in all the systems, being the values obtained in the 40 – 80 ºC temperature range for CsH_2PO_4 the following; (1) b ~ 162 mV dec^{-1} at the low overpotential region (2) b ~ 75 mV dec^{-1} at the moderate overpotential region and (3) b ~ 220 mV dec^{-1} at the high overpotential region. The first Tafel region was attributed to the electro-oxidation process of iridium, presumably Ir^{IV}/Ir^{VI}. The second and third Tafel regions were attributed to the OER by the *electrochemical oxide path* mechanism (reactions 6.9 - 6.11), where the rate determining step of the reaction changes from the second step (reaction 6.10) being the

r.d.s. at moderate overpotentials, to the first step (reaction 6.9) being r.d.s. at high overpotentials. The high Tafel slope values obtained at the high overpotential region (b ~ 220 mV dec^{-1}) were attributed to the high pH environment provided by the electrolyte (pH = 4.63), which is considered to affect the oxygen evolution reaction in iridium oxide by the following mutually related reasons:

- The oxidation process of iridium requires a protonation step (equation 6.1) in order to create a hydrated oxide layer active towards OER. The high pH of the electrolyte, close to neutral, would not provide enough proton concentration, creating an oxide layer with different characteristics and lower activity towards OER.
- The acidic reaction mechanism considered in this process, equations 6.9 – 6.11, relies on the active sites of iridium oxide to carry out the oxygen evolution reaction by the adsorption of intermediate species, such as $S\text{-}OH_{ads}$ or $S\text{-}O_{ads}$ and by the release of protons. The low proton concentration of the electrolyte would affect the activity of the catalytic sites towards OER by altering the affinity of the oxide surface to the intermediates of the reaction mechanism.

On the other hand, the low relative humidity in the electrolysis system at intermediate temperature and ambient pressure, RH ~ 3.0 % at 250 ºC, may affect the performance of the system in terms of mass transport. Besides, it is proposed in this research that the low water concentration in the catalytic layer may cause a catalytically driven dehydration of CsH_2PO_4 to use the produced water as reactant. In other words, at the conditions applied, it may be more favourable for IrO_2 to obtain water from the structure of CsH_2PO_4 than from the vapour phase.

Therefore, in order to study the feasibility of CsH_2PO_4 as solid electrolyte in an IT-PEMWE system, the compatibility of this material for a good kinetic performance with both platinum and iridium oxide and the stability of the electrolyte under operation conditions were addressed.

7.2. Experimental

Electrolytes

CsH_2PO_4 polycrystalline powder was synthesised as explained in section 4.2. Pellets were fabricated by pressing the powder at 7×10^3 kg cm^{-2} at room temperature for 30 min.

Pellets were approximately 300 µm thick (although exact thickness was measured for each one of the samples) and 1.8 cm diameter. CsH_2PO_4-based glass fibre reinforced composite membranes (CDP_{GF}) were fabricated as explained in section 5.2.3. The thicknesses of these composite membranes were ca. 85±5 µm.

Cathodes

Cathodes for water electrolysis were fabricated by spraying the required amount of Pt black ink dispersion on carbon paper (Freudenberg H2315-I2-C8, with microporous layer) at 80 °C. Pt loadings in these electrodes varied between 0.5 – 2.0 mg Pt cm^{-2}. Pt black inks were prepared by dispersing 3.0 mg ml^{-1} Pt black (Alfa-Aesar) in 5 ml isopropanol:water solution (volume ratio, 1:3) and sonicating for 1 h. CsH_2PO_4, as ionomer, was added to the ink dispersion in Pt:CsH_2PO_4 ratios of 2:1, 1:1 and 1:2. Final CsH_2PO_4 ionomer loadings in the electrodes varied between 0 – 2.0 mg CsH_2PO_4 cm^{-2}. Reference electrodes loaded with 2.0 mg Pt black cm^{-2} were fabricated using the same procedure as above. No CsH_2PO_4 was added as ionomer to these electrodes.

Anodes

Anodes for water electrolysis were fabricated by three different methods:

Onto CsH_2PO_4 pellet:

1. Pipetting the required amount of IrO_2 ink dispersion onto the surface of the CsH_2PO_4 pellet at 80 °C. IrO_2 loadings in these electrodes varied between 0.5 – 3.0 mg IrO_2 cm^{-2}. IrO_2 inks were prepared by dispersing 5.0 mg IrO_2 (Sigma-Aldrich) in 2 ml of isopropanol and sonicating for 2 h. CsH_2PO_4, as ionomer, was added to the ink dispersion in IrO_2:CsH_2PO_4 ratios of 2:1, 1:1 and 2:3. Final CsH_2PO_4 ionomer loadings in the electrodes varied between 0 – 3.0 mg CsH_2PO_4 cm^{-2}. IrO_2 loadings were verified by weighing the pellet before and after the ink deposition. Pellets were kept at 80 °C for 24 h prior to the first weight measure.

Onto CDP_{GF} composite membrane:

2. Spraying the required amount of IrO_2 ink dispersion onto the surface of CDP_{GF} composite membrane at 80 °C. Electrodes with 2.0 mg IrO_2 cm^{-2} were fabricated. IrO_2 inks were prepared by dispersing 5.0 mg IrO_2 (Sigma-Aldrich) in 2 ml of isopropanol and sonicating for 2 h. CsH_2PO_4, as ionomer, was added to the ink dispersion in 1:1

IrO_2:CsH_2PO_4 ratio. IrO_2 loadings were verified by weighing the CDP_{GF} membranes before and after the ink deposition. Membranes were kept at 80 °C for 24 h prior to the first weight measure.

3. Using the *Decal method*; spraying the required amount of IrO_2 ink dispersion onto the surface of a teflon sheet and drying it at 80 °C for 4 h. The sprayed teflon and the CDP_{GF} membrane were compressed at 0.5 kg cm^{-2} for 5 min at room temperature for a complete transfer of the catalyst. Electrodes with 2.0 mg IrO_2 cm^{-2} were fabricated. IrO_2 inks were prepared by dispersing 5.0 mg IrO_2 (Sigma-Aldrich) in 3 ml isopropanol:water solution (volume ratio, 1:3) and sonicating for 2 h. CsH_2PO_4 was added as ionomer to the ink dispersion in 1:1 IrO_2:CsH_2PO_4 ratio. IrO_2 loadings were verified by weighing the CDP_{GF} membranes before and after the ink transfer. Membranes were kept at 80 °C for 24 h prior to the first weight measure.

Membrane Electrode Assembly (MEA)

MEAs were fabricated in-situ by assembling together the Pt-loaded carbon paper (cathode), the anode-deposited electrolyte and the gold-coated titanium mesh in the cell. The torque provided to the system was 3 atm by a pressurised piston. The MEA was sealed using high temperature silicone (ACC silicones, silicoset 158).

7.3 Cathode performance

Platinum-based cathodes were characterised in terms of electrochemical active surface and activity towards the hydrogen evolution reaction (HER). The effect of the platinum loading and CsH_2PO_4 loading (as ionomer) on the electrode performance was characterised by cyclic and linear sweep voltammetry. The kinetic parameters of these electrodes towards HER were calculated. CsH_2PO_4 pellet (thickness of ca. 300 μm) was used as electrolyte in all experiments. All experiments were performed between 235 and 275 ºC.

7.3.1 Electrochemical Active Surface (EAS)

Cyclic voltammetry was used in order to estimate the catalyst utilisation of the fabricated platinum-based cathodes. Experiments were carried out using the methodology explained in section 3.2.2, by feeding 50 ml min^{-1} H_2 gas to the reference (and counter) electrode and 50 ml min^{-1} N_2 gas to the working electrode. Platinum black loadings were varied between

0.5 - 2.0 mg Pt cm^{-2}. In figure 7.1 the cyclic voltammograms of these electrodes are shown in the potential range 0 – 1000 mV (vs RHE). A CV of Pt black electrode in a saturated aqueous solution of CsH_2PO_4 is shown as an inset in figure 7.1.

The increasing Pt loading did not show any significant effect in the shape or coulombic charge of the voltammograms performed. A slight increase in the double layer of the voltammogram in the 500 – 800 mV range was attributed to the increasing thickness of the catalytic layer when the loading increased. As potentials higher than 1000 mV (vs RHE) were not applied, platinum oxidation did not take place in the electrode and therefore no platinum reduction peak at ca. 800 mV appeared in the backward scan.

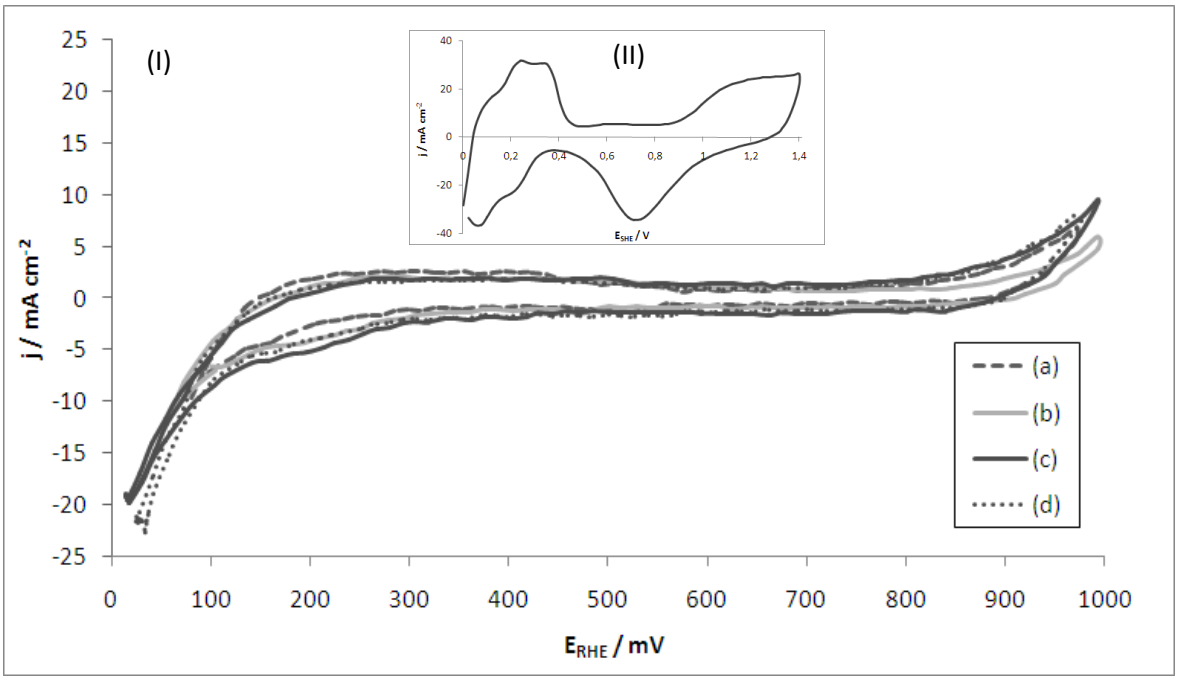

Figure 7.1. (I) Cyclic voltammograms of cathodes (cycles nº 10) with (a) 0.5 mg Pt cm^{-2}, (b) 1.0 mg Pt cm^{-2}, (c) 1.5 mg Pt cm^{-2} and (d) 2.0 mg Pt cm^{-2} at 100 mV s^{-1} and 245 ºC (reference loading = 2.0 mg Pt cm^{-2}, no ionomer). (II) Cyclic voltammogram of Pt black (cycle nº 10) in 5.15 M CsH_2PO_4 solution at 40 ºC and 100 mV s^{-1}.

Table 7.1. Coulombic charge (Q) of cathodes with different Pt loadings (no ionomer).

Pt loading / mg cm^{-2}	**Q / mC cm^{-2}**
0.5	52.4
1.0	62.0
1.5	56.5
2.0	48.2

As the CVs did not show a clear hydrogen desorption area in the 0 – 400 mV range, EAS values (obtained by equation 3.3) could not be calculated. Instead, the charge value of the entire CV was calculated for each sample and compared as shown in table 7.1. It needs to be clarified that the charge obtained by the integration of the whole CV did not represent the EAS of platinum of the electrode, as other parameters (i.e. double layer or platinum oxidation charge) were included in the value. Nevertheless, considering the similarity between all voltammograms, the charge obtained was used as an indicator of the amount of active platinum for comparison between electrodes.

As shown in table 7.1, the difference in platinum loading on the electrode did not affect significantly the coulombic charge obtained by the integration of the voltammograms. All electrodes show a relatively constant value between 48.2 – 62.0 mC cm^{-2}. Assuming these values to be proportional to the catalyst utilisation in terms of ESA, the catalyst loading increase was not considered to enhance significantly platinum utilisation. This is explained by considering only the catalytic layer in contact with the electrolyte surface active in the process. The platinum in contact with the electrolyte provided a triple-phase-boundary where electrons, protons and reactants could be transported by electric (platinum), protonic (electrolyte) and gaseous (pores) pathways, respectively. The excess of platinum standing on top of the first catalytic active layer was not active in the process because of the absence of protonic pathways from the catalytic site to the electrolyte. The addition of a proton conducting agent to act as ionomer in the catalytic layer was therefore required in order to provide greater amount of active catalytic sites in the electrode and thus, to increase the ESA of the electrode.

CsH_2PO_4 in its polycrystalline form was added as ionomer to the catalytic layer. CsH_2PO_4 loadings of 0.5, 1 and 2 mg cm^{-2} were added in order to estimate the optimum value of ionomer required to provide ionic pathways while adding the minimum resistance possible to the electrode. In figure 7.2-I the cyclic voltammograms of CsH_2PO_4-loaded electrodes are plotted and compared to an electrode with no CsH_2PO_4 as ionomer. As an indicator of the catalyst utilisation on the electrode, as CVs did not show clear hydrogen desorption area, the charge value of the entire CV was calculated and compared as shown in table 7.2. A CV of Pt black electrode in a saturated aqueous solution of CsH_2PO_4 is shown as an inset in figure 7.2.

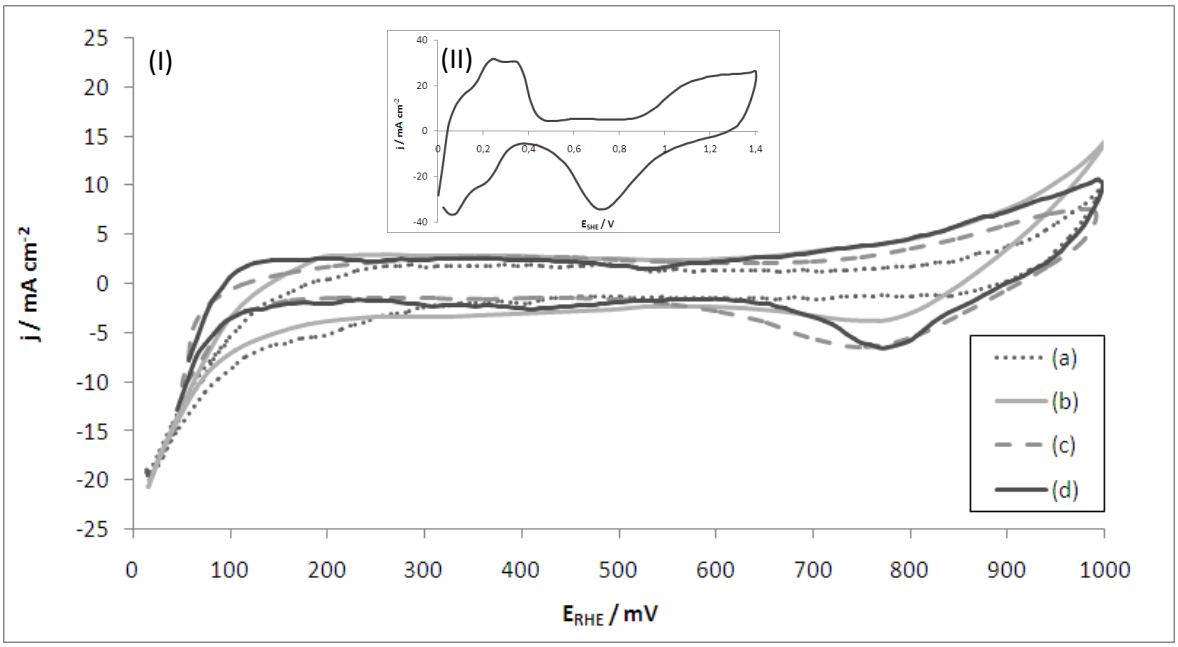

Figure 7.2. (I) Cyclic voltammograms of cathodes (cycles nº 10) with 1.0 mg Pt cm^{-2} and CsH_2PO_4 loadings of (a) 0 mg cm^{-2}, (b) 0.5 mg cm^{-2} (c) 1.0 mg cm^{-2} and (d) 2.0 mg cm^{-2} at 100 mV s^{-1} and 245 ºC (reference loading = 2.0 mg Pt cm^{-2}, no ionomer). (II) Cyclic voltammogram of Pt black (cycle nº 10) in 5.15 M CsH_2PO_4 solution at 40 ºC and 100 mV s^{-1}.

Table 7.2. Coulombic charge (Q) of cathodes with different CsH_2PO_4 loadings (1.0 mg Pt cm^{-2}).

CsH_2PO_4 loading / mg cm^{-2}	**Q / mC cm^{-2}**
0	62.0
0.5	95.5
1.0	97.4
2.0	103

The shape of the voltammograms changed when CsH_2PO_4 was added as ionomer, being noticeable more defined platinum oxidation/reduction area and a small increase in the double layer charge. Although the hydrogen desorption peak at 0 – 400 mV did not exhibit significant changes, the appearance of a platinum reduction peak at 700 – 800 mV suggests that CsH_2PO_4 had an effect in the catalyst utilisation of the electrode.

Charge values obtained by the integration of the CV increase considerably by the addition of CsH_2PO_4 as ionomer. The difference is mainly attributed to the area of platinum oxidation/reduction region, making charge values increase by ca. 60 % when 0.5 – 2 mg cm^{-2} CsH_2PO_4 was added as ionomer. The slight increase in the double layer charge was

attributed to the greater thickness and the capacitance added to the catalytic layer by the solid acid.

Comparing the shape of the CVs of the electrodes in the solid sate system to that of the CsH_2PO_4 aqueous solution (figure 7.2-II) the difference in the hydrogen desorption/ adsorption area can be addressed. The significant difference between both systems is caused by the higher mobility and accessibility of protons in the aqueous solution. The low catalyst utilisation in the solid system is therefore attributed to the low availability of protons in the catalytic sites of platinum.

The activity of these electrodes towards hydrogen evolution reaction was analysed and the kinetic parameters calculated in order to address the contribution of the cathodes to the overall losses of the electrolysis system.

7.3.2 Hydrogen Evolution Reaction (HER)

The activity of platinum-based cathodes towards hydrogen evolution was evaluated by quasi-steady linear sweep polarisations of a Pt/CsH_2PO_4/Pt MEA system. The electrolysis cell was operated in 'hydrogen pump mode' (see section 3.2.3) in order to estimate the kinetic limitations of the electrodes towards HER and their contribution to the overall electrolysis performance losses. The understanding of the effect of the electrolyte on the kinetic parameters of platinum towards HER is fundamental for a successful application of this catalyst in the electrolyser cell. The linear sweeps were performed at the temperature range of 235 – 275 °C using as electrolyte a solid CsH_2PO_4 pellet of ca. 300 µm thickness.

In figure 7.3 HER polarisations of 1.0 mg cm^{-2} platinum loaded electrode, with no CsH_2PO_4 ionomer, at 235, 245, 255 and 265 °C are shown. These polarisations showed an expected tendency of increasing activity with temperature, attributed to faster reaction kinetics and lower ohmic resistance of the electrolyte at higher temperatures. However, as shown in figure 7.4, the performance of the electrode at temperatures higher than 265 °C decreases. This decrease in the activity of the electrode is attributed to the melting of the electrolyte at those temperature and humidity conditions (P_{H2O} = 0.95 atm). The melting of the electrolyte could on one hand, partially occlude the porosity of the electrode, difficulting the access of gas to the electrochemically active catalytic sites, and on the other hand, affect the stability of the catalyst due to phosphate adsorption. Both theories explain the considerable decrease in activity of electrodes at temperatures higher than 265 °C. This

temperature was therefore considered as the maximum operating temperature of the system. The iR values measured did not show any significant change from 265 to 275 °C (figure 7.6) and therefore the electrolyte resistance was not considered responsible for the decrease in activity, bearing in mind that the opposite effect was expected .

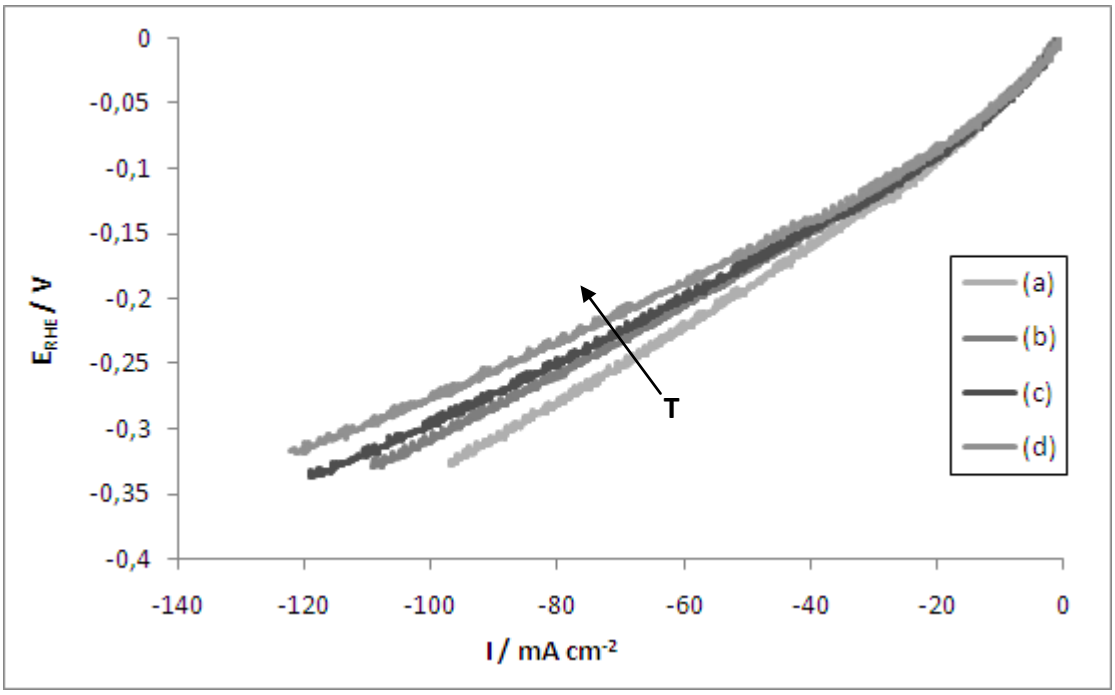

Figure 7.3. HER polarisations of a cathode with 1.0 mg Pt cm^{-2} and no CsH_2PO_4 ionomer at (a) 235°C (b) 245°C (c) 255°C and (d) 265°C (sweep rate = 1 mV s^{-1}).

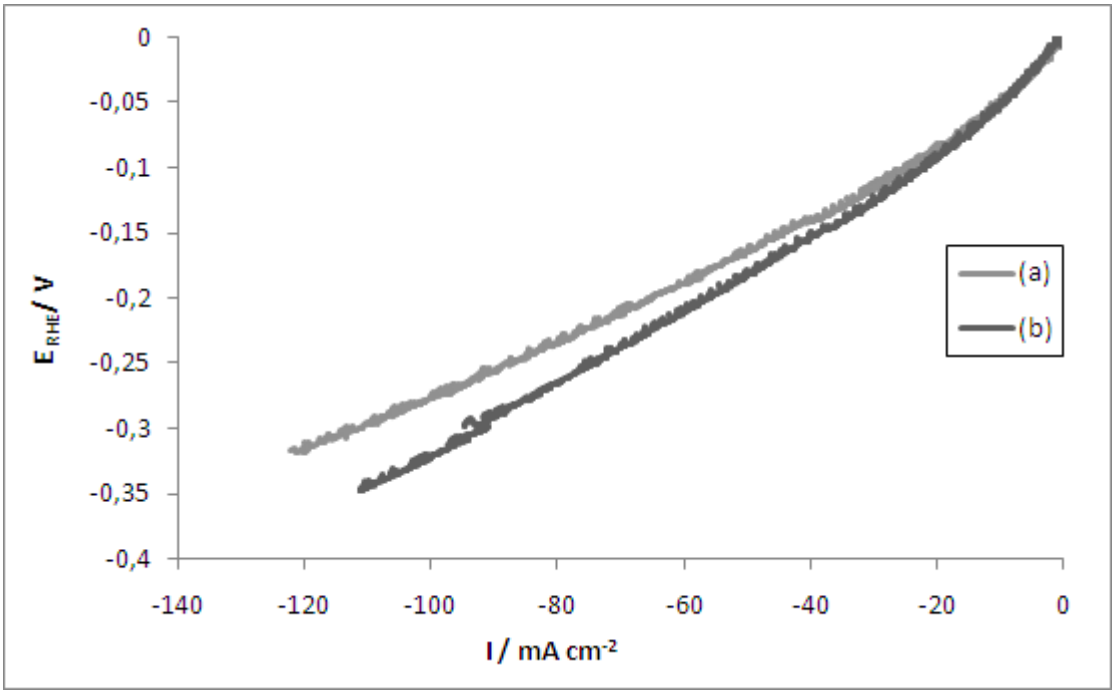

Figure 7.4. HER polarisations of a cathode with 1.0 mg Pt cm^{-2} and no CsH_2PO_4 ionomer at (a) 265 °C (b) 275°C (sweep rate = 1 mV s^{-1}).

The effect of CsH_2PO_4 as ionomer in the HER electrodes was evaluated by measuring their activity at -100 and -300 mV overpotential. The activity of electrodes with 0, 1.0 and 2.0 mg cm^{-2} CsH_2PO_4 as ionomer are plotted and compared in figure 7.5. The addition of CsH_2PO_4 as ionomer to the catalytic layer did not have any significant effect on the activity of the electrodes towards HER. The reason of absence of effect in the HER activity was attributed to the physical morphology of CsH_2PO_4, that is, discrete particles. In order to act as a proton conducting agent in the catalytic layer, the ionomer must fulfil two main requirements; (1) it has to exhibit good *percolation degree* and (2) it has to allow gases reaching and leaving the catalytic site.

The first of these requirements means that the ionomer in contact with the catalytic site must build a well interconnected framework able to transport protons from the reaction site to the electrolyte. In low temperature electrodes this is achieved by adding an optimum amount of polymeric ionomer (i.e. Nafion®) which creates an extremely thin film (ca. 0.5 - 1 nm) on top of the catalyst, which on one hand, provides proton conducting pathways to the electrolyte and one the other hand, is thin enough to avoid blocking the access of reactants to the catalytic site [5, 6]. In this case, however, the morphology of CsH_2PO_4 as discrete particles distributed in the catalytic layer did not allow building an interconnected framework of it and therefore no access of the electrochemically produced protons to the electrolyte was possible. For this reason it is suggested that even in CsH_2PO_4 ionomer-loaded electrodes only the first catalytic layer, in contact with the pellet surface, was active in the hydrogen evolution reaction.

Due to the absence of any significant effect in activity by adding CsH_2PO_4 as ionomer, the electrode with no ionomer and 1.0 mg cm^{-2} was used in further electrolysis experiments.

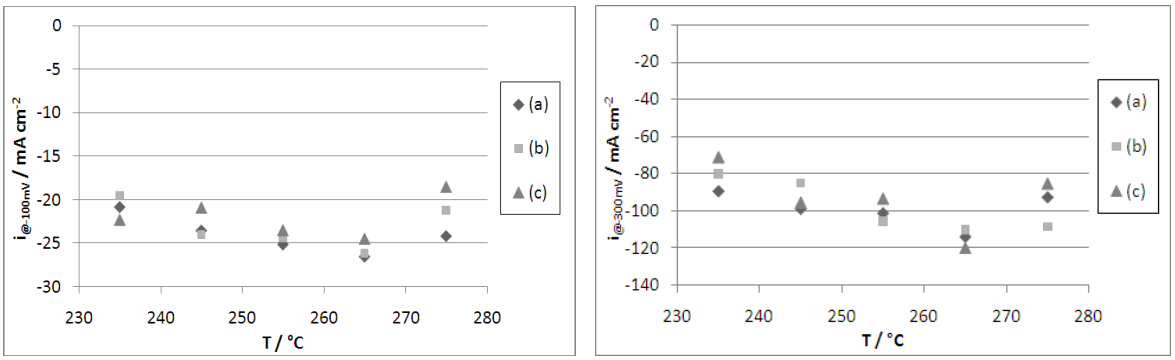

Figure 7.5. HER activity of 1.0 mg Pt cm^{-2} electrode with CsH_2PO_4 loadings of (a) 0 mg cm^{-2} (b) 1.0 mg cm^{-2} and (c) 2.0 mg cm^{-2} at (I) -100 mV and (II) -300 mV overpotential.

The kinetic parameters of this electrode towards HER were calculated and discussed. The linear sweeps were performed at the temperature range of 235 – 275 °C and corrected for the ohmic resistance provided by the electrolyte, a solid CsH_2PO_4 pellet (thickness of ca. 300 µm). The iR contribution of the electrolyte was measured at each temperature by electrochemical impedance spectroscopy and its effect subtracted from the HER polarisations. The Nyquist plots obtained are shown in figure 7.6. The resistance of the electrolyte was obtained from the high frequency intercept with the real axis of the spectrum, varying from 1.93 Ω cm^2 at 235 °C to 1.57 Ω cm^2 at 265 °C. At 275 °C the resistance of the electrolyte was slightly increased, about 100 mΩ, presumably due to the melting of the electrolyte and its flow to the electrodes.

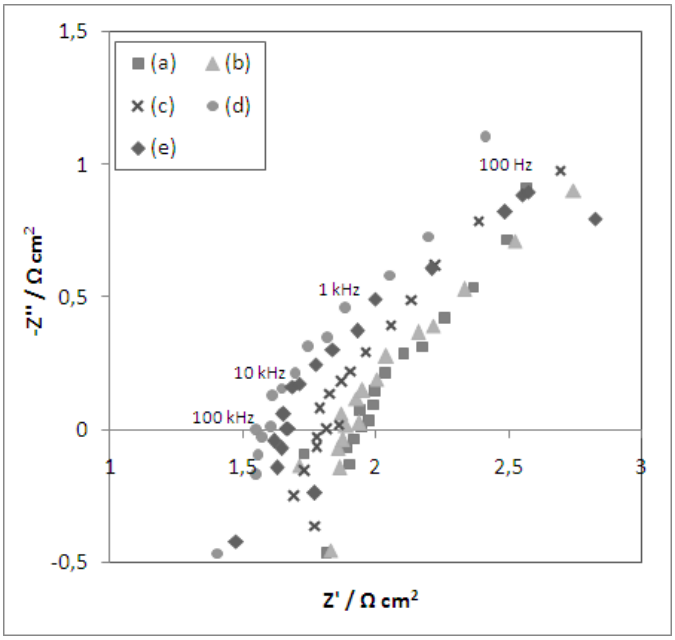

Figure 7.6. Nyquist plot of the electrolyte resistance (CsH_2PO_4 pellet, ca. 300 µm thickness) at (a) 235°C (b) 245°C (c) 255°C (d) 265°C and (e) 275 °C.

Tafel plots of the iR corrected polarisations were plotted at all temperatures and the linear region corresponding to the Tafel region identified. From this linear region the Tafel slope of the electrode towards HER was fitted and calculated (figure 7.7). Tafel slopes were fitted in the potential range of -30 to -80 mV as this was identified as the most linear region in the logarithmic plot. The minimum regression obtained for the linear fitting was R^2 = 0.979 at 245 °C, which was high enough to consider it as a linear region. The exchange current densities were calculated by extrapolating the Tafel linear equation to the reversible potential for HER at the conditions of each polarisation. All Tafel and exchange current densities obtained for each temperature are shown in table 7.3.

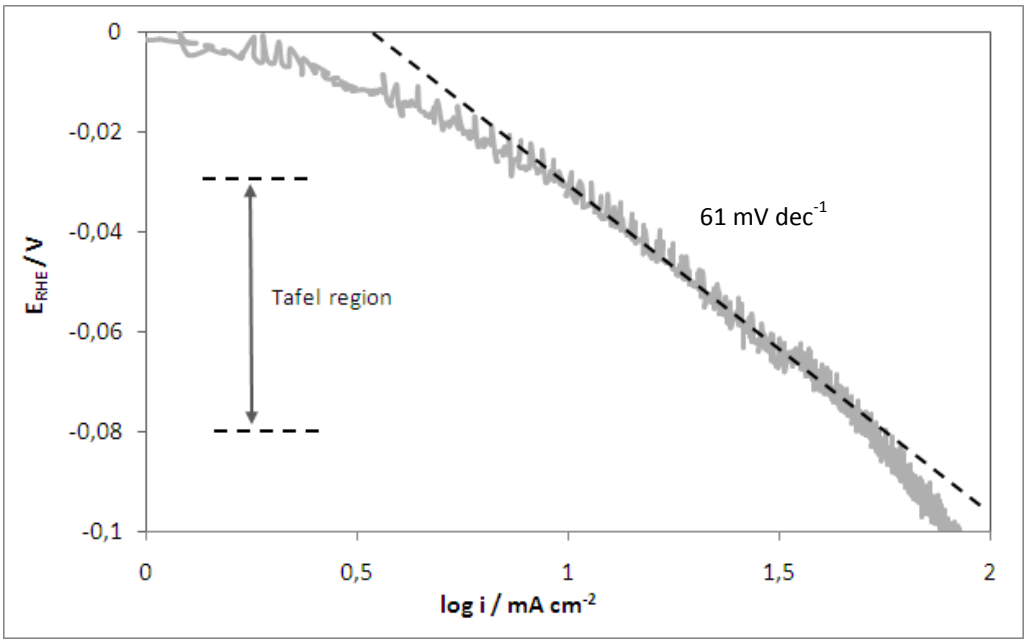

Figure 7.7. Tafel slope of 1.0 mg Pt cm^{-2} electrode at 245°C (iR corrected).

The Tafel values obtained decrease from 87 to 52 mV dec^{-1} when increasing the temperature from 235 to 265 ºC. At 275 ºC the Tafel value increases to 83 mV dec^{-1} caused presumably by the melting of the electrolyte. This increase in the slope at 275 ºC could be attributed either to slower kinetics in the melted form of CsH_2PO_4 or to other kinetic process happening at those conditions, such as phosphate adsorption, due to a higher mobility of anions in the melted material.

Table 7.3. Kinetic parameters of HER of 1.0 mg Pt cm^{-2} electrode (no ionomer).

Temperature / °C	**Tafel slope / mV dec^{-1}**	**Exchange current density, j_0 / mA $cm^{-2}_{[XRD]}$**
235	87	1.35×10^{-2}
245	67	1.30×10^{-2}
255	61	1.27×10^{-2}
265	52	1.28×10^{-2}
275	83	1.61×10^{-2}

Tafel slope values reported for platinum in acid solution exhibit values of 30 – 40 mV dec^{-1} at low overpotentials and room temperature [7,8]. The commonly accepted HER mechanism in acidic media is given by a combination of equations 7.1 – 7.3 [14, 17].

$$S + H^+ + e^- \rightarrow S\text{-}H_{ads} \quad \text{(Volmer reaction)} \quad (7.1)$$

$$2\ S\text{-}H_{ads} \rightarrow 2S + H_2 \quad \text{(Tafel reaction)} \quad (7.2)$$

$$S\text{-}H_{ads} + H^+ + e^- \rightarrow S + H_2 \quad \text{(Heyrovsky reaction)} \quad (7.3)$$

According to this mechanism, first a proton and an electron combine on the catalyst surface into an adsorbed hydrogen atom. It can be followed either by a recombination of two adsorbed atoms or by an adsorbed atom combining with a proton and an electron in the catalytic site to form a diatomic hydrogen molecule. *Conway and Bai* [15], proposed a mechanism to justify experimentally obtained 30 mV dec^{-1} Tafel slope (25 ºC), where Tafel and Heyrovsky reactions occur in parallel paths, being Tafel reaction more predominant at low overpotentials and Heyrovsky reaction at high overpotentials. This mechanism is believed to occur in the CsH_2PO_4 system studied, were Tafel slopes exhibit approximately the same expression $\left(\frac{RT}{2F}\right)$ considering the temperature difference.

The exchange current density values were normalised to the area calculated from P-XRD (table 6.1), considering the 1.0 mg cm^{-2} platinum loading on the electrode. The values obtained were lower than the values reported for HER in acidic medium, which commonly show values in the range of 0.1 – 1.0 mA $cm^{-2}_{[XRD]}$ [7, 8], 10 to 100 times higher. This means that at equilibrium, the rate of reaction is lower in the solid CsH_2PO_4 system compared to aqueous acid solutions. This is attributed to a higher mobility of protons in the acid solution compared to that of the solid CsH_2PO_4 system, or in other words, to a higher platinum ESA in the aqueous system. Besides, the interface between the solid pellet electrolyte and the electrode is considered to be less intimate than that of the aqueous solution, making it harder for the electrode to exchange protons with the electrolyte, and therefore, decreasing the exchange current density. It must be pointed, however, that the estimation of j_0 is based on 1 mg cm^{-2} platinum loading considered in the electrode, which is likely to be partially inactive in the electrochemical reaction.

The decreasing tendency of the Tafel slope with temperature caused the exchange current density to keep relatively constant at all temperatures instead of increasing with temperature as it was expected. For this reason the activation energy of the process could not be calculated.

7.4. Anode performance

Iridium oxide-based cathodes were characterised in terms of electrochemical active surface and activity towards oxygen evolution reaction (OER). The effect of IrO_2 loading and CsH_2PO_4 loading (as ionomer) on the electrode performance was characterised by cyclic and linear sweep voltammetry. In order to determine the activity of the fabricated anodes towards OER, the kinetic contribution of the cathode and the ohmic contribution of the electrolyte were subtracted from the polarisation curves. The kinetic parameters of these electrodes towards OER were calculated.

7.4.1. Electrochemical Surface Area (ESA)

The electrochemical surface area of the fabricated anodes was estimated by integrating the charge of cyclic voltammograms performed from 0 – 1.4 V. These anodes were used as working electrodes with 50 ml min^{-1} N_2 flow and the platinum-loaded cathode with 50 ml min^{-1} H_2 flow as reference and counter electrode. Both gases were saturated with 0.95 atm of partial pressure of water. Iridium oxide loadings were varied from 0.5 to 3.0 mg cm^{-2} in order to study the effect of the loading in the EAS of the electrode. CVs are shown in figure 7.8-I. CV of IrO_2 in a saturated solution of CsH_2PO_4 is shown in figure 7.8-II.

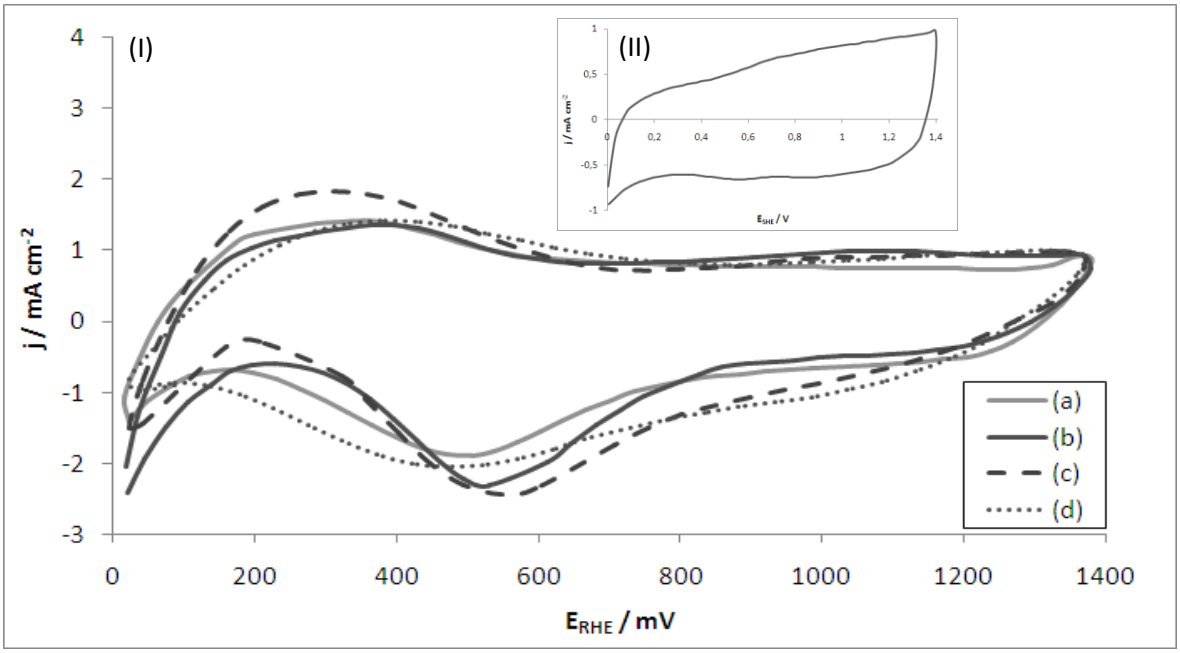

Figure 7.8. (I) Cyclic voltammograms of anodes (cycles nº 10) with no ionomer and IrO_2 loadings of (a) 0.5 mg cm^{-2}, (b) 1.0 mg cm^{-2}, (c) 2.0 mg cm^{-2} and (d) 3.0 mg cm^{-2} at 100 mV s^{-1} and 245 ºC (cathode loading = 1.0 mg Pt cm^{-2}, no ionomer). (II) Cyclic voltammogram of IrO_2 (cycle nº 10) in 5.15 M CsH_2PO_4 solution at 40 ºC and 100 mV s^{-1}.

Table 7.4. Charge of the integrated CVs of anodes with different IrO_2 loadings (no ionomer).

IrO_2 loading / mg cm^{-2}	**Q / mC cm^{-2}**
0.5	12.4
1.0	11.9
2.0	15.0
3.0	14.0

All electrodes exhibit a similar shape with a broad oxidation peak between 100 – 500 mV and a notorious reduction peak at approximately 550 mV. The shape of the CV differs considerably from that obtained in the aqueous solution, where two non-well defined iridium redox couples were identified at ca. 0.7 and 1.0 V (figure 7.8-II), attributed to Ir/Ir^{III} and Ir^{III}/Ir^{IV} respectively (see section 6.3.3).

The charge values obtained from the integration of the CVs, given in table 7.4, suggest that no significant increase in the IrO_2 utilisation is achieved by increasing catalyst loading. This agrees with the idea of being just the catalyst in contact with the electrolyte, the first layer of IrO_2 deposited on top of the pellet, active in the electrode. The absence of ionomer, and therefore, proton conducting paths in the catalytic layer, causes the catalyst on top of the first layer to be inactive. All integrated charge values obtained were in the range of 11.9 – 15.0 mC cm^{-2}. These values are similar to the charge obtained by the integration of the CV in the aqueous solution, 16.2 mC cm^{-2}. Despite the similarity in charge values, it is important to note the high contribution of the reduction peak at ca. 550 mV to the whole charge of the CVs of the solid state system. This significant peak, not exhibited in the aqueous system, is not considered to correspond to a redox couple of iridium despite being included in the charge values given. The charge value of this peak is similar in all the electrodes analysed, exhibiting values of ca. 3.1 ± 0.5 mC cm^{-2}.

In order to increase the catalyst utilisation in the catalyst layer, CsH_2PO_4 was added as ionomer in the electrode to provide higher amount of triple phase boundary areas by building proton conducting paths. Electrodes with IrO_2:CsH_2PO_4 mass ratios of 2:1, 1:1 and 2:3 were characterised by cyclic voltammetry and the integrated charge compared to an electrode with no ionomer. CVs and charge values are shown in figure 7.9 and table 7.5.

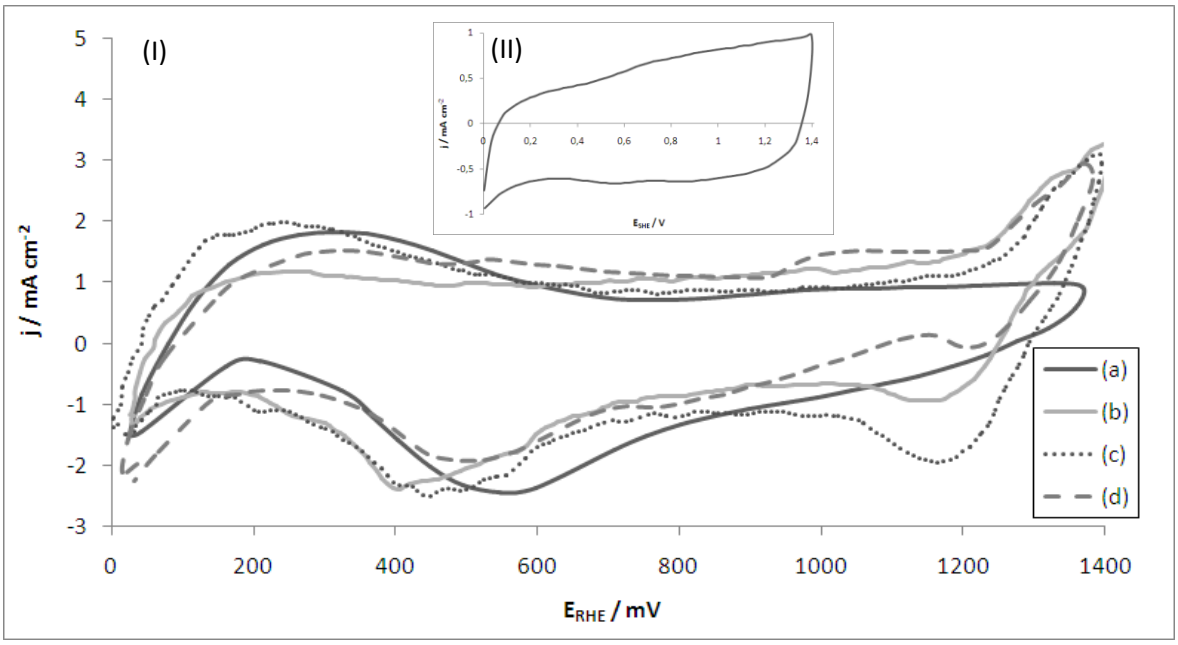

Figure 7.9. Cyclic voltammograms of anodes (cycles nº 10) with 2.0 mg cm^{-2} and CsH_2PO_4 loadings of (a) 0 mg cm^{-2}, (b) 1.0 mg cm^{-2} (c) 2.0 mg cm^{-2} and (d) 3.0 mg cm^{-2} at 100 mV s^{-1} and 245 ºC (cathode loading = 1.0 mg Pt cm^{-2}, no ionomer). (II) Cyclic voltammogram of IrO_2 (cycle nº 10) in 5.15 M CsH_2PO_4 solution at 40 ºC and 100 mV s^{-1}.

Table 7.5. Charge of the integrated CVs of anodes with different IrO_2 loadings (no ionomer).

CsH_2PO_4 loading / mg cm^{-2}	**Q / mC cm^{-2}**
0	16.5
1.0	14.9
2.0	17.9
3.0	14.1

The charge values obtained, between 14.1 – 17.9 mC cm^{-2}, did not change significantly with CsH_2PO_4 loading, suggesting that the solid acid did not provide significant ionomeric properties to the catalytic layer. This could be attributed to the discrete particle morphology of CsH_2PO_4 which did not provide an interconnected framework of ionomer to connect the catalytic site with the electrolyte, that it to say, ionomer percolation. At potentials higher than ca. 1.2 V, however, the shape of the CVs differs considerably when CsH_2PO_4 is present in the catalytic layer. At those potentials samples exhibit an oxidation tendency in the forward scan and a reduction peak in the backward scan. One could attribute this peak to the oxidation of iridium, presumably Ir^{IV} / Ir^{VI}, suggesting that the

presence of CsH_2PO_4 provides a proton source to the catalyst to oxidise and create the so-called hydrated oxide (equation 6.2). If that was so, the improved kinetics would be attributed to some positive effect of the ionomer, which would act as a proton donor for iridium enabling the oxidation step, and therefore, percolation would be achieved at some extent. Nevertheless, the CVs exhibit a potential shift of ca. 200 mV in the reduction peak at 400 – 600 mV. If all CVs were lined up taking this reduction peak as reference, the non-CsH_2PO_4 loaded electrode CV would stop at ca. 1.2 V and therefore, the oxidation peak would not yet be visible. For this reason, a positive effect arising from CsH_2PO_4 as ionomer was not considered.

In order to estimate an approximate value of catalyst usage for each electrode, the minimum IrO_2 loading was taken as a reference, 0.5 mg IrO_2 cm^{-2}, considering that all catalyst was electrochemically active in the reaction. From this assumption, that is, a 100 % utilisation of IrO_2 in this electrode, the estimated catalyst active loading and utilisation for the rest electrodes was calculated (table 7.6).

From the values obtained for the estimated catalyst loading and utilisation, it can be concluded that, for the all catalyst and ionomer loadings evaluated, the amount of catalyst electrochemically active in the electrode was relatively constant. This was explained by considering the first layer of catalyst, in intimate contact with the electrolyte, active in the electrode, fulfilling the three conditions required for a triple phase boundary; protonic, electrical and gaseous connection paths.

Table 7.6. Comparative values of IrO_2 utilisation in the fabricated anodes.

IrO_2 loading / mg cm^{-2}	**CsH_2PO_4 loading / mg cm^{-2}**	**Estimated IrO_2 loading / mg cm^{-2}**	**IrO_2 utilisation / %**
0.50	0	0.50	100
1.0	0	0.49	49
2.0	0	0.68	34
	1.0	0.58	29
	2.0	0.71	35
	3.0	0.57	28
3.0	0	0.57	19

7.4.2. Oxygen Evolution Reaction (OER)

The oxygen evolution reaction taking place in the anode of the electrolysis cell is the limiting reaction of the system due to its slow kinetics. As discussed in Chapter 6, the OER in aqueous CsH_2PO_4 is less favourable than in other acids i.e. sulfuric or phosphoric acids. This is mostly influenced by the low acidity of CsH_2PO_4 saturated solution (pH = 4.63). In order to determine the OER performance of IrO_2 on the solid state system, the polarisations performed in the electrolysis cell were corrected for the iR contribution of the electrolyte and the kinetic contribution of HER of the cathode.

For these experiments a 300 µm thickness CsH_2PO_4 pellet was used as electrolyte. The iR contribution of the electrolyte was estimated by electrochemical impedance spectroscopy, from the high frequency intercept with the real axis of the Nyquist spectrum. The system exhibited resistances between 1.55 – 1.90 Ω cm^2 at the temperature range of 235 – 265 ºC. The kinetic contribution of the cathode was measured from the HER polarisation curves (figure 7.3) after correcting them for iR. The resulting corrected linear sweep corresponded to presumably pure OER kinetics of IrO_2 in contact with a solid CsH_2PO_4 electrolyte.

As shown in figure 7.10, the contribution of the iR and HER to the total operating performance was relatively low due to the small current densities obtained and the relatively fast kinetics of HER on platinum, respectively. In order to calculate the kinetic parameters for OER in the electrode, 2.0 mg IrO_2 cm^{-2}-loaded electrode was used as anode. This was the best IrO_2 loading for the electrolysis performance, as shown in section 7.5. The electrolysis cell was operated at temperatures between 235 – 265 ºC with a 1.0 mg Pt cm^{-2}-loaded anode. No CsH_2PO_4 was used as ionomer in any of the electrodes. The kinetic parameters for each temperature, Tafel slope and exchange current density, were calculated and summarised in table 7.7. In figure 7.11, OER polarisations of IrO_2 at different temperatures are shown.

Although low performance was achieved in this system, with a maximum activity of 16 mA cm^{-2} at 1.70 V and 265 ºC, it is worth noting the low onset potential of the reaction. The onset potential values varied between 1.16 – 1.20 V, which considering the reversible potential value for OER at 235 – 265 ºC, gives overpotentials between 50 – 70 mV. These low overpotentials differ considerably to those of the aqueous system, where values between 210 - 300 mV were obtained. The significantly lower onset potential in the solid

state system could be attributed to the absence of phosphate adsorption onto the catalyst surface due to a lower mobility of these species in solid state than in aqueous solution.

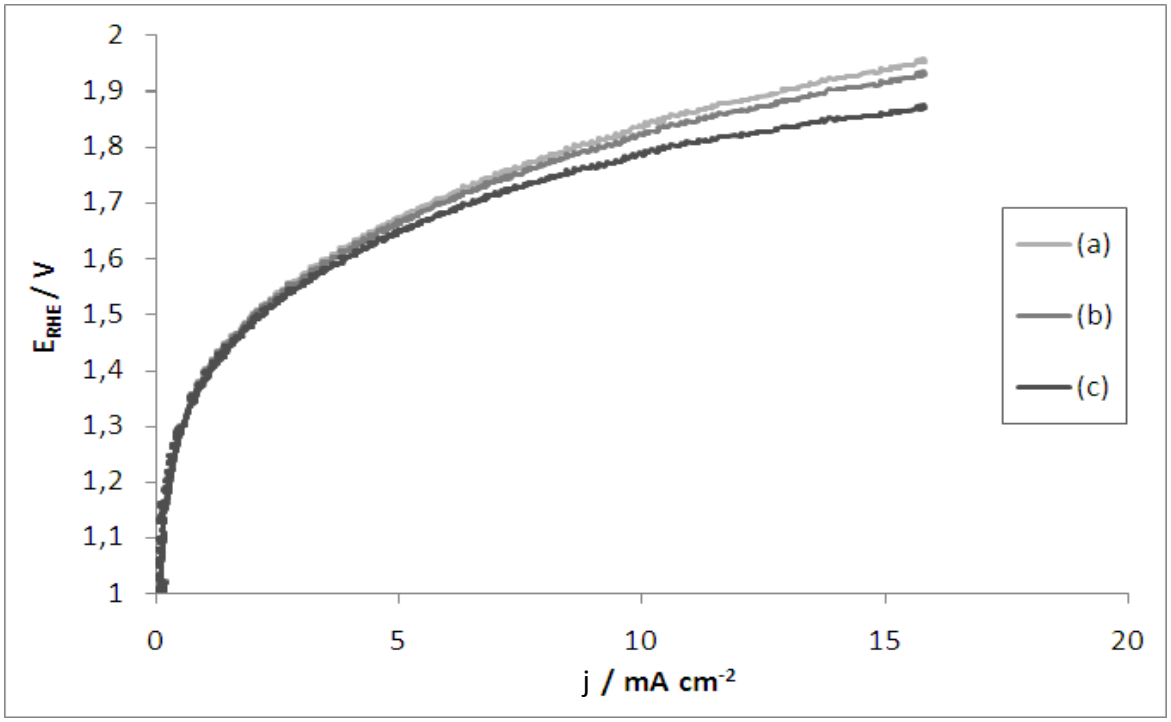

Figure 7.10. Electrolysis polarisation with no ionomer and 2.0 mg cm^{-2} IrO_2 (a) obtained curve, (b) iR corrected, and (c) HER corrected (pure OER polarisation) at 245 ºC (sweep rate = 1 mV s^{-1}).

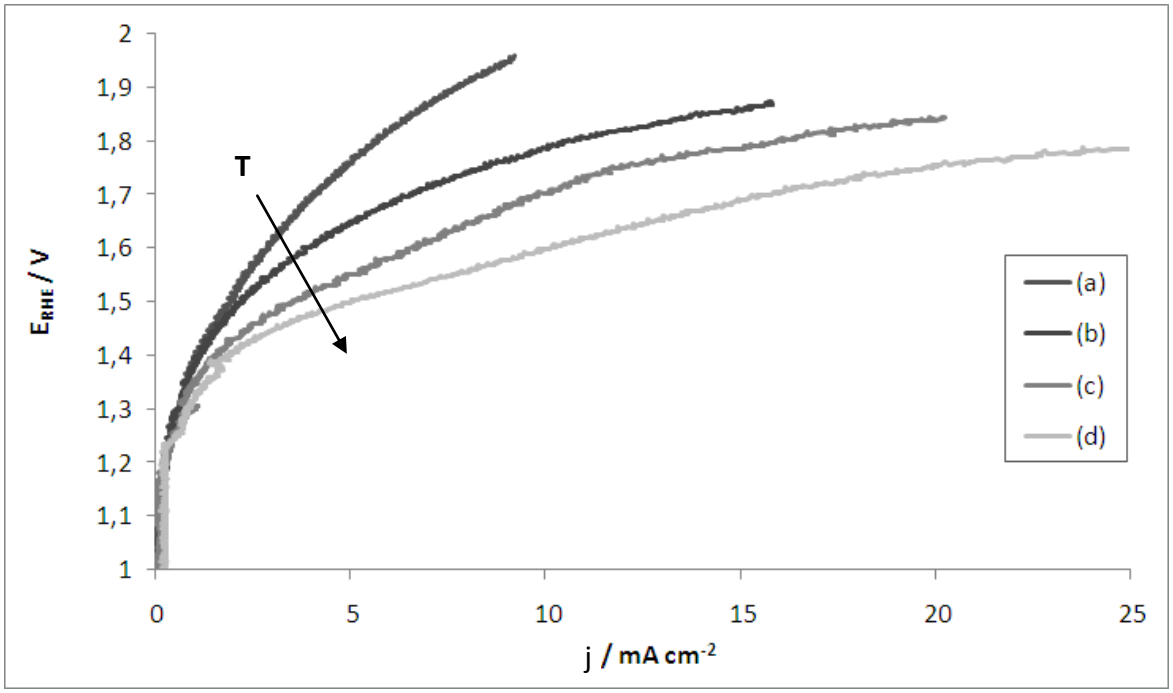

Figure 7.11. Pure OER polarisation with no ionomer and 2.0 mg cm^{-2} IrO_2 at (a) 235 ºC (b) 245 ºC (c) 255 ºC and (d) 265 ºC (sweep rate = 1 mV s^{-1}).

Logarithmic plots of the OER polarisation reveal two main Tafel regions; a low overpotential region with potentials between 1.25 -1.55 V and a high overpotential region, with potentials between 1.55 – 1.85 V (figure 7.12). Both regions show high Tafel slopes at temperatures of 235 – 265 ºC, between 239 – 304 mV dec^{-1} at the low overpotential region and 439 - 497 mV dec^{-1} at the high overpotential region. These two regions (along with a third at the low overpotential range) were identified in the half-cell OER studies of IrO_2, displayed in chapter 6, and were attributed to two different rate determining steps of the OER mechanism (equations 6.9 – 6.11):

1. *Low overpotential region:* the rate determining step is the second step of the reaction mechanism ($S–OH_{ads} \rightarrow S–O_{ads} + H^+ + e^-$), where the hydroxyl consumption takes place releasing a proton, an electron and an adsorbed oxygen atom. A theoretical Tafel slope of $\left(\frac{2RT}{3F}\right)$ is attributed to this step [13].

2. *High overpotential region:* the rate determining step is the first step of the reaction mechanism ($S + H_2O \rightarrow S–OH_{ads} + H^+ + e^-$), where the hydroxyl group is adsorbed onto the catalyst surface. A theoretical Tafel slope value of $\left(\frac{2RT}{F}\right)$ is attributed to this step as the r.d.s. [13].

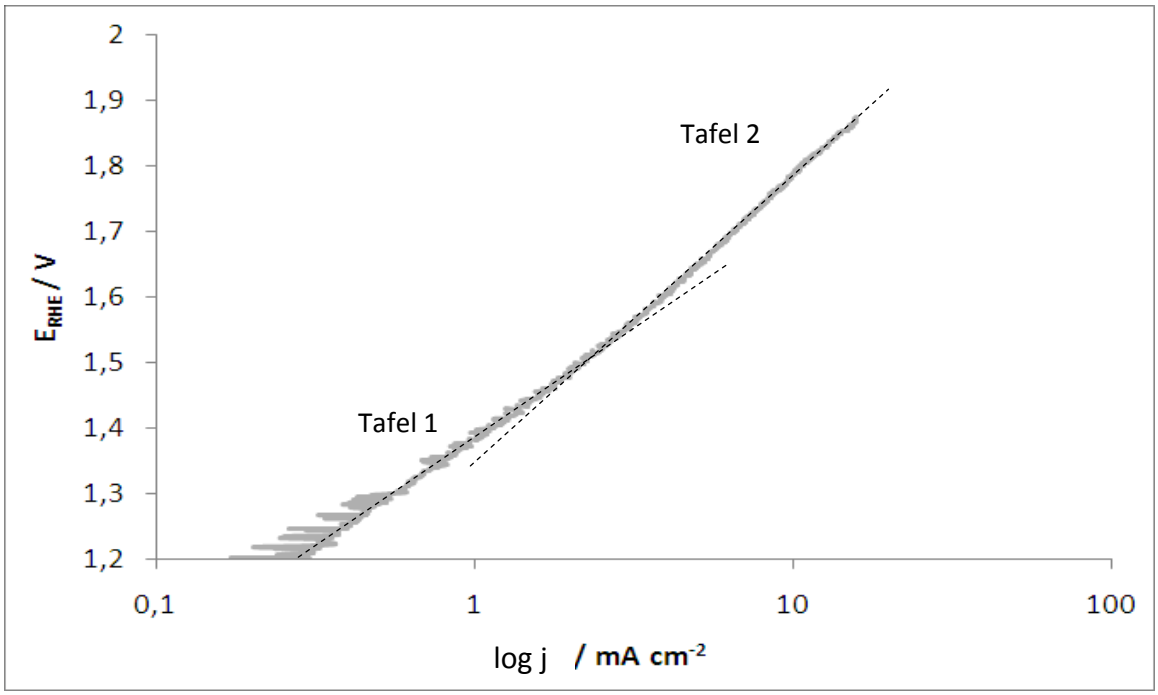

Figure 7.12. Tafel plot of OER for a cathode with no ionomer and 2.0 mg cm^{-2} IrO_2 at 245 ºC. The two Tafel regions identified are highlighted.

Table 7.7. Kinetic parameters of OER of 2.0 mg Pt cm^{-2} electrode (no ionomer).

Temperature / °C	Tafel region 1 (1.25 – 1.55 V)		Tafel region 2 (1.55 – 1.85 V)	
	Tafel slope / mV dec^{-1}	Exchange current density, j_0 / mA $cm^{-2}_{[XRD]}$	Tafel slope / mV dec^{-1}	Exchange current density, j_0 / mA $cm^{-2}_{[XRD]}$
235	268	1.8×10^{-3}	481	2.2×10^{-3}
245	304	1.4×10^{-3}	439	3.1×10^{-3}
255	281	1.7×10^{-3}	497	6.7×10^{-3}
265	239	1.5×10^{-3}	453	8.3×10^{-3}

The first Tafel region (Tafel 1, figure 7.12) was also identified in the OER polarisations performed in a saturated CsH_2PO_4 solution (chapter 6), exhibiting Tafel slopes between 72 - 80 mV dec^{-1}. The potential range of this Tafel region was 1.45 – 1.65 V whereas in solid state system the same region was identified at 1.25 – 1.55 V. The difference in potential is attributed to the potential shift arising from the temperature difference; the reversible potential at 25 ºC, 1.229 V, shifts to 1.131 V at 250 ºC. The overpotential difference between both processes, considering the approximate 100 mV potential shift caused by temperature, was therefore very similar.

The higher Tafel slope values obtained in the aqueous solution comparing to the theoretical slope stated for the second step of the *electochemical oxide path* mechanism, that is , b ~ $\left(\frac{2RT}{3F}\right)$ [13], are attributed to the effect of the oxide layer characteristics. *Gottesfeld et al.* [9], proved that the Tafel slope in the low overpotential region could increase by the properties and thickness of the oxide layer, exhibiting Tafel slopes between $\left(\frac{RT}{F}\right)$ and $\left(\frac{3RT}{2F}\right)$. The Tafel slopes obtained for the solid state CsH_2PO_4 system at the low overpotential region were in the range of 239 – 304 mV dec^{-1}, corresponding to slopes between $\left(\frac{4RT}{F}\right)$ and $\left(\frac{5RT}{F}\right)$. These high slope values are mainly attributed to the different characteristics of the iridium oxide layer in the solid system, where the low concentration and mobility of H^+ do not allow the formation of an active hydrous oxide layer of iridium. As the electrochemical oxidation of iridium requires protons in order to build a hydrated oxide active for OER (equation 6.1), the absence of free protons in the solid system would difficult the oxide formation process increasing significantly Tafel slope values.

In the high overpotential region, at potentials higher than 1.55 V, Tafel slope values between 453 – 497 mV dec^{-1} were measured at 235 – 265 ºC. This same region was also identified in the aqueous solution system where values as high as 230 mV dec^{-1} were obtained in potentials over 1.65 V. The 100 mV difference in potential would correspond to the potential shift arising from the temperature difference.

As discussed in chapter 6, the high Tafel slope values obtained at this overpotential were related to the high pH of the electrolyte. The Tafel slope follows an increasing tendency with pH at the high overpotential region, being close to 120 mV dec^{-1}, $b \sim \left(\frac{2RT}{F}\right)$, in low pH solutions (i.e. H_2SO_4) and high ca. 220 mV dec^{-1}, $b \sim \left(\frac{4RT}{F}\right)$, in a saturated CsH_2PO_4 solution (pH = 4.63). The values obtained in the solid state system, between 453 – 497 mV dec^{-1}, correspond approximately to the same Tafel slope value of the aqueous system at high overpotentials, $b \sim \left(\frac{4RT}{F}\right)$. This Tafel slope is approximately twice as high as the theoretical Tafel value attributed to the first step of the reaction mechanism being the r.d.s. This difference is attributed to the effect of the high pH of the electrolyte on the properties of the oxide layer of iridium. At such low proton concentration, the oxidation path to a hydrated iridium oxide layer, active towards OER, is expected to be inhibited to some extent by the low concentration of H^+. The new oxide layer, presumably of higher density and lower electronic conduction [18], would exhibit different affinity for the reaction intermediates and the adsorption/desorption energies of these species and the interactions between them and the reactants will change, resulting in a higher Tafel slope. Although it could be argued that the r.d.s. or even the reaction mechanism could change by the high pH environment, no theoretical Tafel slope of $\left(\frac{4RT}{F}\right)$ based on conventional electrochemistry is reported for any of the OER mechanisms proposed in the literature [13,16].

The exchange current densities of each of the temperatures were calculated by extrapolating the Tafel equation to the reversible potential at the given temperature. The values obtained are displayed in table 7.7 for both, high and low overpotential regions. At 235 – 265 ºC the reversible voltage range is 1.135 – 1.127 V. All exchange current densities were normalised by the theoretical catalyst area calculated from P-XRD. Although 2.0 mg cm^{-2} IrO_2 loading was used on the electrode, the electrochemically active loading should be estimated. To obtain an approximate value of the active catalyst loading, the charge obtained by the integration of the CV at the electrode with 0.5 mg cm^{-2} IrO_2,

24.4 mC cm^{-2} (table 7.4), was used as a reference value, considering that all catalyst was electrochemically active in the electrode. The IrO_2 loading was calculated from the relative ratio of charge between the actual and the reference electrode. This way, a value of 0.68 mg IrO_2 cm^{-2} was estimated in the electrode and using the 16.30 m^2 g^{-1} value obtained by P-XRD for IrO_2 (table 6.1) an estimated area of 187 .21 cm^2 for IrO_2 was determined.

At the low overpotential region (1.25 – 1.55 V) the exchange current densities exhibited constant values of ca. 1.6×10^{-3} mA cm^{-2}, approximately three to four orders of magnitude higher that those obtained in the half cell, using saturated CsH_2PO_4 solution. At the high overpotential region however, j_0 increase with temperature and the values obtained, between $2.2 – 1.3 \times 10^{-3}$ mA cm^{-2}, which are closer to those obtained in the aqueous solution, approximately one order of magnitude higher. The higher j_0 obtained in the solid system is attributed to faster kinetics at higher temperatures and therefore higher reaction rate at equilibrium.

The activation energy for the high overpotential Tafel region was calculated using the Arrhenius relation showed in equations 3.13 – 3.14. In figure 7.13 the Arrhenius plot for the low and high overpotential regions are shown. The activation energy was calculated from the value of the slope obtained ($-E_a/2.3R$).

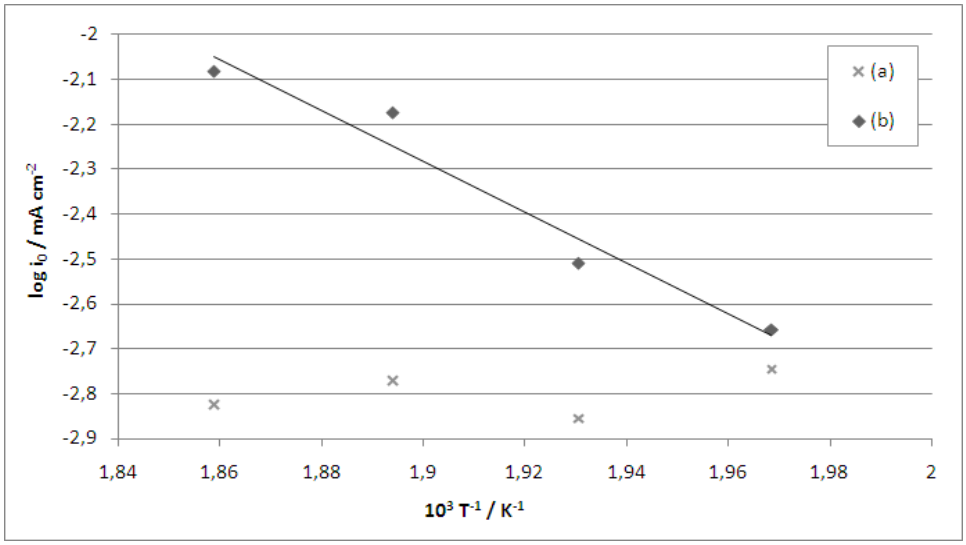

Figure 7.13. Arrhenius plot of log i_0 vs. T^{-1} at (a) low overpotential and (b) high overpotential region. E_a calculated from the slope.

At the low overpotential region, the exchange current density did not exhibit any variation with temperature and therefore E_a could not be calculated. This was attributed to the effect of other processes taking place at that potential range, such as the electro-oxidation of

iridium, from Ir^{IV} to Ir^{VI}. At the high overpotential region, j_0 exhibits a clear increasing tendency with temperature, leading to an E_a value of 108 kJ mol^{-1}. The high overpotential activation energy value, attributed to OER, is considerably higher than that obtained in aqueous solution, 15 kJ mol^{-1}.

The significant difference between E_a in aqueous and solid state system could be attributed to the energy requirement to adsorb reactant water on the catalytic surface. The low relative humidity of the cell at atmospheric pressure, ca. 3.0 %, could have an effect in the capacity of IrO_2 to adsorb and oxidise the water provided as a gas to the electrode. Instead, it is proposed that the water IrO_2 used to perform OER could be the structural water of the CsH_2PO_4 in contact with the catalyst. According to this theory, IrO_2 would catalyse a dehydration reaction on CsH_2PO_4 using the structural water of the solid acid as reactant in the electrolysis cell. The dehydrated CsH_2PO_4 would be again rehydrated with the water provided to the system until equilibrium is reached. This hypothesis is further proposed and debated in section 7.5.2, where the resistance of the electrolyte was monitored during an electrolysis durability test under current loading. According to this theory, the high E_a exhibited by the solid state system could be attributed to the energy requirement to 'strip' a water molecule from the CsH_2PO_4 structure.

7.5. Single cell water electrolysis

The performance of the $Pt/CsH_2PO_4/IrO_2$ MEA in a single electrolysis cell was measured. As seen in the previous section, the oxygen evolution reaction provides the system with the highest losses, compared to those arising from the hydrogen evolution reaction in the cathode and the iR losses provided by the ohmic resistance of the electrolyte (figure 7.10). The effect of the anode in the overall performance of the cell is therefore of mayor importance. The optimisation of the catalytic layer in terms of catalyst and ionomer loading was carried out and the performance in a single electrolysis cell evaluated.

Figures 7.14 and 7.15 show polarisation obtained for a system with a 300 μm thickness pellet as electrolyte and 1.0 mg cm^{-2} Pt loaded electrode as cathode. No correction was performed for these polarisations, as the iR contribution and the HER kinetic contribution of all MEAs was considered to be the same for all the fabricated MEAs. The IrO_2 and CsH_2PO_4 (as inonomer) loadings on the anode were changed in order to study their effect in the overall performance of the system. The activity values of the polarisation obtained at 1.40 V and 1.80 V are summarised in table 7.8.

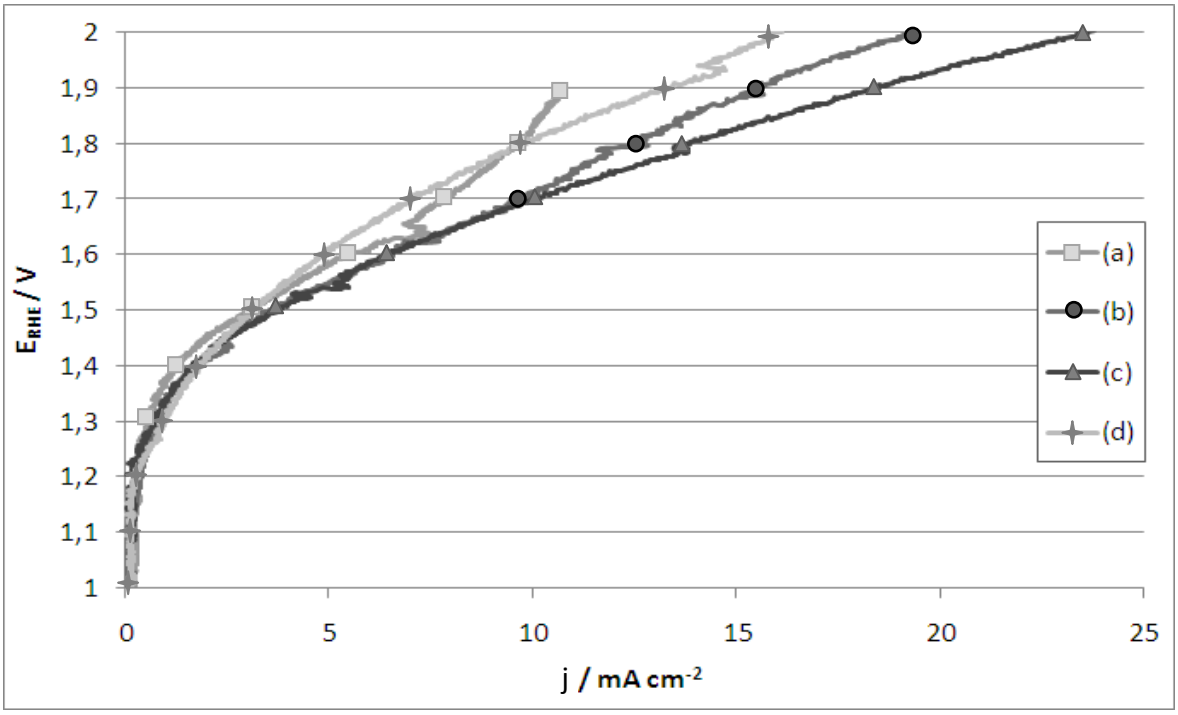

Figure 7.14. Polarisations of $Pt/CsH_2PO_4/IrO_2$ electrolysis cell system at 265 ºC with IrO_2 loadings on the anode of (a) 0.5 mg cm^{-2}, (b) 1.0 mg cm^{-2}, (c) 2.0 mg cm^{-2} and (d) 3.0 mg cm^{-2} at 1 mV s^{-1} (cathode loading = 1.0 mg Pt cm^{-2}, no ionomer).

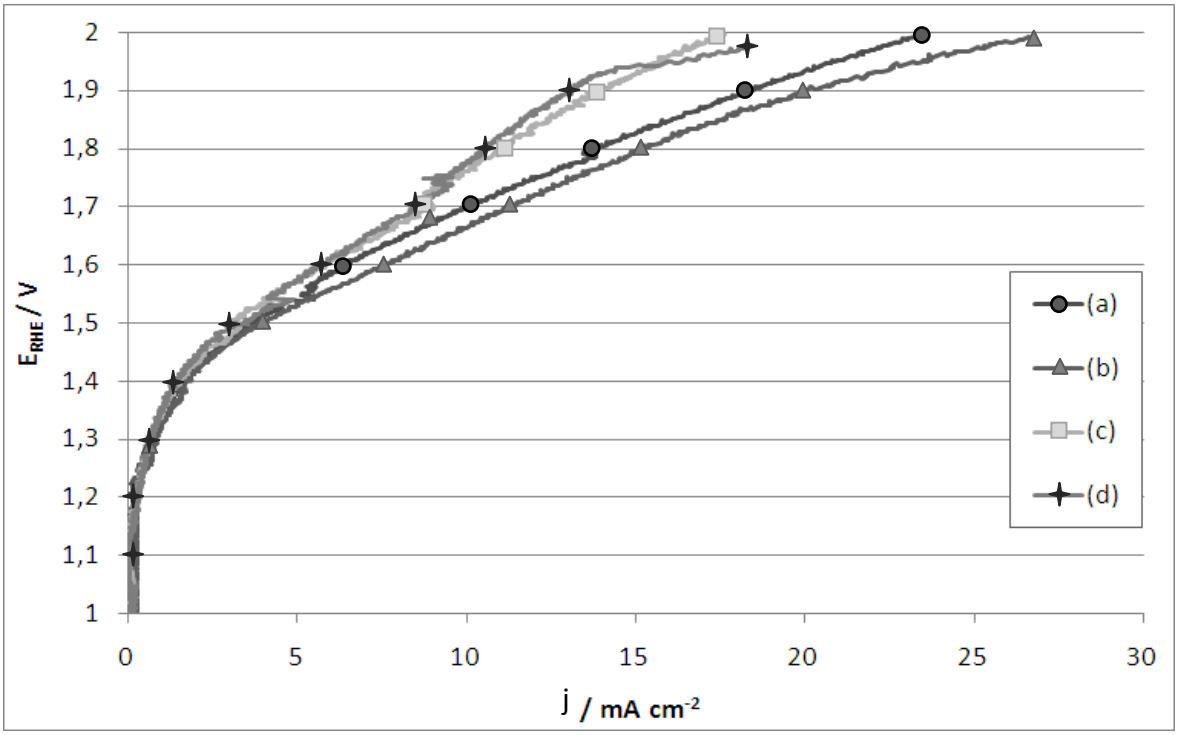

Figure 7.15. Polarisations of $Pt/CsH_2PO_4/IrO_2$ electrolysis cell system at 265 ºC with 2.0 mg cm^{-2} IrO_2 loading and CsH_2PO_4 loadings of (a) 0 mg cm^{-2}, (b) 1.0 mg cm^{-2}, (c) 2.0 mg cm^{-2} and (d) 3.0 mg cm^{-2} at 1 mV s^{-1} (cathode loading = 1.0 mg Pt cm^{-2}, no ionomer).

Table 7.8. Activity values of the electrolysis cell at low and high overpotentials.

Characteristic of the anode		**Activity**	
Catalyst loading / mg IrO_2 cm^{-2}	**Ionomer loading / mg CsH_2PO_4 cm^{-2}**	**j / mA cm^{-2} at 1.40 V**	**j / mA cm^{-2} at 1.80 V**
0.5	0	1.3	9.6
1.0	0	1.7	12.4
2.0	0	1.7	13.8
	0.5	1.3	13.4
	1.0	1.4	14.9
	2.0	1.4	10.6
	3.0	1.4	10.4
3.0	0	1.8	9.7

The purely kinetic region considered for all polarisations, between 1.20 – 1.50 V, showed very similar shape and activity in all cases. All activity values varied between 1.31 – 1.80 mA cm^{-2} at 1.40 V regardless of the IrO_2 or CsH_2PO_4 loadings. This supports the view that just the first catalytic layer in contact with the electrolyte is only active in the anode. No effect in the OER kinetics arising from different IrO_2 or CsH_2PO_4 loadings in the catalytic layer was exhibited. At a higher overpotential region, between 1.50 – 2.0 V, the slope of the polarisation changed slightly with the different anodes. In terms of IrO_2 loading, best performance was obtained by a 2.0 mg cm^{-2} IrO_2-loaded anode. The difference between them was mainly attributed to mass transport issues arising from the difference in the thickness of the catalytic layer. The diffusion of water as reactant to reach the active site of the catalyst and the release of gaseous O_2 as product were considered responsible for the difference in the polarisations.

In the case of anodes with different CsH_2PO_4 loadings, the effect was similar, exhibiting slightly different slopes in the high overpotential region of the polarisations. These differences were also attributed to mass transport issues generated by the presence of CsH_2PO_4 in the catalytic layer, which would change the thickness, porosity and electrical conductivity of the catalytic layer. Nevertheless, the activity for all MEAs at 1.80 V did not differ significantly, being all in the range of 9.6 – 14.9 mA cm^{-2}.

The same electrolysis system based on a CsH_2PO_4 glass-fibre reinforced composite membrane (85 µm thickness) was evaluated. These CsH_2PO_4-based membranes (CDP_{GF}) were found to exhibit the best compromise between proton conductivity and tensile strength among all fabricated membranes ($\sigma = 4 \times 10^{-3}$ S cm^{-1} at 250 °C and Y = 0.14 GPa) (see section 5.3.4). For CDP_{GF} membranes anodes were deposited by spraying (figure 7.16-b) and by Decal method (figure 7.16-c) as explained in the experimental section of this chapter.

The kinetic region of the polarisation curves exhibited higher activity in the system using a pure CsH_2PO_4 pellet comparing to that of the composite membranes. This difference in the kinetics is attributed to a more intimate interface between the catalyst layer and the electrolyte in the case of CsH_2PO_4 pellet. As discussed before, the first layer of IrO_2 is considered to be the electrochemically active catalyst in the electrode as it is in contact with the electrolyte, where the conditions for a triple phase boundary are achieved. In CDP_{GF} membranes, as part of the volume of the membrane is formed by non-conductive glass-fibres, less catalyst is expected to be in contact with CsH_2PO_4, and therefore, lower catalyst utilisation was achieved. This is clearly exhibited in the exponential region of the polarisation curves.

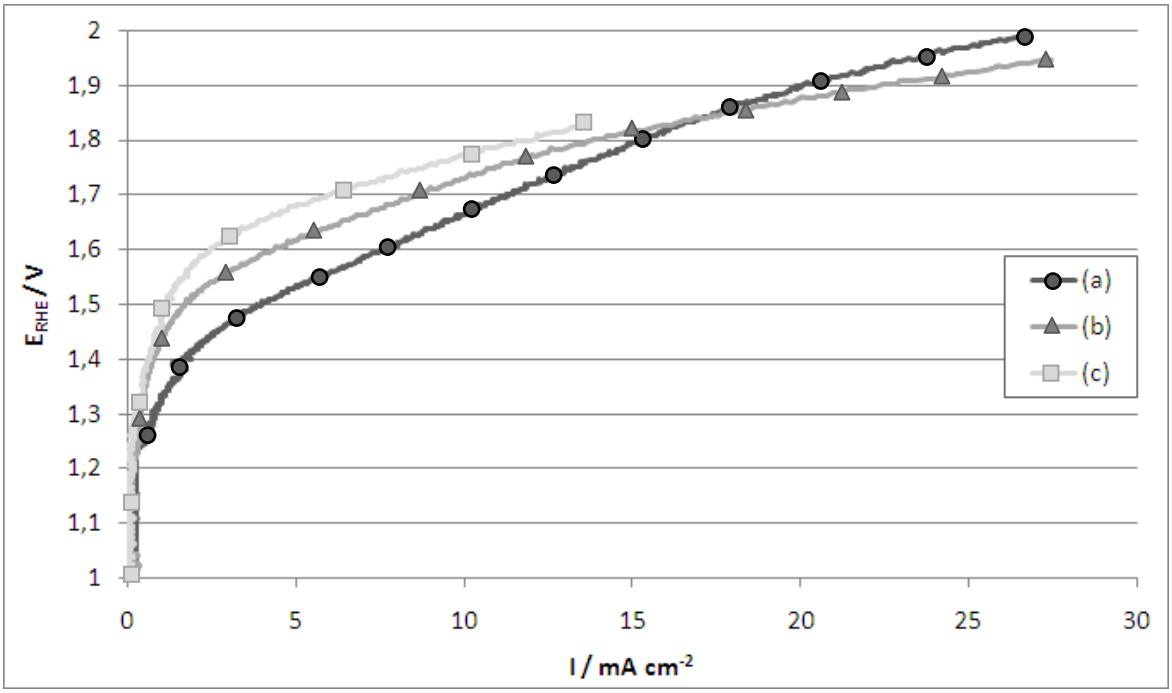

Figure 7.16. Polarisations of electrolysis cell system at 265 ºC with (a) 350 µm thickness CsH_2PO_4 pellet and (b,c) 85 µm thickness glass-fibre reinforced CsH_2PO_4 membrane with anode deposited by spraying and by Decal method, respectively.

At higher potentials, where a more linear region is regarded, systems using CDP_{GF} membranes showed lower slope comparing to that of the CsH_2PO_4 pellet. This difference in the slope of the polarisation is mostly attributed to the difference on the iR between both electrolytes, which showed values of ca. 1.0 and 1.5 Ω cm^2 measured by impedance for CDP_{GF} membrane and CsH_2PO_4 pellet, respectively. However, some mass transport contribution is also expected at high potentials, by mainly water and O_2 diffusion in the anodic catalytic layer. Even if high current densities were not achieved, the low relative humidity in the conditions applied (ca. 3.0 %) could cause mass transport issues. The difference in the slope of the high potential region of the polarisations in figure 7.16 is therefore attributed to the ohmic resistance of the electrolyte and to the difference in water transport caused by the different characteristics (i.e. thickness, porosity) of the anodes.

The two different techniques used for anode deposition on CDP_{GF} membranes, spraying and Decal method, caused a significant effect in the kinetic region of the polarisations. The overpotential of MEA with the sprayed anode at 2.0 mA cm^{-2} was 50 mV smaller than the MEA with anode deposited by Decal method. This difference is mostly attributed to the contact of the IrO_2/CsH_2PO_4 interface in the anode.

7.5.1 Fuel Cell system

The poor performance shown by the electrolysis system is mostly attributed to the slow kinetics of the oxygen evolution reaction. The low proton concentration of the electrolyte is believed to affect the oxidation state of IrO_2 inhibiting to some extent the formation of a hydrated oxide layer active towards OER.

It was reported by various authors that CsH_2PO_4-based fuel cell systems exhibit an acceptable performance, as high as 415 mW cm^{-2} at 250 ºC [2]. This promising value was achieved by fabricating a thin pellet as electrolyte (ca. 25 µm) to reduce the ohmic losses in the system. The oxygen reduction reaction (ORR), taking place in the cathode of a fuel cell, although is considered to be responsible of the major losses in the system, is fast enough to make the system achieve the values reported.

The fuel cell MEA was loaded with 1.0 mg cm^2 platinum black in both carbon paper electrodes (no ionomer) and 50 ml min^{-1} of pure H_2 and O_2 were fed to anode and cathode respectively (P_{H2O} = 0.75 atm). The MEA of the electrolysis cell was loaded with 1.0 mg cm^{-2} platinum black on the carbon paper anode and 2.0 mg IrO_2 and 1.0 mg CsH_2PO_4 on

the carbon paper cathode. 50 ml min^{-1} of pure H_2 and N_2 were fed to the cathode and anode respectively, both with a water partial pressure of 0.95 atm. The performance of the fuel cell system, operating with a 300 µm-thick CsH_2PO_4 electrolyte at 265 ºC, is shown in figure 7.17 and compared to the operation obtained in the electrolysis cell. Linear sweep polarisations for both systems and iR corrected sweeps are shown.

Taking as reference the reversible potential at 265 ºC, 1.127 V, the electrolysis cell system exhibits a considerable lower performance. The polarisations of the electrolysis cell (figure 7.17 – a,b) showed that the iR effect of the electrolyte is considerably small which, as discussed in section 7.4, attributes most of the losses of the sweep to the OER. Despite the high temperature, the kinetics on the anode were too slow and therefore high overpotentials were required to provide some activity to the system.

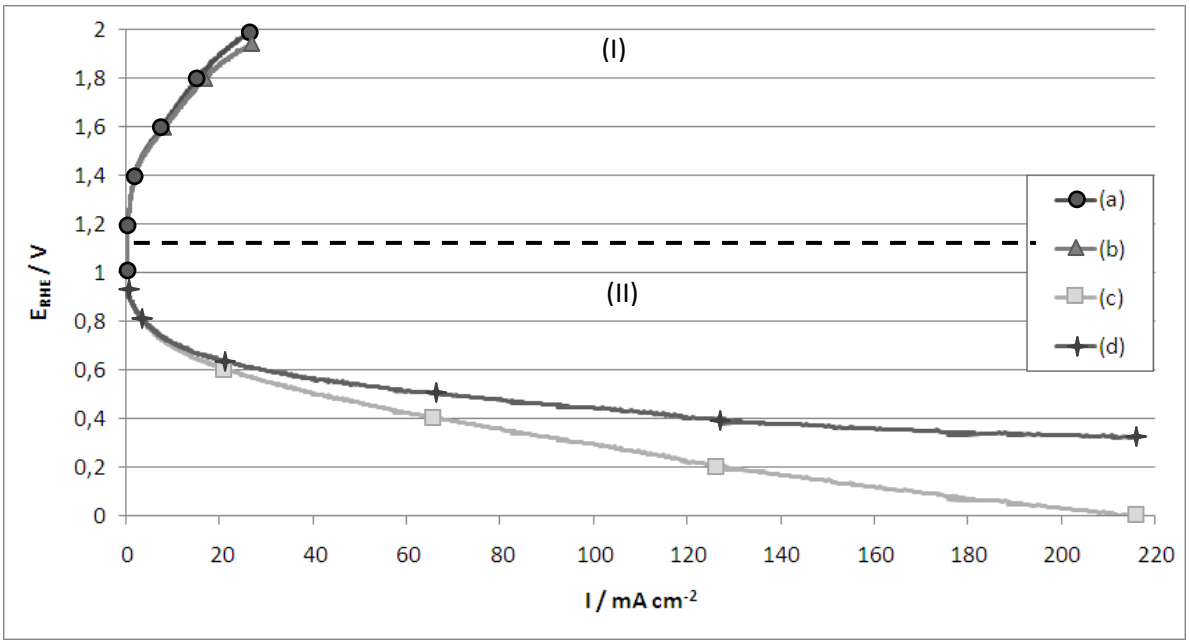

Figure 7.17. Polarisations of (I) electrolysis and (II) fuel cell system with 300 µm CsH_2PO_4 pellet as electrolyte at 255 ºC, (a,c) raw data and (b,d) iR corrected. (scan rate = 1 mV s^{-1})
(I) Electrolysis cell: anode = 2.0 mg cm^{-2} IrO_2 + 1.0 mg cm^{-2} CsH_2PO_4; cathode = 1.0 mg cm^{-2} Pt (no ionomer). **(II) Fuel cell (H_2/O_2):** anode = 1.0 mg cm^{-2} Pt (no ionomer); cathode = 1.0 mg cm^{-2} Pt (no ionomer)

To provide the system with 20 mA cm^{-2} activity 750 and 530 mV overpotentials were required for the electrolysis and fuel cell systems, respectively. The 220 mV overpotential difference between both systems is mainly attributed to the faster kinetics of the oxygen reduction reaction compared to those of oxygen evolution. Although in both electrodes the

same reaction in opposite directions takes place there are few aspects that must be taken into account:

1. The catalyst used in both systems, Pt for ORR and IrO_2 for OER, have an effect on the reaction mechanism altering the path and activation energy of the reaction. The operating potential of both systems is different, being considerably higher in the electrolyser, and therefore the influence of the potential in the surface properties of the catalyst must be taken into account. The significant effect of the oxide layer characteristics of IrO_2 towards OER activity could be, for instance, a differential factor in the activity between both catalysts.

2. The concentration of reactants in the fuel cell system is significantly higher than that of the electrolysis system. Whereas in the fuel cell pure O_2 was fed to the ORR electrode, ca. P_{O2} = 1.0 atm, the high temperature of the system (265 ºC) drops significantly the P_{H2O} = 0.9 atm fed in the N_2 to the electrolyser cell, to a relative humidity value of approximately 3.0 % (see figure 4.14). The low water concentration could affect the system in terms of mass transport, although no limiting currents were obtained at potentials of 2.0 V. The low concentration is expected to have an effect in the reaction kinetics by reactant diffusion to the catalytic sites. Higher water concentration levels in the electrode could only be achieved by pressurising the system.

3. As reported by various authors, the activity of a H_3PO_4-doped PBI membrane fuel cell (ca. 900 mA cm^{-2} at 0.50 V) [10] is higher and more stable than that of the same electrolyte electrolysis cell (ca. 500 mA cm^{-2} at 1.75 V) [11]. The analogy between both systems, H_3PO_4-doped membrane and CsH_2PO_4, was also considered to be related to the phosphate presence in the catalytic environment. It is proposed that, due to the low relative humidity at the temperatures these systems operate, 180 and 265 ºC respectively, the water used as reactant in the OER could be provided by the H_3PO_4 or CsH_2PO_4 in contact with the catalyst. It would be considered as a catalytically induced dehydration reaction of both compounds. If this was so, the system would have to overtake the activation energy equivalent to ‘stripping’ a molecule of water from the intrinsic structure of the phosphates. This would also decrease the conductivity of the electrolyte in contact with the catalyst providing higher ohmic losses in the electrode and electrolyte.

The low electrolysis performance of CsH_2PO_4-based system was attributed to the above-mentioned aspects, focusing the main losses of the system in the oxygen evolution reaction on IrO_2. The high pH of the electrolyte, which is considered to affect the oxidation properties of IrO_2, and therefore, its activity towards OER, seems to at a less extent affect the Pt reaction path towards ORR. Unlike on IrO_2, oxide-free platinum sites must exist in the catalytic layer of the fuel cell cathode in order to ORR to take place. For this reason the characteristics of the oxide layer would not have such an effect as it does in IrO_2 and therefore the high pH of the electrolyte is believed to have a less significant effect on the ORR on Pt. The oxidation of platinum in an acidic medium, taking place at potentials higher than ca. 0.7 V, is not considered to be involved in the oxygen reduction reaction mechanism.

7.5.2 Durability and system limitations

The stability of the electrolysis system was analysed during 48 h. The system was maintained at a fixed potential of 1.80 V while the current density of the system was monitored. Impedance measurements were performed in order to address the value of resistance provided by the electrolyte during the experiment obtained from the high frequency intercept with the real axis of the Nyquist spectrum. The results obtained are shown in figures 7.18 and 7.19.

In figure 7.18 the value of current density of the system is shown at 255 ºC and 1.80 V. For the impedance measurements the potentiostat was disconnected (for approximately 30 s) and reconnected after, creating high current peaks (marked with '*' in the plot). A high and fast decrease in current density was exhibited after each peak until reaching a stable value of ca. 8.5 mA cm^{-2}. The system showed an overall decreasing trend in activity with time, showing an approximate decay of 0.5 mA cm^{-2} day^{-1}, considering the stable regions in the plot. The resistance of the electrolyte was also monitored during the test in order to verify if the ohmic resistance of the electrolyte affected the stability of the system.

As shown in figure 7.19, the initial impedance measurement, before the system was polarised, exhibited a resistance of 1.60 Ω cm^2, which was an expected value for a 300 µm electrolyte with 1.5×10^{-2} S cm^{-1} proton conductivity. The resistance of the electrolyte however, increased considerably (to values over 5.4 Ω cm^2) when the system was initially polarised. Once the system stabilised at a current density of ca. 8.5 mA cm^{-2}, the resistance

of the electrolyte stabilised at values close to 2.5 Ω cm^2, however, a constant decreasing tendency, proportional to the current density decrease, was shown. After the test was performed and the system stabilised for 2 h under no external potential, the electrolyte exhibited a resistance of 1.70 Ω cm^{-2}, slightly higher than the initial resistance value.

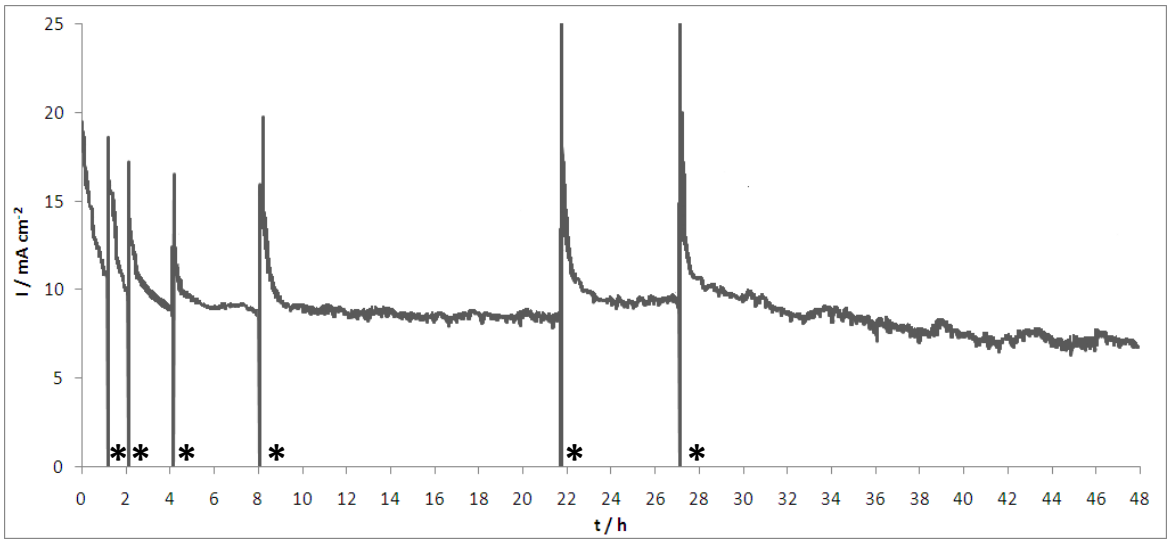

Figure 7.18. Analysis of the stability of the electrolysis cell at 1.80 V for 48 h at 255 ºC. Impedance measurements marked by (*).

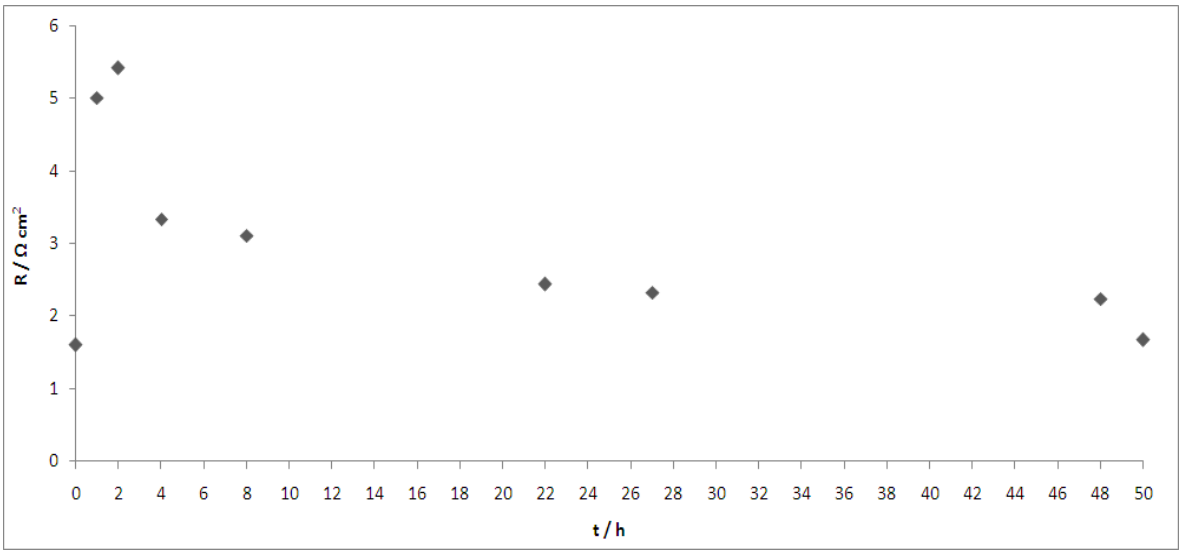

Figure 7.19. Analysis of the electrolyte resistance during the stability of the electrolysis cell at 1.80 V for 48 h at 255 ºC.

The unstable iR contribution of the electrolyte and the current density flowing in the system are believed to keep a direct relation. It is proposed that due to the low relative humidity in the cell, the water used as reactant in the anode of the electrolysis cell could

come from the structural water of the CsH_2PO_4 in contact with the catalyst. IrO_2 could act as a catalyst for the dehydration of CsH_2PO_4 using the water produced as reactant in the system. Equally, the dehydrated CsH_2PO_4 would find rehydration equilibrium with the relative humidity provided to the cell. According to this theory the decrease in conductivity would be proportionally related to the amount of current density flowing in the system. This is considering that all the increase in the resistance of the system is derived from CsH_2PO_4 proton conductivity loss, although it could be argued that the electrical resistance of the IrO_2 layer could contribute to it. As mentioned before, the high pH of the electrolyte would affect the characteristics of the oxide layer by driving the oxidation path towards a non-hydrated oxide and changes in potential and time would affect the thickness of the oxide layer. Although it is likely that these parameters have an effect in the resistance of the electrode, considering the electrical resistivity reported for IrO_2 to be 1.50×10^{-6} Ω cm [12], the contribution of IrO_2 to the overall resistance is considered negligible.

7.5. Conclusions

The performance of electrolysis cell with a solid CsH_2PO_4 electrolyte was studied. The contributions of the hydrogen and oxygen evolution reactions and the iR effect of the electrolyte to the overall losses of electrolysis system were separately analysed.

The iR contribution of the electrolyte was calculated by electrochemical impedance spectroscopy. Minimum resistance of 1.5 Ω cm^2 was obtained for a 300 µm thick pellet and 1.0 Ω cm^2 for a 85 µm glass-fibre reinforced membrane. The hydrogen evolution reaction (HER) contribution to the overall losses of the system was estimated by quasi-steady linear sweep polarisations, obtaining a maximum activity value of 20 mA cm^{-2} at 50 mV overpotential and 265 ºC. Tafel slope values between 87 and 52 mV dec^{-1} and exchange current densities of ca. 1.30×10^{-2} mA $cm^{-2}_{[XRD]}$ were obtained. Oxygen evolution reaction (OER) exhibited the higher contribution to the losses of the electrolyser. The maximum activity obtained was 20 mA cm^{-2} at ca. 600 mV overpotential and 265 ºC. Two Tafel regions were identified; a low overpotential region with Tafel slope values varying between 304 – 239 mV dec^{-1} and current exchange densities of ca. 1.6×10^{-3} mA $cm^{-2}_{[XRD]}$ and a high overpotential region with Tafel slopes of 497 – 453 mV dec^{-1} and current exchange densities of between $8.3 - 2.2 \times 10^{-3}$ mA $cm^{-2}_{[XRD]}$. The two different Tafel regions, at low and high overpotentials, were attributed the second and the first step of the reaction mechanism for OER being the r.d.s., respectively. The high Tafel slope values obtained for both regions, b ~ $\left(\frac{5RT}{F}\right)$ and $\left(\frac{4RT}{F}\right)$ comparing to the theoretical values of b ~ $\left(\frac{2RT}{3F}\right)$ and $\left(\frac{2RT}{F}\right)$ reported for the electrochemical oxidation mechanism for OER in acidic media, is attributed to the different characteristics of the oxide layer of IrO_2 formed in the high pH environment provided by CsH_2PO_4. The low proton concentration provided by the solid acid is considered to be responsible of the formation of a non-hydrated oxide, with less activity towards OER.

The electrolysis system exhibited a maximum activity of 20 mA cm^{-2} at 1.90 V and 265 ºC. The poor activity of the system is mainly attributed the low water concentration in the anode at the operation conditions, RH = 3.0 %, and to the low activity of non-hydrated iridium oxide towards OER, caused by the high pH of the electrolyte.

The durability of the system under constant potential application (1.80 V) showed that current density undergoes a decay of approximately 0.5 mA day^{-1}. This is mainly attributed

to catalyst deactivation caused by the low proton concentration in the system and to the increase in the ohmic resistance of the electrolyte. This last effect is proposed to be caused by a catalytically driven dehydration of CsH_2PO_4 by IrO_2, which presumably utilised the water produced as reactant in the system. This could explain the higher value obtained for the E_a in the solid system, 108 kJ mol^{-1}, comparing to that obtained in the half-cell in aqueous solution.

7.6. References

1. Haile, S.M., Boysen, D.A. and Chisholm, CRI., *Solid acids as fuel cell electrolytes.* Nature, 2001. **410**(6831): p. 910-913.
2. Boysen, D.A., Uda, T., Chisholm, C.R.I. and Haile, SM. , *High-performance solid acid fuel cells through humidity stabilization.* Science, 2004. **303**(5654): p. 68-70.
3. Uda, T. and S.M. Haile, *Thin-membrane solid-acid fuel cell.* Electrochemical and Solid-State Letters, 2005. **8**(5): p. A245-A246.
4. Roen, L., C. Paik, and T. Jarvi, *Electrocatalytic corrosion of carbon support in PEMFC cathodes.* Electrochemical and Solid-State Letters, 2004. **7**(1): p. A19-A22.
5. Antolini, E., et al., *Influence of Nafion loading in the catalyst layer of gas-diffusion electrodes for PEFC.* Journal of Power Sources, 1999. **77**(2): p. 136-142.
6. Sasikumar, G., J.W. Ihm, and H. Ryu, *Dependence of optimum Nafion content in catalyst layer on platinum loading.* Journal of Power Sources, 2004. **132**(1–2): p. 11-17.
7. Bockris, J.O.M., I.A. Ammar, and A.K.M.S. Huq, *The Mechanism of the Hydrogen Evolution Reaction on Platinum, Silver and Tungsten surfaces in Acid Solutions.* The Journal of Physical Chemistry, 1957. **61**(7): p. 879-886.
8. Chen, W.F., et al., *Hydrogen-Evolution Catalysts Based on Non-Noble Metal Nickel–Molybdenum Nitride Nanosheets.* Angewandte Chemie International Edition, 2012. **51**(25): p. 6131-6135.
9. Gottesfeld, S. and S. Srinivasan, *Electrochemical and optical studies of thick oxide layers on iridium and their electrocatalytic activities for the oxygen evolution reaction.* Journal of Electroanalytical Chemistry and Interfacial Electrochemistry, 1978. **86**(1): p. 89-104.
10. Mamlouk, M. and K. Scott, *The effect of electrode parameters on performance of a phosphoric acid-doped PBI membrane fuel cell.* International Journal of Hydrogen Energy, 2010. **35**(2): p. 784-793.
11. Aili, D., et al., *Phosphoric acid doped membranes based on Nafion®, PBI and their blends – Membrane preparation, characterization and steam electrolysis testing.* International Journal of Hydrogen Energy, 2011. **36**(12): p. 6985-6993.
12. Liu, Y., Masumoto, H. and Goto, T., *Electrical and Optical Properties of IrO_2 Thin Films Prepared by Laser-ablation.* Materials transactions, 2004. **45**(10): p. 3023-3027.
13. Damjanovic, A., Dey, A. and Bockris, O´M., *Kinetics of oxygen evolution and dissolution on platinum electrodes.* Electrochimica Acta, 1966. **11**: p. 791-814.
14. Travares, M. C., Machado, S.A.S and Mazo, L. H., *Study of hydrogen evolution reaction in acid medium on Pt microelectrodes.* Electrochimica acta, 2001. **46** (28): p. 4359 -4369.
15. Conway, B.E. and Bai, L., *Determination of adsorption of OPD H species in the cathodic hydrogen evolution reaction at Pt in relation to electrocatalysis.* J. Electroanal. Chem., 1986. **198**: p. 149-175.
16. Bockris, J.O'M., *Kinetics of activation controlled consecutive electrochemical reactions: anodic ecolution of oxygen.* Journal of Chemical Physics, 1955, **24** (4): p. 817.
17. Cheng, J., Zhang, H., Ma, H., Zhong, H. and Zou, Y., *Study of carbon supported IrO_2 and RuO_2 for use in the hydrogen evolution reaction in a solid polymer electrolyte electrolyzer.* Electrochimica acta, 2010. **55**: p. 1855-1861.
18. Burke, L.D. and Whelan, D.P., *A voltammetric investigation of the charge storage reactions of hydrous iridium oxide layers.* J. Electroanal. Chem., 1984. **162**: p.121-141.

CHAPTER 8

CONCLUSIONS AND FUTURE WORK

In this chapter, the main conclusions obtained in this research are summarised and the applicability of CsH_2PO_4 as proton conducting material in an intermediate temperature PEM water electrolysis system evaluated. Different approaches and suggestions for potential application of inorganic proton conductors in PEM water electrolysis and other electrochemical devices are proposed.

8.1. Conclusions

Phosphate-based solid acids (MH_2PO_4, where M = Li, K, Rb, Cs, NH_4) were synthesised and characterised in order to address their physico-chemical and electrochemical properties.

- All solid acids exhibited a clear transition to proton conductors in the intermediate temperature range (150 – 300 ºC). Maximum values of proton conductivity, over 10^{-2} S cm^{-1}, were obtained for CsH_2PO_4 at temperatures between 230 and 280 °C.
- Although it is reported that no water is required for proton transport in solid acids, in real operating conditions water must be provided to the system in order to maintain proton conductivity and material stability.
- A significant mass loss takes place for all phosphate-based solid acids close to the proton conducting transition temperatures when no humidification is provided, which is attributed to dehydration for all cases except of $NH_4H_2PO_4$, where chemical decomposition to ammonia and phosphoric acid is assumed.
- CsH_2PO_4 exhibited good stability in terms of water solubility at high humidification rates and dehydration was proved to be avoided when $P_{H2O} > 0.12$ atm is applied to the system. Rehydration of the material, this is, hydrolysis of condensed phosphates, can be carried out at $P_{H2O} > 0.31$ atm being the rehydration rate faster at higher water partial pressures. Higher humidification rates are therefore needed to trigger rehydration than to avoid dehydration.

Five different methods were proposed for the fabrication of CsH_2PO_4-based composite membranes; (1) casting of CsH_2PO_4/polymer membrane, (2) CsH_2PO_4-doped polymeric membrane, (3) glass-fibre reinforced membranes, (4) electrospinning of CsH_2PO_4 fibre mat and (5) the casting of partially polymerised CsH_2PO_4.

- Membranes fabricated by the glass-fibre reinforced method exhibited the highest proton conductivity, 8×10^{-3} S cm^{-1} at 275 °C.
- All methods using polymer as a binder, doped membrane or to occlude porosity, show low proton conductivity, $< 3 \times 10^{-4}$ S cm^{-1}, caused by the isolating properties of the polymer and low acid uptake.
- Membranes fabricated by the casting of partially polymerised CsH_2PO_4 exhibited a maximum conductivity value of 2×10^{-3} S cm^{-1} at 250 °C.

The effect of pH and anion concentration on the electrochemical active surface (EAS) of IrO_2 and Pt black and the activity of IrO_2 towards OER were addressed in a half-cell using a saturated solution of CsH_2PO_4. Results were compared to those obtained in H_2SO_4 and H_3PO_4 aqueous electrolytes.

- Lower pH values increase the integrated charge for both catalysts explained by higher proton accessibility to the catalytic sites. Anion adsorption onto the catalyst surface affects the amount of free catalyst and thus, EAS for both Pt and IrO_2.
- The performance of IrO_2 in saturated solution of CsH_2PO_4 shows a significantly low activity towards OER. Steady-state linear sweeps suggest that the activity of IrO_2 towards OER is strongly dependant on the pH. The main reason for the poor performance on CsH_2PO_4 is attributed to the high pH of the solution (pH = 4.63). Onset potential for OER in CsH_2PO_4 shows the highest overpotential of all electrolytes (> 200 mV), attributed to the stronger adsorption of phosphates compared to sulphate anions and to the highest anionic concentration of all solutions.
- The kinetic study of IrO_2 in the different electrolytes proves that the oxidation of iridium towards a more active oxidation state for OER take place before the actual reaction. All solutions exhibited similar Tafel slopes at the moderate overpotential region, ca. $\left(\frac{RT}{F}\right)$, attributed to the second step of the reaction mechanism being the r.d.s. The high overpotential Tafel region, attributed to the first step of the reaction

mechanism as the r.d.s, exhibited a very significant difference in Tafel slopes between CsH_2PO_4 and the rest of the acids. This suggests that the limiting step of this reaction is highly dependent on the proton concentration in solution.

- CsH_2PO_4 in solution is not a favourable electrolyte for IrO_2 towards OER. The low acidity inhibits the activity of the catalyst driven presumably by a modification of the oxide layer thickness and composition, to a non-hydrated and less active oxide.

CsH_2PO_4 was evaluated as solid-state proton conducting electrolyte in a single-cell electrolyser at the intermediate temperature range (235 – 275 ºC).

- Minimum resistance of 1.5 Ω cm^2 was obtained for a 300 μm thick pellet and 1.0 Ω cm^2 for an 85 μm glass-fibre reinforced membrane.
- The hydrogen evolution reaction (HER) under platinum exhibited a maximum activity value of 20 mA cm^{-2} at 50 mV overpotential and 265 ºC. Tafel slope values between 87 and 52 mV dec^{-1} and exchange current densities of ca. 1.3×10^{-2} mA $cm^{-2}_{[XRD]}$ were obtained.
- Oxygen evolution reaction (OER) exhibited the highest contribution to the losses of the electrolyser. The maximum activity obtained was 20 mA cm^{-2} at ca. 600 mV overpotential and 265 ºC. Two Tafel regions were identified; a low overpotential region with Tafel slope values varying between 304 – 239 mV dec^{-1} and current exchange densities of ca. 1.6×10^{-3} mA cm^{-2} and a high overpotential region with Tafel slopes of 497 – 439 mV dec^{-1} and exchange current densities of $8.3 – 2.2 \times 10^{-3}$ mA cm^{-2}. Apparent E_a of 108 kJ mol^{-1} was estimated for the high overpotential region.
- The electrolysis system exhibited a maximum activity of 20 mA cm^{-2} at 1.90 V and 265 ºC. The poor activity of the system is mainly attributed the low water concentration in the anode at the operation conditions, RH = 3.0 %, and to the low activity of iridium oxide towards OER, caused by the high pH of the electrolyte.
- The durability of the system under constant potential application (1.80 V) showed that current density undergoes a decay of approximately 0.5 mA day^{-1}. This is attributed to catalyst deactivation caused by the low proton concentration in the system and to the increase in the ohmic resistance of the electrolyte. This last effect is proposed to be caused by a catalytically driven dehydration of CsH_2PO_4 by IrO_2, which presumably utilised the water produced as reactant in the system.

Considering all the conclusions derived from the analysis of the data obtained in this research, it is concluded that, opposite to what it was expected, CsH_2PO_4 is not a favourable electrolyte for application in an intermediate temperature PEM water electrolysis system. The main drawback for the application of this material is the low oxygen evolution reaction rate of iridium oxide in the high-pH electrolytic environment provided by CsH_2PO_4. Other issues, such as the ohmic resistance provided by the high thickness electrolyte or its durability under long-term operation or pressurised conditions make CsH_2PO_4, and presumably the rest of phosphate-based solid acids, non applicable in this electrochemical system.

8.2. Future work

The high pH environment provided by CsH_2PO_4 in the catalytic region reduces dramatically the activity of iridium oxide towards oxygen evolution reaction, even at intermediate temperatures, where kinetics are enhanced. A suggestion for a further analysis and development of this water electrolysis system is proposed:

- The kinetic study of IrO_2 towards oxygen evolution reaction in aqueous solution carried out in this research and its comparison to the solid state system rather 'risky' because of the difference between both system, in ion movility or water concentration for instance. For further analysis of iridium oxide performance towards OER, the kinetic study of IrO_2 in melted CsH_2PO_4 is suggested. For this purpose, a standard half-cell setup with a IrO_2 microelectrode to avoid mass transport issues is proposed. The system should be fed with water-saturated N_2 in order to avoid dehydration and provide reactant for the reaction.
- The use of alternative non-precious metal based catalysts may provide higher activity at the low acidic / neutral environment, reducing also the overall cost of the system. Co and Ni –based catalyst are proposed in the literature as alternative catalyst for OER in neutral conditions. Cobalt phosphate catalyst or other non precious metal-based phosphates may present an interesting alternative for a suitable compatibility between both phosphate-based electrolyte and catalyst [1-3].

Phosphate-based solid acids, specially CsH_2PO_4 due to its highest conductivity, could be applied as solid proton conducting agents in other different electrochemical devices rather than PEM water electrolysis. Electrochemical systems could benefit from the intermediate

temperature operation range and the mild acidity conditions provided by these materials. Next some suggestions of electrochemical systems are proposed:

- The methodology developed in this research for the fabrication of CsH_2PO_4 microfibers could be used for the preparation of CsH_2PO_4–based electrodes for intermediate temperature fuel cells. CsH_2PO_4 fibers would act as catalyst support providing a highly interconnected proton conducting framework in the catalyst layer increasing the triple-phase boundary on the electrode. The deposition of platinum on the CsH_2PO_4 fibers-mat could be carried out by sputtering techniques [4].
- Electrochemical sensors integrated in systems where the temperature reaches the intermediate range (150 – 300 ºC) may benefit from a solid acid electrolyte, as few other materials conduct protons at intermediate temperatures. The sudden transition of most solid acids to a proton conducting state at the intermediate temperature range could also be use as an indicator in these electrochemical devices.
- Electrochemical H_2 purification systems, commonly based in low temperature proton conductors, may benefit of a higher efficency at higher operation temperatures. The temperature limitations provided by the polymeric electrolyte (i.e. Nafion®) could be overcome by the use of a solid acid as electrolyte.

8.3. References

1. Esswein A. J., Surendranath, Y., Reece, S.Y. and Nocera, D.G., *Highly active cobalt phosphate and borate based oxygen evolving catalysts operating in neutral and natural waters.* Energy Environ. Sci., 2011. **4**: p. 499 – 504.
2. Surendranath, Y., Kanan. M.W. and Nocera, D. G., *Mechanistic Studies of the Oxygen Evolution Reaction by a Cobalt-Phosphate Catalyst at Neutral pH.* J. Am. Chem. Soc., 2010. **132** (46): pp. 16501–16509.
3. Lin, H., Zhang, Y., Wang, G. and Li, J-B., *Cobalt-based layered double hydroxides as oxygen evolving electrocatalysts in neutral electrolyte.* Frontiers of Materials Science, 2012. **6** (2): pp. 142-148.
4. Louie, M. W., Sasaki, K. and Haile, S. M., *Towards Understanding Electrocatalysis in CsH_2PO_4-Based Fuel Cells: Platinum and Palladium Thin Film Electrodes*. ECS transactions, 2008. **13** (28): p. 57-62.

APPENDIX A

SUPPORTING INFORMATION

In this section the data not exhibited in the thesis is included as supporting information for the reader. All figures exhibited in this section were addressed in the text.

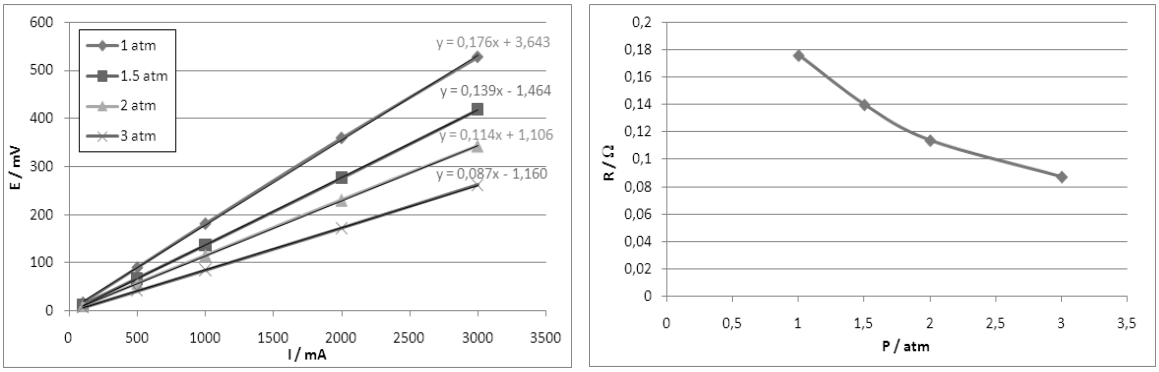

Figure A.1. Electrical resistance of electrolysis cell (figure 3.10) at different pressures applied by the piston.

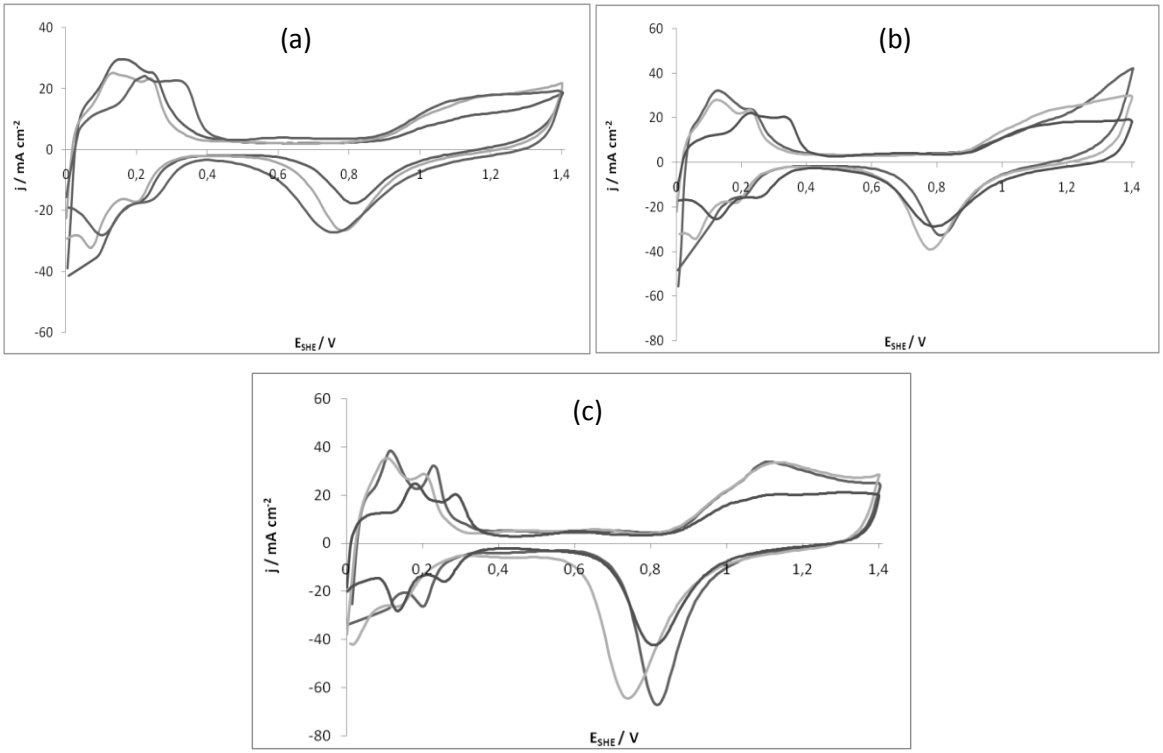

Figure A.2. CVs of Pt in 5.15 M (—**)** H_2SO_4. (—**)** H_3PO_4 and (**—)** CsH_2PO_4 at (a) 40 ºC, (b) 60 ºC and (c) 80 ºC (scan rate = 50 mV sec^{-1}).

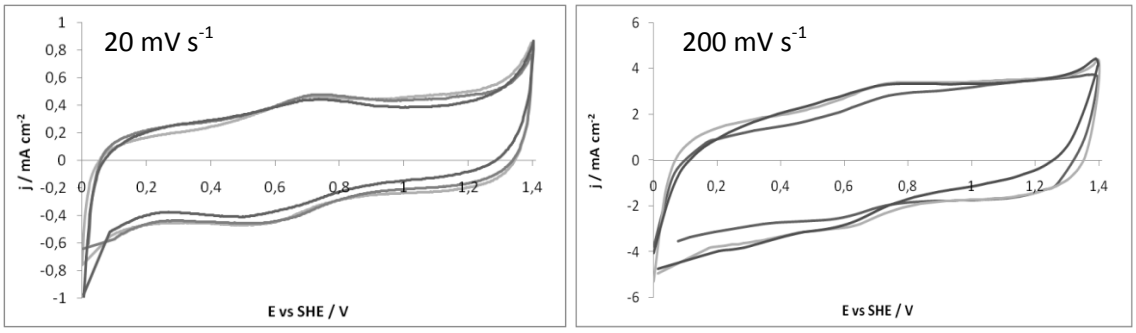

Figure A.3. CVs of IrO_2 in 5.15 M H_2SO_4 at **(—)** 40 ºC, (—**)** 60 ºC, (—**)** 80 ºC.

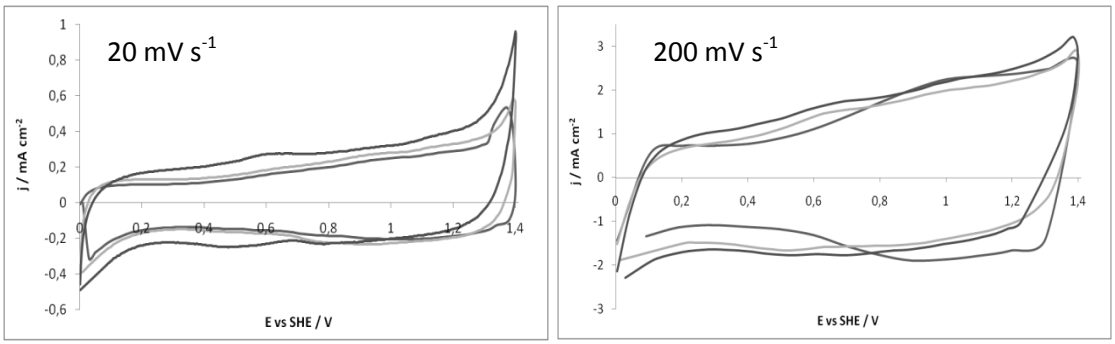

Figure A.4. CVs of IrO_2 in 5.15 M H_3PO_4 at **(—)** 40 ºC, (—**)** 60 ºC, (—**)** 80 ºC.

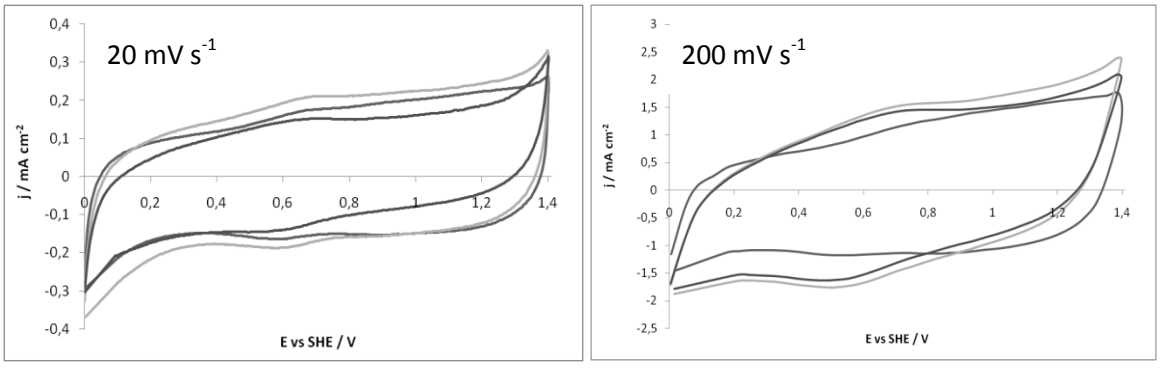

Figure A.5. CVs of IrO_2 in 5.15 M CsH_2PO_4 at **(—)** 40 ºC, (—**)** 60 ºC, (—**)** 80 ºC.

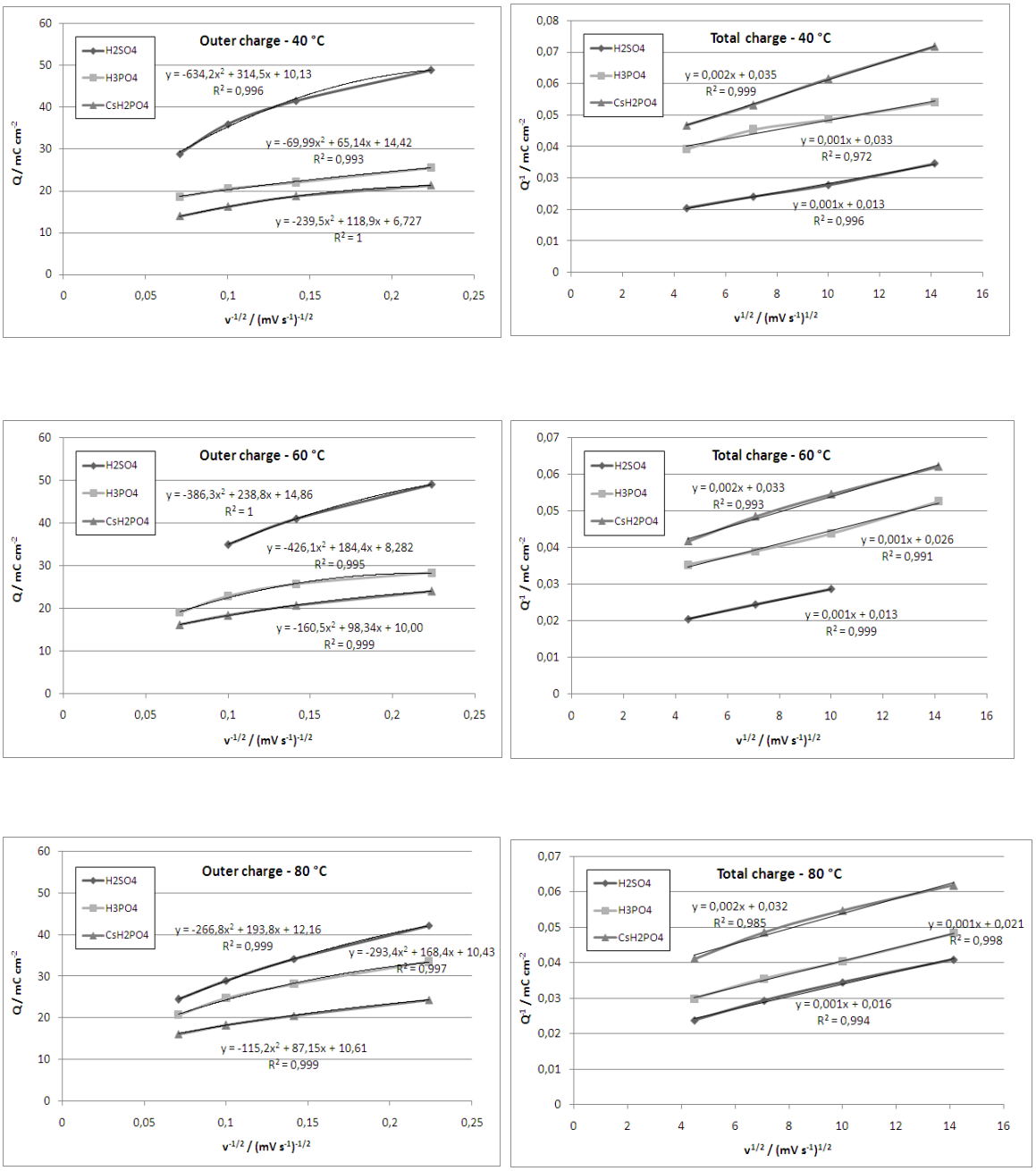

Figure A.6. Outer charge (left) and total charge (right) calculation plots for 5.15 M H_2SO_4, H_3PO_4 and CsH_2PO_4 aqueous electrolytes at 40, 60 and 80 °C.

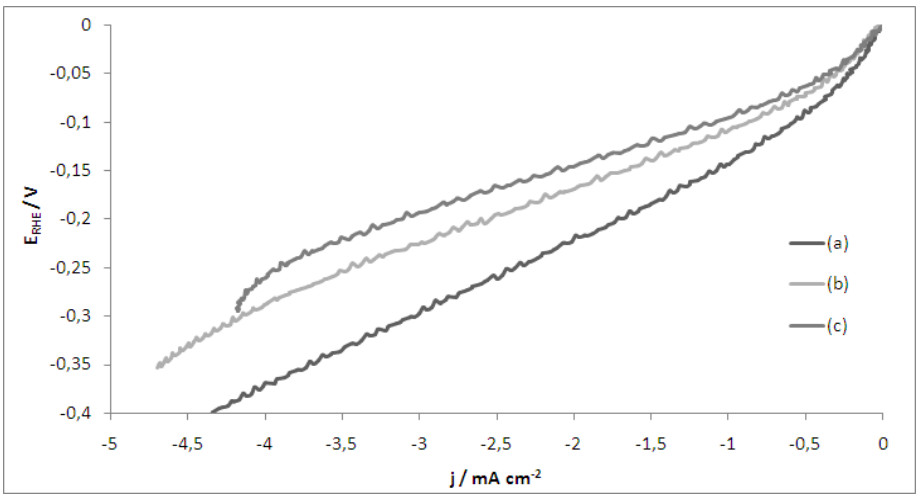

Figure A.7. HER polarisations with 1.0 mg Pt cm^{-2} and 5.15 M aqueous CsH_2PO_4 (sweep rate = 1 mV s^{-1}).

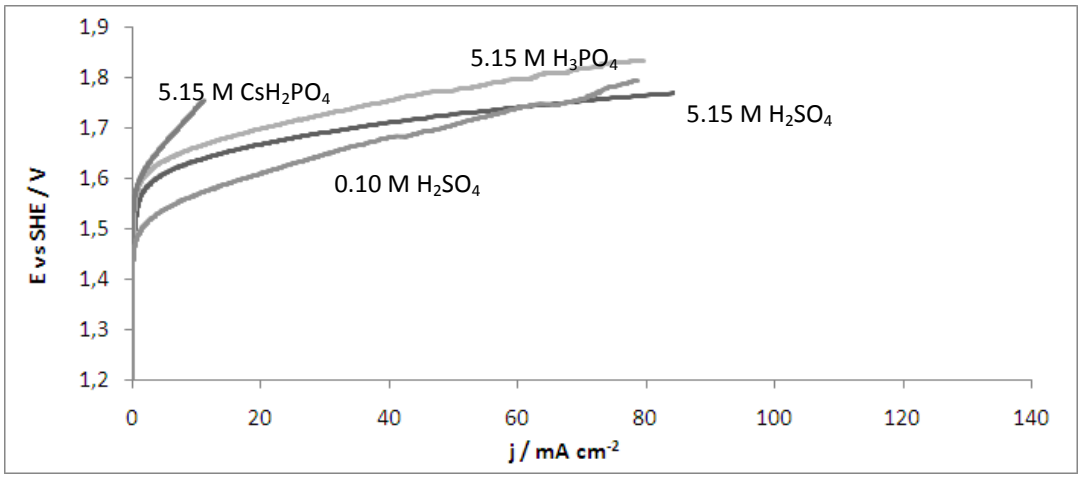

Figure A.8. OER polarisations of IrO_2 at 40°C (sweep rate = 1 mV s^{-1}).

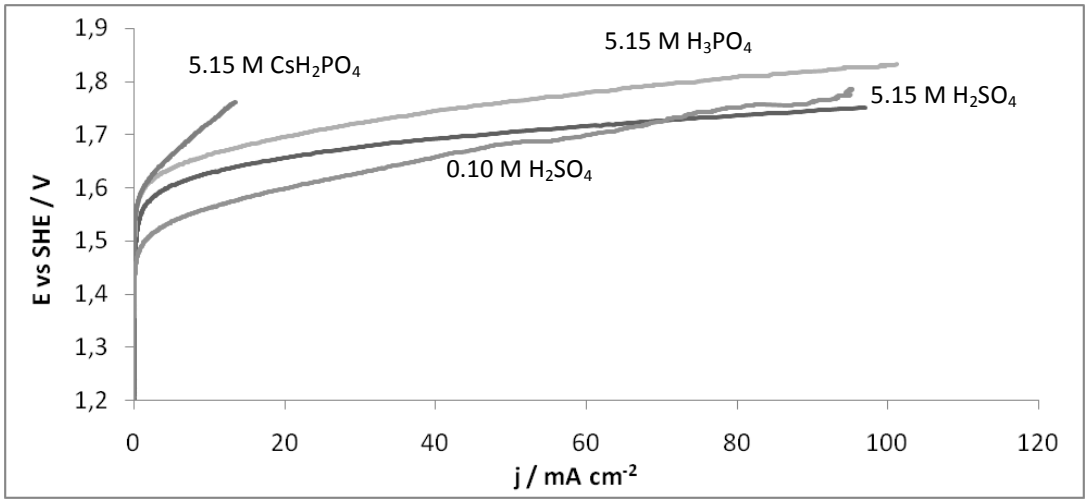

Figure A.9. OER polarisations of IrO_2 at 50°C (sweep rate = 1 mV s^{-1}).

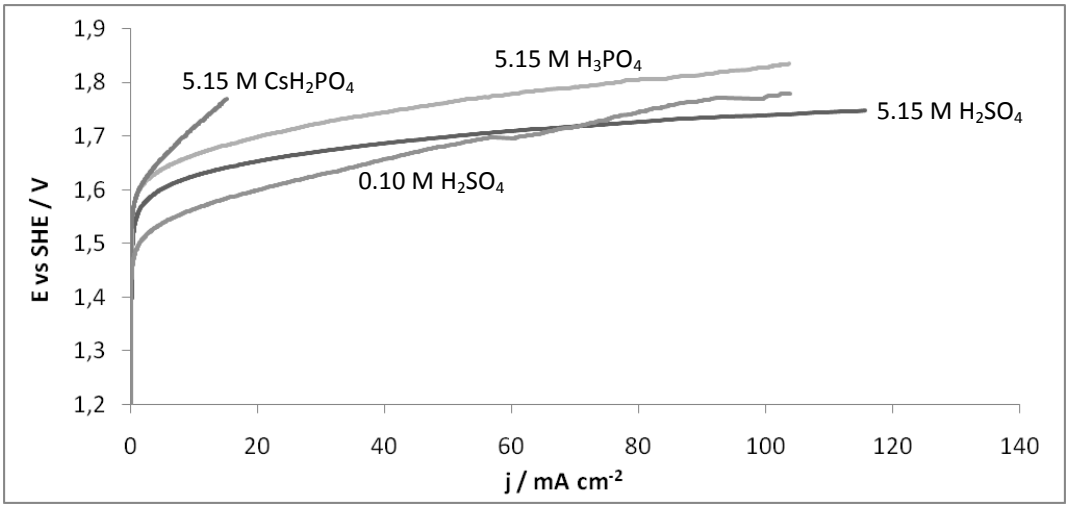

Figure A.10. OER polarisations of IrO_2 at 60°C (sweep rate = 1 mV s^{-1}).

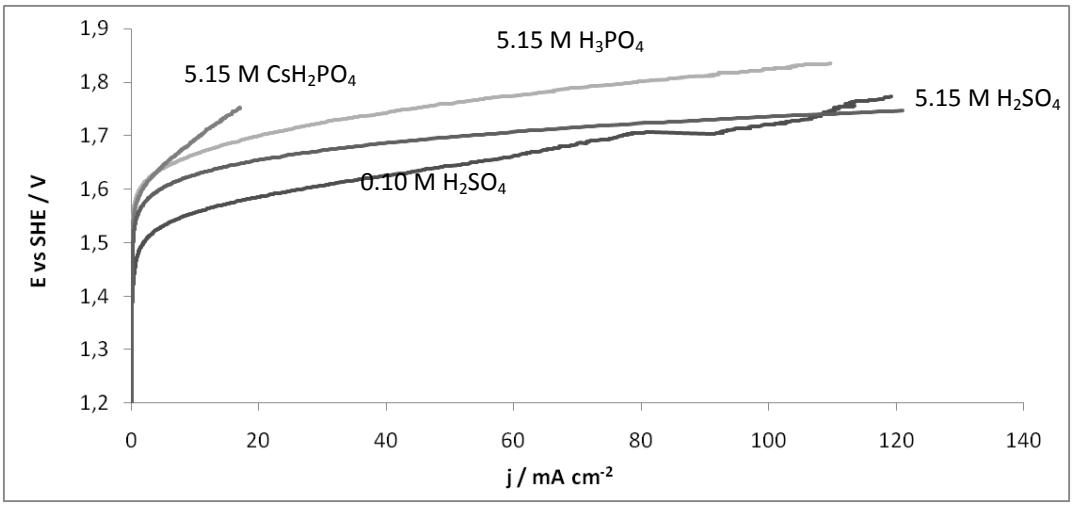

Figure A.11. OER polarisations of IrO_2 at 70°C (sweep rate = 1 mV s^{-1}).

APPENDIX B

LIST OF PUBLICATIONS AND DISSEMINATION

PUBLICATIONS:

Published papers in scientific journals:

1. A. Goñi-Urtiaga, D. Presvytes and K. Scott, *Solid acids as electrolyte materials for Proton Exchange Membrane (PEM) electrolysis: Review*. International Journal of Hydrogen Energy, 2012, **37**(4).
2. A. Goñi-Urtiaga, K. Scott, S. Cavaliere, D. J. Jones and J. Roziére, *A new fabrication method of an intermediate temperature proton exchange membrane by the electrospinning of* CsH_2PO_4. Journal of Material Chemistry, 2013, 1.

Papers to submit to scientific journals:

3. A. Goñi-Urtiaga, M. Mamlouk and K. Scott, *Cesium dihydrogen phosphate as electrolyte for PEM water electrolysis. Part 1 – The influence of the aqueous electrolyte on the oxygen evolution reaction behavior of iridium oxide.*
4. A. Goñi-Urtiaga and K. Scott, *Cesium dihydrogen phosphate as electrolyte for PEM water electrolysis. Part 2 – The application of a solid electrolyte in an intermediate temperature water electrolyser*.

CONFERENCES:

Oral presentations:

5. A. Goñi-Urtiaga and K. Scott, *Membrane materials for PEM electrolysers*. 9th ISCARW hydrogen safety course, Belfast, UK, 11 – 15 October 2010.
6. D. Prevytes, A. Goñi-Urtiaga and K. Scott. *Towards a High Temperature Water Electrolyser - Electrocatalysis and Membranes.* Electrochem 2011 conference, Bath (UK), 5 – 6 September 2011.
7. A. Goñi-Urtiaga and K. Scott, *Development of Composite Membranes based on Solid Acids for Medium Temperature PEM Electrolyser*. CEAM postgraduate student research conference, Newcastle upon Tyne (UK), 19 – 20 March 2012.
8. A. Goñi-Urtiaga, K. Scott, D.J. Jones and J. Roziére, *Fabrication of a intermediate temperature proton conducting membrane by the electrospinning of phosphate-based solid acids*. E-MRS 2012 Spring Meeting, Strasbourg (France), 14 – 18 May 2012.
9. A. Goñi-Urtiaga and K. Scott, *Development of* CsH_2PO_4 *– based composite membranes for Medium Temperature PEM Electrolyser*. CEAM postgraduate student research conference, Newcastle upon Tyne (UK), 20 – 21 March 2013.

10. A. Goñi-Urtiaga and K. Scott, *Development of composite membranes of phosphate-based solid acids for medium temperature PEM fuel cell and electrolyser.* 4th European PEFC and H_2 forum, Lucerne (Switzerland), 2 – 5 July 2013. (oral presentation)

11. A. Goñi-Urtiaga and K. Scott, *Cesium dihydrogen phosphate as electrolyte for Intermediate Temperature Proton Exchange Membrane Water Electrolysis (IT-PEMWE).* SUSHGEN final workshop, Paris (France), 29 November 2013.

Poster presentations:

12. A. Goñi-Urtiaga and K. Scott, *Membrane materials for PEM electrolysers.* Carisma II International Conference on medium and high temperature proton exchange membrane fuel cells, La Grande Motte (France), 20 – 24 September 2010.

13. A. Goñi-Urtiaga and K. Scott, *Fabrication of solid acid based composite membranes for medium temperature PEM electrolysis.* 'Water electrolysis and hydrogen as part of the future renewable energy system' symposium, Copenhagen (Denmark), 10 – 11 May 2012.

14. A. Goñi-Urtiaga and K. Scott, *Development of composite membranes of phosphate-based solid acids for medium temperature PEM fuel cell and electrolyser.* 4th European PEFC and H_2 forum, Lucerne (Switzerland), 2 – 5 July 2013. (poster presentation)